Republic of Iraq
Ministry of Higher Education and Scientific Research
University of Babylon
College of Education for Pure Sciences
Department of Physics

Synthesis of New Bionanocomposites and Recent Applications in Environmental Fields

A Dissertation
Submitted to the Council of the College of Education for Pure Sciences,
University of Babylon in Partial Fulfillment of the Requirements for the
Degree Doctor of Philosophy in Education / Physics

By

Mohanad Hasan Meteab Flaifel

B. Sc. in Physics
(University of Babylon, 2010)

M. Sc. in Physics
(University of Babylon, 2018)

Supervised by

Prof. Dr. Bahaa Hussien Salih Rabee

Prof. Dr. Ahmed Hashim Mohaisen Hamad

2023 A.D. **1445 A.H.**

بِسْمِ اللَّهِ الرَّحْمَٰنِ الرَّحِيمِ

﴿ أَنزَلَ مِنَ السَّمَاءِ مَاءً فَسَالَتْ أَوْدِيَةٌۢ بِقَدَرِهَا
فَاحْتَمَلَ السَّيْلُ زَبَدًا رَّابِيًا ۚ وَمِمَّا يُوقِدُونَ عَلَيْهِ
فِي النَّارِ ابْتِغَاءَ حِلْيَةٍ أَوْ مَتَاعٍ زَبَدٌ مِّثْلُهُ ۚ كَذَٰلِكَ
يَضْرِبُ اللَّهُ الْحَقَّ وَالْبَاطِلَ ۚ فَأَمَّا الزَّبَدُ فَيَذْهَبُ
جُفَاءً ۖ وَأَمَّا مَا يَنفَعُ النَّاسَ فَيَمْكُثُ فِي الْأَرْضِ ۚ
كَذَٰلِكَ يَضْرِبُ اللَّهُ الْأَمْثَالَ ﴾

صَدَقَ اللَّهُ الْعَلِيُّ الْعَظِيمُ

القران الكريم / سورة الرعد - الآية (١٧)

Dedication ...

To my parents for their endless love,

support and encouragement

To whose love flows in my veins,

and my heart always remembers them,

to my brothers, sisters, wife and children.

To my teachers ...

Who provide me the confidence and success

The martyrs of Iraq with all the love and appreciation.

Finally, this Dissertation is dedicated to all those who

believe in the richness of learning

✍

Mohanad

Acknowledgement …

First and foremost, I have to thank and Praise ***Allah****, who gave me health and strength to carry out the present research. In the second place, I thank the Beloved of God, the Prophet of Mercy and the Messenger of Humanity, the Prophet* ***Mohammad****, and the* ***family of Mohammad****, the lights of guidance and the signs of piety, the good and the pure, God's peace be upon them all.*

We would like to express my deep thanks to my supervisor ***Prof. Bahaa Hussien Salih (Ph.D.) and Prof. Ahmed Hashim Mohaisen (Ph.D.)*** *and for his encouragement, valuable guidance, helpful advice and efforts during the preparation of this work.*

I would like to express my deep thanks to ***The Dean of the College of Education for Pure Sciences*** *and* ***Head of the Physics Department*** *in the University of Babylon for their help in completing this work.*

Finally, special thanks to my ***mother, father, brothers, sisters, wife, children (Narjes, Jumana, Mohamad, Noor)****, and all my* ***friends*** *for their encouragement and unending support.*

✍

Mohanad

Supervisor Certification

We certify that this dissertation entitled **" Synthesis of New Bionanocomposites and Recent Applications in Environmental Fields"** is prepared by the student (**Mohanad Hasan Meteab**) under our supervision at the College of Education for Pure Sciences, University of Babylon as partial fulfillment of the requirement for the Degree Doctor of Philosophy in Education / Physics.

Signature:	Signature:
Name: **Dr. Bahaa Hussien Salih**	Name: **Dr. Ahmed Hashim Mohaisen**
Title: Professor	Title: Professor
Date: / / 2023	Date: / / 2023

Head of the Department Certificate

In view of the available recommendations, I forward this dissertation for debate by the examining committee.

Signature:
Name: **Dr. Khalid Haneen Abass**
Title: Professor
(Head of Physics Department)
Date: / / 2023

Examining Committee Certification

We certify that we have read this dissertation, entitled **"Synthesis of New Bionanocomposites and Recent Applications in Environmental Fields"** and as committee, examined the student (**Mohanad Hasan Meteab**) its contents, and that in our opinion it meets the standards of a dissertation for the Degree of Philosophy in Education / Physics.

Signature:
Name: Dr. Hamid Ibrahim Abbood
Title: Professor
Address: Al-Zahraa University for Women
Date: / / 2023
(Chairman)

Signature:
Name: Dr. Mohanad Hussein Oleiwi
Title: Professor
Address: University of Babylon
Date: / / 2023
(Member)

Signature:
Name: Dr. Nidhal Mohammed Obaid
Title: Assistant Professor
Address: University of Babylon
Date: / / 2023
(Member)

Signature:
Name: Dr. Huda Bukheet Hasan
Title: Assistant Professor
Address: University of Babylon
Date: / / 2023
(Member)

Signature:
Name: Dr. Ali Salah Hasan
Title: Assistant Professor
Address: University of Babylon
Date: / / 2023
(Member)

Signature:
Name: Dr. Bahaa Hussien Salih
Title: Professor
Address: University of Babylon
Date: / / 2023
(Member/Supervisor)

Signature:
Name: Dr. Ahmed Hashim Mohaisen
Title: Professor
Address: University of Babylon
Date: / / 2023
(Member/Supervisor)

Approved by the Council of the College of Education for Pure Sciences.

Signature:
Name: Dr. Bahaa Hussien Salih
Title: Professor
Address: Dean of the College of Education for Pure Sciences, University of Babylon.
Date: / / 2023

Scientific Supervisor's Certification

This is to certify that I have read this dissertation, entitled (**Synthesis, Characteristics and Recent Applications of New Bionanocomposites to Utilize in Environmental Fields**) and I found that this dissertation is qualified for debate.

Signature:
Name: Dr. Ali Hussain Abdalrazzaq
Title: Professor
Address: University of Kerbala
Date: / / 2023.

Scientific Supervisor's Certification

This is to certify that I have read this dissertation, entitled (**Synthesis, Characteristics and Recent Applications of New Bionanocomposites to Utilize in Environmental Fields**) and I found that this dissertation is qualified for debate.

Signature:
Name: Dr. Saleh Hasson Abud
Title: Professor
Address: University of Kufa
Date: / / 2023.

Linguistic Supervisor's Certification

This is to certify that I have read this dissertation, entitled (**Synthesis, Characteristics and Recent Applications of New Bionanocomposites to Utilize in Environmental Fields**) and corrected its grammatical mistakes; therefore, it has qualified for debate.

Signature:
Name: Dr. Ahmed Rawdhan Salman
Title: Assistant Professor
Address: AL- Mustaqbal University
Date: / / 2023.

Summary

In this study, new types (PC-PS/SiC-MnO_2), and (PC-PS/SiC-Co_2O_3) bionanocomposites based on the (PC/PS) polymeric blend, were synthesized by employing the solution casting technique. The basic composites of (PC/PS) polymeric blend was fabricated at a content of (50 wt.%) of polycarbonate and (50 wt.%) of polystyrene as well as silicon carbide (SiC) nanoparticles was added to (PC/PS) polymeric blend and then the manganese dioxide (MnO_2) nanoparticles, and cobalt trioxide (Co_2O_3) nanoparticles into (PC/PS) polymeric blend with different weight percentages as (1.3, 2.6, 3.9 and 5.2) wt.%. The impact of silicon carbide, manganese dioxide and cobalt trioxide nanoparticles additives on the structural, morphological, optical, (D.C and A.C) electrical characteristics of (PC/PS) polymeric blend, (PC-PS/SiC-MnO_2), and (PC-PS/SiC-Co_2O_3) bionanocomposites were studied for antibacterial activities, photodegradation, and pressure sensor applications have been prepared.

Fourier transformation spectroscopy (FT-IR) results displayed that there are no chemical interactions between the polymer matrix, (SiC/MnO_2, and SiC/Co_2O_3) nanoparticles, and the surface morphology of (PC–PS/SiC-MnO_2), and (PC–PS/SiC-Co_2O_3) nanocomposites were analyzed by optical microscope (OM) and field emission scanning electron microscope (FE-SEM) which showed good homogeneous and were distributed uniformly throughout of the (PC/PS) polymeric blend.

The optical characteristics of polymeric blend and nanocomposites were studied in the wavelength range (260-860) nm. The experimental results showed that the absorbance, absorption coefficient, Urbach energy, refractive index, extinction coefficient, (real and imaginary) dielectric constants and optical conductivity of nanocomposites were increased with an increase of the additive of (SiC/MnO_2 and SiC/Co_2O_3) nanoparticles contents, while transmittance, skin depth, and energy band gap were decreased with increasing the (SiC/MnO_2 and SiC/Co_2O_3) nanoparticles contents.

The results displayed that the D.C electrical conductivity of nanocomposites increases with increasing the (SiC/MnO_2 and SiC/Co_2O_3) nanoparticles contents and temperatures. The A.C electrical characteristics of nanocomposites were studied in the frequency ranging $(100 - 5 \times 10^6)\ Hz$ at standard room temperature. The experimental results showed that the dielectric constant, dielectric loss and A.C electrical conductivity of nanocomposites were increased with increasing the (SiC/MnO_2 and SiC/Co_2O_3) nanoparticles contents. The dielectric constant and dielectric loss of nanocomposites was decreased with increasing the frequency of the applied electric field, while A.C electrical conductivity increases with increasing the frequency and contents of (SiC/MnO_2 and SiC/Co_2O_3) nanoparticles.

The antibacterial activities of (PC/PS) polymeric blend, (PC-PS/SiC-MnO_2), and (PC-PS/SiC-Co_2O_3) bionanocomposites have been tested against pathogen (Staphylococcus aureus as Gram-positive bacteria, and Salmonella enterica as Gram-negative bacteria). The results showed that the inhibition zone diameter increases with increasing of (SiC, MnO_2 and Co_2O_3) nanoparticles additives weight ratio, and the Gram-positive bacteria have greater resistance to these nanoparticles compared to Gram-negative bacteria. The results showed that strong activities are the inhibition zone was increased with the increases of (SiC, MnO_2 and Co_2O_3) nanoparticles contents.

The absorbance of methylene orange dye decreased with adding SiC/MnO_2 nanoparticles, and SiC/Co_2O_3 nanoparticles contents. Also, the absorbance of methylene orange dye of (PC/PS) polymeric blend, (PC-PS/SiC-MnO_2), and (PC-PS/SiC-Co_2O_3) bionanocomposites samples decreases with an increase in the time of the irradiation. The photodegradation percentages for nanocomposites increase with the increase the time of the irradiation which leads to increase the photocatalytic reaction and reduced electron/hole recombination. The results show that the photocatalytic activity of nanocomposites was increased with increase the contents of (SiC, MnO_2 and Co_2O_3) nanoparticles. It is found the best photocatalytic activity for (PC-PS-SiC-Co_2O_3) nanocomposites was 27.94% within 30 minutes and 73.26% within 90 minutes at content (5.2 wt.%) of (SiC/Co_2O_3) nanoparticles. As a result, the nanocomposites have good photodegradation for organic pollutants.

The measurements of the pressure sensor for bionanocomposites were studied in the applied pressure range (80-160) bar using a locally manufactured system with high sensitivity. The results showed that the electrical capacitance of nanocomposites increases with increasing contents of additives and applied pressure. From the measurements of the sensing properties of nanocomposites for 160 bar, it is clear that nanocomposites are a good sensor for this pressure. It was found that the best sensitivity for nanocomposites (PC-PS/SiC-MnO_2) is 69.85% at a content of 5.2 wt.% and as a result, the nanocomposites (PC-PS-SiC-Co_2O_3) have higher sensitivity to pressure.

Content

Chapter One: Introduction and Literature Survey

Chapter Two: Theoretical Background

Chapter Three: Experimental Procedures

Chapter Four: Results and Discussions

Chapter Five: Conclusions and Future Works

List of Symbols

Symbols	Definition	Unit's
A	Absorbance	a.u.
A_0	Initial absorbance of methyl orange	a.u.
A_s	Constant area	cm^2
A_t	Absorbance after UV-Irradiation time	a.u.
c	Velocity of light in a vacuum	m/s
C_0	Vacuum capacitor	pF
C_b	Capacitances for blend	pF
C_n	Capacitances for nanocomposites	pF
C_p	Parallel capacitance	pF
C'_p	Heat capacity	J/kg. K
D	Dispersion factor	Unit less
$\overrightarrow{D_e}$	Electric displacement	A · s · cm^{-2}
$D_{inhibition}$	Diameter of the inhibition zones of the sample where bacteria were killed	mm
D_{MO}	Methyl orange degradation	Unit less
$D_{uninhibition}$	Diameter of the inhibition zones of the sample where no bacteria were killed	mm
$E_{act.}$	Activation energy	J
E_g	Band gap	J
$E_g^{Opt.}$	Energy gap between direct transition	J
$\overrightarrow{E_\iota}$	Internal electric field	V/cm
E_U	Urbach energy	J
$\vec{F}$	Normal force	N
$h\nu$ or $E_{ph.}$	Photon Energy	J

Symbols	*Definition*	*Unit's*
I	Intensity of incident photons	$\mathrm{W/m^2}$
I_0	Incident light intensity	$\mathrm{W/m^2}$
I_A	Absorbed light intensity	$\mathrm{W/m^2}$
I_T	Transmitting light intensity	$\mathrm{W/m^2}$
k	Extinction coefficient	Unit less
k_B	Boltzmann constant	J/K
n	Refractive index	Unit less
$N(E)$	Density of states	$J^{-1} \cdot m^{-3}$
n^*	Complex refractive index	Unit less
N_V	Number of molecules per unit volume	$\mathrm{molecules/cm^3}$
P	Pressure	bar
$\overrightarrow{P_\iota}$	Total dipole moment	$\mathrm{A \cdot s \cdot cm^{-2}}$
R	Reflectance	a.u.
r	Radius	cm
R_D	Overlapping respiratory inhibition ratios of bacteria	Unit less
R_v	Volumetric electrical resistance	Ω
S_{AP}	Pressure sensor sensitivity	Unit less
T_r	Transmittance	a.u.
T	Absolute temperature	K
t	Thickness	cm
T_g	Glass transition temperature	K
T_m	Melting temperature	K
v	Velocity of light in a sample	$\mathrm{m/s}$
w_b	blend weight	$\mathrm{wt.\%}$
w_f	filler weight	$\mathrm{wt.\%}$
α	absorption coefficient	$\mathrm{cm^{-1}}$
β	Constant depends on the type of material	Unit less
γ	exponential constant	Unit less
ΔG_b	Change in free energy	J

Symbols	Definition	Unit's
ΔH_b	Change in enthalpy	J
ΔK	Electron wave vector	cm^{-1}
ΔS_b	Change in entropy	J
δ	Skin depth	cm
ε	Complex dielectric coefficient	Unit less
ε'	Dielectric constant	Unit less
ε''	Dielectric loss	Unit less
ε_0	Permittivity in vacuum	$\mathrm{C/V.cm}$
$\mathrm{\varepsilon}_a$	Real part of the complex permittivity	$\mathrm{C/V.cm}$
$\mathrm{\varepsilon}_b$	Imaginary part of the complex permittivity	$\mathrm{C/V.cm}$
$\mathrm{\varepsilon}_i$	Imaginary part of the dielectric constant	Unit less
$\mathrm{\varepsilon}_r$	Real part of the dielectric constant	Unit less
κ_d	First-order rate constant	min^{-1}
λ	Wavelength of photon	nm
$\overrightarrow{\mu_\iota}$	Electric mobility	$\mathrm{cm}^2 \cdot \mathrm{V}^{-1} \cdot \mathrm{s}^{-1}$
$\bar{\nu}$	Wavenumber	cm^{-1}
$\rho_{D.C}$ or ρ_V	Resistivity	$\Omega\,.\,\mathrm{cm}$
ρ_p	Density	$\mathrm{g/cm}^3$
$\sigma_{A.C}$	Alternating conductivity	$\mathrm{S} \cdot \mathrm{cm}^{-1}$
$\sigma_{D.C}$	Direct current conductivity	$\mathrm{S} \cdot \mathrm{cm}^{-1}$
$\sigma_{Opt.}$	Optical conductivity	s^{-1}
σ_0	Direct current conductivity at absolute zero of temperature	$\mathrm{S} \cdot \mathrm{cm}^{-1}$
σ_T	Total electrical conductivity	$\mathrm{S} \cdot \mathrm{cm}^{-1}$
τ	Irradiation time	min
$\tau_{1/2}$	Half-life time	min
ω	Angular frequency	$\mathrm{rad/s}$

List of Abbreviations

Abbreviation	Definition
BNCs	Bionanocomposites
C.B	Conduction band
CMNC	Ceramic matrix nanocomposites
Co_2O_3	Cobalt trioxide
D.C	Direct current
FESEM	Field emission scanning electron microscope
FT-IR	Fourier Transform Infrared
MMNC	Metal matrix nanocomposites
MnO_2	Manganese dioxide
MO	Methyl orange
NCs	Nanocomposites
OM	Optical microscope
P_0	Space charge or interfacial polarization
P_d	Rotational or orientation polarization
P_i	Ionic polarization
PC	Polycarbonate
PCs	Polymer composites
PMNC	Polymer matrix nanocomposites
PNCs	Polymer nanocomposites
PS	Polystyrene
SiC	Silicon carbide
UV-Vis	Ultraviolet–visible
V.B	Valance band

List of Figures

List of Tables

Chapter One

Introduction
and
Literature Survey

Chapter Two

Theoretical Background

Chapter Three

Experimental Procedures

Chapter Four

Results
And
Discussions

Chapter Five

Conclusions and Future Works

Appendices

References

Introduction and Literature Survey

Chapter One

1.1 General Introduction

The scientific community is very interested in nanocomposites (NCs) because of their useful properties and wide range of potential uses, such as sensors, conductive coatings, microwave absorbers, energy storage, or other some devices. It is common to practice favoring polymer composites (PCs) with high dielectric constants when developing electrical components and capacitors [1]. According to their dimensions, nanomaterials can be divided into three-dimensional nanoparticles and nanoshells, two-dimensional nanotubes, nanofibers, and nanowires, one-dimensional thick coatings and layers, and zero-dimensional nanospheres and nanoclusters. In general, there is a great deal of interest in metal oxide nanomaterials as a result of their potential use in a vast array of applications, such as antibacterial activity [2].

In recent years, nanotechnology's applications have only increased, with the highest potential application in the field of materials, followed by applications in electronics and medical. The following are some potential nanotechnology applications: Filters for economically efficient desalination of water. Microsensors and diagnostics for antibacterial dressings and coatings that are more effective [3]. The physical, chemical, and structural properties of polymer composites (PCs) are as varied as those of the scientific and technological disciplines. Because of its multifunctional properties, such as low toxicity, simplicity of processing and sterilization, increased shelf life, and the low weight, it is used in various industries, including electronics, robotics, and medicine [4]. However, traditional polymer composites have disadvantages that limit their utility, such as weak mechanical strength and inadequate antibacterial and barrier qualities. Due to nanotechnology and polymer science developments, nanomaterial-based polymer composites (PNCs) have proven to be an effective method of overcoming these limitations [5–7]. Polymer nanocomposites are synthesized by reinforcing nanoparticles of varying shapes and sizes inside a polymer matrix [8]. However, the effectiveness of this reinforcement relies heavily on the aspect ratio, size, orientation, and dispersion of the nanoparticles involved [9]. These nanofillers reinforce polymer nanocomposites, improving their mechanical, thermal, barrier, and flammability qualities without affecting their processability [10, 11]. Nanomaterials such as polymer nanofibers, natural clays, metal oxides, metal particles, and nanomaterials based on carbon allotropes are employed to produce polymer nanocomposites [12].

Massive industrial expansion necessitates increasingly diverse and large quantities of chemicals in industrial processes. However, these activities are always accompanied by a massive degradation of ecosystems due to the production of various pollutants [13]. Worse, the majority of these contaminants are discharged directly into the environment without any treatment, posing not only an aesthetic problem but also a toxicological one, which is regarded as the one of the most pressing problems in the recent decades [14]. Most of these compounds are organic molecules used in things like colours and pharmaceuticals [15]. According to the ionic charge of their molecules, dyes are classified as anionic, cationic, or non-ionic; among these three types, the cationic group is regarded as the most poisonous [16]. Pharmaceuticals, such as the anti-inflammatory medications, antibiotics, analgesics, and others, are known to be highly reactive and potent carcinogenic compounds that cause damage to the DNA of cells. The toxicity of these substances varies according to their chemical makeup and the mechanism of action [17]. As a result of their widespread application, effluents from industries including the medical sectors, tanning, textile, leather finishing, pulp and paper, cosmetics,... etc., are becoming increasingly chemically concentrated [18].

1.2 Polymers

A polymer is a large molecule, or micromolecule, composed of many repeated subunits. Because of their broad range of properties, both synthetic and natural polymers play an essential and ubiquitous role in everyday life. Polymers range from familiar synthetic plastics such as polystyrene to natural biopolymers such as DNA and proteins that are fundamental to biological structure and function. Polymers, both natural and synthetic, are created via polymerization of many small molecules, known as monomers [19]. Their consequently large molecular mass relative to small molecule compounds produces unique physical properties, including toughness, viscoelasticity, and a tendency to form glasses and the semicrystalline structures rather than crystals [20].

Most commercial polymers are insulators due to how easily they can be manufactured, but polymers with a certain composition can act as semiconductors and thick films are just one of the many applications for polymeric materials, which can be made and processed in a variety of ways. [21]. It is composed of large organic molecules connected by chains of varying lengths, and these molecules are composed of monomers held together by covalent bonds [22]. In recent years, the functionalities of polymers that are synthesized to meet specific requirements of daily life have become increasingly important. Therefore, it is necessary to understand the properties of polymers. Polymers can be formed of chemical bonds such as covalent bonds, which are responsible for linking long polymer chains, and physical bonds including Van der Waals forces, dipolar bonds, and hydrogen bonds. Physical bonds such as hydrogen bonding have a significant impact on the physical properties of polymers. They depended on the molecular weight, polymer content, and solvent method varieties [23].

Polymers can be classified in several kinds based on the following categories [24, 25]. Such as source, polymerization, molecular forces, structure and degradability polymers as shown in Figure 1.1.

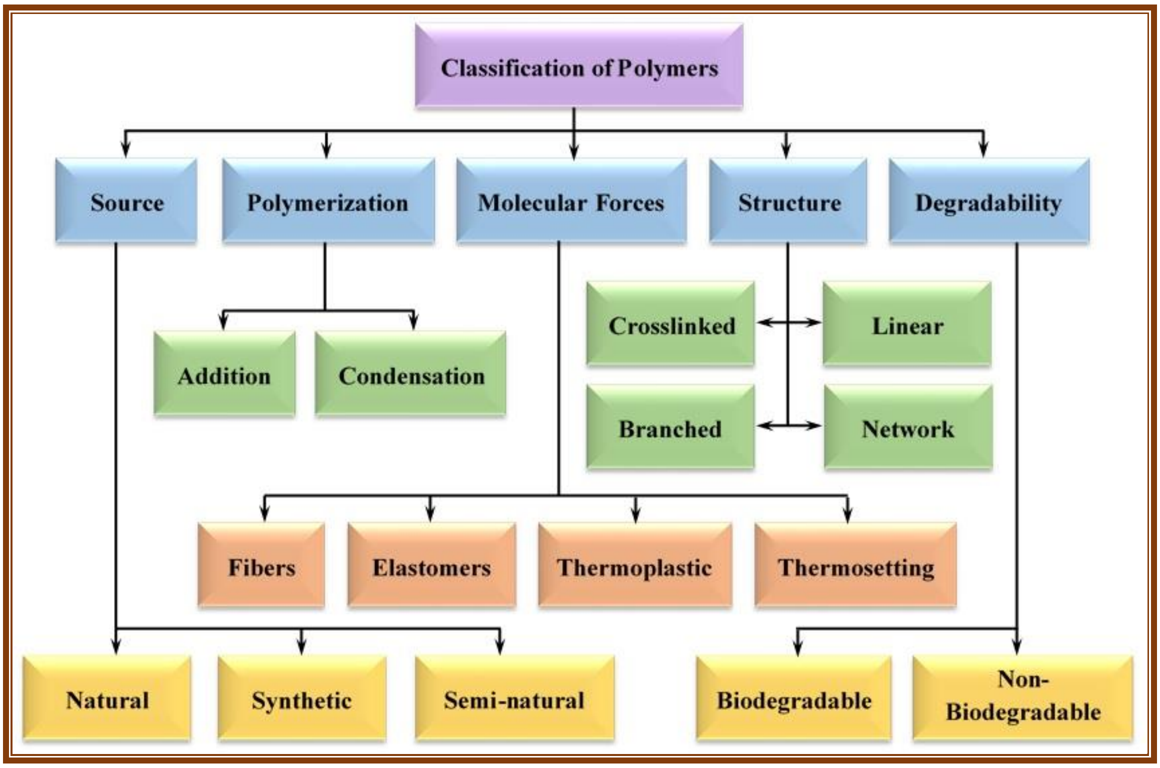

***Figure 1.1: Classification flow chart of Polymers* [24, 25].**

In every aspect of our existence and in every field, polymeric materials are ubiquitous. With all of its wealth and convenience, it is difficult to envision the modern world without polymeric materials. Polymer science is cutting-edge, thrilling, and straightforward to implement in a variety of contexts. Despite these significant characteristics, the polymer's structure flaws result in poor mechanical properties [26]. As a result, researchers have been working to create new methods and strategies for developing polymers of high quality, such as electrical, physical, thermal, and mechanical properties, that may have a variety of applications [27]. Nanotechnology is one of the finest and most successful methods that have been applied; polymer nanocomposite has been involved more and is receiving more attention from researchers, engineers, and the industrial sector in order to improve the performance of the new nanocomposite [28]. Utilised nanofillers, interface interaction, component quality, and a host of other variables all influence enhancement [29]. Where nanofillers have an impact on material properties. Assuming that interaction occurs between the dispersed particles and the matrix, the carbon family has recently been regarded as the most important nanofiller due to its ability to modify and enhance the properties of the materials [30].

Polymers have advanced significantly over the past decade. Scientists are currently developing polymers of the utmost quality for use in a variety of applications, and polymer research is rapidly advancing in a number of fascinating ways [31]. In addition, it expanded into numerous industries and applications, including photovoltaic cells, optoelectronics, and the medical field [32].

1.3 Polymer Blends

Polymers blended were the result of simple mechanical mixing of two or more polymers, which is considered a polymer modification operation. Like a metal alloy, a polymer blend consists of at least two distinct polymers that have been combined to create a new material with unique features [33]. The fate of polymer blends is derived from the compatibility and or miscibility of their components [34]. The majority of experimental studies have been conducted via casting from solution, whereas the majority of commercial polymer mixtures are prepared via melt mixing by twin-screw extrusion. Specific interactions between polymer chains determine the miscibility of two polymers. The entropy factor in equation (1.1), which represents the second law of thermodynamics, can explain this phenomenon [35].

$$\Delta G_b = \Delta H_b - T\,\Delta S_b \tag{1.1}$$

where, ΔG_b is change in free energy, ΔH_b is change in enthalpy, ΔS_b is change in entropy, and T is absolute temperature.

For a homogeneous miscible mixture, the Gibbs free energy of combining must be negative. For polymer mixtures with a high molecular weight, the increase in entropy is negligible. Consequently, the free energy of mixing can only be negative if the mixture heat is negative. This necessitates exothermic mixing, which typically necessitates specific interactions between the components of the composite. Hydrogen bonding, ion-dipole, dipole-dipole, and donor-acceptor interactions are examples of interactions that can range from strongly ionic to feeble and non-bonding [36]. On the basis of miscibility, three classes of mixtures can be distinguished: (**I**) completely miscible mixtures, (**II**) partially miscible mixtures, and (**III**) completely immiscible mixtures. Completely miscible mixtures consist of a single phase. This form of blend possesses a single glass transition temperature (T_g) that lies between the T_g of both blend components and is closely related to the blend's composition. Partially miscible mixtures, in which a portion of one mixture component is dissolved in the other, typically exhibit excellent compatibility and delicate phase morphologies. However, entirely immiscible mixtures display a coarse phase morphology with a sharp interface and poor adhesion between the two phases. This is the reason for the frequently observed subpar properties of immiscible blends, which are highly dependent on the phase sizes and distributions [37].

Polymer mix formation is a time-honored technique for creating novel materials with improved characteristics. Most polymer blends tend to phase split due to the substantial unfavourable enthalpy, leading to subpar mechanical characteristics. Since the performance of polymer blends is dependent on the interface between polymer components, managing the phase behaviour and morphology becomes an important factor. For decades, scientists have relied on block and graft copolymers to fortify interfaces and stabilise morphologies. However, they are system-dependent, complex to build and manufacture, and prohibitively expensive for systems with more than two parts [38].

There are several reasons to add filler of polymers, and polymeric blends are [39]:

1. Filler in a polymer can be used to create composites.
2. Pigments are used to colour the final polymer product.
3. Fillers are widely available and inexpensive; therefore, the price of the final polymer product can be estimated.
4. For better mechanical (toughness, bending, and strength), electrical (conductivity), and optical (dispersion) qualities in polymers.

1.4 Nanocomposites Materials

In the context of multiphase materials, nanocomposites are those in which one of the phases contains nanoscale additives. Nanocomposites can be broken down into three different types based on the matrix materials they are made of the ceramic matrix nanocomposites ($CMNC$), the polymer matrix nanocomposites ($PMNC$), and the metal matrix nanocomposites ($MMNC$) [40]. Due to their high resistivity and dielectric characteristics, polymers have been utilised as insulators since the beginning of scientific literature. Insulators made of polymers are used in electronics to keep conductors apart without conducting electricity. Electronics, printed circuit boards, and cable sheathing are all examples of insulator applications of polymers. Polymers' many benefits include their inexpensive price, simple production, adaptability, high strength, and excellent mechanical qualities. As part of the photolithography procedure, it is essential in the production of microelectronics [41].

In recent years, one category of materials known as polymeric nanocomposites, which are made up of inorganic nanoparticles and organic polymers, has attracted a significant amount of attention [42]. The nanocomposites applications are quite promising in the fields of microelectronic packaging, medicine, automobiles, optical integrated circuits, drug delivery, injection molded products, sensors, membranes, aerospace, packaging materials, coatings, fire-retardants, adhesives, consumer goods, … etc [43].

Bionanocomposites (BNCs) represent a promising frontier in nanotechnology life sciences and materials. Bionanocomposites consist of a polymer matrix and an organic/inorganic substance that has at least one nanoscale dimension [44]. Bionanocomposites constitute an intriguing interdisciplinary field that combines materials science, biology, and nanotechnology. New bionanocomposites have an effect on many fields, particularly biomedical science [45].

1.5 Applications of Polymer Nanocomposites

General Nanocomposites are materials in which at least one of the phases has nanoscale dimensions [46]. Their capabilities are so promising that they may be used in a wide range of applications from packaging to biomedicine [47]. Polymer nanocomposites have gotten a lot of attention in academia and industry over the last few decades and they've become a key component in the development of novel advanced materials for a variety of applications including electrical engineering [48]. Nanotechnology is a new science that has developed in which it has been observed that materials exhibit significantly different properties at nanometer sizes compared to properties of the same material at larger particle sizes. Nanotechnology is an emerging multidisciplinary technology that has flourished in many fields during the last decade, including science materials, mechanics, electronics, optics, medicine, plastics, energy and aerospace [49].

There are many studies on characteristics of composites and nanocomposies included optical properties, electrical and dielectric characteristics, to employ in various applications involved piezoelectric and sensors, biomedical, environmental and radiation shielding, electronic and optoelectronics, and energy storage [50, 51].

1.6 The Characteristics of Materials Used in Present Study

1.6.1 Polycarbonate (PC)

Polycarbonate (PC) is an example of a complex thermoplastic material that is used a lot these days. It is tough, has good mechanical properties, and is clear. Polycarbonate is also very stable at high temperatures, easy to work with, resistant to stains, non-toxic, and has low water absorption. Polycarbonate is great for electrical uses because it has a high dielectric strength and resistivity in volume that only goes down as the temperature is raised [52]. as shown in Figure 1.2, (Designed by the GaussView 6 program).

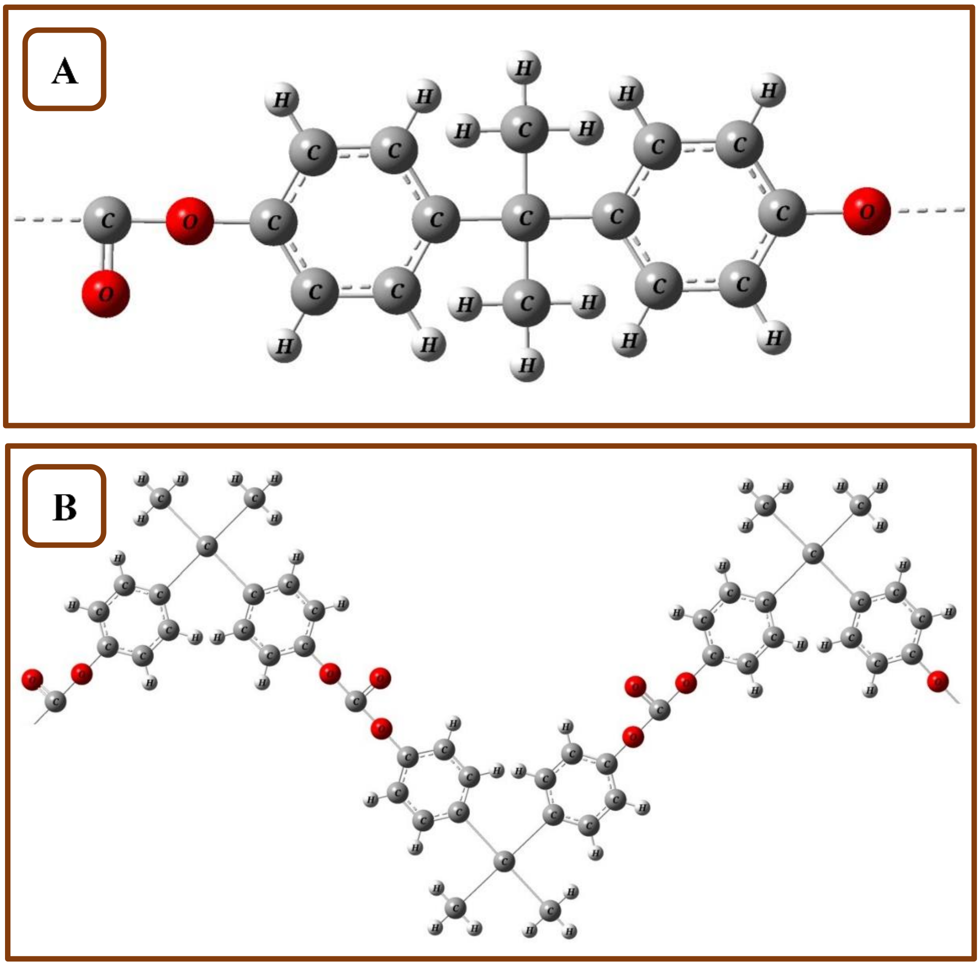

Figure 1.2: The molecular structure of polycarbonate: A) 1-monomer, and B) 3-monomers

Polycarbonate is mainly used in electronic applications that take advantage of security features. Being a good electrical insulator with heat-resistant and flame-retardant properties, it is used in many products associated with telecommunication devices and electrical appliances and can also act as an electrical insulation in highly stable capacitors [53]. PC's got their name because they are polymers containing carbonate groups abalance of beneficial features, including temperature resistance, shock resistance, and optical properties, places polycarbonate between commodity plastics and engineering plastics [53, 54]. PC characteristics are shown in Table 1.1.

Table 1.1: Characteristics of the polycarbonate polymer [54].

No.	Property	Value (unit)
1	Chemical formula	$[C_{15}H_{16}O_2]_n$
2	Band gap (E_g)	$4.45\ eV$
3	Dielectric constant (ε)	$(2.8 - 3.4)$
4	Resistivity ($\rho_{D.C}$)	$\left(10^{15} - 10^{18}\right)\ \Omega\,.cm$
5	Density (ρ_p)	$(1.19 - 1.22)\ g/cm^3$
6	Refractive index (n)	1.57 at $\lambda = 573.1\ nm$
7	Glass transition temperature (T_g)	$(158 - 134)$ ℃
8	Melting temperature (T_m)	$(255 - 267)$ ℃
9	Heat capacity (C_p')	$1.302\ KJ/Kg.K$

1.6.2 Polystyrene (PS)

Polystyrene (PS) is one of the most common thermoplastic polymers used in many industries, such as food packaging. Due to its high stiffness, strength, durability, good thermal properties, low moisture absorption, transparency, light density, ease of processing and molding, and low cost, this polymer is often used to package food [55]. PS is a flexible plastic that is commonly used in several aspects of human life and industry due to its low cost, light weight, ease of fabrication, flexibility, thermal efficiency, durability, and moisture resistance. However, polystyrene is exceptionally stable and difficult to degrade in the surroundings after disposal [56]. PS characteristics are shown in Figure 1.3, (Designed by the GaussView 6 program).

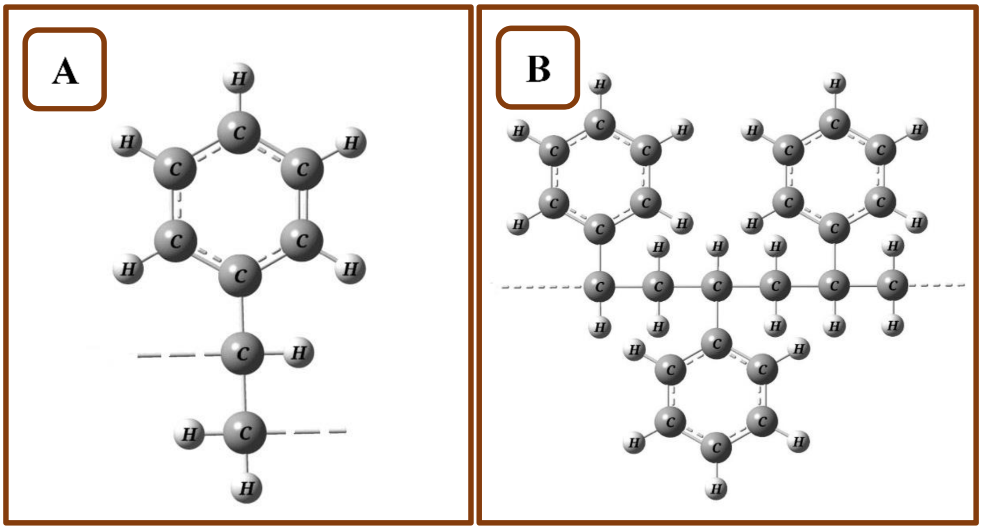

Figure 1.3: The molecular structure of polystyrene: A) 1-monomer, and B) 3-monomers

Model cars and airplanes are made from polystyrene, and it is also made in the form of foam packaging and insulation, Clear plastic drinking cups are made of polystyrene. So are a lot of the molded parts on the inside of your car, like the radio knobs. Polystyrene is also used in toys, and the housings of things like hairdryers, computers, and kitchen appliances. Polystyrene is produced by free radical vinyl polymerization, from the monomer styrene [57]. Table 1.2 show's the some characteristics of Polystyrene (PS).

Table 1.2: Characteristics of the polystyrene polymer [58].

No.	Property	Value (unit)
1	Chemical formula	$[C_8H_8]_n$
2	Band gap (E_g)	$4.59\ eV$
3	Dielectric constant (ε)	$(2.49-2.55)$
4	Resistivity ($\rho_{D.C}$)	$\left(10^{20}-10^{22}\right)\ \Omega.cm$
5	Density (ρ_p)	$(1.04-1.065)\ g/cm^3$
6	Refractive index (n)	1.59 at $\lambda = 589.3\ nm$
7	Glass transition temperature (T_g)	$(97-110)$ °C
8	Melting temperature (T_m)	(240) °C
9	Heat capacity (C_p')	$1.185\ KJ/Kg.K$

1.6.3 Silicon carbide nanoparticles (SiC NPs)

The silicon carbide (SiC) properties that make it useful in a wide range of applications include its high thermal stability, mechanical strength, electrical conductivity, pore volume, surface area, and roughness. Therefore, using SiC as a composite material would be highly advantageous in boosting the photocatalytic activity of the semiconductor metal oxides [59]. SiC offers superior resistance to wear and mechanical strength. SiC particles in the reinforced particulate can serve as both a cutting edge and an abrasive at the tool-work piece interface during machining. It also impacts the mechanical properties of composites, such as tensile strength and hardness. The presence of abrasive regions within the metal work piece causes rapid tool wear, increases cutting power, and significantly impacts the machined surface quality [60]. SiC may offer a safe way to protect vital surfaces against bacterial adherence and degradation without sacrificing the bulk rates of conventional dental material technologies [61]. Figure 1.4, shows the lattice structure of SiC and the important characteristics of the SiC nanoparticles can be summarized in Table 1.3. General representation of [A) the molecular structure B) the crystalline structure] of the SiC nanoparticles, (Designed by the A-GaussView 6, and B-VESTA program).

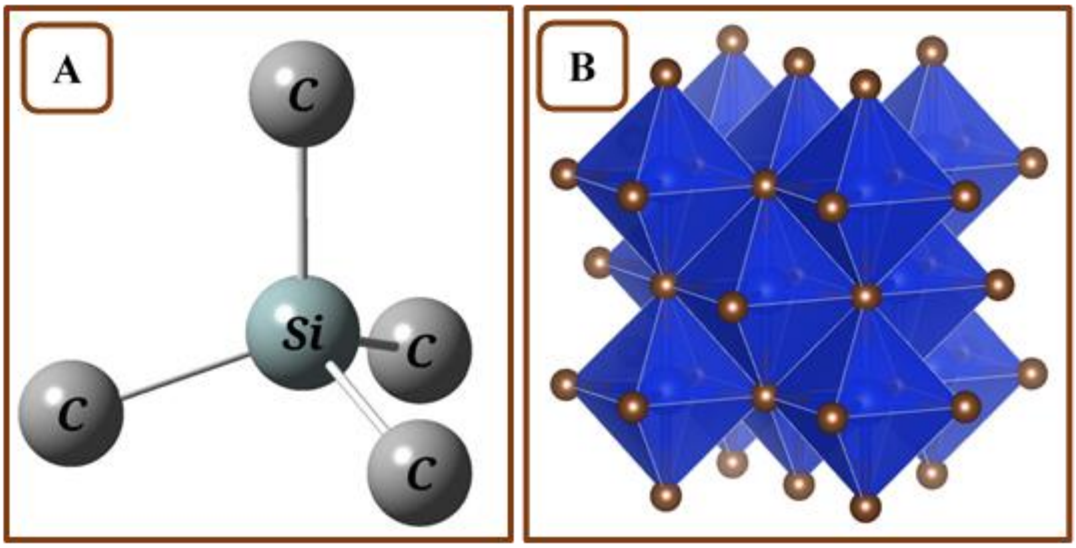

Figure 1.4: General representation of [A) the molecular structure B) the crystalline structure] for SiC nanoparticles

Table 1.3: Characteristics of Silicon Carbide nanoparticles [62].

No.	Property	SiC
1	Direct band gap (E_g)	$3.26\ eV$
2	Indirect band gap (E_g)	$2.58\ eV$
3	Color	$Silver - black\ solid$
4	Crystal Structure	$Fm\bar{3}m$, Cubic
5	Density	$(3.21)\ g/cm^3$
6	Lattice Constants	a=b=c=4.0502 A°
7	Melting Point	$(2760 - 2850)$ ℃
8	Solubility in water	$insoluble$
9	Molar mass	$40.096\ g/mol$

1.6.4 Manganese dioxide nanoparticles (MnO_2 NPs)

Manganese (IV) oxide or manganese dioxide is the inorganic compound with the formula (MnO_2). This blackish or brown solid occurs naturally as the mineral pyrolusite, which is the mainore of manganese and a component of manganese nodules. MnO_2 acts as a diverse material in technical and fundamental aspects [63].

Manganese dioxide exhibited various feasibilities in wide application such as catalysis, molecular adsorption, sensors, energy storage electrodes, etc. . In addition, MnO_2 can also be available for environmental technology such as dye degradation, wastewater treatment, photocatalytic degradation of organic pollutants and photo-electrochemical hydrogen production [64]. Figure 1.5, shows the lattice structure of MnO_2 and the important characteristics of the MnO_2 nanoparticles can be summarized in Table 1.4.

The manganese oxide nanoparticles (MnO_2) have a lot of potential for long-term nanotechnology. Due to their favorable physical and chemical properties, MnO_2 can be used in molecular sieves, solar cells, batteries, catalysts, magnetic materials, optoelectronics, drug delivery ion-sieves, and other areas such as imaging contrast agents, magnetic storage devices, and water treatment and purification. Furthermore, Mn-oxides are often less poisonous materials than other compounds on which NPs are based, such as various chalcogenides, and they have environmental friendliness, high specific capacitance, and cost-effectiveness [65]. General representation of [A) the molecular structure B) the crystalline structure] of an MnO_2 nanoparticles, (Designed by the A-GaussView 6, and B-VESTA program).

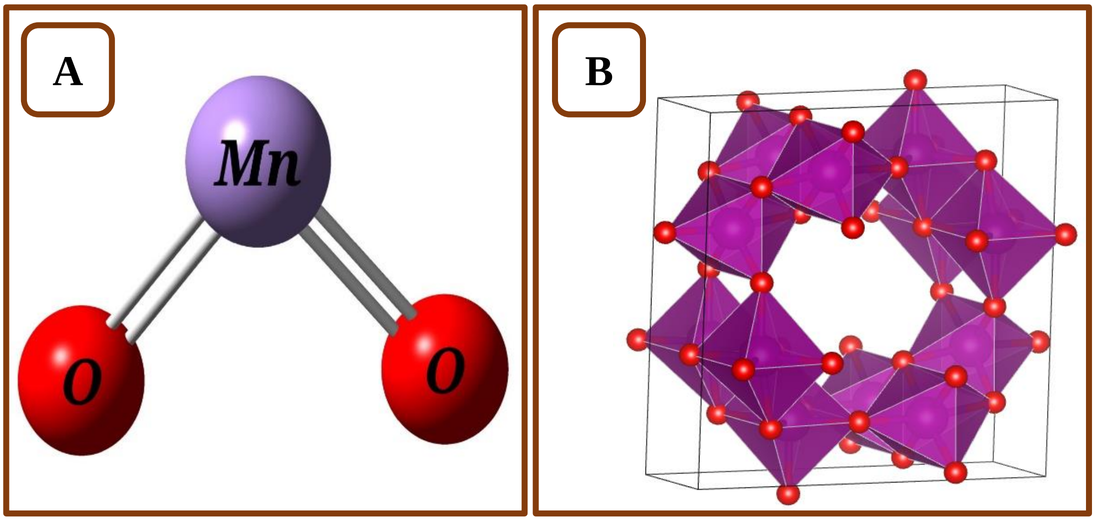

Figure 1.5: General representation of [A) the molecular structure B) the crystalline structure] for MnO_2 nanoparticles

Table 1.4: Characteristics of Manganese (IV) Oxide nanoparticles [66].

No.	Property	MnO_2
1	Direct band gap (E_g)	$3.70\ eV$
2	Indirect band gap (E_g)	$2.41\ eV$
3	Color	$Brown - black\ solid$
4	Crystal Structure	$I4/m$, Tetragonal
5	Density	$(3.19)\ g/cm^3$
6	Lattice Constants	a=b= 9.71686 $A°$ c= 2.85470 $A°$
7	Melting Point	$(2760 - 2850)$ °C
8	Solubility in water	$insoluble$
9	Molar mass	$40.096\ g/mol$

1.6.5 Cobalt trioxide nanoparticles (Co_2O_3 NPs)

Cobalt trioxide (Co_2O_3) is a highly insoluble thermally stable Cobalt source suitable for glass, optic and ceramic applications. Oxide compounds are not conductive to electricity. However, certain perovskite structured oxides are electronically conductive finding application in the cathode of solid oxide fuel cells and oxygen generation systems. They are compounds containing at least one oxygen anion and one metallic cation [67]. They are typically insoluble in aqueous solutions (water) and extremely stable making them useful in ceramic structures as simple as producing clay bowls to advanced electronics and in light weight structural components in aerospace and electrochemical applications such as fuel cells in which they exhibit ionic conductivity. Metal oxide materials have increasing demand in the scientific community due to their eco-friendliness, stability, natural abundance ease of synthesis, and wider application purposes [68]. Figure 1.6, shows the lattice structure of Co_2O_3 and the important characteristics of the Co_2O_3 nanoparticles can be summarized in Table 1.5. General representation of [A) the molecular structure B) the crystalline structure] of an Co_2O_3 nanoparticles, (Designed by the A-GaussView 6, and B-VESTA program).

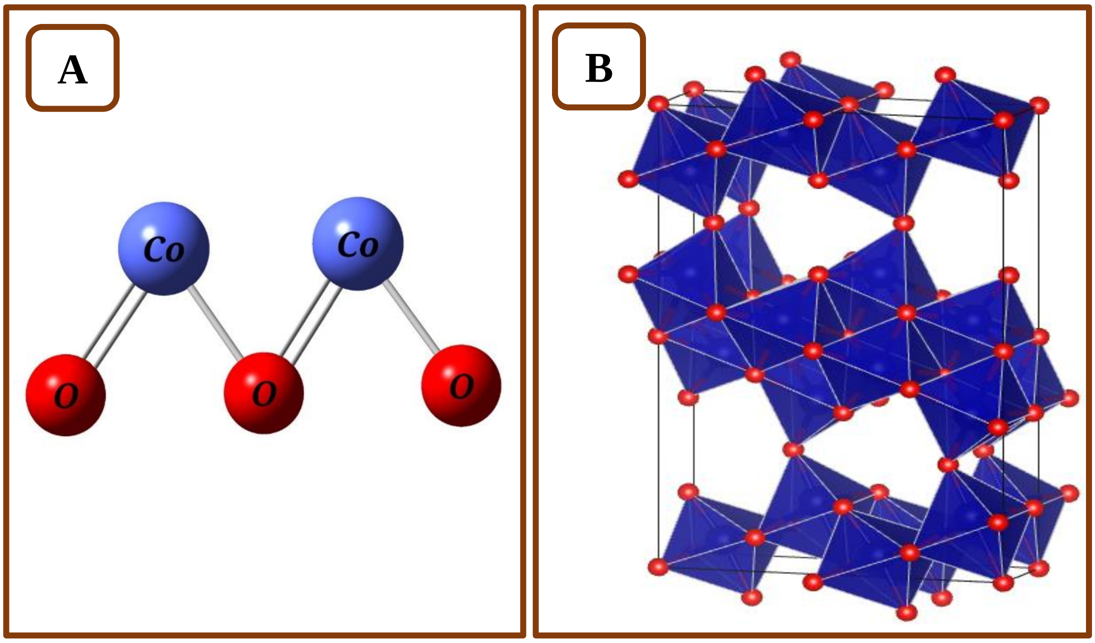

Figure 1.6: General representation of [A) the molecular structure B) the crystalline structure] for Co_2O_3 nanoparticles

Cobalt oxide nanostructures have been considered as promising electrode materials for various electrochemical applications, especially for supercapacitors, batteries, and electrocatalysis, owing to their unparalleled advantages of high theoretical capacity, highly-active catalytic characteristics, and outstanding thermal/chemical stability [69].

Table 1.5: Characteristics of Cobalt (III) Oxide nanoparticles [67, 70].

No.	Property	Co_2O_3
1	Direct band gap (E_g)	3.27 eV and 2.65 eV
2	Indirect band gap (E_g)	2.04 eV and 1.79 eV
3	Color	$black\ solid$
4	Crystal Structure	$Cmcm$, Orthorhombic
5	Density	(5.87) g/cm^3
6	Lattice Constants	a= 3.01850 $A°$ b= 9.84905 $A°$ c= 15.21637 $A°$
7	Melting Point	(840 – 895) °C
8	Solubility in water	$insoluble$
9	Molar mass	240.83 g/mol

1.7 Literature Survey

There are many applications for nanocomposites as medical and industrial applications. So, the structural, morphological, electrical and optical characteristics were studied by many researchers, to know the advantages for their applications.

In 2012, B. S. Rathore *et al.* [71], examined the polycarbonate/polystyrene composite sheets were bombarded with 55 MeV Carbon ions at $1\times10^{11} – 1\times10^{13}$ ions/cm^2. Polymer composites films were made via solution mixing. UV-vis, FT-IR, and optical microscopy were used to study the impacts of the ion beam on PC/PS composite films' structural, optical, and surface morphology. As fluences increase, UV-vis spectra show that energy band gap and transmittance drop and carbon atoms increase. At high ion fluences, FT-IR spectra showed little change in crosslinking and chain scissoring, but optical microscopy showed a colour change.

In 2013, B. Tripathi [72], used the solvent casting was presented work deals with Multiwall Carbon Nanotube (MWNT) / polycarbonate (PC) nanocomposites have been synthesized by solution cast method and characterized by various techniques for their use as an energy storage system. Ultraviolet-Visible (UV-VIS) spectra show enhanced optical absorption. Cyclic voltammetric results show enhanced capacitance at higher concentration of MWNTs in PC matrix. Optical micrographs show optical uniformity and surface morphology of MWNT/PC nanocomposites.

In 2014, B. H. Rabee *et al.* [73], investigated the impact of Zinc chlorides on optical and electrical properties of (PS-PMMA) copolymer have been investigated. The samples of composites were prepared by using casting technique. The optical properties measured in the wavelength range from 200 nm to 800 nm. The experimental results showed that the absorbance, absorption coefficient, energy band gap, extinction coefficient, refractive index and real and imaginary parts of dielectric constants are increasing with the increase of the Zinc chloride concentration. The electrical properties measured in temperature range from 300°C to 800°C. The results showed that the D.C electrical conductivity (PS/PMMA) copolymer is increased with the increasing of the weight percentages of Zinc chloride and temperature. The activation energy of composites decreases with increase of Zinc chloride concentration.

In 2015, M. S. Gaur and B. S. Rathore [74], performed by using a solution-mixing method, Polycarbonate (PC)/Zinc oxide (ZnO) nanocomposite films were made and then blasted with Swift heavy ions at different fluences ranging from 1×10^{11} to 3×10^{13}. Fourier transform infrared spectroscopy (FTIR), and differential scanning calorimetry, Thermogravimetric (TG), and thermally stimulated discharge current (TSDC) were used to look at the surface morphology, structure, and thermal properties of untreated and irradiated PC/ZnO nanocomposite films. The TSDC test shows that there are different kinds of ways to relax. For -relaxation peak, the activation energy released charge and charge carrier mobility go down, while the relaxation time and peak current go up. With more ions, TG measurements show that temperature stability and mass loss go down. In PC and nanocomposite films, FTIR readings show where different bonds are. Ion fluences are seen to make the glass transition temperature of nanocomposites go down.

In 2016, S. Agarwal *et al.* [75], prepared the ZnO nanoparticles that are uniformly dispersed in a Polycarbonate/Polymethylmethacrylate (PC/PMMA) blend nanocomposites simple chemical method has been utilized. The size of the nanoparticles has been confirmed to be approximately 11 nm using Transmission Electron Microscopy (TEM). Optical constants, such as band gap, extinction coefficient, refractive index, and the real & imaginary parts of the dielectric constant, have been determined from the absorption spectra, which were obtained using a UV-Visible spectrophotometer. The results demonstrate that the band gap reduces as the ZnO weight percentage increases in the blend nanocomposites. Moreover, an increase in the refractive index has been observed with the increasing content of ZnO. These types of blend nanocomposites have practical applications in UV-shielding and waveguide technologies.

In 2017, G. Santhosh *et al.* [76], manufactured the solution intercalation with halloysite nanotubes (HNTs) reinforced polycarbonate (PC) nanocomposites was used. The structural and dielectric characteristics of HNT content were examined. To determine how nano-fillers affect PC's electrical properties, the films' qualities were examined. HNT's reinforcing effect improves performance. Polycarbonate's electrical conductivity improved with more than 4 wt% HNT. Interestingly, HNT incorporation greatly boosts the dielectric permittivity of composite films with low dielectric loss, making nanocomposites interesting for practical applications such electrical devices, electrical packaging, and capacitors. Fourier transform infrared spectroscopy, and scanning electron microscopy revealed structural details.

In 2018, S. Li *et al*. [77], synthesized the zein, poly propylene carbonate (PPC), and nano-TiO_2 were extruded into composite films. SEM, DSC, FTIR, and mechanical characteristics were used to characterise the samples. The Halsey equation predicts composite film tensibility under varying humidity conditions by relating tensile strength to relative humidity. Zein and PPC formed a homogenous network structure and consistent nano-TiO_2 distribution in films, according to the SEM investigation. Additionally, the composite films were thermally stable. The structural study showed that ester groups formed complexes. The photocatalytic degradation of methyl orange (MO) followed pseudo first-order kinetics and removed up to 85.06% of MO. Zein/PPC/nano-TiO_2 film performed well against E. coli, S. aureus, and salmonella in the antibacterial trial. The proposed film may be a food packaging option, according to the results.

In 2019, Y. Khairy *et al*. [78], adsorbed the cationic and anionic dyes of photodegrading on TiO_2-chitosan nanocomposites. Adsorption, photodegradation, and TiO_2-Chitosan nanocomposite specific surface area, pore volume, and pore size were examined. TiO_2-nanocomposite was combined with cationic and anionic dyes for different contact times and initial dye contents to get the desired results. Chitosan content (TiO_2/Chit 0.13) lowered the nanocomposite's SBET. Chitosan surface-NH_2 and -OH contents impacted nanocomposite adsorption. TiO_2-chitosan nanocomposites removed anionic dye better than cationic dye, with MO having a higher maximum adsorption capacity (qm) and even higher reported reaction constant (kObs).

In 2019, A. M. Patki *et al.* [79], studied the solution-pressed hexagonal boron nitride (h-BN) reinforced polycarbonate (PC) composites were made. h-BN was 0–60 wt.% (~ 44.4 vol%). Composite morphology, electrical volume resistivity, microhardness, and dielectric characteristics were characterised. SEM demonstrated homogeneous h-BN particle distribution in the PC matrix. Fourier transforms infrared spectroscopy demonstrated no change in composite PC shape. 60 wt.% h-BN composites had 3.9 dielectric constants. The composites have a dissipation factor of less than 0.007 and a steady dielectric constant from 1 kHz to 10 MHz compared to pure PC. Composites have electrical volume resistivity similar to pure PC. At 50 wt.% h-BN content, microhardness climbed 25%, then decreased somewhat.

In 2020, M. F. H. Al-Kadhemy *et al.* [80], prepared the Pure blend Polycarbonate-Polystyrene (PC-PS) and doped blend films with various volume of Coumarin dye were prepared by using the casting method. The absorption and transmission spectra for these films were measured using UV/VIS spectrometer technique in order to assess the type of transition which was found to be an indirect transition. The optical energy gaps of pure PC was 4.24 eV, pure PS was 4.39 eV, Coumarin dye was 4.08 eV, and the pure blend was 4.1 eV. After doping blend with Coumarin dye, the energy gap was decreased by 0.06 eV in a volume of 12 ml. The results showed that the absorption coefficient and energy band gap are affected by doping. When the Coumarin dye was added to the pure blend with different concentrations (12, 24, 36, and 48) ml, the FTIR spectrum was affected by the disappearance of peaks and appearance of new ones.

In 2021, N. A. H. Al-Aaraji *et al.* [81], improved the PVA/CuO-SiC nanocomposites' dielectric characteristics for electronics. PVA films and CuO-SiC NPs-doped PVA were cast. PVA/CuO-SiC nanocomposites were examined using FTIR and optical microscopy. LCR metres measured dielectric characteristics from 100 Hz to 5 MHz. Structural properties of PVA/CuO-SiC nanocomposites showed no chemical interactions. PVA matrix CuO-SiC NPs are also abundant. Dielectric characteristics of PVA increased with CuO-SiC NPs content. PVA/CuO-SiC nanocomposites dielectric characteristics vary with frequency. Finally, the structural and dielectric features of PVA/CuO-SiC nanocomposites make them suitable for lightweight, flexible, and corrosion-resistant electronics applications.

In 2021, Y. K. Saraswat *et al.* [82], used the solvent casting was presented work deals with the structural and optical properties of chemically synthesized TiO_2 nanoparticles filled PC/PS blend nanocomposites. A series of PC/PS (100/0, 50/50, 0/100 wt.%/wt.%) -TiO_2 (1, 2, 3 wt %) blend nanocomposites have been prepared by solution casting method. Prepared blend nanocomposites have been subjected to SEM and FTIR for structural analysis. Optical constants have been analyzed using UV-Vis spectroscopy. The SEM and FTIR spectrum confirms the formation of PC/PS-TiO_2 blend nanocomposites. Results reveal the decrease in band gap and enhancement in optical constants like, extinction coefficient, refractive index and dielectric constants of blend nanocomposites with nanofiller TiO_2 content.

In 2022, Y. Chen *et al.* [83], used the two processes, CeO_2 nanoparticles (NPs) crystallise on polyaniline (PANI)-modified polystyrene (PS) latexes. UV–Vis spectra, Fourier-transform infrared, and photoluminescence (PL) spectroscopy characterised the polymer/CeO_2 products. Photocatalysts, core/shell polymer/CeO_2 composites destroyed methylene blue dye molecules in water. PS/PANI/CeO_2 ternary hybrids were compared to PS/CeO_2 binary composites for UV photocatalysis. UV–Vis and PL spectra showed that PS/PANI/CeO_2 had a lower bandgap, a wider light response range, and a greater separation efficiency of photogenerated electron–hole pairs, which boosted photocatalytic activity. As expected, the tri-layer PS/PANI/CeO_2 hybrids demonstrated greater photodegradation efficiency than PS/CeO_2 and commercial CeO_2 NPs, probably due to CeO_2 and PANI synergy. Tri-layer PS/PANI/CeO_2 hybrids photodegrade organic dye-containing wastewater.

In 2022, A. H. Mohammed, and M. A. Habeeb [84], formed the solution casting (PVA-PVP-Co_2O_3) nanocomposites with 0–6.4 nanoparticle weight percent ratios. Optical imaging shows a continuous network of high-content cobalt oxide nanoparticles in polymers (6.4 wt.%). SEM demonstrates that (PVA-PVP-Co_2O_3) films have a uniform, cohesive surface with numerous aggregates. film optics. The weight percentages of Co_2O_3 enhanced the absorption coefficient, absorbance, refractive index, extinction coefficient, real and imaginary dielectric constants, optical conductivity, and transmittance, while transmittance decreased. The optical energy gap of (PVA-PVP-Co_2O_3) nanocomposites ranged from 4.58 eV for the blend to 3.82 eV for allowed indirect transition and 4.03 to 3.21 eV for banned indirect transition at 6.4 wt.% Co_2O_3. These findings may help photonics and optoelectronic nanocomposites.

In 2022, H. A. J. Hussien *et al*. [85], controlled the research fabricates a (PEO-PVP) mix doped with SnO_2/MnO_2 NPs for photodegradation of organic contaminants with cheap cost, high activity, propagation, and anti-aggregation. The polymer mix was 80 wt.% PEO and 20% PVP. In wavelength range (220–820) nm, (PEO-PVP-SnO_2-MnO_2) nanocomposites were examined for structural and optical characteristics. Photodegradation of (PEO-PVP-SnO_2-MnO_2) nanocomposites against organic contaminants was examined. Adding 4.5 MnO_2NPs increased (PEO–PVP) mix absorbance by 51%. By adding 4.5 MnO_2NPs, the energy gap for permitted and prohibited transitions dropped 55% and 91%, respectively. This behaviour is beneficial for optoelectronics, photocatalysis, solar cells, and diodes since it is cheap and light. Finally, MnO_2 NPs ratios improved photodegradation activity of (PEO-PVP) mix and (PEO-PVP-SnO_2). (PEO–PVP–SnO_2–MnO_2) NCs with 4.5 wt% MnO_2 NPs photodegrade 59%.

In 2022, A. J. K. Algidsawi *et al.* [86], the measured the PVA/PVP/MnO_2 nanostructure films for pressure sensors are lightweight, flexible, and inexpensive. The structural, dielectric, and optical properties of PVA/PVP/MnO_2 nanostructures have been examined. The dielectric constant, dielectric loss, and A.C electrical conductivity of PVA/PVP mix increased increasing MnO_2 NPs content. As frequency rises, dielectric constant and loss decrease and AC electrical conductivity rises. The absorbance of PVA/PVP/MnO_2 nanostructures increased with MnO_2 NPs content. The indirect energy gap of PVA/PVP mix decreased with MnO_2 NPs content. With increasing MnO_2 NPs content, blend optical constants vary. The electrical capacitance (C_p) rises with applied pressure in PVA/PVP/MnO_2 nanostructure pressure sensors.

In 2023, A. A. El-Gamal [87], created the composite and the effect of casting a polystyrene (PS)/poly-methyl methacrylate (PMMA) polymer blend with semiconductor and insulator fillers. We use a consistent (1 wt.%) content of semiconductors [multiwalled carbon nanotubes (MWCNTs), polyaniline (PANI), zinc oxide nanoparticles (NPs), and titanium dioxide NPs] and insulator [silicon dioxide NPs] fillers is used. Transmission electron microscopy scans reveal MWCNTs with an average diameter of 7-11 nm. Additionally, Fourier-transform infrared spectroscopy confirms shape and interaction of PS/PMMA polymer blend and additives. Different techniques are used to study polymer nanocomposites' structural, mechanical, optical, and dielectric properties. Absorbance, reflection, bandgap energy (E_g), and real and imaginary optical dielectric components are investigated. The results show that pure ${}_{20}PS/{}_{80}PMMA$ film has $E_g(\text{direct}) = 4.46$ eV, which decreases with filler addition. Due to conductive routes between the filler and blending matrix, MWCNTs and PANI improve PS/PMMA blend electrical conductivity.

1.8 Aims of The Present Work

The principle aims of this work are:

1. Synthesis a new types of (PC-PS/SiC-MnO_2), and (PC-PS/SiC-Co_2O_3) nanocomposites that they used in a wide variety of biomedical and industrial applications.
2. The structural, morphological, optical, and (D.C and A.C) electrical characteristics of (PC-PS/SiC-MnO_2), and (PC-PS/SiC-Co_2O_3) nanocomposites are studied.
3. The biomedical and industrial applications of (PC-PS/SiC-MnO_2) and (PC-PS/SiC-Co_2O_3) nanocomposites are investigated.

Chapter Two

2.1 Introduction

This chapter includes general descriptions of the theoretical part of the current study, the physical concepts, relationships, and the laws used to interpret the obtained results. There is increasing research in nanocomposites due to improvements in optical, electrical, thermal, mechanical characteristics of the materials [88]. In particular, nanoparticles represent as advanced technological materials due to their attractive electrical/optical characteristics and high refractive index [89].

Nanocomposites of organic and inorganic materials can have advantages of both organic polymers (ductility, dielectric, flexibility) and inorganic materials (high thermal stability, strength, rigidity, hardness and high refractive index), thus have many applications [90].

2.2 The Linear Optical Characteristics

In recent years, the search for optical characteristics has increased due to its applications in integrated optics such as optical information, storage optical data, optical modulation [91]. The optical properties of materials can be defined as any property that involves the interaction between electromagnetic radiation or light with the matter, including absorption, polarization, reflection, and scattering effects [92]. When nanoparticles are added to the polymer, they lead to the development of the electrical, optical, and mechanical characteristics of the materials. Nanoparticles with polymers have been studied as alternative materials for optical applications such as planar waveguide devices and micro optical elements [93].

2.2.1 Absorbance (A)

Absorbance can be defined as the ratio between the absorbed light intensity (I_A) by material and the intensity of incident light (I_o) [94].

$$A = \frac{I_A}{I_0} \tag{2.1}$$

2.2.2 Transmittance (T)

The transmittance is given by the ratio of the intensity of the transmitting rays (I_T) through the film to the intensity of the incident rays (I_0), on it as follows [95]:

$$T_r = \frac{I_T}{I_0} \tag{2.2}$$

The reflectance (R) can be obtained from absorption and transmission spectra in accordance with the law of conservation of energy by the following relation [96].

$$R = 1 - (A + T) \tag{2.3}$$

2.2.3 Fundamental absorption regions

The absorption regions can be classified into three regions;

2.2.3.1 High absorption region

The region is shown in Figure 2.1.A. In the firstly section, it is expressed that the nature of the electron transitions is direct. The magnitude of the coefficient of absorption is greater than or equal to $(10^4)\ cm^{-1}$ [97].

2.2.3.2 Exponential region

The region is shown in Figure 2.1.B. In the secondly section, it is expressed the transition from extended levels in the valence band to the localization of levels in the conduction band. Also, from localizing levels in the top valence band to extended levels in the bottom conduction band. The value of the coefficient of absorption between $(1 < \alpha < 10^4)\ cm^{-1}$ [98].

2.2.3.3 Low absorption region

The absorption coefficient (α) in this region is very small, it is about ($\alpha < 1$) cm^{-1}. The transitions of the electrons in this region attribute to density as a result of structural defects, which as shown in Figure 2.1.C, in the thirdly section [98].

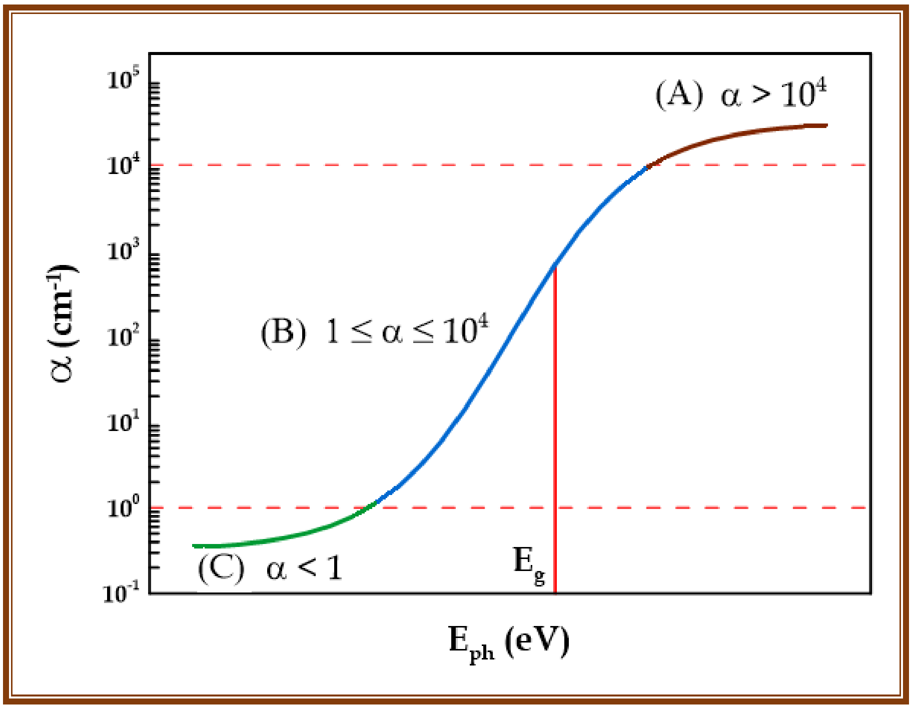

Figure 2.1: The variation of absorption edge with absorption regions [99].

2.2.4 Urbach's Tail Energy

The empirical Urbach law describes the tailing of the optical absorption edge in terms of Urbach energy in this material [100];

$$\alpha = \alpha_0 e^{h\nu/E_U} \tag{2.4}$$

$$E_U = \left[\frac{d\ln\alpha}{dh\nu}\right]^{-1} \tag{2.5}$$

Where α_0 is a constant. E_U is the width of the exponential absorption edge, and describes the optical transition between occupied states in the (V.B) tail to unoccupied states of the (C.B) edge. It is also called Urbach energy, Urbach tail, or Urbach width, and this is illustrated by Figure 2.2, and which represents the plot of energy against density of states (DOS) [101].

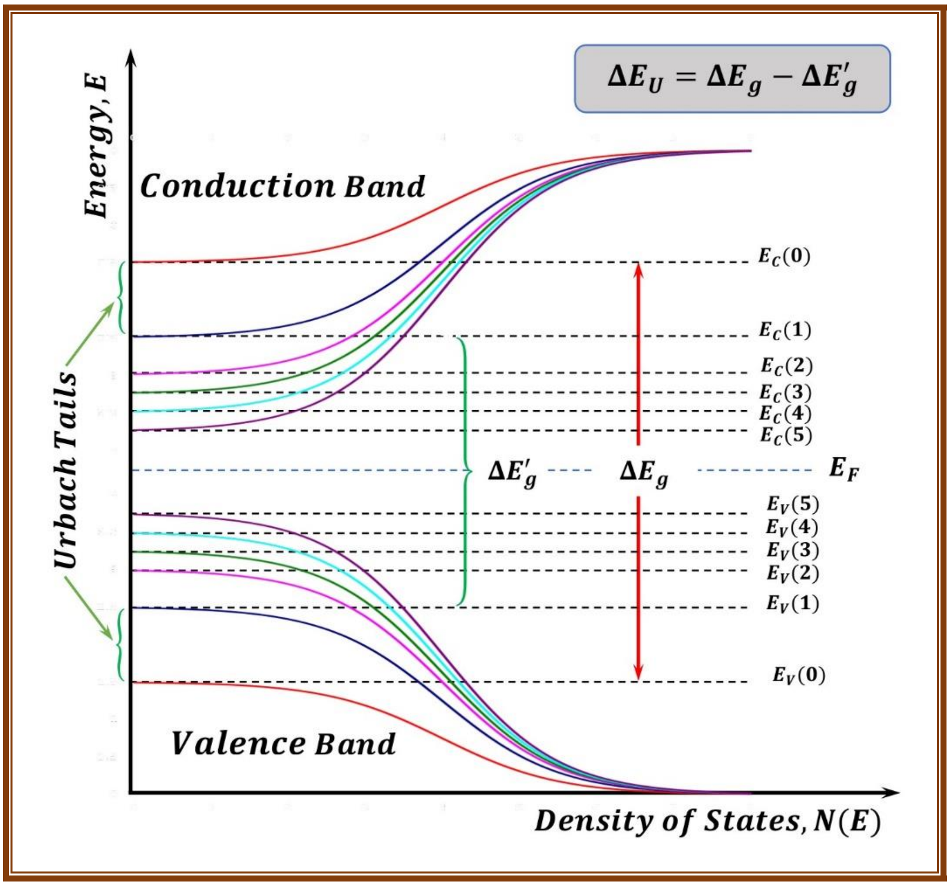

Figure 2.2: Diagrammatic illustration of Urbach tail states in a semiconductor [102].

2.2.5 The Electronic Transitions

The electronic transitions can be classified into two types:

2.2.5.1 Direct transitions

This transition occurs in semiconductors when the bottom of the conduction band $(C.B)$ is exactly over the top of the valence band $(V.B)$. This means that they have the same value of the wave vector, i.e. $(\Delta K = 0)$ in this state the absorption appears when $(h\upsilon = \mathrm{E}_{\mathrm{g}}^{\mathrm{opt.}})$. This transition type is required for the laws of conservation of energy and momentum. These direct transitions have two types [103]:

The first type is a direct allowed transition, this transition occurs from the upper points in the $(V.B)$ and the lowest point in the $(C.B)$, as shown in Figure 2.3.A.

The second type is direct forbidden transitions, this transition occurs from near upper points of ($V.B$) and the lower points of ($C.B$) as shown in Figure 2.3.B.

2.2.5.2 Indirect transitions

In the type of these transitions, the bottom of C.B is not over the top of V.B in a curve (E-K). The electron transiting from V.B to C.B. is not vertical where the value of the wave vector of the electron before and after the transition is not equal zero ($\Delta K \neq 0$). This type of transition occurs with the help of a particle called "Phonon", for the conservation of the energy and momentum law. There are two types of indirect transitions [103]. The first type is allowed indirect transitions, these transitions occur between the top of ($V.B$), and the bottom of ($C.B$) located in the different regions of (K-$space$) as in Figure 2.3.C. The second type is forbidden indirect transitions, these transitions occur between near points at the top of ($V.B$) and near points at the bottom of ($C.B$) as shown in Figure 2.3.D.

The absorption coefficient for this transition using Tauc and Davis-Mott power law is given by [99, 104];

$$(\alpha h\nu)^{\gamma} \;=\; \beta(h\nu - E_g^{Opt.}); \quad if\ h\nu > E_g^{Opt.} \tag{2.6}$$

$$(\alpha h\nu)^{\gamma} \;= 0; \quad if\ h\nu < E_g^{Opt.} \tag{2.7}$$

Where ($\gamma = 1/r$): exponential constant, its value depends on the type of transition. The values of exponential constant (r) for different modes are ($1/2$, $2/3$, 2, or 3) for allowed direct, forbidden direct, (when $\Delta k = 0$) allowed indirect, and forbidden indirect (when $\Delta k \neq 0$) transitions, respectively [105].

β : constant depends on the type of material.

$E_{ph.}$: energy of phonon, is ($+$) when phonon emission and ($-$) when phonon absorption.

$E_g^{Opt,}$: energy gap between direct transition.

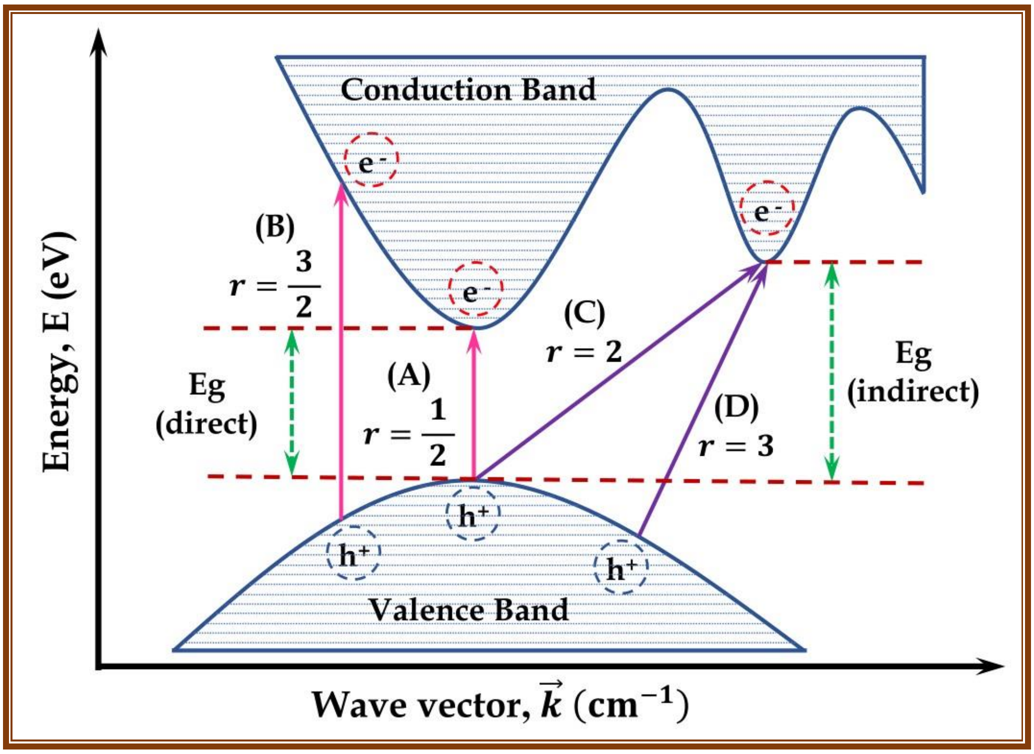

Figure 2.3: Kinds of electronic transitions: direct [A) Allowed, and B) Forbidden] transfers, and indirect [C) Allowed, and D) Forbidden] transitions [106].

2.2.6 Optical Constants

The optical constants are very important parameters because they describe the optical behavior of the materials. The optical constants can be classified into:

2.2.6.1 Absorption coefficient (α)

The absorption coefficient of the material is very strong function of photon energy and band gap energy [107]. Absorption coefficient (α) is defined as the ability of a material to absorb the light of a given wavelength. Absorption coefficient depends on the energy of the incident photon ($h\nu$). The energy of photon is given by the following equation [108];

$$E_{ph.} = h\nu \tag{2.8}$$

When the energy of incident photon is less than energy band gap, then the photon will be transmitted, and the transmittance gives the following equation [109];

$$T = (1 - \mathrm{R})^2 e^{-\alpha t} \tag{2.9}$$

By assuming thickness of sample is (dt) that decreases intensity of incident photon by (dI) which direct proportion with both of intensity (I) and thickness (dt); where (α) is constant proportion [110].

$$dI = -\alpha I\, dt \tag{2.10}$$

If intensity of incident ray (I_0) which incident on the material of thickness (t) and intensity of transmittance ray (I_T) then integration procedure, will obtain and which is given by the following Beer-Lambert law [110].

$$\int_{I_0}^{I_T} \frac{dI}{I} = -\int_0^t \alpha\, dt \tag{2.11}$$

$$Ln(I_T) - Ln(I_0) = -\alpha t$$

$$I_T = I_0\, e^{-\alpha t} \tag{2.12}$$

$$\frac{I_T}{I_0} = e^{-\alpha t}$$

$$T = e^{-\alpha t} \tag{2.13}$$

$$1/T = e^{\alpha t}$$

$2.3031 \log(1/T) = \alpha t$; But: $A = \log(1/T)$

$$\alpha = 2.3031\,(A/t) \tag{2.14}$$

The skin depth (δ) was computed using [105, 111];

$$\delta = 1/\alpha \tag{2.15}$$

2.2.6.2 The Refractive index (n) and extinction coefficient (k)

Refractive index of the material is the ratio of the velocity of light in a vacuum (c) to the velocity of the light in the sample (ν) [112];

$$n = c/\nu \tag{2.16}$$

$$n^* = n - jk \tag{2.17}$$

n^*: is the complex refractive index, n: is a real part of the refractive index and k : is an imaginary part of the refractive index (extinction coefficient).

The relation between absorption coefficient and the extinction coefficient (k) is [113];

$$k = \frac{\alpha \lambda}{4\pi} \tag{2.18}$$

λ: wavelength of photon. The refractive index (n) can be expressed through the following equation [75];

$$n = \left[\left(\frac{1+R}{1-R}\right)^2 - (k^2+1)\right]^{1/2} + \frac{1+R}{1-R} \tag{2.19}$$

Since the value of extinction coefficient (k) is very small, then the equation (2.19) will become as follows [75];

$$n = \frac{1+\sqrt{R}}{1-\sqrt{R}} \tag{2.20}$$

2.2.6.3 The dielectric constant (ε)

The real part of the dielectric constant shows how much it will slow down the speed of light in the sample and the imaginary part of the dielectric constant shows how a dielectric absorbs energy from an electric field due to the movement of the dipole. The real and imaginary part of the dielectric constant was determined by [114];

$$\varepsilon = \varepsilon_r - j\varepsilon_i \tag{2.21}$$

$$\varepsilon = (n^*)^2 \tag{2.22}$$

$$(n - ik)^2 = \varepsilon_r - j\varepsilon_i$$

$$\varepsilon = (n^2 - k^2) - j(2nk) \tag{2.23}$$

The dielectric coefficient (ε) can be calculated from refractive index (n), joining complex dielectric coefficient (ε) with complex refractive index (n^*) from equation (2.21) and equation (2.23), real and imaginary complex dielectric coefficient can be written as in following equation [115];

$$\varepsilon_r = n^2 - k^2 \tag{2.24}$$

$$\varepsilon_i = 2nk \tag{2.25}$$

2.2.6.4 Optical conductivity ($\sigma_{Opt.}$)

The optical conductivity ($\sigma_{Opt.}$) depends directly on the refractive index (n) and extinction coefficient (k) by the following relation [115];

$$\sigma_{Opt.} = 2nk\omega\varepsilon_0 \tag{2.26}$$

Where ω: is the angular frequency, ε_0: is the permittivity in the free space. By substituting equation (2.18) in equation (2.26) with simplified, the optical conductivity can be expressed by the following equation [115];

$$\sigma_{Opt.} = \frac{\alpha nc}{4\pi} \tag{2.27}$$

2.3 The D.C Electrical Characteristics

The studies on the electrical characteristics of polymers have included great interest in their applications in electronic and optical devices. Electrical conduction in polymers has been extensively studied to understand the nature of charge transport in polymers [116].

In previous years, polymers were used as insulators because of their high resistance and dielectric characteristics. The $D.C$ electrical conductivity studies aim to understand the numbers of types of charge carriers, their source and how they are transported through the material [117].

The volumetric electrical resistance (R_V) can be calculated for a regular body with a section having a sample area ($A_s = \pi r^2$) along the thickness (t), using the following relation [118];

$$R_V = \rho_V \left(\frac{t}{A_s}\right) \tag{2.28}$$

Where: ρ_V is the volume resistively that is different according to the substance, it is equal to the inverse of the bulk conductivity. This means that the conductivity of the volume is [118];

$$\sigma_{D.C} = \frac{1}{\rho_V} = \frac{t}{R_V\ A_s} \tag{2.29}$$

The electrical conductivity of polymers increases exponentially with the increase of temperature according to the Arrhenius equation [119, 120];

$$\sigma_{D.C} = \sigma_0 \exp\left(-E_{act.}/k_\beta T\right) \tag{2.30}$$

Where: $\sigma_{D.C}$ is conductivity at $(T + \Delta T)$ temperature, σ_0 is the conductivity at absolute (T) zero of temperature, $E_{act.}$= activation energy, and k_β = Boltzmann constant. In conclusion, thermal activation energy and interaction velocity define diverse polymer nanocomposites behaviors. A lower activation energy can lead to stronger polymer-nanoparticle connections, while a greater interaction velocity can lead to more frequent contacts, which can also alter nanocomposite qualities. This is due to the Boltzmann-Maxwell distribution law, mostly easily seen in Figure 2.4 [119]:

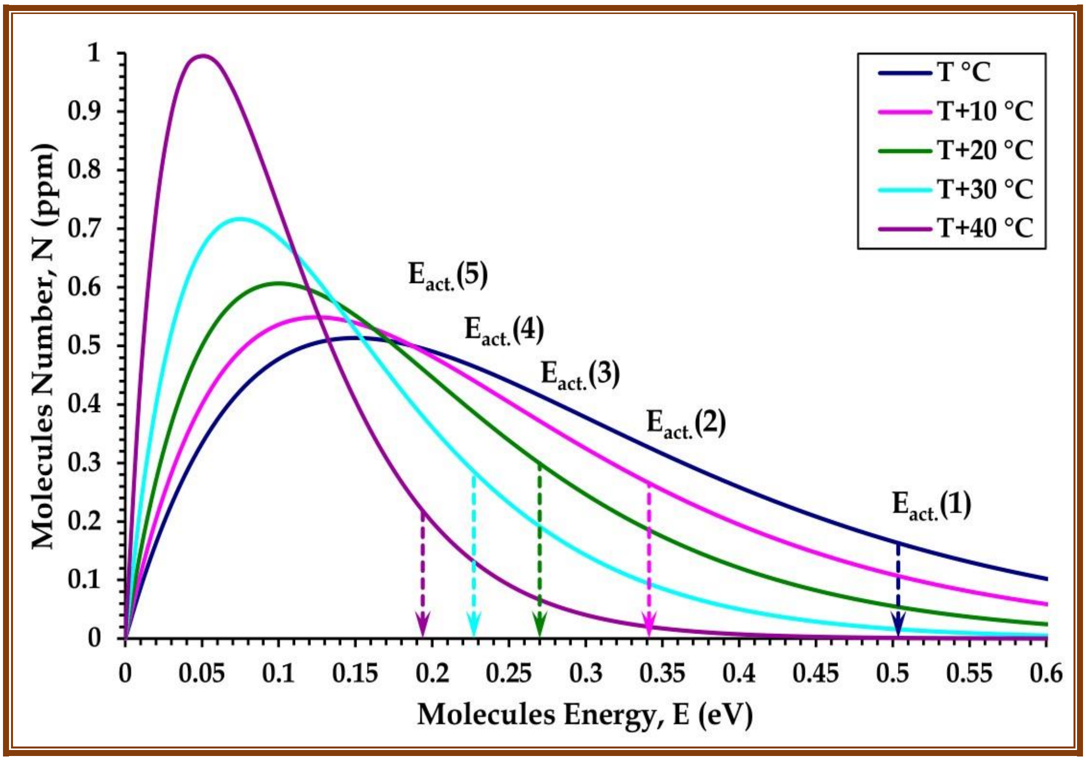

***Figure 2.4: Statement of the Boltzmann distribution between the energy of molecules and different temperatures and the impact of thermal activation energy on the reaction rate* [121].**

In general terms, the behavior of electrical resistance depends upon the type of the substance thus, in the case of metals, electrical resistance increases (i.e. their conductivity decreases) as temperature rises. For semiconductors, resistance decreases (i.e. their conductivity increases) as temperature rises while in impure semiconductors, resistance increases as temperature rises a certain degree and their conductivity decreases [122].

2.4 Electrical Polarization

When the insulation material is under the influence of an electric field, the charges associated with the atoms and molecules in the material will rearrange themselves in the direction of the electric field, which creates a local electric field. This process is called polarization. The polarization value is equal to the sum of the moments of all dipoles in the unit volume of the material [123];

$$\overrightarrow{\mu_i} = \alpha_i \overrightarrow{E_i} \tag{2.31}$$

Where: $\overrightarrow{E_i}$ is the internal field of a molecule α_i: is the polarity of an atom or a molecule and $\overrightarrow{\mu_i}$: is the electrical dipole moment. The total dipole moment ($\overrightarrow{P_i}$) for a unit volume is [124];

$$\overrightarrow{P_i} = N_V \overrightarrow{\mu_i} \tag{2.32}$$

Where: N_V is the number of molecules per unit volume.

The increase in the charge density ($\varepsilon_0 \overrightarrow{E_i} + \overrightarrow{P_i}$) causes an increase in the electrical displacement ($\overrightarrow{D_e}$), which can be defined as [124];

$$\overrightarrow{D_e} = \varepsilon_0 \overrightarrow{E_i} + \overrightarrow{P_i} \tag{2.33}$$

There are four types of polarization that can be classified with different frequencies [125, 126]:

2.4.1 Electronic polarization (P_e)

Electronic polarization may be accruing due to distortion in the distribution of the charge when the electric field applied. The separation of the positive charge of the nucleus and the center of the negative charge, resulting in the generation of induced dipoles as shown in Figure 2.5.A. This polarization occurs through ($< 10^{-15}$) s this is the same period of ultraviolet rays and is independent of temperature [125].

2.4.2 Ionic polarization (P_i)

It is formed in an ionic compound with ionic characteristics. It occurs when the matter is under an electric field that changes the lengths of the ionic bond, resulting in the generation of a net dipole moment that has not been existed in the molecule before as shown in Figure 2.5.B. Ionic polarization occurs through $(10^{-15} - 10^{-10})\ s$ this is the same period infrared ray. So, it also called infrared polarization. This type of polarization is independent of temperature [126].

2.4.3 Rotational or orientation polarization (P_d)

This polarization accrues in materials that have a permanent dipole moment. When applying an electric field, dipoles revolve around the axis and arrange themselves in the direction of the field as shown in Figure 2.5.C. This type of polarization is dependent on temperature and occurs through $(10^{-10} - 10^{-5})\ s$ [126].

2.4.4 Space charge or interfacial polarization (P_0)

This type of polarization occurs when the substance contains impurities, structural or vacuum defects, which leads to the content of the opposite charge on the ends of the impurities, and this means the generation of a dipole in an atom, molecule, or region of the material as shown in Figure 2.5.D. This type of polarization depends on the homogeneity of the material and the type of defects [126]. They most often occur in radio waves and can extend beyond sound frequencies, depending on the defect that causes polarization and is independent of temperature, as shown in Figure 2.6 [127].

However, the movement of charges through the material may be slowed down when the charge carriers encounter another phase with lower electric conductivity. This causes the accumulation of charges at the interfaces. This interfacial polarization manifests itself to an outside observed as an increase in the permittivity [125].

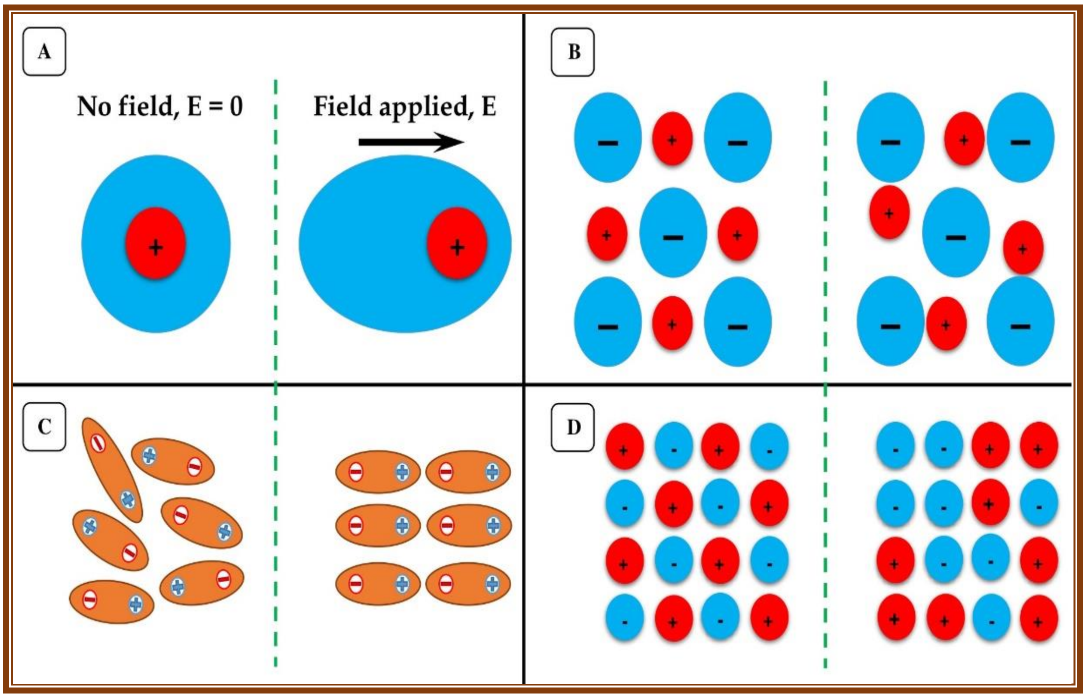

Figure 2.5: Schematic representation of different kinds of [A) Electronic, B) Ionic, C) Orientation, and D) Space charge] polarization, in the absence of an electric field, and the presence of an electric field [125].

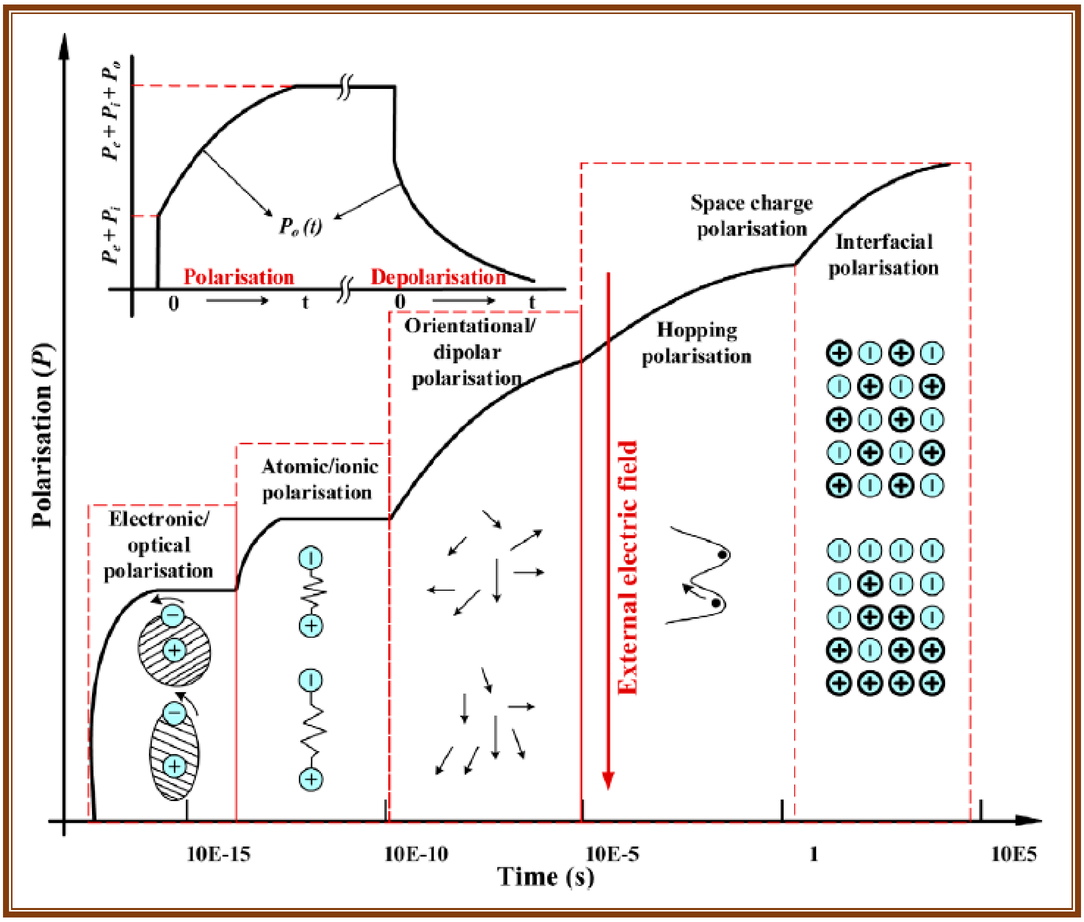

Figure 2.6: The variation of different types of polarization with time under a step-function electric field [127].

2.5 The A.C Electrical Characteristics

Insulating materials can be used to save electrical energy in the shape of charge separation when the electron distributions around constituent atoms or molecules are polarized by an external electric field. The complex permittivity of a material is given by [128];

$$\varepsilon^* = \varepsilon_a - j\varepsilon_b \tag{2.34}$$

Where ε_a, and ε_b are the real and imaginary parts of the complex permittivity and $j = \sqrt{-1}$.

The real part of the permittivity can be expressed by [128];

$$\varepsilon_a = \varepsilon_0\, \varepsilon' \tag{2.35}$$

Where: ε' is dielectric constant. The magnitudes of ε_a, and ε_b depend on the frequency (ω) of the applied electric field. The magnitude of ε_a (or the dielectric constant) refers to the material's ability to store energy from the applied electric field [128]. The capacitance of a capacitor consists of two parallel plates given by relationship [129];

$$C_p = \frac{\varepsilon_0 \varepsilon' A}{t} \tag{2.36}$$

Where: t is the thickness of the sample, ε_0 is a vacuum permittivity. The dielectric constant is defined as the ratio between the capacitance of the capacitor containing an insulator material between its conducting plates to the capacity of the same size with a vacuum between the plates. The dielectric constant is given by [130];

$$\varepsilon' = \frac{C_p}{C_0} \tag{2.37}$$

Where C_p is parallel capacitance and C_0 is a vacuum capacitor. Due to the different polarization of matter under the influence of an electric field, some of the applied electric field energy is dissipated by charge migration (i.e. conduction) or converted into heat energy (for example, molecular vibration). Ceramic capacitors based on highly polarizable inorganic materials have been used extremely to meet the need for pulse power applications. Dielectric loss (ε'') can be expressed by [131];

$$\varepsilon'' = \varepsilon' D \tag{2.38}$$

Where: D is the dispersion factor. The dispersion factor measures the electrical energy lost in the sample from the applied electric field, which turns into thermal energy in the sample. The dissipated power in the dielectric is represented by the presence of alternating potential as a function of alternating conductivity is given by [132];

$$\sigma_{A.C} = \omega\, \varepsilon_0 \varepsilon'' \tag{2.39}$$

This conductive does not represent the property of the conductive which is characterized by the materials, (i.e. the ability of these materials to connect electric current) but is a measure of the capacity lost when the applying alternative field through the insulation which is the measure of the amount of heat that is generated as a result of friction between the diodes due to collisions between other molecules in the insulating materials [133].

The total electrical conductivity σ_T for polymeric material can be express as follow [134];

$$\sigma_{tot.} = \sigma_{D.C} + \sigma_{A.C} \tag{2.40}$$

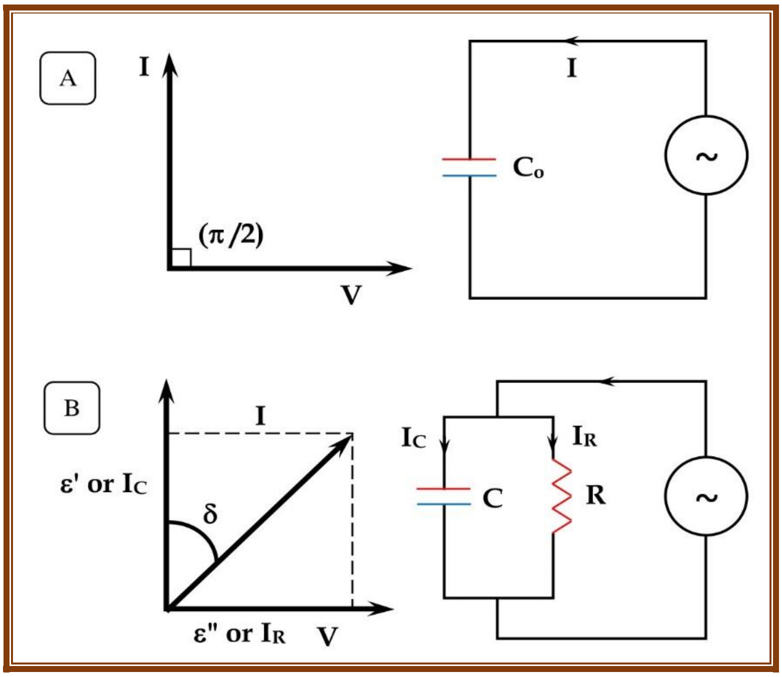

Figure 2.7: The circuit equivalent of; A) ideal capacitor, and B) non-ideal capacitor.

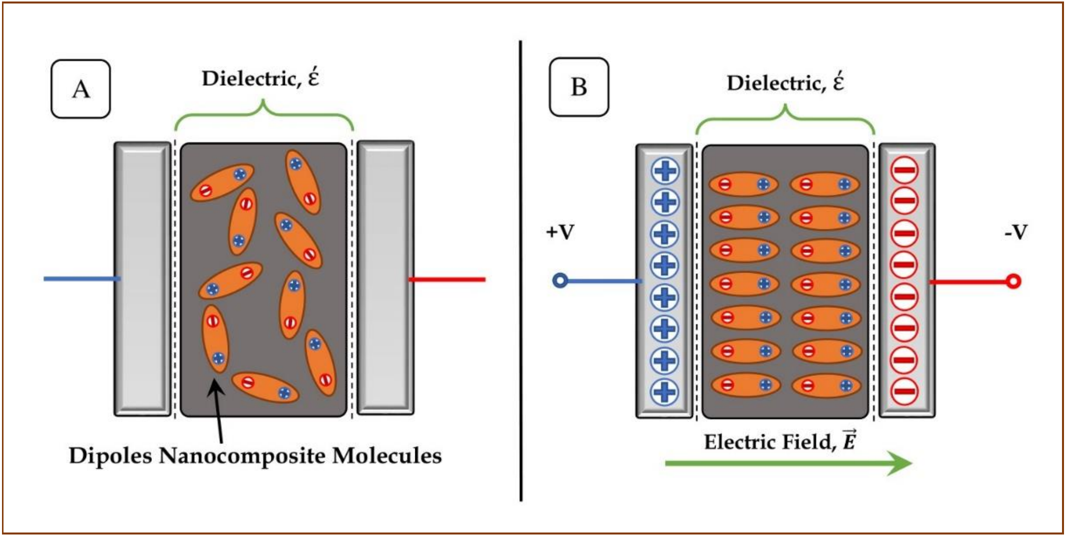

Figure 2.8: Schematic diagram of the capacitance showing the behavior of dielectric constant; (A) In the absence of an electric field. (B) In the presence of an electric field.

2.6 Applications of Nanocomposites

2.6.1 Antibacterial activity

An inverse relationship between the size of the nanoparticles and antimicrobial activity has been clearly demonstrated, where particles in the range of $(1-10)\ nm$ in size have demonstrated greater killing activity against bacteria compared to larger particles. It is reported that in gram negative bacteria nanoparticles acted mainly in the range of $(1-10)\ nm$ [135]. In addition, by adhering to the surface of the cell membrane, they drastically disrupt its functions, such as permeability and cellular respiration. They are able to penetrate into the bacteria and cause further damage by possible interactions with sulfur and phosphorus containing compounds such as DNA. They release ions, which will make an additional contribution to the bactericidal effect of nanoparticles. However, in the case of silver nanoparticles, it has been shown that smaller nanoparticles are more toxic than larger particles, even when they are oxidized [136].

As an antibiotic, the nanocomposites was used. When the ratio of diameter of inhibition is taken from the diameters of bacterial inhibition for the sample that killed the most bacteria compared to the sample that didn't kill the bacteria, the following equation was used to figure out the overlapping respiratory inhibition ratios of bacteria [137];

$$R_D(inhibition)\% = \left(1 - \frac{D_{uninhibition}}{D_{inhibition}}\right) \times 100\% \qquad (2.41)$$

Where: $R_D(inhibition)\%$ is the percentage increase in the diameter of the inhibition zone of the bacterial respiratory overexpression inhibition zone after adding the nanocomposite, $D_{inhibition}$ is the diameter of the inhibition zone of the sample where bacteria were killed and $D_{uninhibition}$ is the diameter of the inhibition zones of the sample where no bacteria were killed.

The antimicrobial mechanism of action of NPs is generally described as adhering to one of three models: oxidative stress induction, metal ion release, or non-oxidative mechanisms. These three types of mechanisms can occur simultaneously. Certain studies have proposed that nanomaterials prompt neutralization of the surface electric charge of the bacterial membrane and change its penetrability, ultimately leading to bacterial death. Moreover, the generation of reactive oxygen species (ROS) inhibits the antioxidant defense system and causes mechanical damage to the cell membrane. According to existing research, the major processes underlying the antibacterial effects of NPs are as follows [138, 139]:

1. Disruption of the bacterial cell membrane.
2. Generation of ROS.
3. Penetration of the bacterial cell membrane.
4. Induction of intracellular antibacterial effects, including interactions with DNA and proteins.

2.6.2 Photocatalytic degradation

Photocatalysis is described as the photoreaction acceleration process by the presence of a catalyst. A catalyst is a material that makes a chemical reaction more likely to happen by reducing the activation energy needed to start it. A catalyst speeds up a chemical reaction and does not vary in itself or being expended in the chemical reaction [140]. Most organic pollutants can be degraded by heterogeneous photocatalysis. Semiconductor nanoparticles meet the requirements for good photocatalysts because semiconductor materials have a small energy gap between valence band and conduction band. The energy band gap of semiconductors are in the range (1-4) eV [141].

In general, the photocatalytic degradation involves several steps such as adsorption-desorption, electron-hole pair production, recombination of electron pair and chemical reaction [142]. The general mechanism of photocatalytic degradation of organic molecules is explained in the Figure 2.9 [143]. The addition of polymeric materials to the nanoparticles leads to the dispersion of the nanoparticles and preventing them from sedimentation, and this leads to a reduction in electron-hole recombination, thus increasing the photocatalytic efficiency of the nanoparticles. For the photocatalysis process to take place, the semiconductor material absorbs a photon of energy from the direct sun's rays or from an ultraviolet source that is equal or greater than to its band gap ($h\nu \geq E_g$), the electrons move from the valence band to the conduction band, and the pairs of (electrons-holes) are generated [144]. The electrons contribute to the reduction reactions by the formation of superoxide radicals ($O_2^{\bullet -}$) , and the holes contribute to the oxidation of organic compounds by the formation of hydroxyl radicals ($OH^{\bullet}$). These radicals will be attacked by the organic molecule, which is finally oxidized to become CO_2, H_2O and HCl. The processes of photodegradation include the following [145, 146]:

1. Formation of excitons by absorption of photons by photocatalyst nanocomposites.

$$\text{Photocatalysts} + h\nu \longrightarrow h^+ + e^- \tag{2.42}$$

Where the electrons (e^-) are generated in the conduction band and holes (h^+) are generated in the valence band.

2. Formation of superoxide anion ($O_2^{\bullet -}$)

$$\mathrm{O}_2 + e^- \longrightarrow O_2^{\bullet -} \tag{2.43}$$

3. Formation of hydroxyl radicals ($OH^{\bullet}$).

$$H_2O + h^+ \longrightarrow H^+ + OH^{\bullet} \tag{2.44}$$

4. Neutralization of superoxide anion by protons and formation of Hyper oxide radical ($HO_2^{\bullet}$).

$$O_2^{\bullet -} + H^+ \longrightarrow HO_2^{\bullet} \tag{2.45}$$

5. Formation of hydrogen peroxide (H_2O_2) and dismutation of oxygen.

$$2HO_2^\bullet \longrightarrow H_2O_2 + O_2 \tag{2.46}$$

$$H_2O_2 + e^- \longrightarrow OH^- + OH^\bullet \tag{2.47}$$

6. Formation of degradation products.

$$MO\ dye + H_2O_2 + OH^\bullet + O_2^{\bullet -} \longrightarrow CO_2 + H_2O \tag{2.48}$$

$$h^+ + MO\ Molecules \rightarrow dye^{\bullet +} \rightarrow Oxidation\ of\ dye \tag{2.49}$$

$$\text{MO dye} + \text{OH}^\bullet \rightarrow CO_2 + H_2O + Degradation\ products \tag{2.50}$$

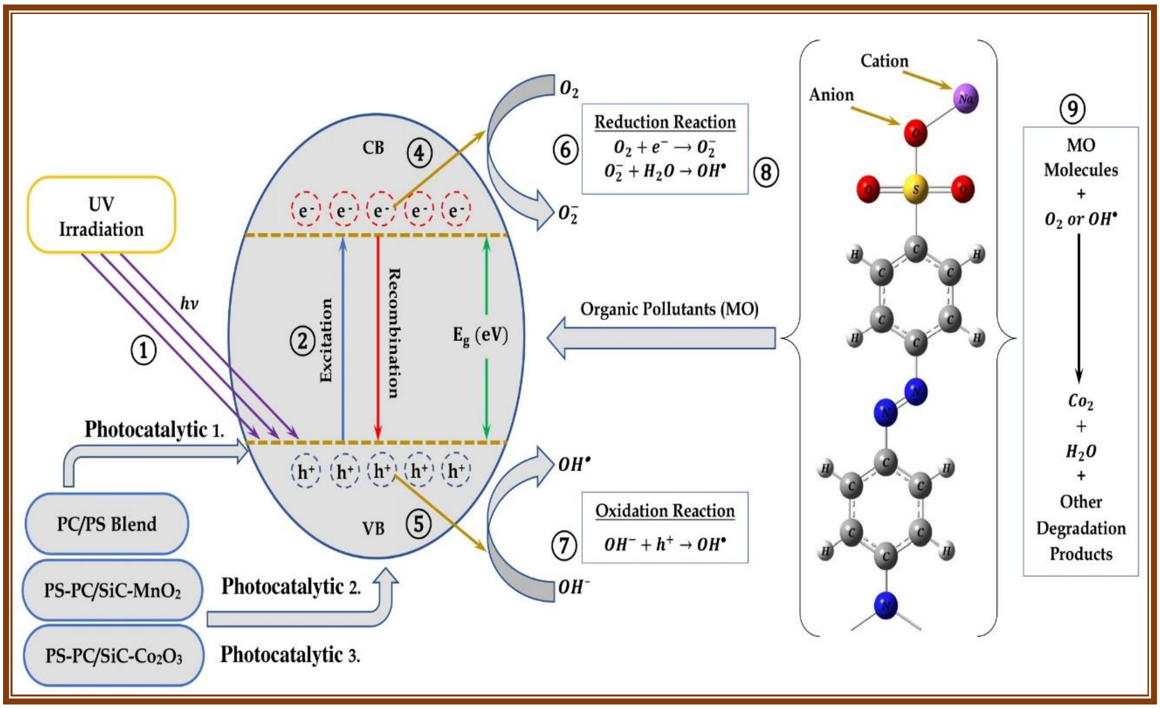

Figure 2.9: The mechanism of photocatalysis degradation process

There are three important mechanisms of recombination [147, 148]:

1. Direct recombination, the photo electron in conductive band drops directly into an unoccupied state in the valance band and combines with the photo hole by electrostatic attraction.
2. Surface recombination is lower probability, due to the surface species which can capture the photogenerated charge carriers (photo electron-hole) and undergo the chemical reaction.
3. Recombination at recombination centres (volume recombination) is of high probability, because the recombination centres lies at lattice sites transition within the bulk of the crystal and the transition beyond to initial ground state.

These types of recombination are pictorially shown in Figure 2.10.

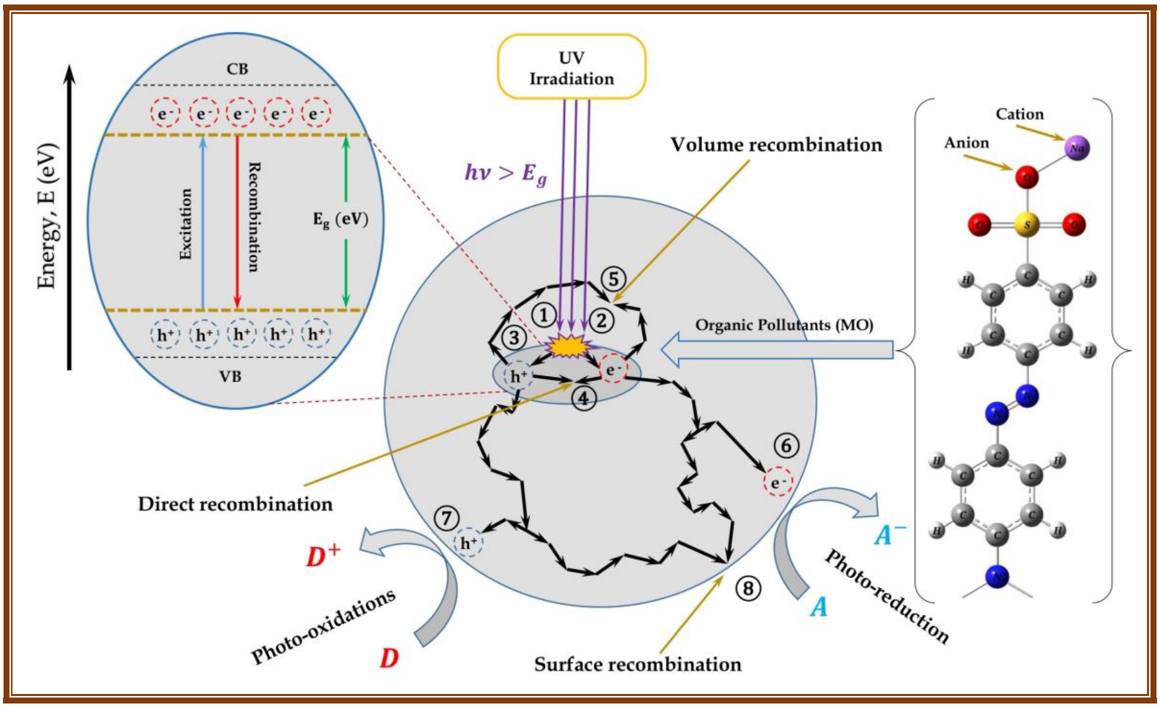

Figure 2.10: Principal processes occurring on a semiconductor particle (a) photogeneration of electron-hole pair (b) reduction of electron acceptors (c) oxidation of electron donors (d) and (e) Recombination of electron hole

The methyl orange degradation percentage was evaluated by involving equation. (2.51) as given below [149];

$$D_{MO}(\%) = \left(1 - \frac{A_t}{A_0}\right) \times 100\% \qquad (2.51)$$

where A_0 is the initial absorbance of methyl orange, obtained before illumination and A_t is a absorbance after UV-Irradiation time, respectively.

Because the rate of photocatalytic processes is irrespective of hydroxyl amount, the observational data was fitted with a pseudo first-order kinetics model [150]. The first-order rate constant κ_d (min^{-1}) can be calculated from a straight line whose slope line for plot of ln (A_t/A_0) versus time leads using the absorbance-time equation (2.52) [151];

$$Ln\frac{\mathrm{A}_t}{A_0} = \kappa_d\tau \qquad (2.52)$$

The half-life time $(\tau_{1/2})$ was obtained for first-order kinetics using equation (2.53) [152];

$$\tau_{1/2} = \frac{ln\,2}{\kappa_d} \tag{2.53}$$

2.6.3 Pressure sensor

Pressure sensors based on polymer nanocomposites have been developed and studied extensively. Polymer nanocomposites are materials composed of a polymer matrix and nanoparticles, which can enhance the mechanical, electrical, and optical properties of the composite material [153].

Polymer nanocomposite pressure sensors can be made by embedding nanoparticles, such as carbon nanotubes, graphene, or metal oxide nanoparticles, into a polymer matrix. The nanoparticles can act as stress-sensitive elements that change their properties, such as electrical resistance or capacitance, in response to mechanical deformation caused by pressure [154].

Polymer nanocomposite pressure sensors have potential advantages over traditional pressure sensors, such as higher sensitivity, lower power consumption, and lower cost. They can also be easily integrated into flexible or wearable devices, due to the flexibility and stretchability of the polymer matrix [154].

A pressure is a force per unit area applied in a direction perpendicular to the surface of an object. The formula is commonly written as follows [155];

$$P = \frac{\vec{F}}{A} \tag{2.54}$$

Where P is the pressure, $\vec{F}$ is the normal force, and A is the area of the surface of contact, which is illustrated by the Figure 2.11.

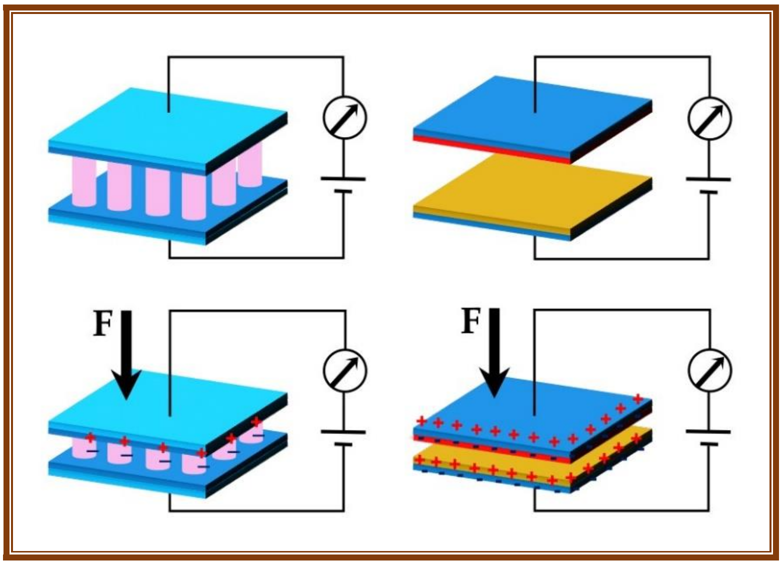

Figure 2.11: The circuit equivalent of presure sensor [154].

When two objects are contacted, they exert force on each other. Thus, the average interface pressure is the total force divided by the interface region. A sensor is a device that detects and converts a physical quantity into a signal that an observer or an instrument can interpret. Pressure sensors are used for control and monitoring in thousands of everyday applications. Many pressure sensors classify according to the sensing mechanisms which include capacitive sensing, piezoelectric sensing, and piezoresistive-sensing. Pressure-sensitive materials are widely used due to their attractive advantages, including feasible preparation, low cost, and easy signal collection [155].

The use of polymers and polymeric blend as sensors offers the advantage of processing flexibility, because they are tough, light weight, readily manufactured into large areas, and can be cut and formed into complex shapes. Other features of polymers are high strength, high impact resistance, low elastic stiffness, low dielectric constant and low density which result in a high voltage sensitivity (excellent sensor characteristic). For capacitive pressure sensors, pressure sensor sensitivity can be defined as follows [156];

$$S_{AP}(\%) = \left(1 - \frac{C_b}{C_n}\right) \times 100\% \tag{2.55}$$

Where C_b and C_n are the capacitances for blend and nanocomposites, respectively.

Experimental Procedures

Chapter Three

3.1 Introduction

This chapter covers the stages of samples preparation of (PC-PS/SiC-MnO_2), and (PC-PS/SiC-Co_2O_3) nanocomposites, as well as the stages of sample testing and measurement, which include the following: Infrared radiation transformed using the Fourier transform, optical microscopic, a field emission scanning electron microscope, optical measurements, D.C electrical conductivity measurements, A.C electrical conductivity measurements, antibacterial activity application measurements, photodegradation application measurements, and pressure sensors application measurements.

3.2 The Raw Materials Used in Work

3.2.1 Matrix materials

Two types of polymers are used in this present study:

3.2.1.1 Polycarbonate (PC)

The polymer is used as powder. Manufactured by Teijin Human Chemistry - Japan company. It was utilized after having been ground by manual mill.

3.2.1.2 Polystyrene (PS)

The polymer is used as granular form and could be obtained from local markets. It was used after being grounded with hand mill, and high purity (99.97%).

3.2.2 Filler materials

One metal carbide, and two types of metal oxides are used in this work:

3.2.2.1 Silicon Carbide (SiC)

It was obtained as nano-powder form, USA Research Nanomaterials, Inc, Houston, USA, high purity 99% with diameter 80 nm, cubic.

3.2.2.2 Manganese Dioxide (MnO_2)

It was obtained as nano-powder form, USA Research Nanomaterials, Inc, Houston, USA, high purity 98% with diameter 50 nm, tetragonal.

3.2.2.3 Cobalt Trioxide (Co_2O_3)

It was obtained as nano-powder form, USA Research Nanomaterials, Inc, Houston, USA, high purity 99.7% with diameter 50 nm, Orthorhombic.

3.3 Synthesis of (PC/PS) Polymeric Blend, (PC-PS/SiC-MnO_2) Nanocomposites, and (PC-PS/SiC-Co_2O_3) Nanocomposites

The nanocomposites were made by dissolving one gram of polycarbonate (50%) and polystyrene (50%) in 50 ml of chloroform alcohol, using a magnetic stirrer. After that, the polymers were mixed for 25 minutes at standard room temperature to achieve a more uniform solution and then casting on glass petri dish. Nanoparticles made of Silicon carbide (25%) and Manganese dioxide (75%) were added to the polymer blend solution at contents that are as follows: (1.3, 2.6, 3.9, and 5.2 wt.%) to get the first nanocomposites (PC-PS/SiC-MnO_2), as well as nanoparticles consist of Silicon carbide (25%) and Cobalt trioxide (75%) were added to the polymer blend solution at contents that are as follows: (1.3, 2.6, 3.9, and 5.2 wt.%) to get the second nanocomposites (PC-PS/SiC-Co_2O_3). These contents were calculated according to the following equation (3.1) [157];

$$\chi_{(\mathrm{wt.\%})} = \frac{w_f}{w_f + w_b} \times 100\ \% \tag{3.1}$$

where (w_b) blend weight and (w_f) filler weight is measured in grams as shown in Table 3.1 and Table 3.2.

Nanocomposites of (PC-PS/SiC-MnO_2), and (PC-PS/SiC-Co_2O_3) films are created using a solution casting technique as shown in Figure 3.1 and Figure

3.2, and after that, the solution was transferred to a clean petri dish with a diameter of 10 cm. The samples were then allowed to air dry at room temperature for 72 hours, after which the dried film was readily peeled off using tweezers clamped. A digital micrometer was utilized in order to obtain accurate readings of the samples wall thickness, and the range of thickness have been measured about (130 ± 0.5) µm. Figure 3.3, and Figure 3.4 are illustrate the diagrammatic representation for the preparation approach of the experimental work that was done.

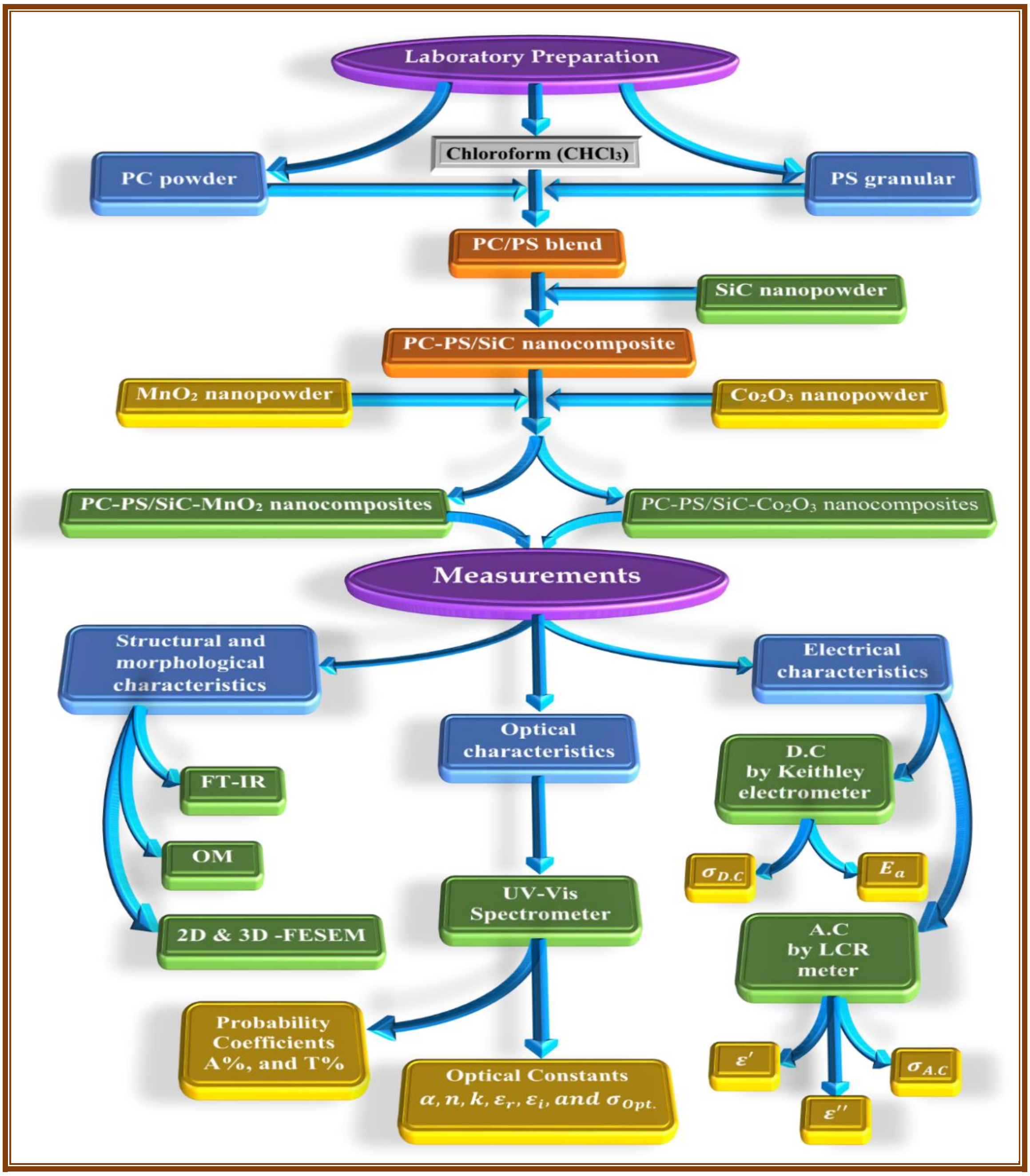

Figure 3.1: Flow chart of experimental present work

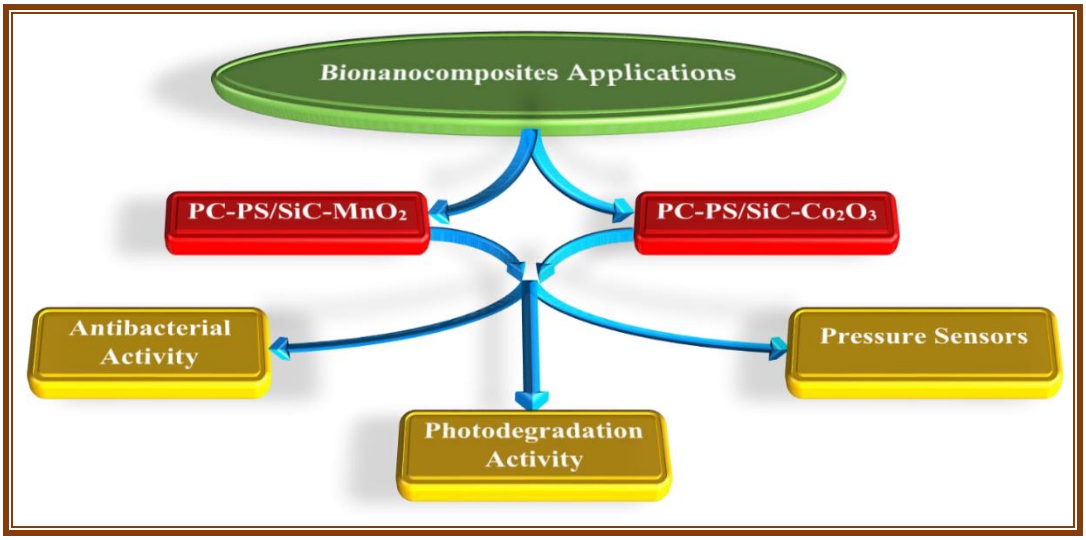

Figure 3.2: Flow chart of present work applications

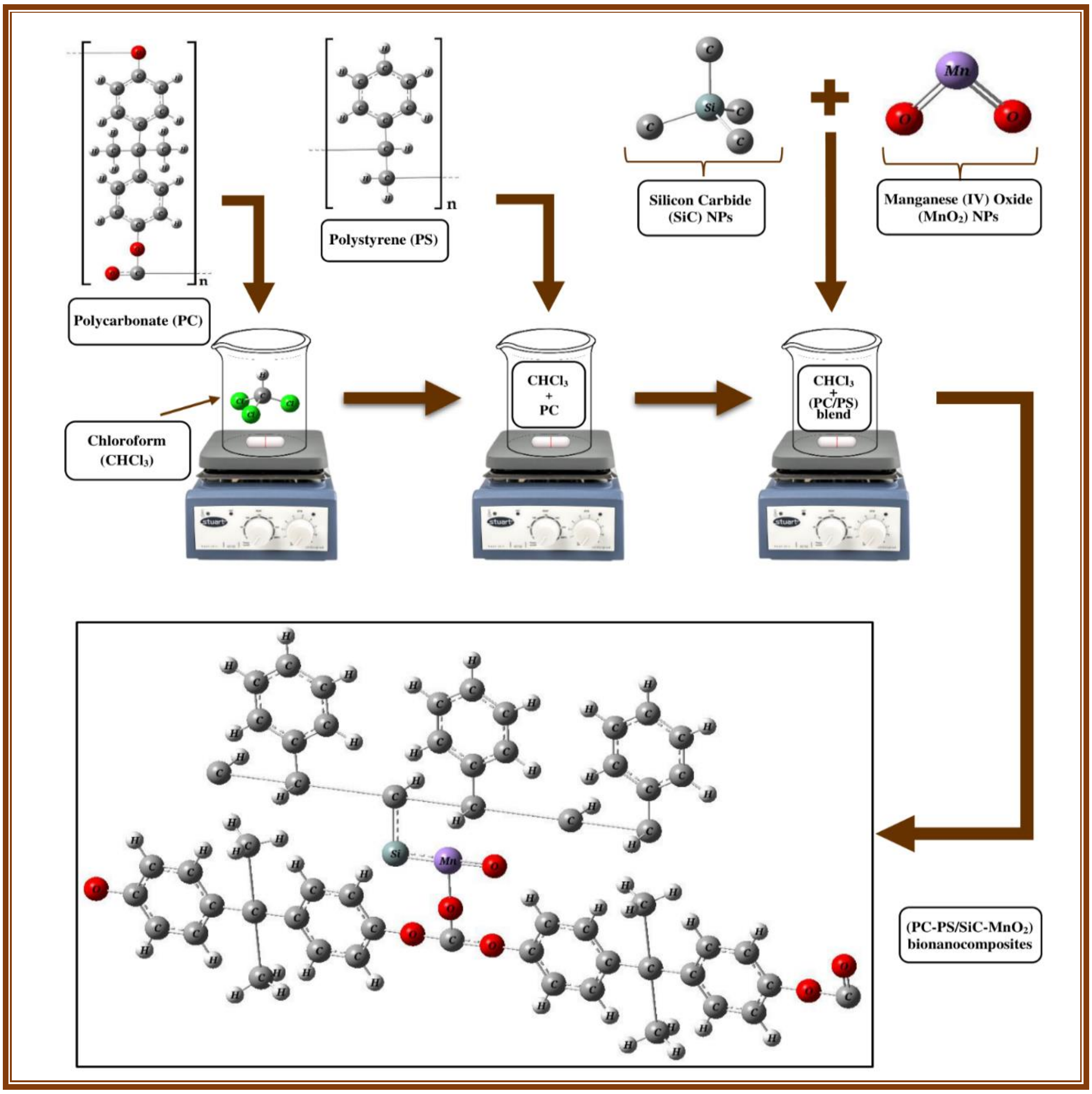

Figure 3.3: The diagrammatic representation for the preparation approach of nanocomposite (PC-PS/ SiC-MnO$_2$) films

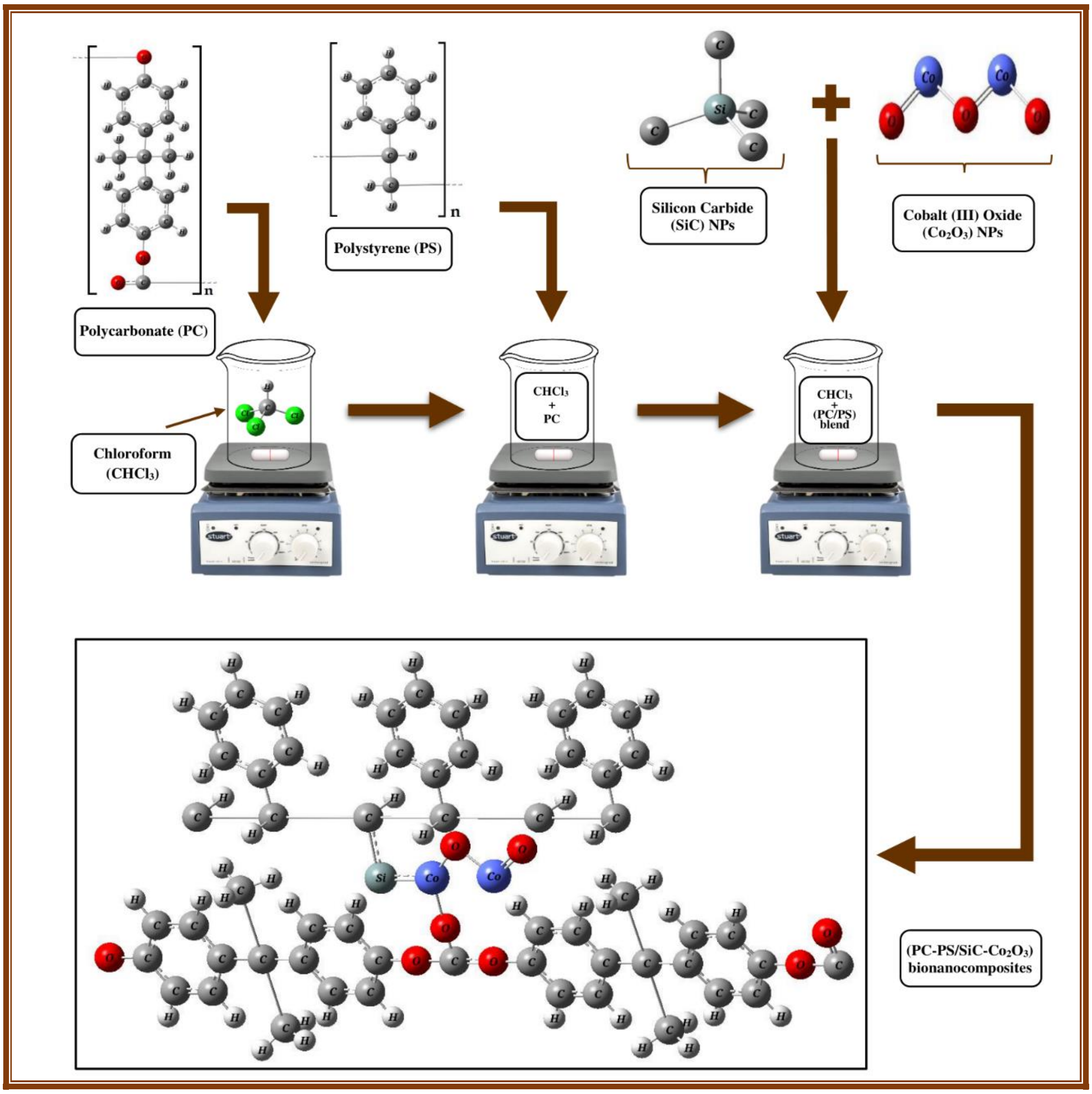

Figure 3.4: The diagrammatic representation for the preparation approach of nanocomposite (PC-PS/ SiC-Co_2O_3) films

Table 3.1: Weight percentages of (PC/PS) polymeric blend, and (PC-PS/SiC-MnO_2) nanocomposites

Contents of SiC/MnO_2 nanoparticles	Material weight (gm)				Weight of sample
	PC (50%)	PS (50%)	SiC (25%)	MnO_2 (75%)	
Pure	0.5000	0.5000	0.00000	0.00000	1 gm
1.3 wt.%	0.4935	0.4935	0.00325	0.00975	
2.6 wt.%	0.4870	0.4870	0.00650	0.01950	
3.9 wt.%	0.4805	0.4805	0.00975	0.02925	
5.2 wt.%	0.4740	0.4740	0.01300	0.03900	

Table 3.2: Weight percentages of (PC/PS) polymeric blend, and (PC-PS/SiC-Co_2O_3) nanocomposites

Contents of SiC/Co_2O_3 nanoparticles	Material weight (gm)				Weight of sample
	PC (50%)	PS (50%)	SiC (25%)	Co_2O_3 (75%)	
Pure	0.5000	0.5000	0.00000	0.00000	1 gm
1.3 wt.%	0.4935	0.4935	0.00325	0.00975	
2.6 wt.%	0.4870	0.4870	0.00650	0.01950	
3.9 wt.%	0.4805	0.4805	0.00975	0.02925	
5.2 wt.%	0.4740	0.4740	0.01300	0.03900	

3.4 Measurements of The Structural and The Morphological Characteristics

3.4.1 Fourier transform infrared spectrometer

FT-IR spectra were recorded by FT-IR (Bruker Company, German origin, type vertex 70). FT-IR was implemented at University of Babylon / College of Education for Pure Sciences - Department of Physics. In this study, the considered wavenumber range (WNR) is (500-4000) cm^{-1}. Figure 3.5, displays a diagram for system of FT-IR measurement.

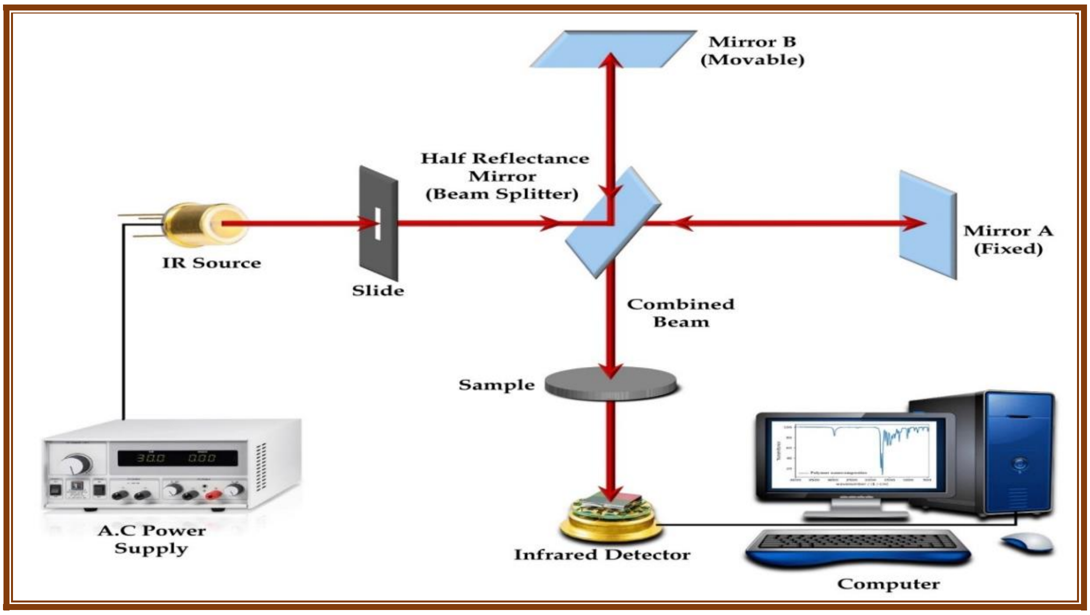

Figure 3.5: The diagrammatic representation system of Fourier transforms infrared spectrometer

3.4.2 Optical microscope

The change of surface morphology samples of (PC-PS/SiC-MnO_2), and (PC-PS/SiC-Co_2O_3) nanocomposites is observed applying the optical microscope. This used optical microscope (OM) was provided by Olympus (Top View, type Nikon-73346), as shown in Figure 3.6, and equipped with light intensity automatic controlled camera. Under magnification (10x), exited at the University of Babylon /College of Education for Pure Sciences-Department of Physics.

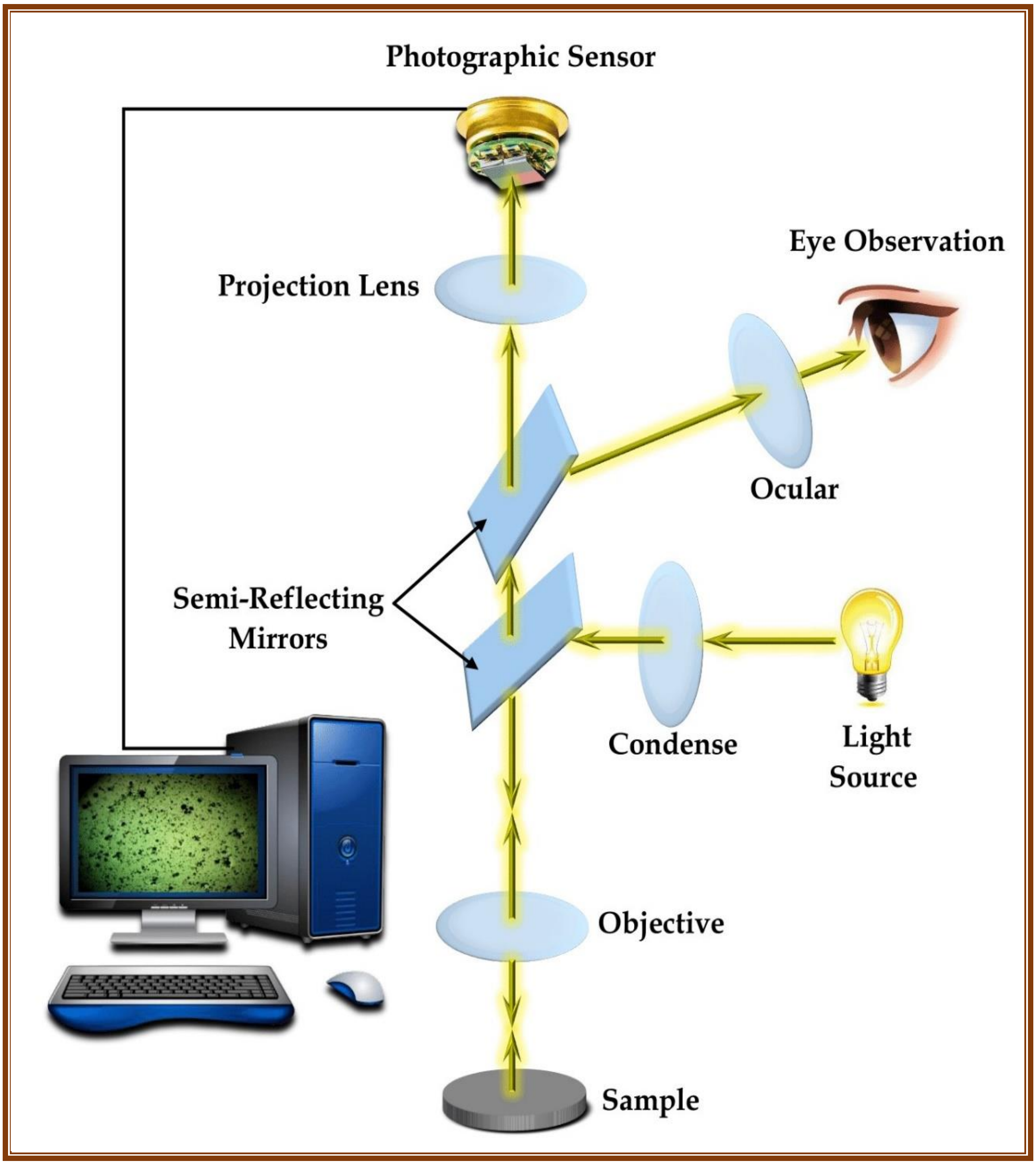

Figure 3.6: The diagrammatic representation system of optical microscope

3.4.3 Field emission scanning electron microscope

The field emission scanning electron microscope (FESEM) is an electron microscope that images the sample surface by scanning it with a high -energy beam of electrons in a raster scan pattern. The specimens for an FESEM testing must be electrically conductive, at least at the surface, and electrically grounded to prevent the accumulation of electrostatic charge at the surface. The surface morphology of (PC-PS/SiC-MnO_2), and (PC-PS/SiC-Co_2O_3) nanocomposites for pure, content (1.3wt.%), (2.6wt.%), (3.9 wt.%), and

(5.2wt.%) are tested by using FESEM (Carl Zeiss, German) in Shahid Behdishti University, Tehran, Iran. Figure 3.7, displays a diagram for system of FESEM measurement.

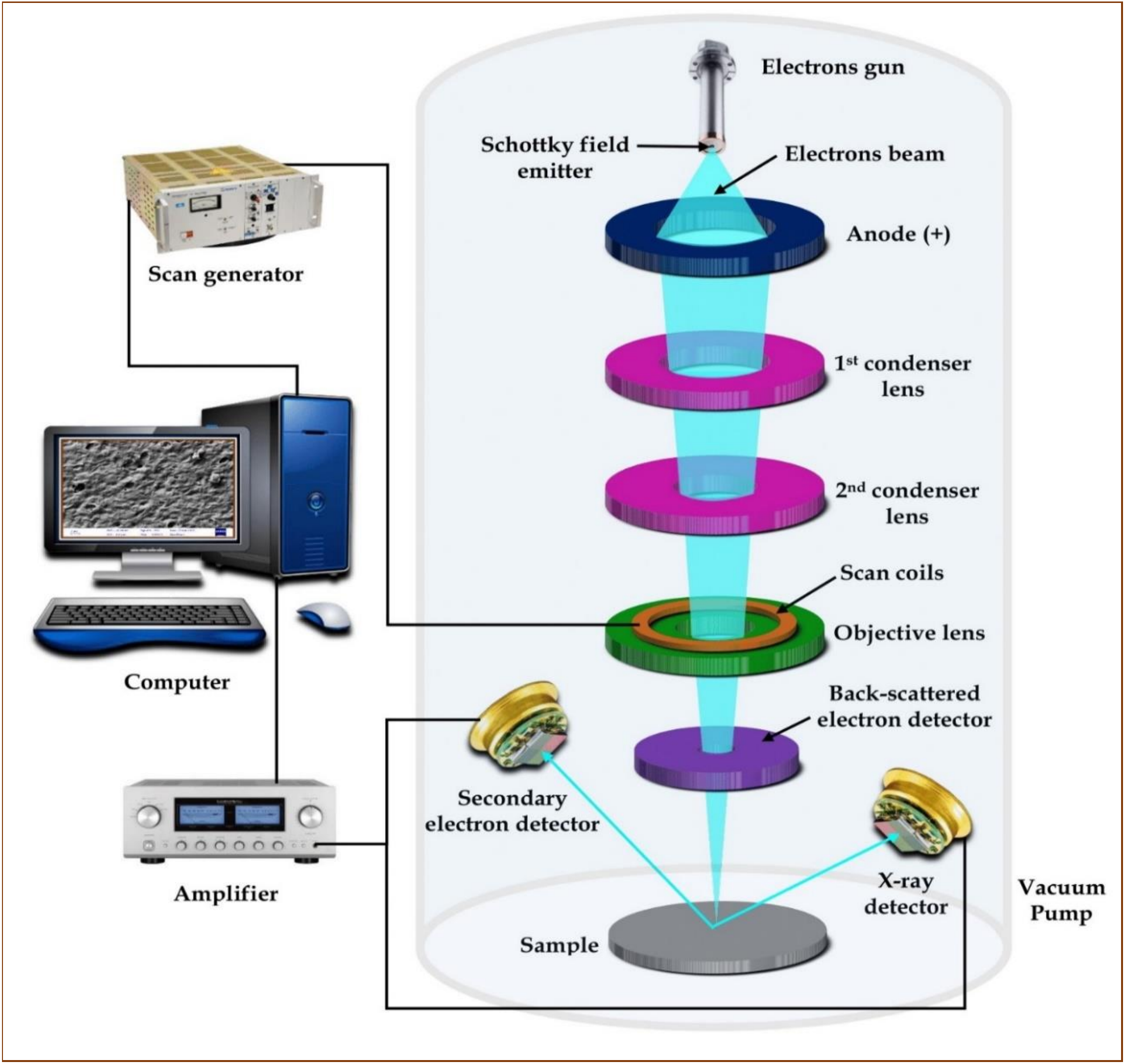

Figure 3.7: The diagrammatic representation system of field emission scanning electron microscope

3.5 Measurements of Linear Optical Characteristics

The double beam spectrophotometer (Shimadzu model UV-1800A° /JAPAN) was used to record the absorption spectrum of (PC-PS/SiC-MnO_2), and (PC-PS/SiC-Co_2O_3) nanocomposites in the wavelength range (260-860) nm. The absorption spectrum was recorded at standard room temperature. A computer (UV-Vis) Code, which was designed according to Appendix A.1, was used to obtain the probability coefficients and optical constants. It is located at the University of Babylon /College of Education for Pure Sciences-Department of Physics, as shown in Figure 3.8.

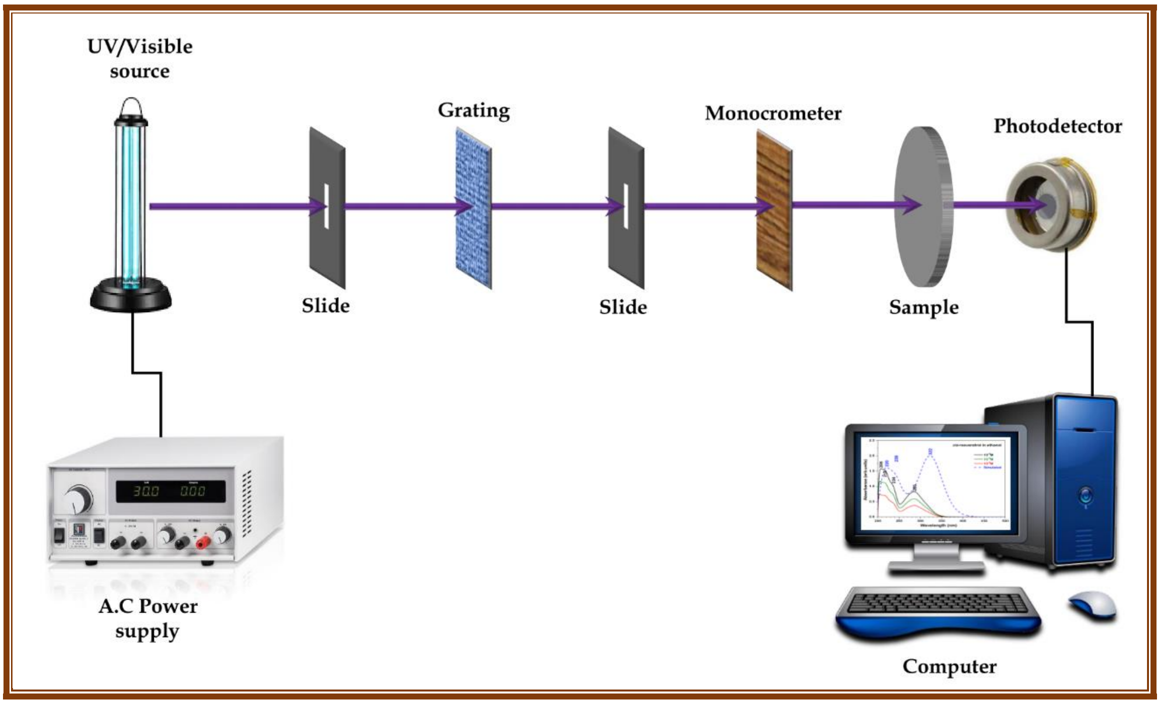

Figure 3.8: The diagrammatic representation system of UV-Vis spectrophotometer

3.6 Measurements of D.C Electrical Characteristics

The D.C electrical conductivity was measured at a temperature degree ranging between (50-100) °C, where the sample was placed into the oven, during that D.C was recorded and the electrical resistance. For accuracy, the sample was kept in the oven for (3-6) minutes before recorded these measurements. The resultant data of the Keithley electrometer (type 2400 source mater) were taken for different temperatures degrees in the University of Babylon / College of Education for Pure Sciences - Department of Physics. Figure 3.9, displays a diagram for system of D.C electrical measurement. A computer D.C electrical characteristics Code, which was designed according to Appendix A.2.

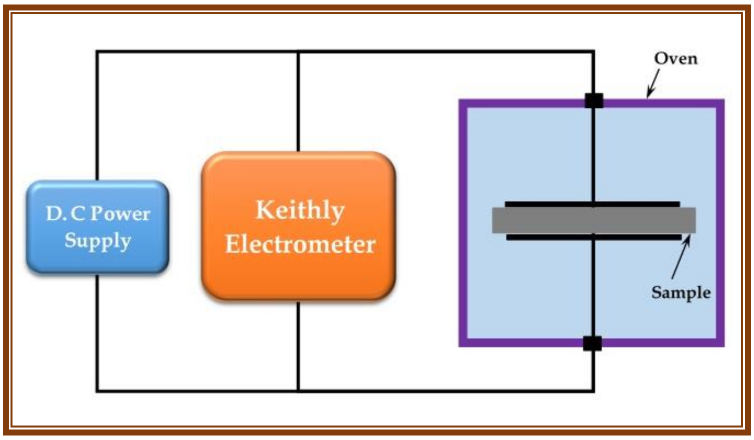

Figure 3.9: The diagrammatic representation system of D.C electrical characteristics

3.7 Measurements of A.C Electrical Characteristics

The A.C. Electrical Conductivity has been measured at (F = 100 Hz to 5 × 10^6 Hz) by LCR meter (HIOKI 3532–50 LCR HI TESTER) in University of Babylon / College of Education for Pure Sciences - Department of physics. Figure 3.10, displays a diagram for system of A.C electrical measurement. Only (1.5 cm) from each one of the samples has been taken and put between two electrodes at standard room temperature. The parallel capacitance (C_p), and dissipation factor (D) have been recorded for all samples. Dielectric constant, dielectric loss and conductivity have been calculated from this data. A computer A.C electrical characteristics Code, which was designed according to Appendix A.3.

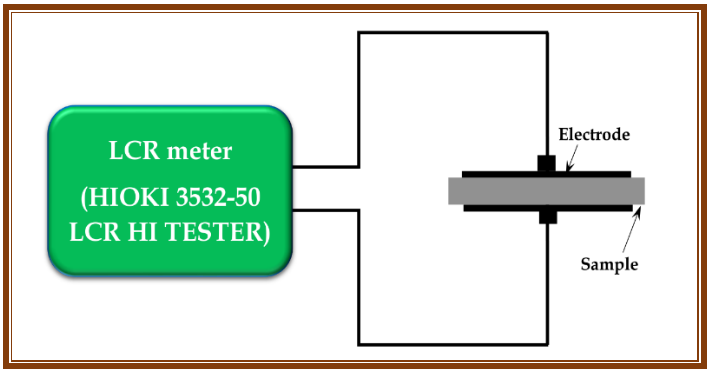

Figure 3.10: The diagrammatic representation system of A.C electrical characteristics

3.8 Measurements of Antibacterial Activity Application

Antimicrobial activity of the (PC-PS/SiC-MnO_2), and (PC-PS/SiC-Co_2O_3) nanocomposites tested samples are determined using a disc diffusion method. The antibacterial activities are done by using gram-positive organisms (Staphylococcus aureus), and gram-negative organisms (Salmonella enterica). Bacteria (Staphylococcus aureus, and Salmonella enterica) were cultured in Muller-Hinton Medium. The disks of the (PC-PS/SiC-MnO_2), and (PC-PS/SiC-Co_2O_3) nanocomposites were placed over the media and incubated at 37°C for 24 hours. The inhibition zone diameter was measured. This work done, in Al-Ameen Center for Researches and Advanced Biotechnologies / Najaf Governorate - Iraq country, as presented in Figure 3.11. A computer A.C electrical characteristics Code, which was designed according to Appendix B.1.

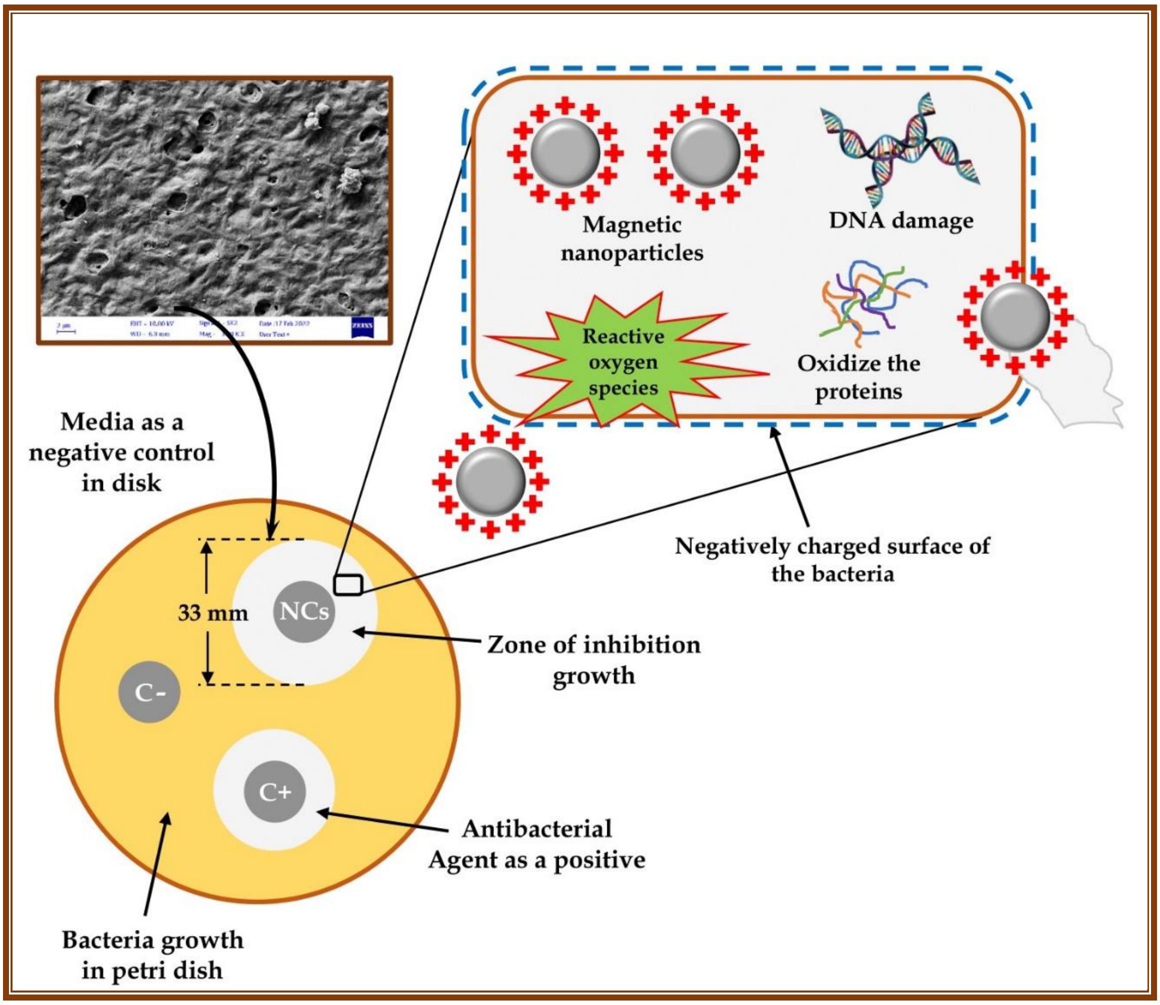

Figure 3.11: Mechanism inhibition bacteria of polymeric blend, and polymer bionanocomposites by employing using disk diffusion method [158].

3.9 Measurements of Photodegradation Activity Application

In order to examine the photocatalytic activity of (PC/PS) polymeric blend, (PC-PS/SiC-MnO_2), and (PC-PS/SiC-Co_2O_3) nanocomposites, an amount of 100 mL ionized distilled water solution of methylene orange dye with content (20 ppm) was placed in Pyrex glass. The prepared samples with a total weight of 0.5 gm were placed in this solution by magnetic stirring. Then, the samples were placed in an ultraviolet light exposure cabinet containing a magnetic stirrer to confirm the homogeneity of the mixture in which they were illuminated with 135W. The solution was kept in the dark under stirring for 90 min to reach the adsorption/desorption equilibrium. Samples were taken from the solution 10 ml of methylene orange solution every 15 minutes for 1.5 hours under UV-A (135 W) for 90 min, after which the molecules of the photocatalyst were separated by centrifugation at 4000 rpm for 20 minutes. MO dye solution has a maximum absorption at about $\lambda_{max} = 460\, nm$. The absorbance was measured using the double beam spectrophotometer (Shimadzu, UV-1800Å), in wavelength 200-600 nm. Figure 3.12, displays a diagram for system of photodegradation measurement. A computer A.C electrical characteristics Code, which was designed according to Appendix B.2.

3.10 Measurements of Pressure Sensors Application

The pressure sensor test for (PC-PS) polymeric blend, the (PC-PS/SiC-MnO_2), and (PC-PS/SiC-Co_2O_3) nanocomposites investigated by measuring the electrical of parallel capacitance (C_p) between two electrodes on the top and bottom of the nanocomposites samples by using an LCR meter (HIOKI 3532-50 LCR HI TESTER) for different pressures range (80-160) bar, it shows the schematic diagram of pressure sensor measurement system which locally manufactured. Figure 3.13, displays a diagram for system of pressure sensos measurement. A computer A.C electrical characteristics Code, which was designed according to Appendix B.3.

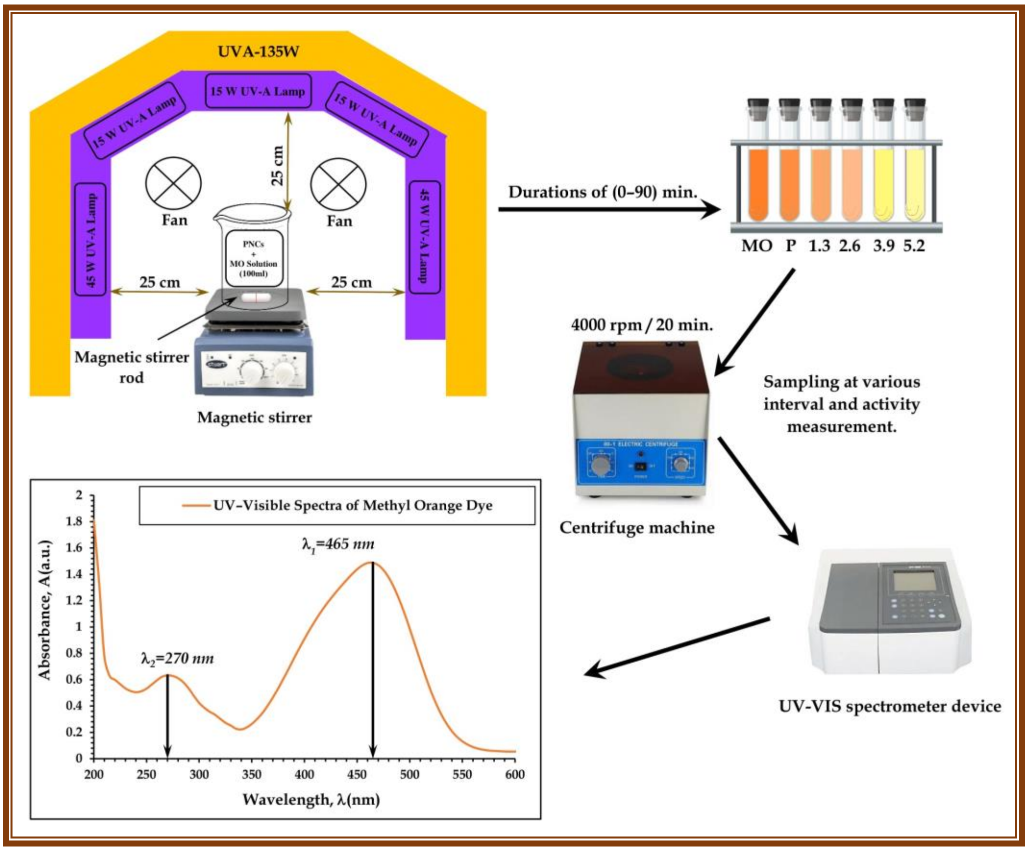

Figure 3.12: The schematic illustration of the preparation of the samples as photocatalytic vs methyl orange (MO) dye

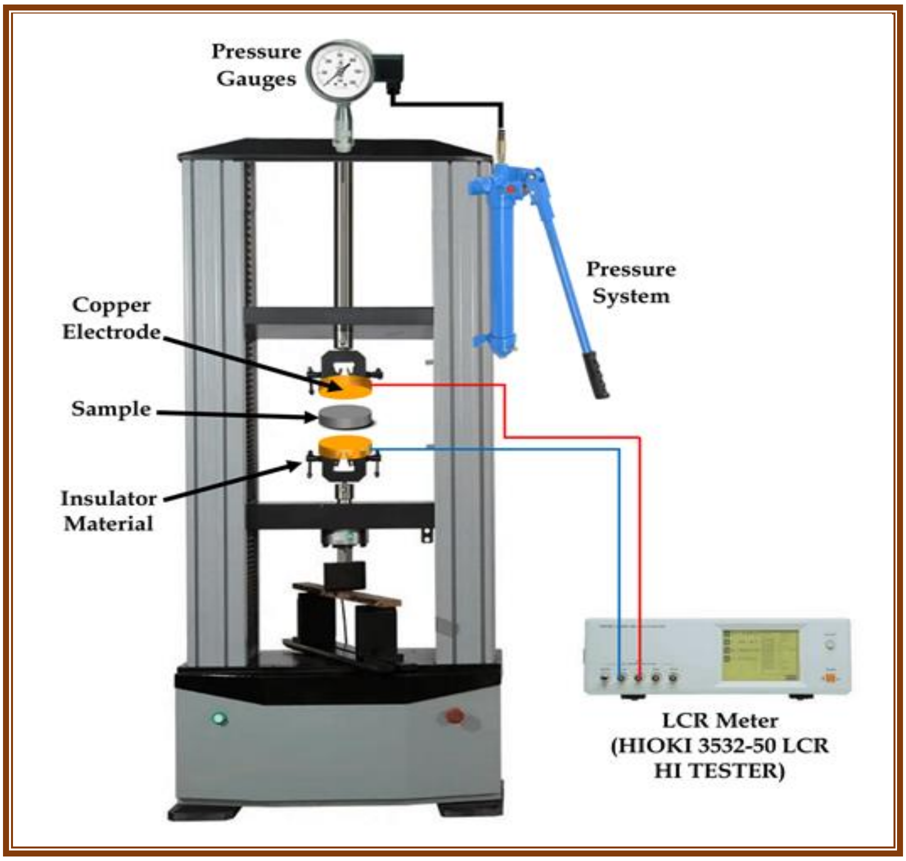

Figure 3.13: Design of a system showing the mechanism of work for the pressure sensor

Results and Discussions

Chapter Four

4.1 Introduction

This chapter includes the results of Structural, optical, direct current (D.C) electrical, and alternating current (A.C) electrical measurements of (PC-PS/SiC-MnO_2), and (PC-PS/SiC-Co_2O_3) nanocomposites and discussions. The Impact of adding the SiC/MnO_2 nanoparticles and SiC/Co_2O_3 nanoparticles on structural, optical, D.C electrical, and A.C electrical characteristics for (PC/PS) polymeric blend is discussed. The Antibacterial, photodegradation, and pressure sensors applications for (PC-PS/SiC-MnO_2), and (PC-PS/SiC-Co_2O_3) nanocomposites are also discussed.

4.2 The Structural, and Morphological Characteristics of (PC-PS/SiC-MnO_2) and (PC-PS/SiC-Co_2O_3) Nanocomposites

4.2.1 Fourier transform-infrared radiation of nanocomposites

FT-IR spectroscopy has been used to analyze the interactions between atoms in the system. These interactions can induce changes in the vibrational modes of the molecules in the polymeric blend. Figure 4.1, and Figure 4.2, show the FT-IR spectrum of (PC-PS/SiC-MnO_2), and (PC-PS/SiC-Co_2O_3) nanocomposites with different (SiC, MnO_2 and Co_2O_3) nanoparticles contents, respectively in the wavenumber, ($\bar{v}$) range (500-4000) cm^{-1}.

The FT-IR studies of nanocomposites show the connections in nanocomposites. The band exhibit at (2922.62) cm^{-1} is specific of an asymmetry stretching mode of CH_2 group of PS/PC polymeric blend [159]. The (C-H) collections were responsible for the band at (2363.10) cm^{-1} [160]. The peak at (1771.57) cm^{-1} were the characteristic of (C=O) functional group of PC while, the peak at (1492.62) cm^{-1} were assigned to CH_2 bending vibration of PS [161]. The stretching of the (C–O) band occurs around (1191.51) cm^{-1} of PC [162]. The peak of polycarbonate samples had aromatic stretches at (1014.72) cm^{-1} [163]. The band at (695.42) cm^{-1} refer to (C-H) bend of PS [164].

Changes in the spectral of (PC/PS) caused by SiC, MnO_2, and Co_2O_3 nanoparticles involve band shifts and intensity changes. The connections of nanoparticles with polymers were responsible for these variations. FT-IR analysis shows no interactions between the (PC/PS) polymeric matrix and the SiC, MnO_2, and Co_2O_3 nanoparticles. The transmittance in Figures decreases slightly as the contents of SiC/MnO_2, and SiC/Co_2O_3 nanoparticles increase, implying that the density of nanocomposites rises. These are consistent with the results of researchers [165, 166].

It is note that the intensity of these peaks are increasing with the increasing of the number of the pulses that was attributed to the increasing of the concentration of the SiC/MnO_2, and SiC/Co_2O_3 nanoparticles in the PC, PS matrix matrix that was confirmed by the dynamic light scattering and also due to indicating that C=O has been established. Strong interaction between the SiC/MnO_2, and SiC/Co_2O_3 nanoparticles in the PC, PS matrix confirmed the good interfacial adhesion, which is an important criterion for the nanocomposite to be used as the pressure sensors and optoelectronic devices This result are agreement with the previous studies [167].

Furthermore, significant changes observed in width and the intensity of the vibrational bands of the (PC/PS) polymeric blend upon addition of SiC/MnO_2, and SiC/Co_2O_3 nanoparticles indicate the strong influence of SiC/MnO_2, and SiC/Co_2O_3 nanoparticles on spectroscopy of polymeric blend [168].

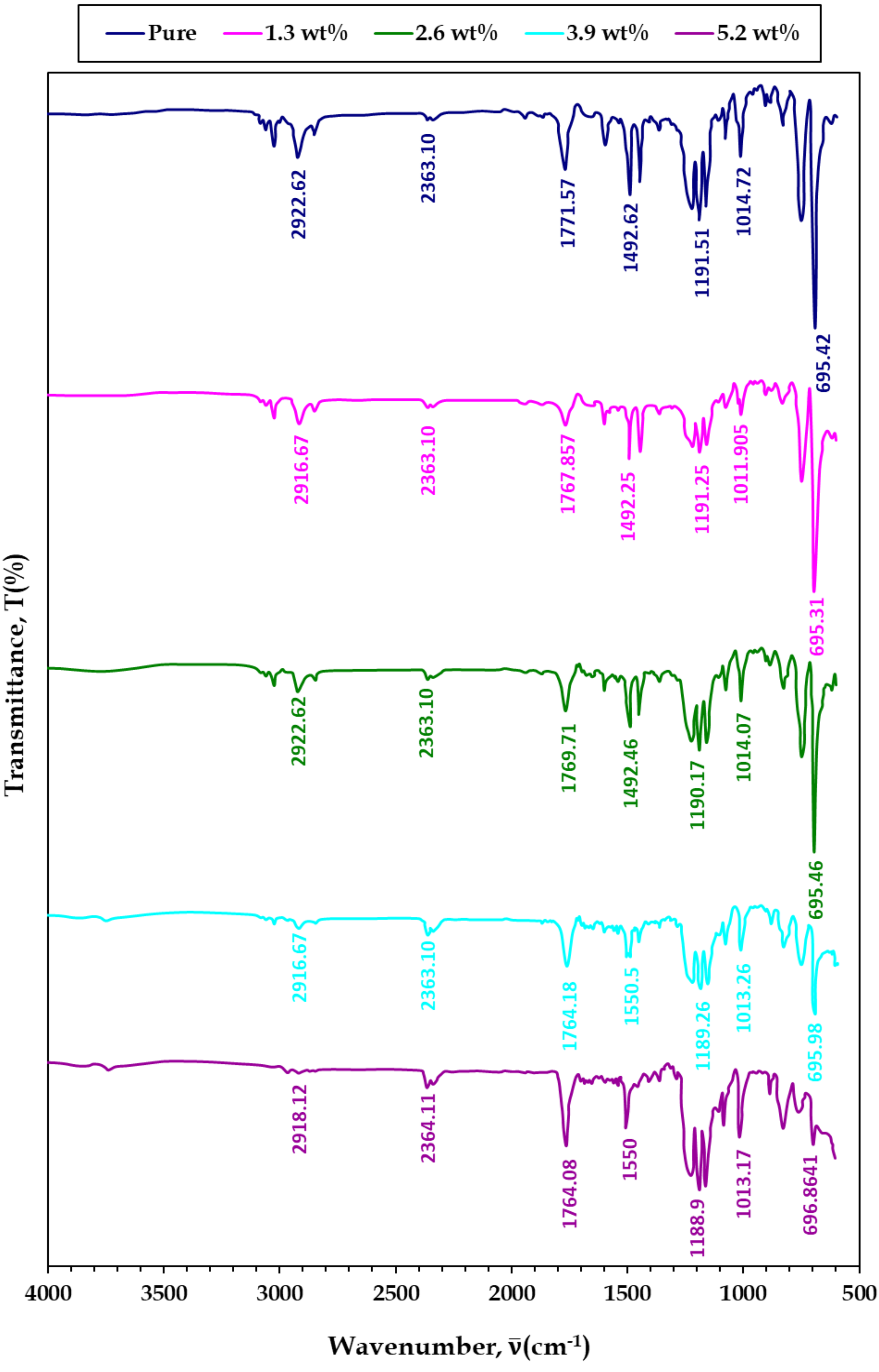

Figure 4.1: FT-IR spectra of (PC/PS) polymeric blend, and (PC-PS/SiC-MnO$_2$) nanocomposites.

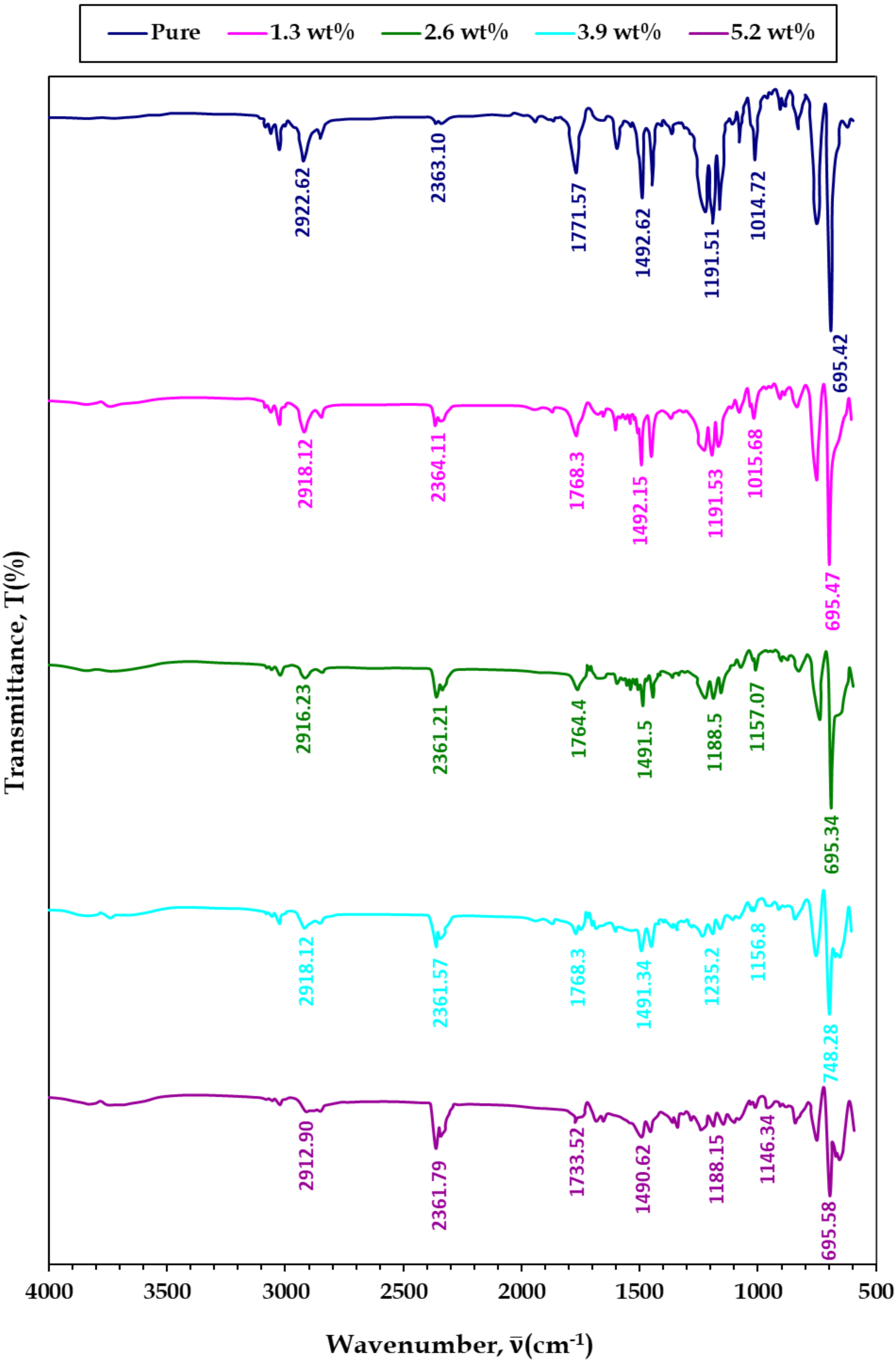

Figure 4.2: FT-IR spectra of (PC/PS) polymeric blend, and (PC-PS/SiC-Co_2O_3) nanocomposites.

4.2.2 Optical microscope of nanocomposites

Microscope of nanocomposites is the examination of the spread of nanoparticles in the polymer mixture. Figure 4.3, and 4.4 display the arrangements of SiC, MnO_2 and Co_2O_3 nanoparticles in (PC/PS) polymer blend at a magnification power (x10) respectively. The microscope images show that the nanoparticles are aggregates as a cluster at lower content. When the content of SiC/MnO_2 nanoparticles and SiC/Co_2O_3 nanoparticles are increased, the nanoparticles form a network of paths within the (PC/PS) polymer blend, hence the charge carriers are allowed to pass through the paths. This is consistent with the results of researcher [169].

The images showed that randomly distributed aggregates or particles on the top surface, which are attributed to the presence of 1.3 wt.% of SiC/MnO_2 and SiC/Co_2O_3, which are aggregated, and cracks in clusters form. With an increase in the number of SiC/MnO_2 nanoparticles and SiC/Co_2O_3 nanoparticles in the matrix, a network is formed. The results show that when the content of nanoparticles rises, the number and size of white dots on the surface increases. This may be attributed to the formation of a larger cluster, which in turn expanded to form network paths of aggregates through the PC/PS blend. The surface morphology of the films displays a homogeneous density of grain boundaries. The results also indicate that nanoparticles prefer to form well-dispersed aggregates in PC/PS blend films, which may be an indication of a homogenous growth process, and that this change is attributed to the strong interfacial reaction of the functional groups on the surface of SiC/MnO_2 nanoparticles and SiC/Co_2O_3 nanoparticles with a blend polymer that exhibited a significant change in the nanocomposite morphology and mechanical response [170].

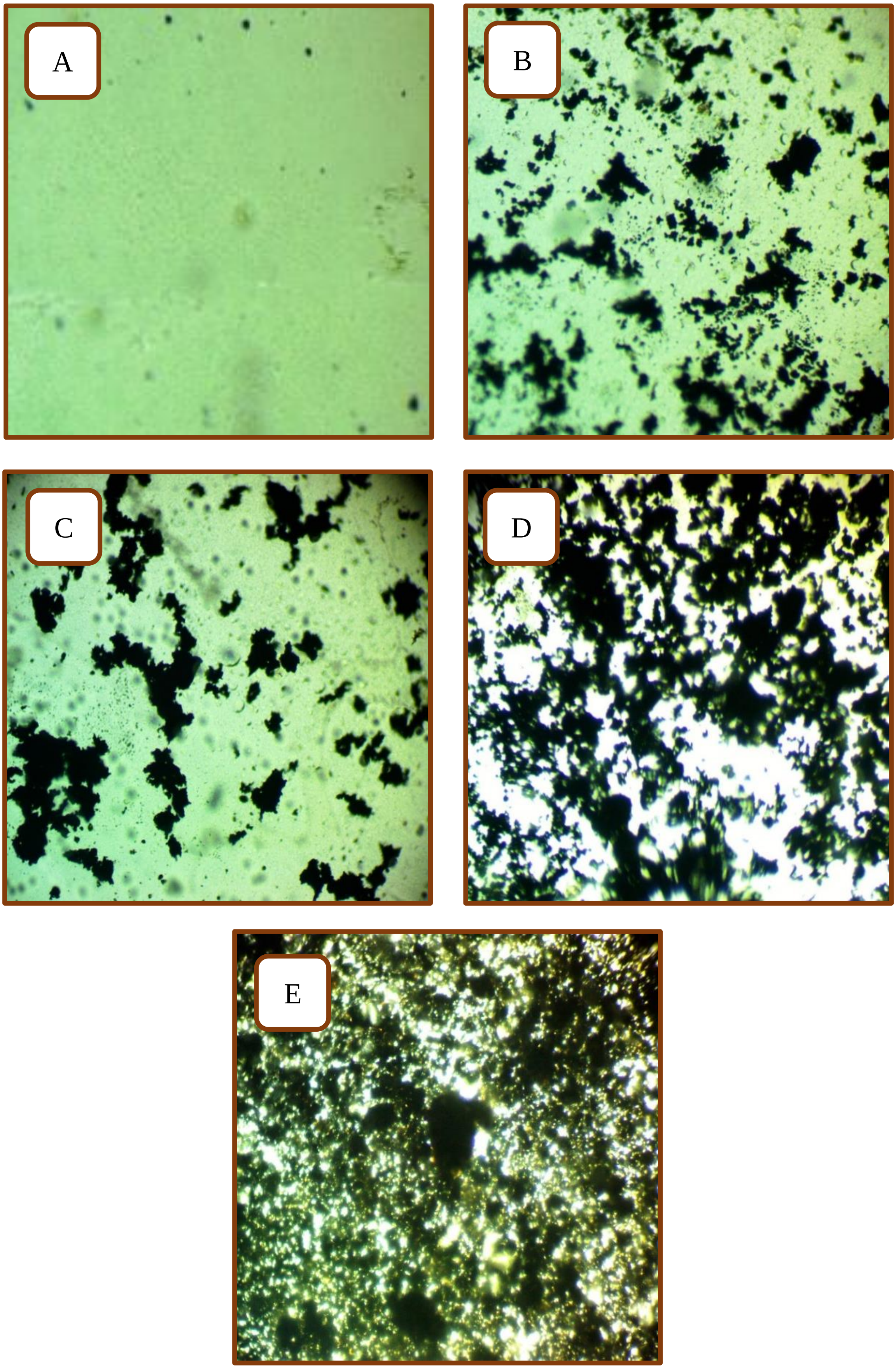

Figure 4.3: Photomicrographs (x10) for (PC-PS/SiC-MnO_2) nanocomposites: (A) for pure (B) for 1.3 wt.% (SiC/MnO_2) NPs , (C) for 2.6 wt.% (SiC/MnO_2) NPs, (D) for 3.9 wt.% (SiC/MnO_2) NPs and (E) for 5.2 wt.% (SiC/MnO_2) NPs

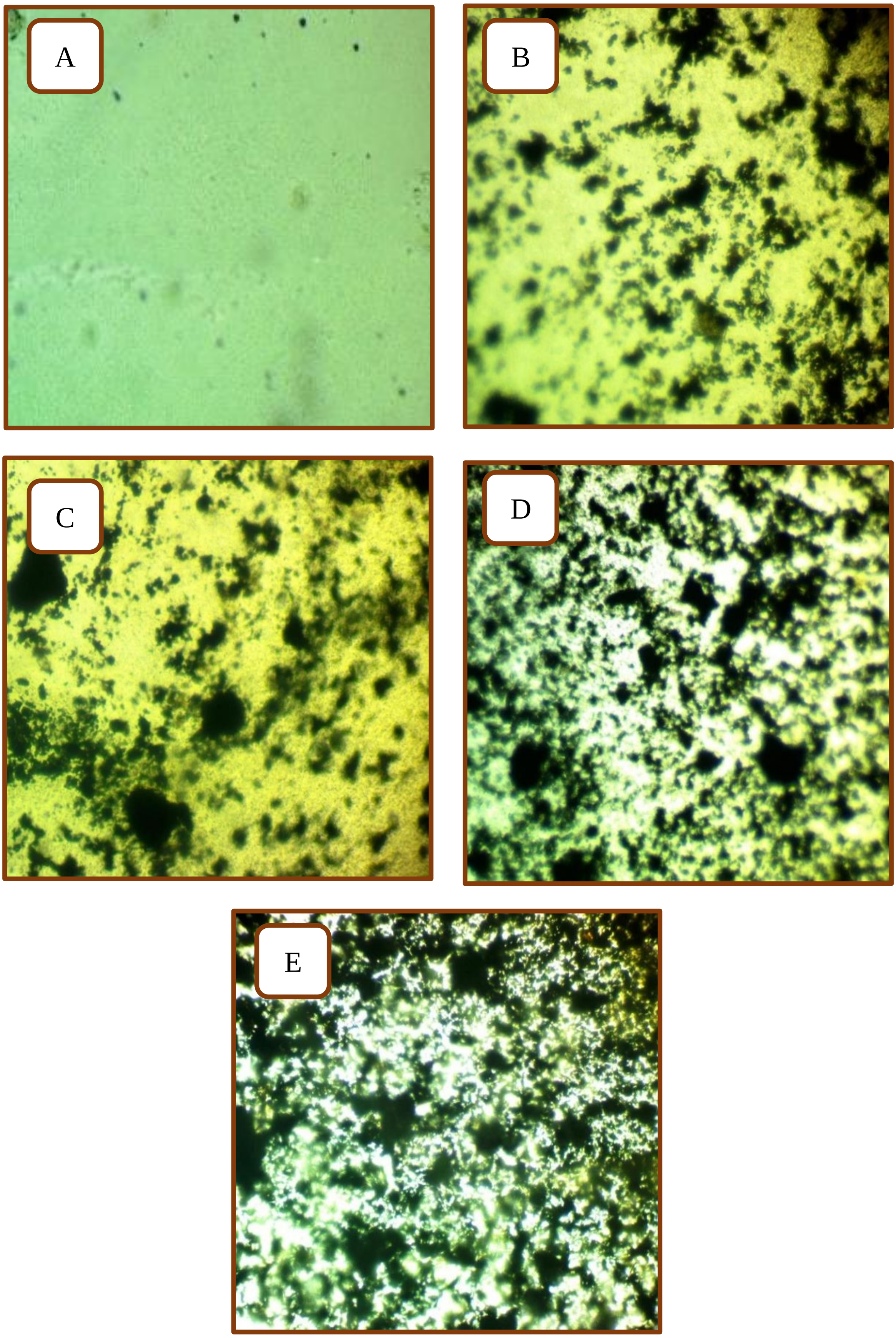

Figure 4.4: Photomicrographs (x10) of (PC-PS/SiC-Co_2O_3) nanocomposites: (A) for pure (B) for 1.3 wt.% (SiC/Co_2O_3) NPs, (C) for 2.6 wt.% (SiC/Co_2O_3) NPs, (D) for 3.9 wt.% (SiC/Co_2O_3) NPs, and (E) for 5.2 wt.% (SiC/Co_2O_3) NPs.

4.2.3 Field emission scanning electron microscope of nanocomposites

Figure 4.5, to Figure 4.8 display the 2D-FESEM and 3D-FESEM images for (PC/PS) blend with different contents of (SiC/MnO_2), and (SiC/Co_2O_3) nanoparticles at different magnification power to study nanocomposite morphology and nanoparticles arrangement at lower and higher contents of (SiC/MnO_2), and (SiC/Co_2O_3) nanoparticles. The (Micro and Nano) FESEM images show that paths network formed of nanoparticles inside the (PC-PS) blend where charge carriers are allowed to pass through the paths [171].

The two-dimensional 2D-field emission scanning electron microscopy (2D-FESEM) is commonly used to identify phase separations and interfaces in polymer films for the purpose of studying their compatibility with one another [172]. The morphology of the PC/PS blend and the films loaded with 1.3, 2.6, 3.9, and 5.2 wt. % of SiC/MnO_2 nanoparticles and SiC/Co_2O_3 nanoparticles films were examined by the 2D-FESEM and representative micro-images are shown in Figures (4.5 and 4.6), respectively. The PC/PS film appears to have a uniform, rough, and homogeneous surface. There are no signs of two polymer phases (PC and PS) that suggest PC chains can be mixed with PS chains in a way that proves the two polymers are the same and can work together. This could be because the filler and matrix have similar chemicals and interact through hydrogen bonds [173]. In addition, the surface morphology of the PC/PS polymer film changes from rougher to smoother (Less rough) with an increasing additive of SiC/MnO_2 nanoparticles and SiC/Co_2O_3 nanoparticles, demonstrating the convenient distribution of SiC/MnO_2 nanoparticles and SiC/Co_2O_3 nanoparticles within the hosting polymer network. As illustrated in Figures (4.7 and 4.8), the nanoparticles form clusters inside the polymer mix as the contents of SiC/MnO_2 nanoparticles and SiC/Co_2O_3 nanoparticles grow in the (PC/PS) blend. When nanoparticle contents reach 5.2 wt.%, the particles form content network routes through which charge carriers can move, resulting in a change in the material's characteristics [174]. The degree of surface roughness increases as the content of SiC/MnO_2 nanoparticles and SiC/Co_2O_3 nanoparticles increases.

The 3D-FESEM micrographs of the corresponding 3D-FESEM nano-images are depicted in Figure 4.9 and Figure 4.10, giving a vivid insight into the surface. The pristine PC/PS is highly smooth, while the surface becomes rougher by introducing of SiC/MnO_2 NPs and SiC/Co_2O_3 NPs into the PC/PS polymer film. The surface roughness of the investigated films was determined in terms of the root mean square roughness (R_q), mean roughness (R_a), maximum peak height (R_p), and maximum pit depth (R_v) parameter by using "Gwyddion" software to acquire 3D-images, and by the following equations [174];

$$R_q = \sqrt{\frac{\sum_{i=1}^{N}(Z_i - Z_{av})^2}{N}} \tag{4.1}$$

$$R_a = \sqrt{\frac{\sum_{i=1}^{N}\left|Z_i - Z_{cp}\right|}{N}} \tag{4.2}$$

where Z_i is a local Z-value, Z_{av} the average Z-value within the investigated area, N expresses number of points within the given area, and Z_{cp} is a Z-value within the center plane. The root mean square (RMS) increased from 18.217 nm at content of 1.3 wt.% to 24.495 nm at content of 5.2 wt.% for PC-PS/SiC-MnO_2 NCPs and it's increased from 20.394 nm at content of 1.3 wt.% to 28.959 nm at content of 5.2 wt.% for PC-PS/SiC-Co_2O_3 NCPs whereas, the percentage increase of the surface roughness is 25.63% and 29.58%, respectively. The RMS roughness of the examined films is listed in Table 4.1, and Table 4.2. The RMS roughness and mean roughness of the project area (1.3 × 1.3) μm^2 increase with the increasing filler content which may attributed to the clustering of nanoparticles. Roughness is very essential parameter in layer device including optoelectronic application where it one of basic reasons for shunt resistance [174].

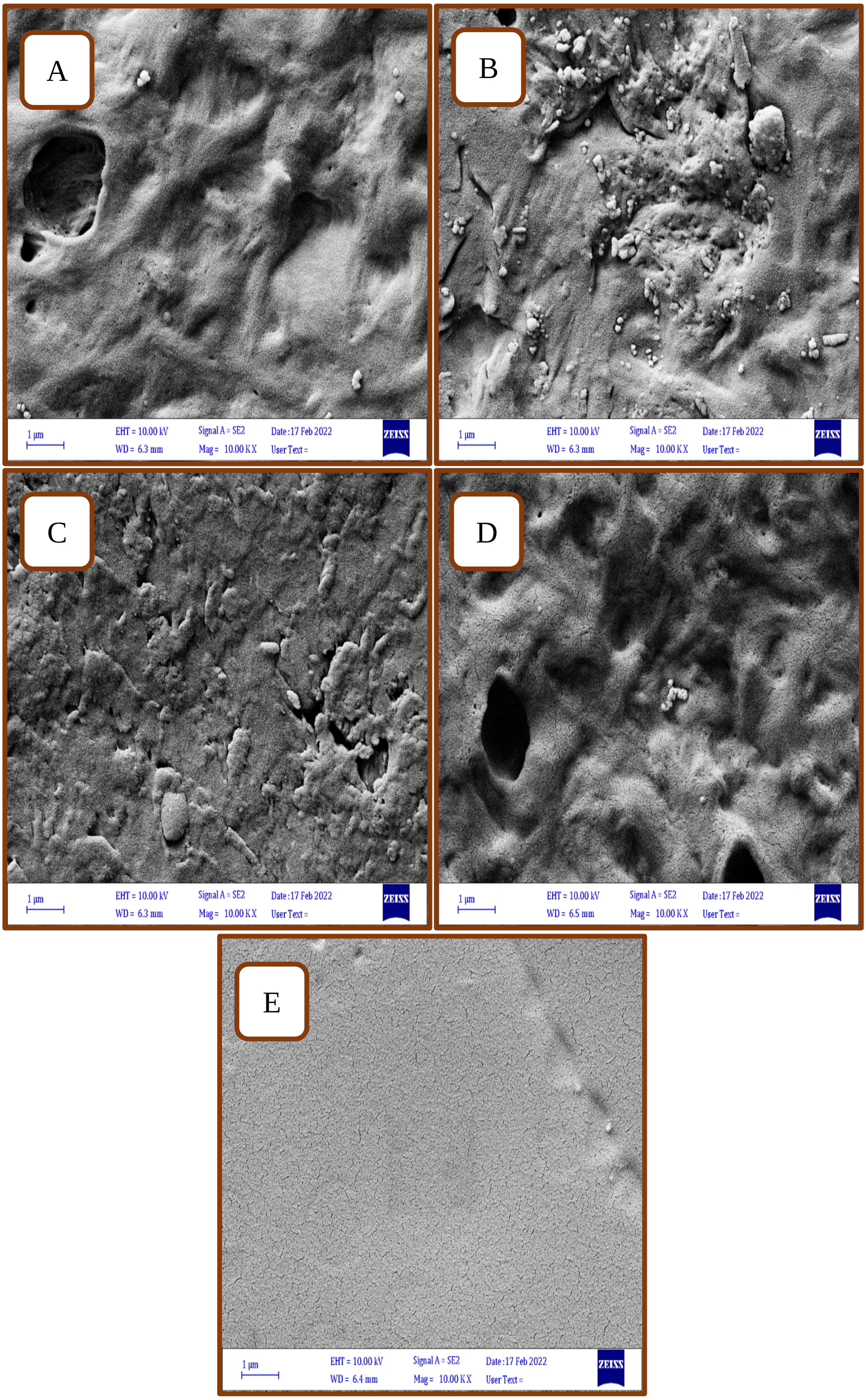

Figure 4.5: 2D-FESEM micro-images of (PC-PS/SiC-MnO$_2$) nanocomposites: (A) for pure (B) for 1.3 wt.% (SiC/MnO$_2$) NPs , (C) for 2.6 wt.% (SiC/MnO$_2$) NPs, (D) for 3.9 wt.% (SiC/MnO$_2$) NPs and (E) for 5.2 wt.% (SiC/MnO$_2$) NPs

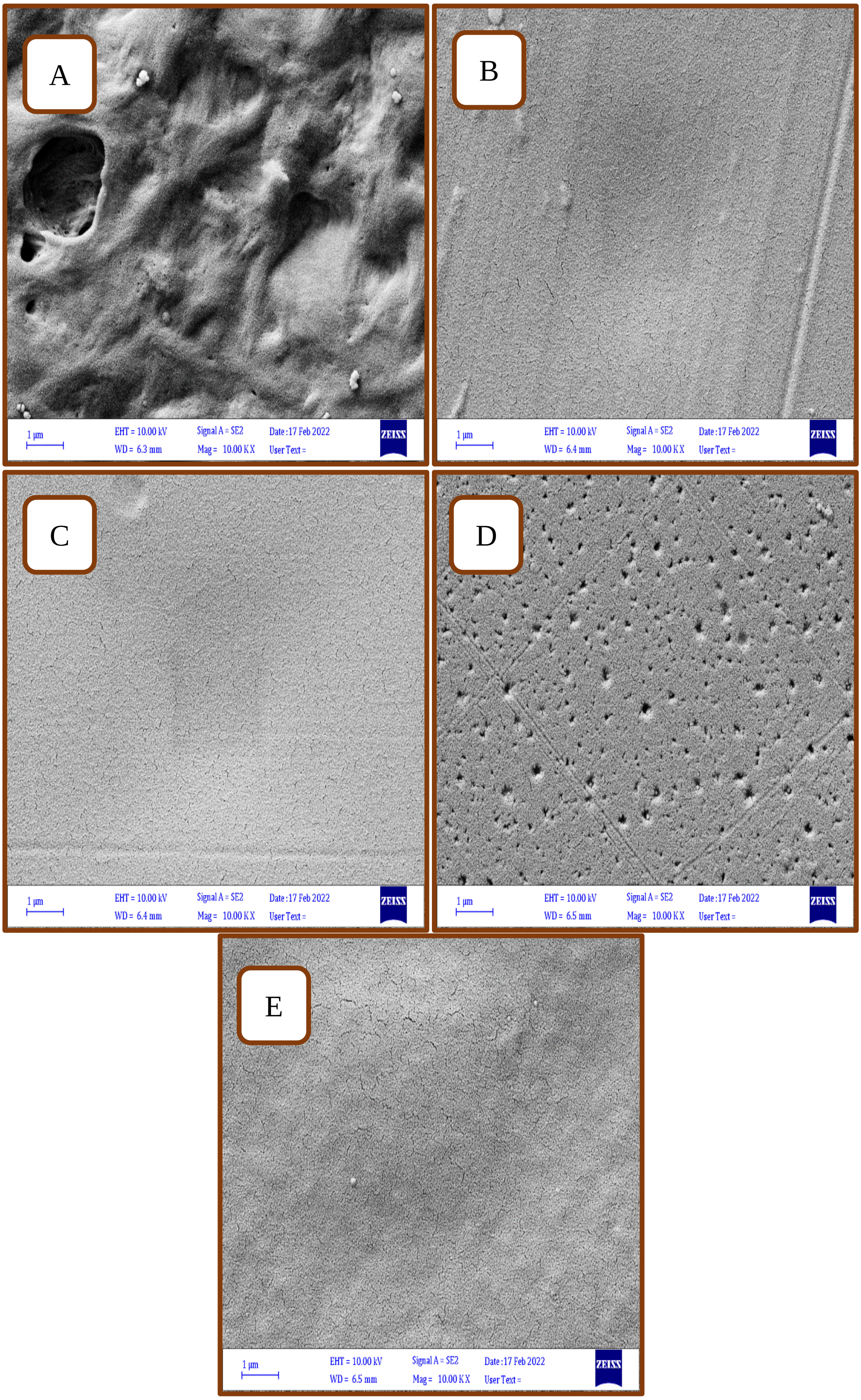

Figure 4.6: 2D-FESEM micro-images of (PC-PS/SiC-Co_2O_3) nanocomposites :(A) for pure (B) for 1.3 wt.% (SiC/Co_2O_3) NPs, (C) for 2.6 wt.% (SiC/Co_2O_3) NPs, (D) for 3.9 wt.% (SiC/Co_2O_3) NPs and (E) for 5.2 wt.% (SiC/Co_2O_3) NPs

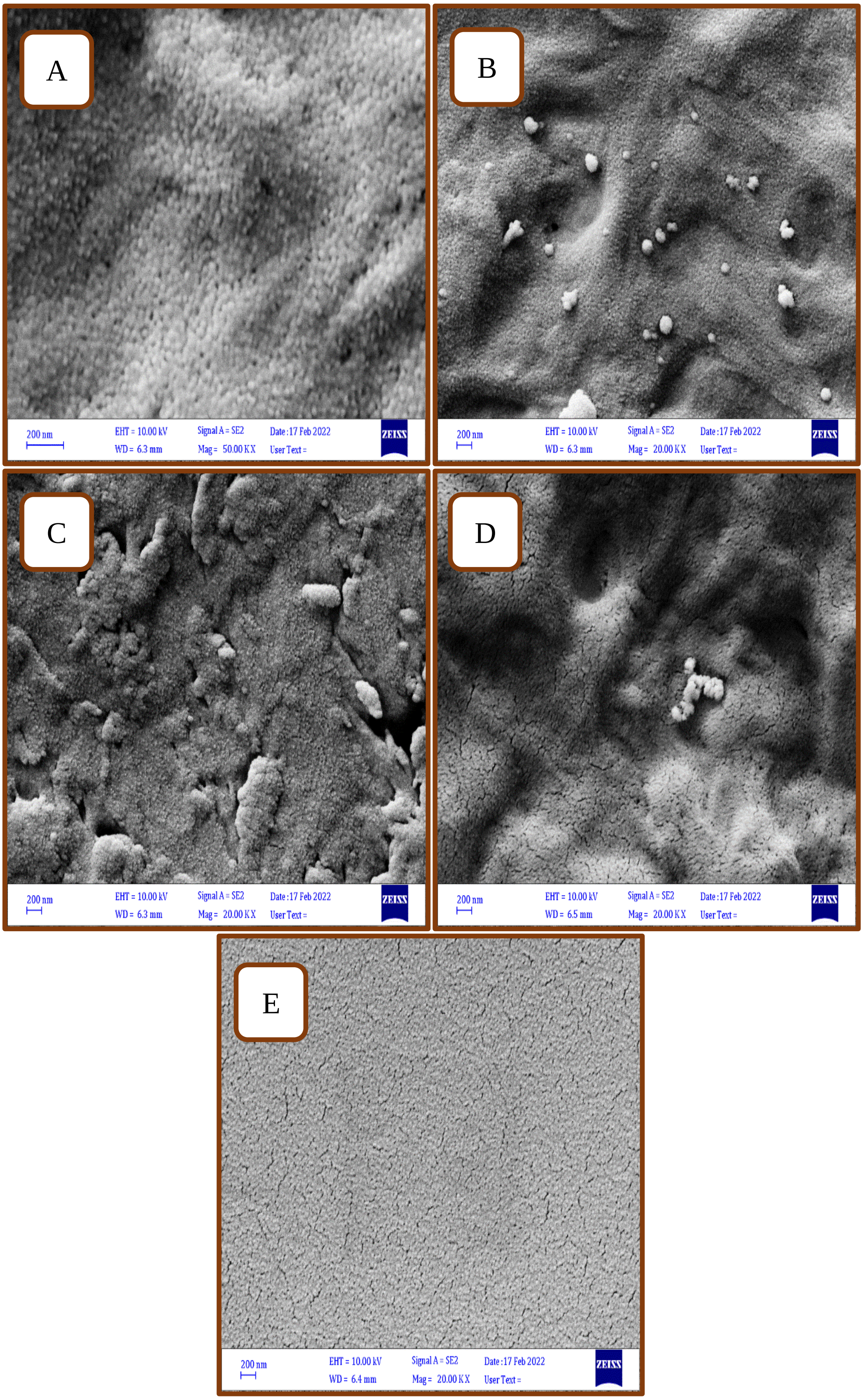

Figure 4.7: 2D-FESEM nano-images of (PC-PS/SiC-MnO$_2$) nanocomposites: (A) for pure (B) for 1.3 wt.% (SiC/MnO$_2$) NPs, (C) for 2.6 wt.% (SiC/MnO$_2$) NPs, (D) for 3.9 wt.% (SiC/MnO$_2$) NPs and (E) for 5.2 wt.% (SiC/MnO$_2$) NPs

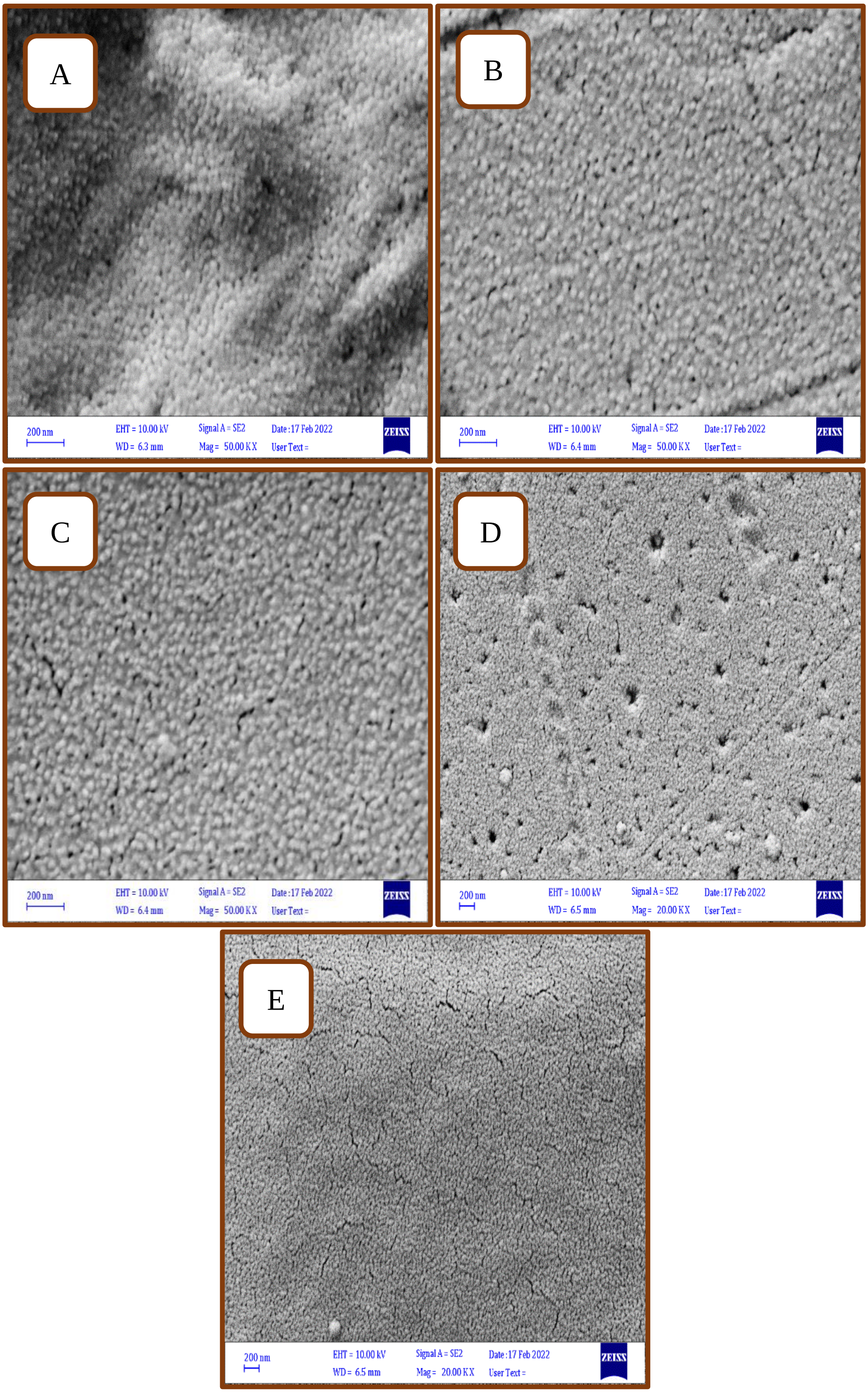

Figure 4.8: 2D-FESEM nano-images of (PC-PS/SiC-Co_2O_3) nanocomposites: (A) for pure (B) for 1.3 wt.% (SiC/Co_2O_3) NPs, (C) for 2.6 wt.% (SiC/Co_2O_3) NPs, (D) for 3.9 wt.% (SiC/Co_2O_3) NPs and (E) for 5.2 wt.% (SiC/Co_2O_3) NPs

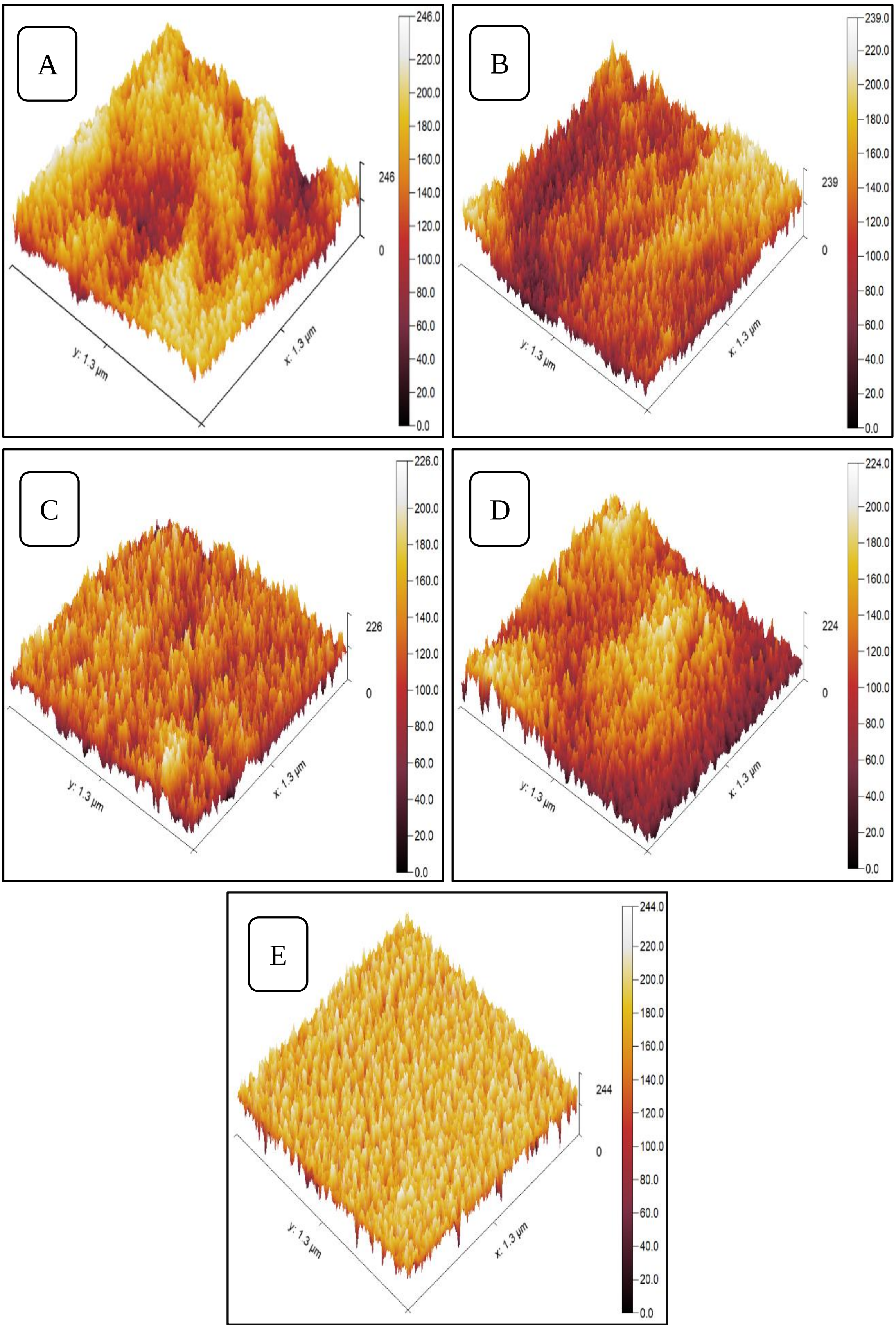

Figure 4.9: 3D-FESEM nano-images of (PC-PS/SiC-MnO_2) nanocomposites: (A) for pure (B) for 1.3 wt.% (SiC/MnO_2) NPs, (C) for 2.6 wt.% (SiC/MnO_2) NPs, (D) for 3.9 wt.% (SiC/MnO_2) NPs and (E) for 5.2 wt.% (SiC/MnO_2) NPs

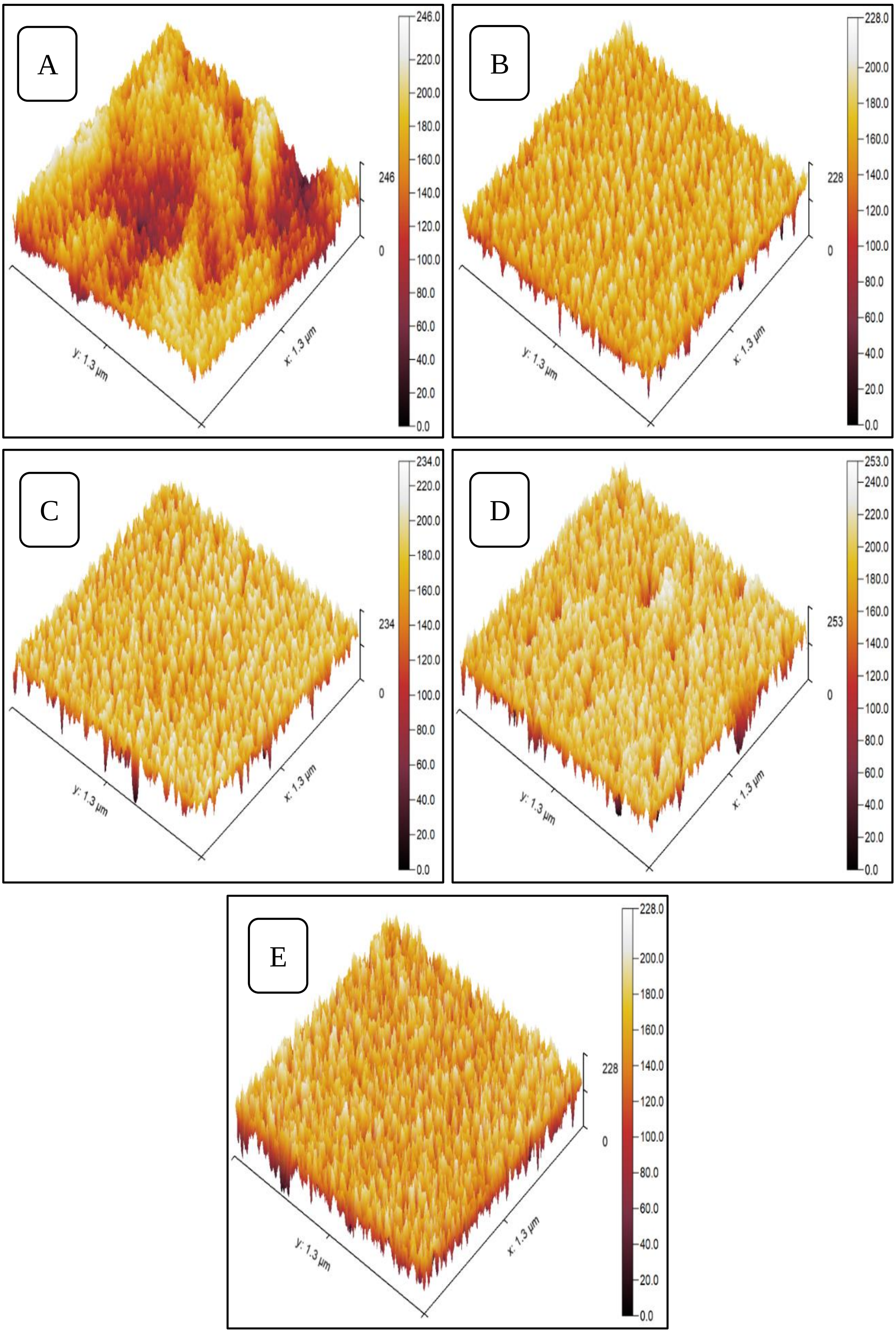

Figure 4.10: 3D-FESEM nano-images of (PC-PS/SiC-Co_2O_3) nanocomposites: (A) for pure (B) for 1.3 wt.% (SiC/Co_2O_3) NPs, (C) for 2.6 wt.% (SiC/Co_2O_3) NPs, (D) for 3.9 wt.% (SiC/Co_2O_3) NPs and (E) for 5.2 wt.% (SiC/Co_2O_3) NPs

Table 4.1: The morphological characteristics of (PC/PS) blend and nanocomposites of (PC-PS/SiC-MnO_2) films at standard room temperature

Contents of SiC/MnO_2 nanoparticles	Roughness mean (Ra)	Root mean square (Rq)	Maximum peak height (Rp)	Maximum pit depth (Rv)
Pure	33.044	40.057	111.158	134.842
1.3 wt.%	18.217	24.715	142.584	96.416
2.6 wt.%	20.526	31.221	127.174	98.826
3.9 wt.%	23.687	32.676	124.566	99.434
5.2 wt.%	24.495	37.485	87.186	156.814

Table 4.2: The morphological characteristics of (PC/PS) polymeric blend and nanocomposites of (PC-PS/SiC-Co_2O_3) films at standard room temperature

Contents of SiC/Co_2O_3 nanoparticles	Roughness mean (Ra)	Root mean square (Rq)	Maximum peak height (Rp)	Maximum pit depth (Rv)
Pure	33.044	40.057	111.158	134.842
1.3 wt.%	20.394	25.956	85.049	142.951
2.6 wt.%	24.272	30.511	79.684	154.316
3.9 wt.%	28.801	35.169	86.515	166.485
5.2 wt.%	28.959	39.815	99.799	128.201

4.3 The Linear Optical Characteristics of (PC-PS/SiC-MnO_2) and (PC-PS/SiC-Co_2O_3) Nanocomposites

The optical characteristics of (PC-PS/SiC-MnO_2) and (PC-PS/SiC-Co_2O_3) nanocomposites include absorbance, transmittance, the absorption coefficient, the skin depth, energy gap, Urbach tails energy, extinction coefficient, refractive index, dielectric constants, and optical conductivity.

4.3.1 The absorbance and transmittance spectrum of (PC-PS/SiC-MnO_2) and (PC-PS/SiC-Co_2O_3) nanocomposites

Figure 4.11 and Figure 4.12 display the variation of absorbance for (PC-PS/SiC-MnO_2) and (PC-PS/SiC-Co_2O_3) nanocomposites with wavelength (λ) of the incident light respectively. As shown in Figures, the absorbance, (A) for all prepared samples of nanocomposites increases with the increase of the contents for SiC/MnO_2 nanoparticles, and SiC/Co_2O_3 nanoparticles, this is due to the increase of the number of charge carriers with increasing content of nanoparticles [175]. The absorbance of nanocomposites increased about 64.32% and 64.15% respectively when reached the SiC/MnO_2 nanoparticles, and SiC/Co_2O_3 nanoparticles content to 5.2 wt.% at $\lambda = 560\ nm$, this behavior useful for optoelectronics, photocatalysis and solar cells. In general, It is observed that the absorbance decreases with the increasing wavelength for all prepared nanocomposites. This physically means that an incident photon has not been able to excite the electron and move it from a lower to a higher energy level because the energy of the incident photon is less than the value of the energy gap of the nanocomposites [176]. In the UV-region, the absorbance of all samples of nanocomposites has a high value, this is due to the excitations of donor level electrons to the conduction band at these energies.

The high absorbance of samples for nanocomposites at UV-region attributed to the energy of photons sufficient to interact with atoms. The absorption spectrum of (PC/PS) blend is limited in the UV region, but it is enhanced when SiC/MnO_2 nanoparticles, and SiC/Co_2O_3 nanoparticles were added, this is due to the high energy gap of the blend. The curves of (PC-PS/SiC-MnO_2) and (PC-PS/SiC-Co_2O_3) nanocomposites of high SiC/MnO_2 nanoparticles, and SiC/Co_2O_3 nanoparticles content showed a clear peak in the UV-region and less absorption in the visible region. The peak of high absorption is observed at around $260\,nm$, this is due to the absorption of SiC/MnO_2 nanoparticles, and SiC/Co_2O_3 nanoparticles as a result of the increase in the number of charge carriers [177].

At visible and near infrared regions, the absorbance for all samples of nanocomposites decreases with increasing the wavelength, this behavior attributed to the energy of incident photons doesn't sufficient energy to interact with atoms, hence the photons will be transmitted when the wavelength increases. The (PC-PS/SiC-MnO_2) and (PC-PS/SiC-Co_2O_3) nanocomposites at 5.2 wt.% content of SiC/MnO_2 nanoparticles, and SiC/Co_2O_3 nanoparticles have the highest absorbance due to the high diffusivity of manganese dioxide nanoparticles in (PC/PS) polymeric blend, these results agreements with the results of the researchers [178].

Figure 4.13, and Figure 4.14 display the variation of transmittance, (T) for (PC-PS/SiC-MnO_2) and (PC-PS/SiC-Co_2O_3) nanocomposites with the wavelength (λ) of the incident light respectively. As shown in the Figures, the transmittance decreases with the increase of the contents for SiC/MnO_2 nanoparticles, and SiC/Co_2O_3 nanoparticles, this is due to the agglomeration of nanoparticles with increasing content and increase of the number of charge carriers. The transmittance of (PC-PS/SiC-MnO_2), and (PC-PS/SiC-Co_2O_3) nanocomposites decreased about 43.08% and 42.85% respectively when reached the SiC/MnO_2 nanoparticles, and SiC/Co_2O_3 nanoparticles content to 5.2 wt.% at $\lambda = 560\,nm$. In general, the transmittance of (PC-PS) blends higher than the transmittance of (PC/PS) blend, (PC-PS/SiC-MnO_2), and (PC-PS/SiC-Co2O3) nanocomposites [179].

In the UV-region, the transmittance of polymeric blend and nanocomposites shows more decrement than in the visible region. The Impact of adding SiC/MnO_2 nanoparticles, and SiC/Co_2O_3 nanoparticles are clear; they have a very low transmittance in the UV region, which decreased with increased content of SiC/MnO_2 nanoparticles, and SiC/Co_2O_3 nanoparticles in nanocomposites [180]. The values of absorbance and transmittance for the prepared nanocomposites at $\lambda = 560\,nm$ are shown in Table 4.4 and Table 4.5, respectively.

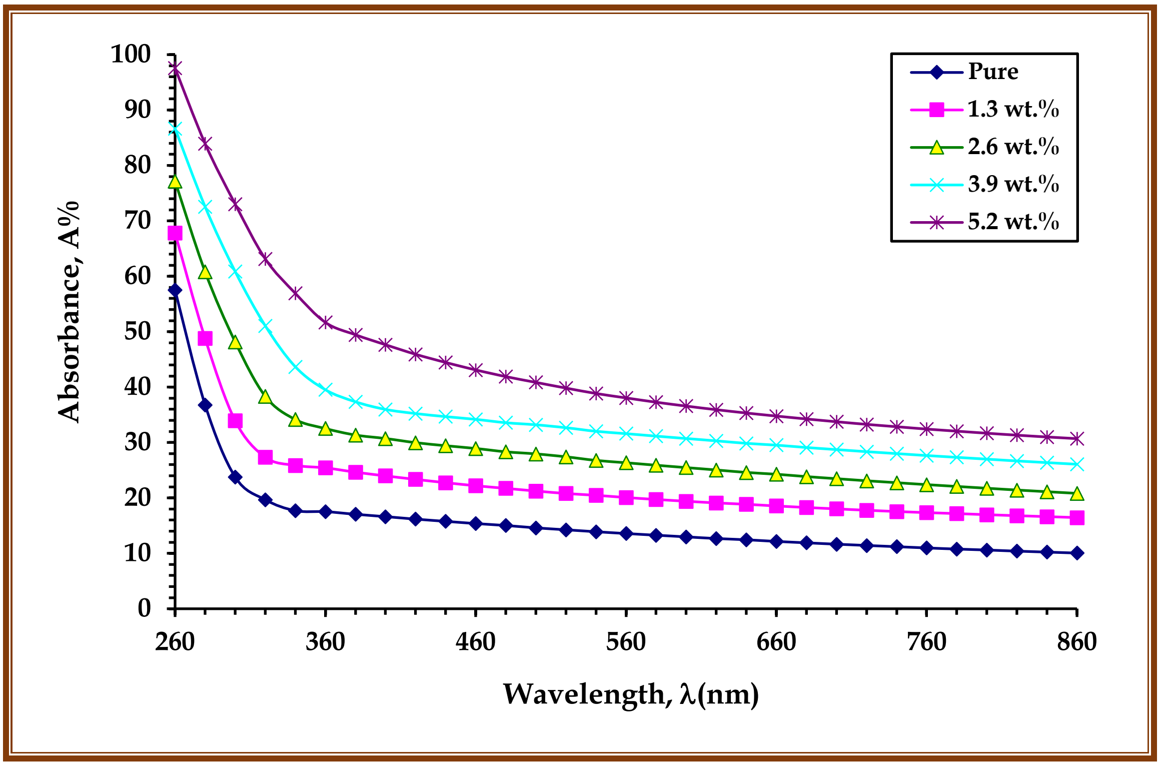

Figure 4.11: The variation absorbance spectrum with wavelength for PC/PS blend anddoped with SiC/MnO_2 nanoparticles at standard room temperature

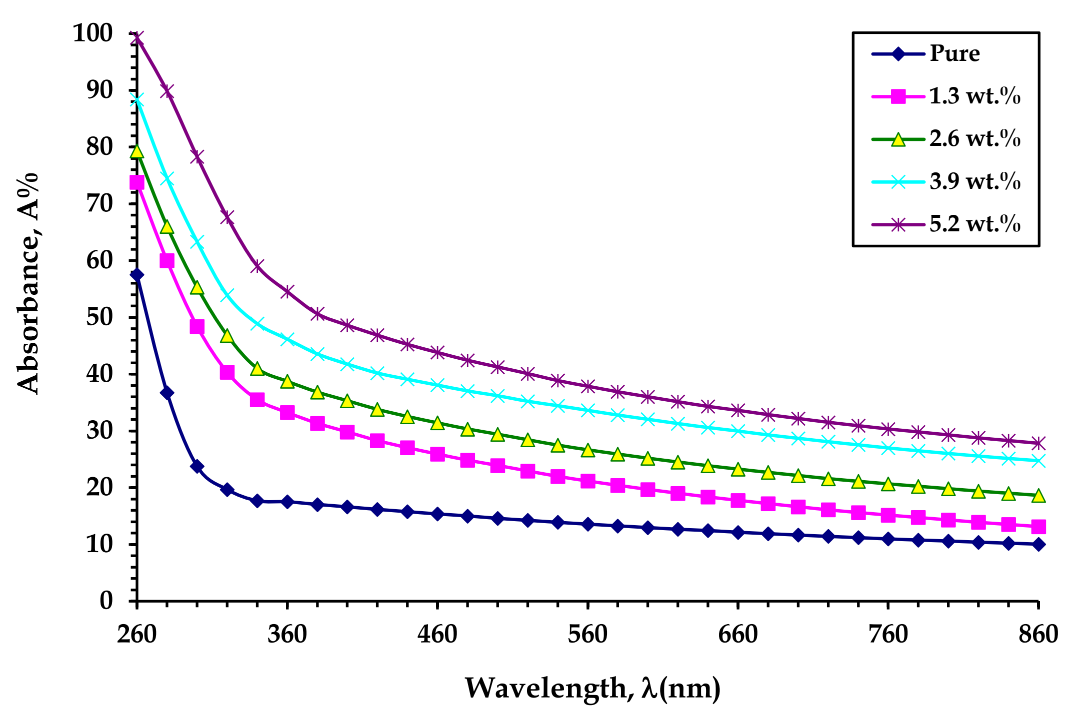

Figure 4.12: The variation absorbance spectrum with wavelength for PC/PS blend anddoped with SiC/ Co_2O_3 nanoparticles at standard room temperature

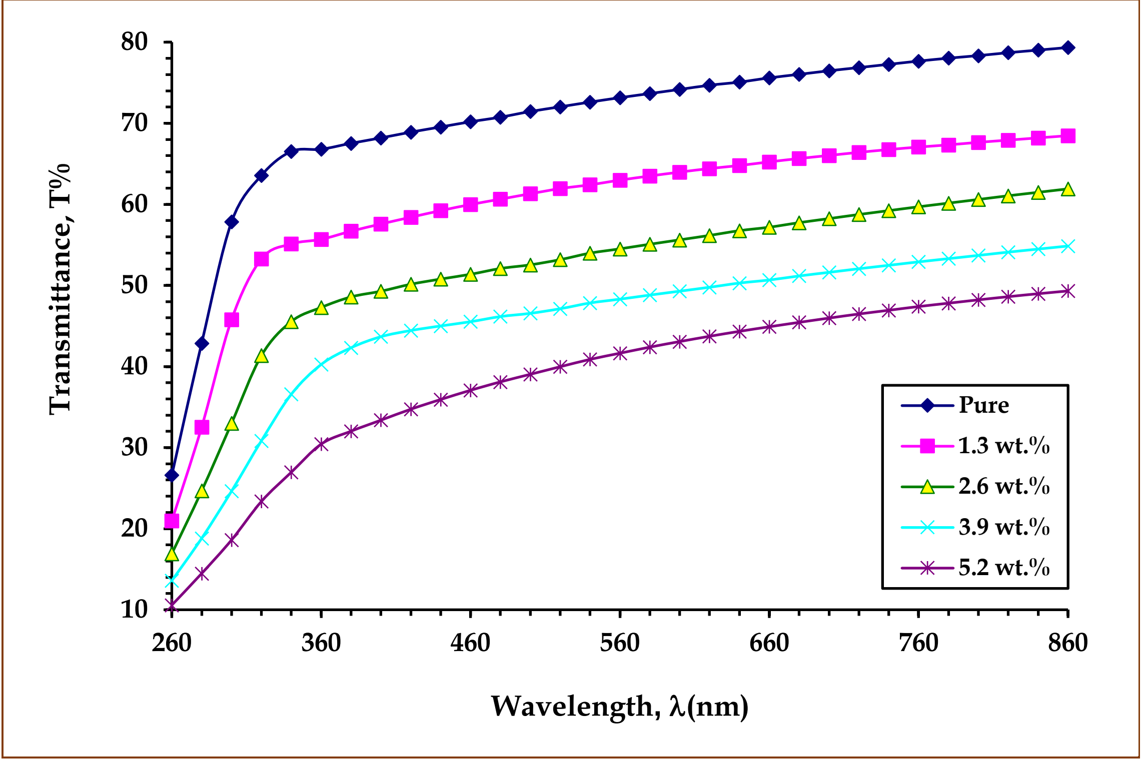

Figure 4.13: The variation transmittance spectrum with wavelength for PC/PS blend anddoped with SiC/MnO_2 nanoparticles at standard room temperature

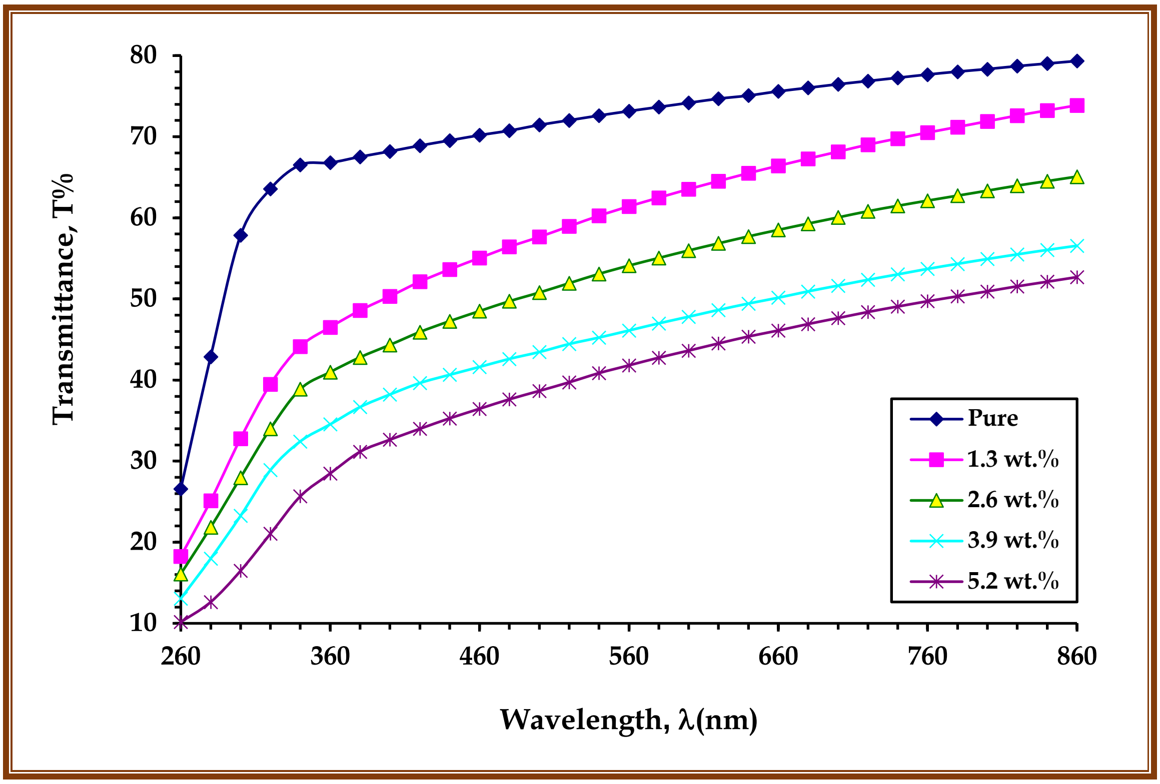

Figure 4.14: The variation transmittance spectrum with wavelength for PC/PS blend anddoped with SiC/Co$_2$O$_3$ nanoparticles at standard room temperature

Table 4.3: The absorbance and transmittance of (PC/PS) blend and (PC-PS/SiC-MnO$_2$) nanocomposites at λ = 560 nm

Samples	Contents of SiC/MnO$_2$ nanoparticles	Absorbance (%)	Transmittance (%)
(PC/PS) blend	**Pure**	13.58	73.16
(PC-PS/SiC-MnO$_2$) nanocomposite	**1.3 wt.%**	20.08	62.99
	2.6 wt.%	26.35	54.51
	3.9 wt.%	31.60	48.31
	5.2 wt.%	38.05	41.64

Table 4.4: The absorbance and transmittance of (PC/PS) blend and (PC-PS/SiC-Co_2O_3) nanocomposites at λ = 560 nm

Samples	Contents of SiC/Co_2O_3 nanoparticles	Absorbance (%)	Transmittance (%)
(PC/PS) blend	**Pure**	13.58	73.16
(PC-PS/SiC-Co_2O_3) nanocomposite	**1.3 wt.%**	**21.18**	**61.41**
	2.6 wt.%	**26.68**	**54.11**
	3.9 wt.%	**33.63**	**46.11**
	5.2 wt.%	**37.88**	**41.81**

4.3.2 The absorption coefficient and skin depth for of (PC-PS/SiC-MnO_2) (PC-PS/SiC-Co_2O_3) nanocomposites.

The absorption coefficient (α) and skin depth (δ) of nanocomposites were measured by using equations (2.14) and (2.15). Figure 4.15 and Figure 4.16 display the variation of the absorption coefficient of (PC-PS/SiC-MnO_2) and (PC-PS/SiC-Co_2O_3) nanocomposites as a function of the photon energy of the incident light respectively. The Figures illustrate that the absorption coefficient of prepared nanocomposites increases with the increasing of the contents of nanoparticles, while the skin depth decreased and this is attributed to the increase of the number of charge carriers in nanocomposites [181]. Figure 4.17 and Figure 4.18 depicts the skin depth with wavelength for (PC-PS/SiC-MnO_2), and (PC-PS/SiC-Co_2O_3) nanocomposites films. The skin depth of (PC-PS/ SiC-MnO_2), and (PC-PS/SiC-Co_2O_3) nanocomposites films were decreases as the photon energy increases, as a result of the increased absorption probability. The absorption coefficient of (PC/PS) polymeric blend increased about 64.32% and 64.15%, respectively when the content of SiC/MnO_2 nanoparticles, and SiC/Co_2O_3 nanoparticles reached to 5.2 wt.% at λ=560 nm, this makes the nanocomposites useful for optoelectronics, photocatalysis, solar cells and many optical applications.

The absorption coefficient of all prepared nanocomposites increases with increasing energy of the incident photon. This means that the electron transition has high probability; i.e. the energy of the incident photon is sufficient to interact with atoms. The absorption coefficient helps to know the electron transition nature [182]. When the values of the absorption coefficient of the material are low in the lower energy $(\alpha < 10^4)\ cm^{-1}$, it's expected that the transition of electrons is indirect transition. While, when the values of the absorption coefficient of the material are high in the higher energy $(\alpha > 10^4)$ cm^{-1}, it's expected that the transition of electrons is direct transition. From the results, it's found that the absorption coefficient of (PC-PS/SiC-MnO_2) and (PC-PS/SiC-Co_2O_3) nanocomposites have values that are less than (10^4) cm^{-1} which means the transition of electrons is indirect [183]. The values of absorption coefficient and skin depth for the prepared nanocomposites at $\lambda = 560\ nm$ are shown in Table 4.5 and Table 4.6, respectively.

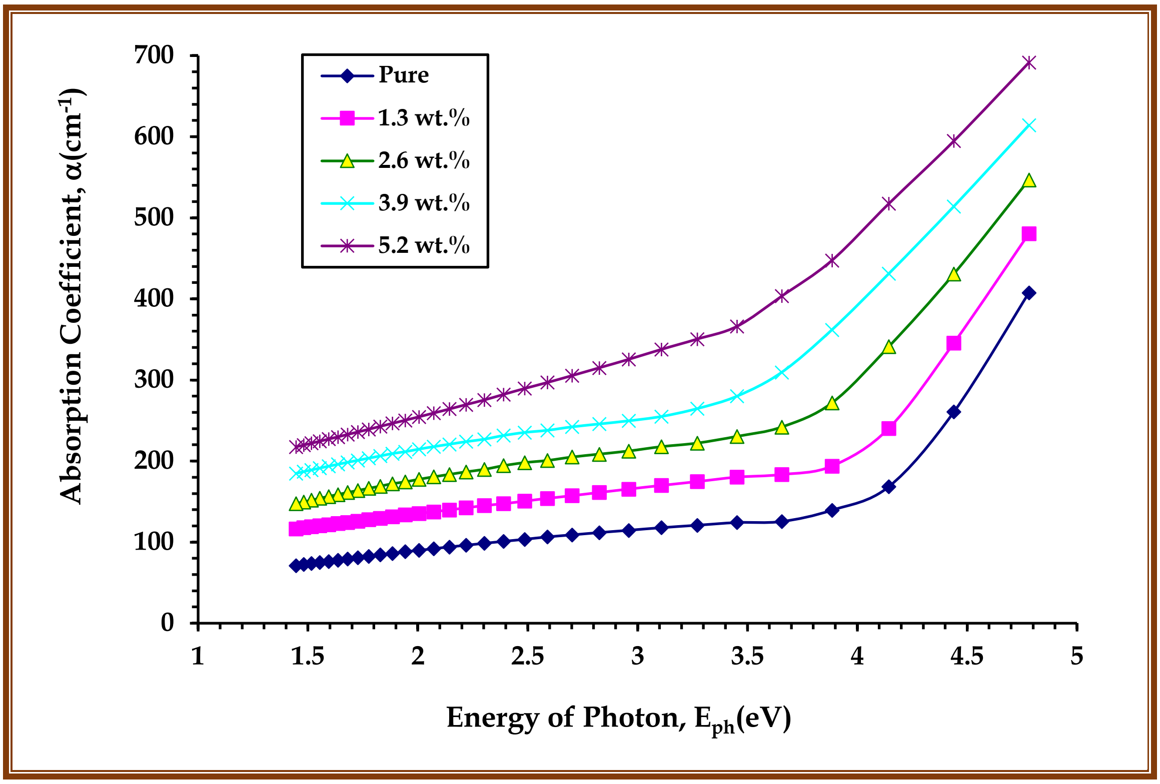

Figure 4.15: Variation of absorption coefficient for (PC-PS/SiC-MnO_2) nanocomposites with photon energy at standard room temperature

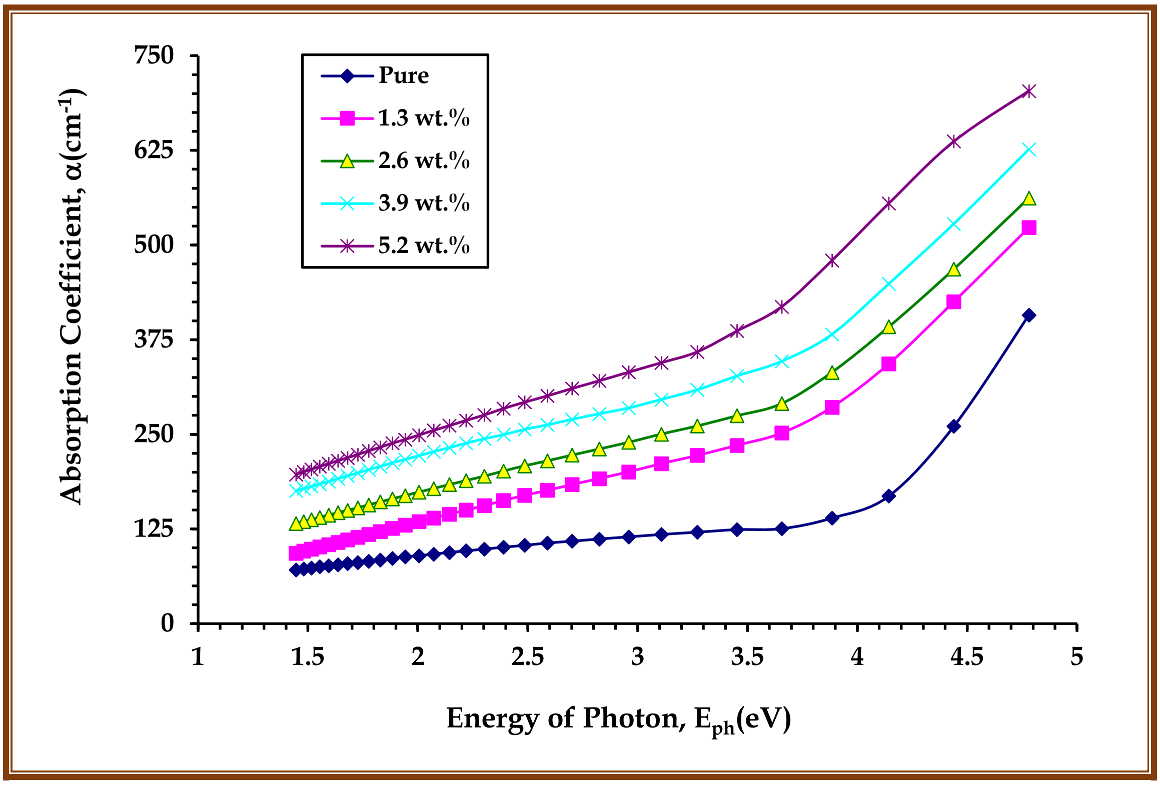

Figure 4.16: Variation of absorption coefficient for (PC-PS/SiC-Co_2O_3) nanocomposites with photon energy at standard room temperature

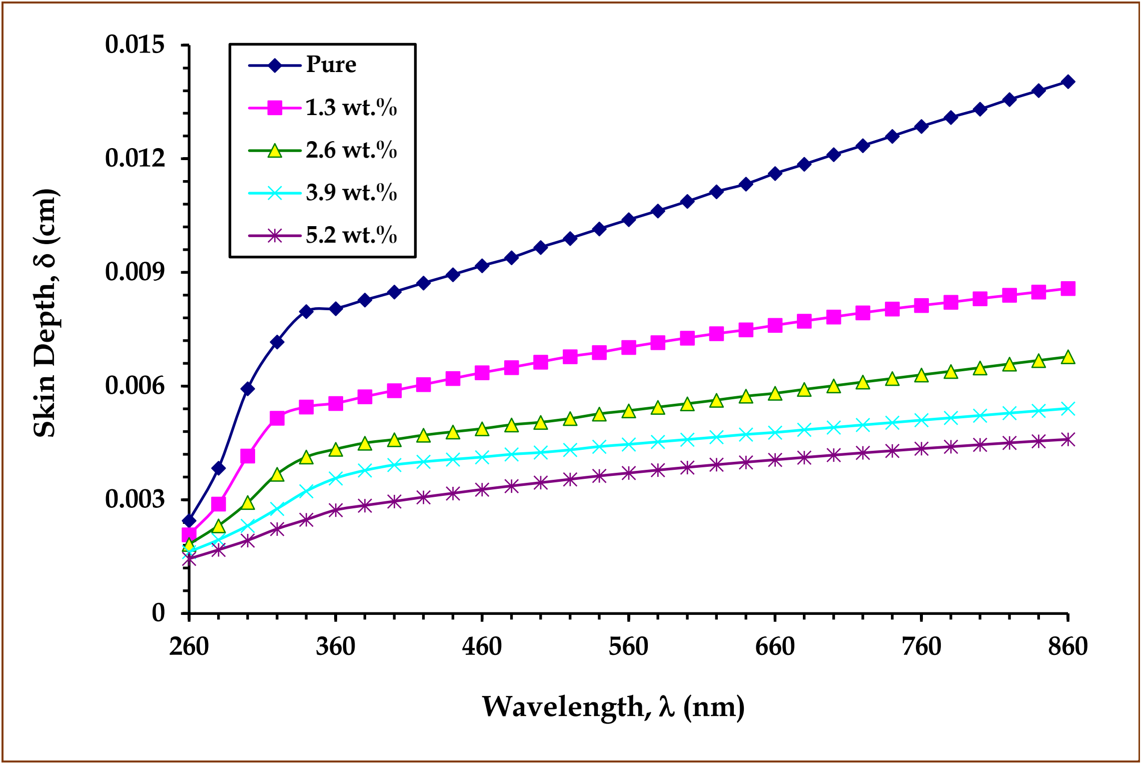

Figure 4.17: Variation of skin depth for (PC-PS/SiC-MnO_2) nanocomposites with wavelength at standard room temperature

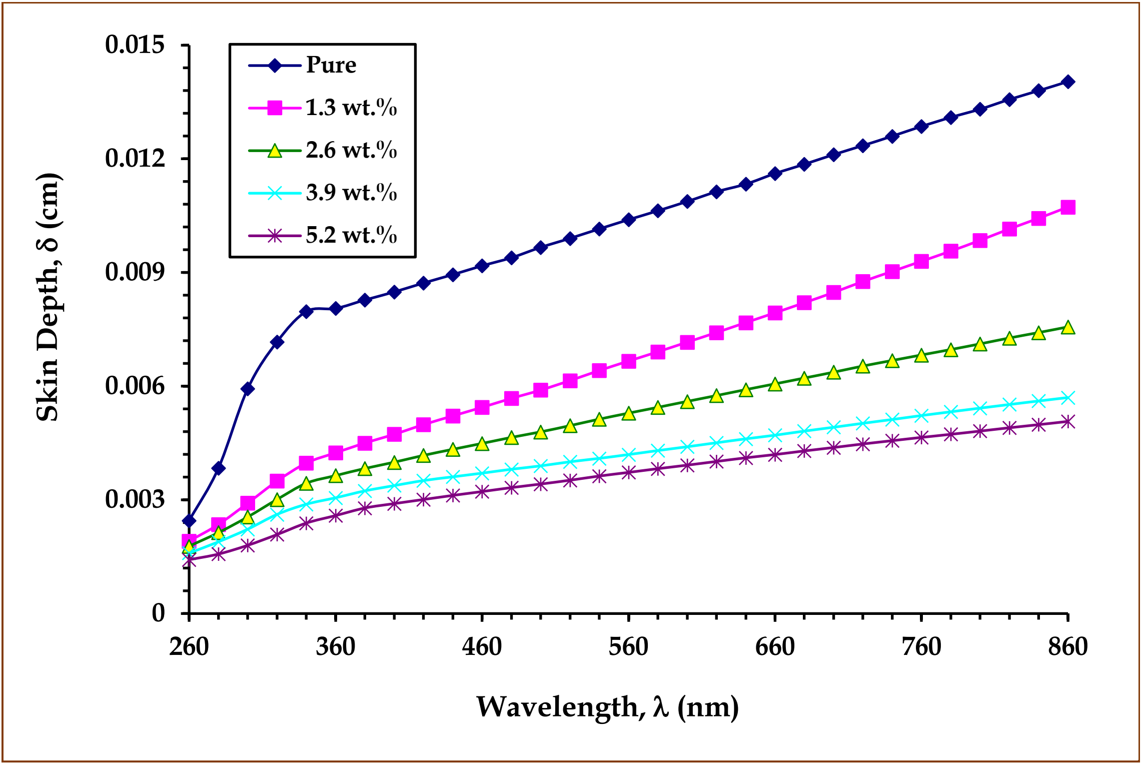

Figure 4.18: Variation of skin depth for (PC-PS/SiC-Co_2O_3) nanocomposites with wavelength at standard room temperature

Table 4.5: The absorption coefficient and the skin depth of (PC-PS/SiC-MnO_2) nanocomposites at λ = 560 nm

Samples	Contents of SiC/MnO_2 nanoparticles	Absorbance coefficient (cm^{-1})	Skin depth (cm)
(PC/PS) blend	**Pure**	96.20	0.0104
(PC-PS/SiC-MnO_2) nanocomposite	**1.3 wt.%**	142.26	0.0070
	2.6 wt.%	186.73	0.0054
	3.9 wt.%	223.93	0.0045
	5.2 wt.%	269.64	0.0037

Table 4.6: The absorption coefficient and the skin depth of (PC-PS/SiC-Co_2O_3) nanocomposites at λ = 560 nm

Samples	Contents of SiC/Co_2O_3 nanoparticles	Absorbance coefficient (cm^{-1})	Skin depth (cm)
(PC/PS) blend	**Pure**	96.20	0.0104
(PC-PS/SiC-Co_2O_3) nanocomposite	**1.3 wt.%**	150.06	0.0067
	2.6 wt.%	189.03	0.0053
	3.9 wt.%	238.28	0.0042
	5.2 wt.%	268.40	0.0036

4.3.3 The energy gaps and Urbach tails energy of (PC-PS/SiC-MnO_2) and (PC-PS/SiC-Co_2O_3) nanocomposites.

The values of the optical energy gap ($E_g^{Opt.}$) of nanocomposites are measured by using the equation (2.6). For all prepared nanocomposites, $E_g^{Opt.}$ is determined by drawing between $(\alpha h\nu)^{1/2}$ as a function of (E_{ph}), by stretching straight curve line and an intersection with x-axis which gives the energy gap value for all prepared nanocomposites. The energy gaps for allowed indirect transitions of (PC-PS/SiC-MnO_2) and (PC-PS/SiC-Co_2O_3) nanocomposites are shown in Figure 4.19 and Figure 4.20 respectively. The energy gaps for forbidden indirect transitions of (PC-PS/SiC-MnO_2), and (PC-PS/SiC-Co_2O_3) nanocomposites are shown in Figure 4.21 and Figure 4.22, respectively. The values have been getting in Table 4.7 and Table 4.8, its showed that the values of (allowed and forbidden) indirect energy gap, and Urbach energy of all prepared nanocomposites decrease with increasing the contents of the SiC/MnO_2 nanoparticles, and SiC/Co_2O_3 nanoparticles. Conventionally, there is an inverse relationship between Urbach energy and optical band gap, therefore a sample with a narrower band gap is anticipated to have a wider band tail [184].

When the content of SiC/MnO_2 nanoparticles, and SiC/Co_2O_3 nanoparticles reached to 5.2 wt.% at λ=560 nm, the energy gap of (PC/PS) blend decreased about 60.39% and 61.09% for allowed indirect transitions respectively, about 96.16% and 95.22% for forbidden indirect transitions respectively, While the values of Urbach energy calculated by slope of equation (2.4) increased by about 73.78% and 78.66%, respectively and as illustrated in Figure 4.23 and Figure 4.24, this behavior make the nanocomposites suitable for lightweight and low-cost electronics and optical devices. The gradual reduction in the values of the energy gap, while Urbach energy increased with increasing, as shows in Figure 4.23 and Figure 4.24, which attributed to the formation of localized levels in the energy gap [185].

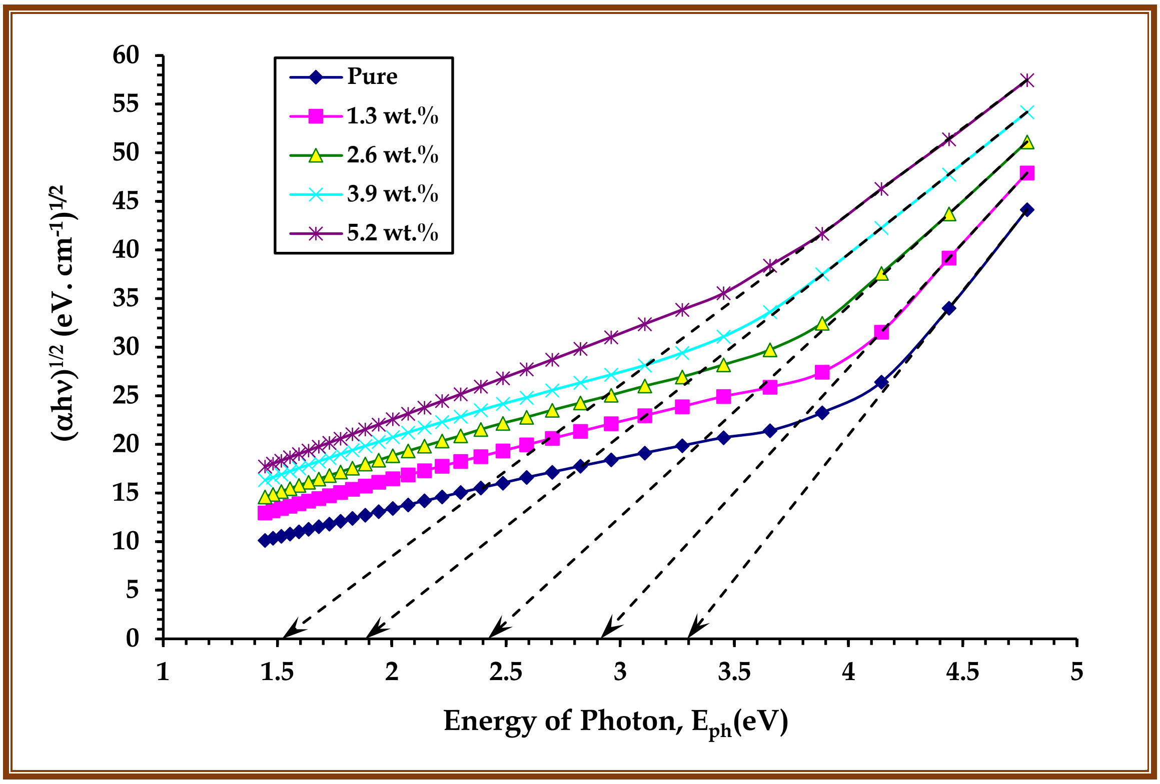

Figure 4.19: Variation of (αhυ)$^{1/2}$ for (PC-PS/SiC-MnO$_2$) nanocomposites with photon energy at standard room temperature

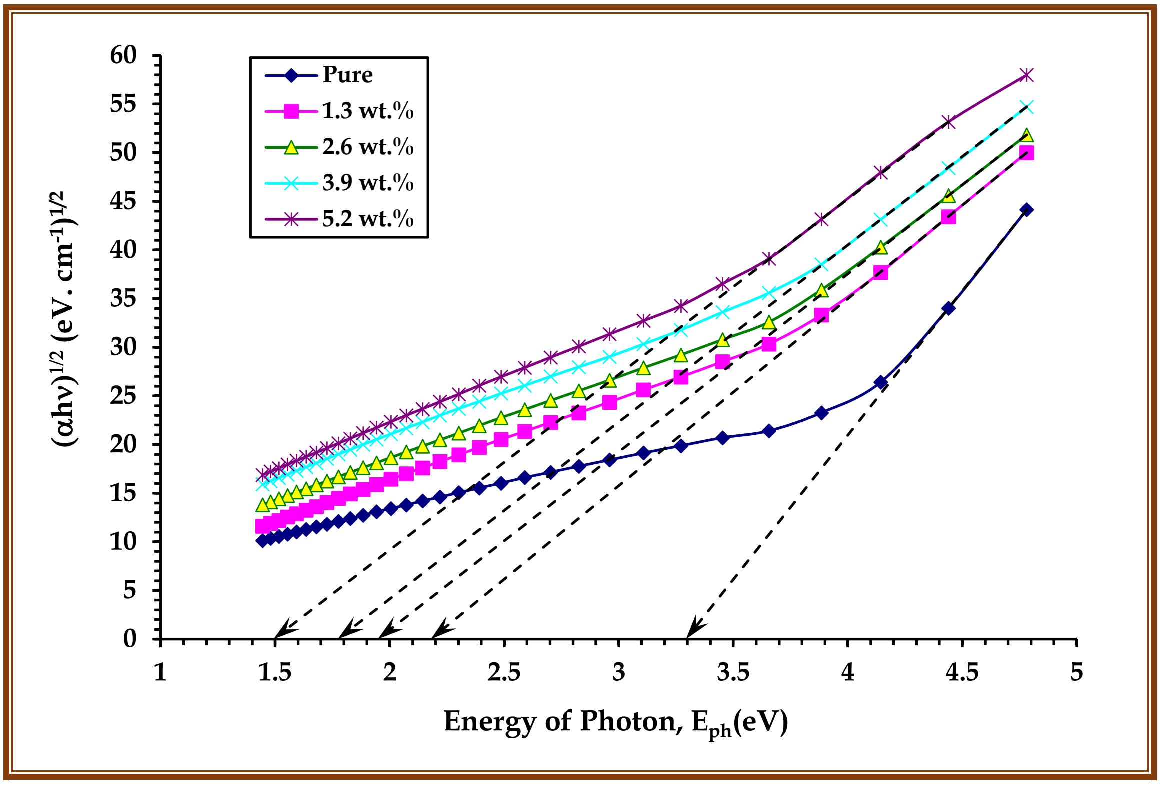

Figure 4.20: Variation of (αhυ)$^{1/2}$ for (PC-PS/SiC-Co$_2$O$_3$) nanocomposites with photon energy at standard room temperature

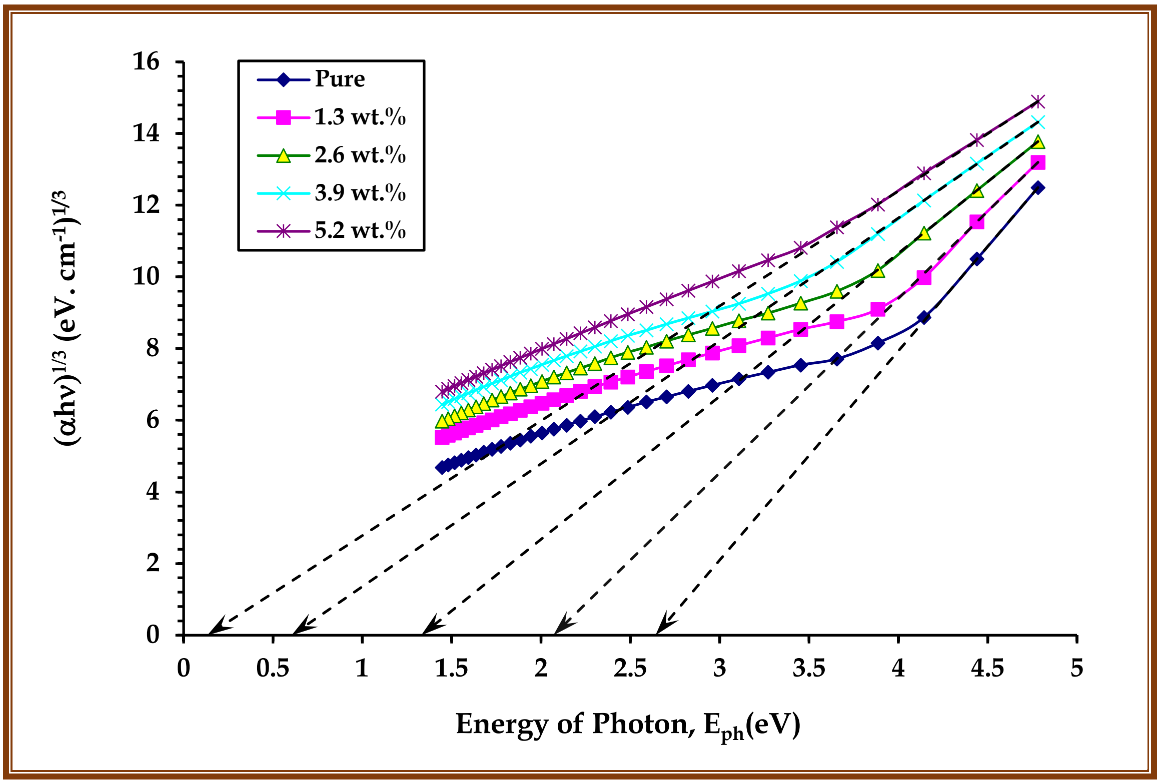

Figure 4.21: Variation of $(\alpha h\upsilon)^{1/3}$ for (PC-PS/SiC-MnO_2) nanocomposites with energy of photon at standard room temperature

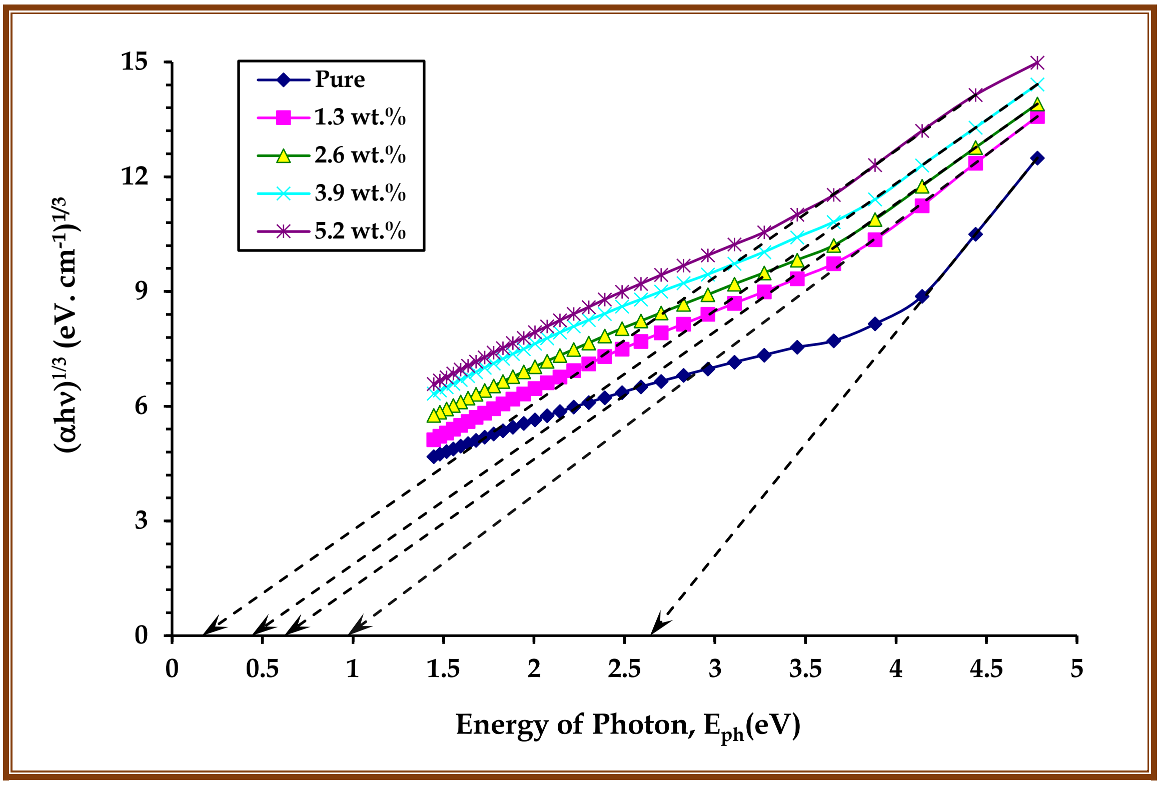

Figure 4.22: Variation of $(\alpha h\upsilon)^{1/3}$ for (PC-PS/SiC-Co_2O_3) nanocomposites with energy of photon at standard room temperature

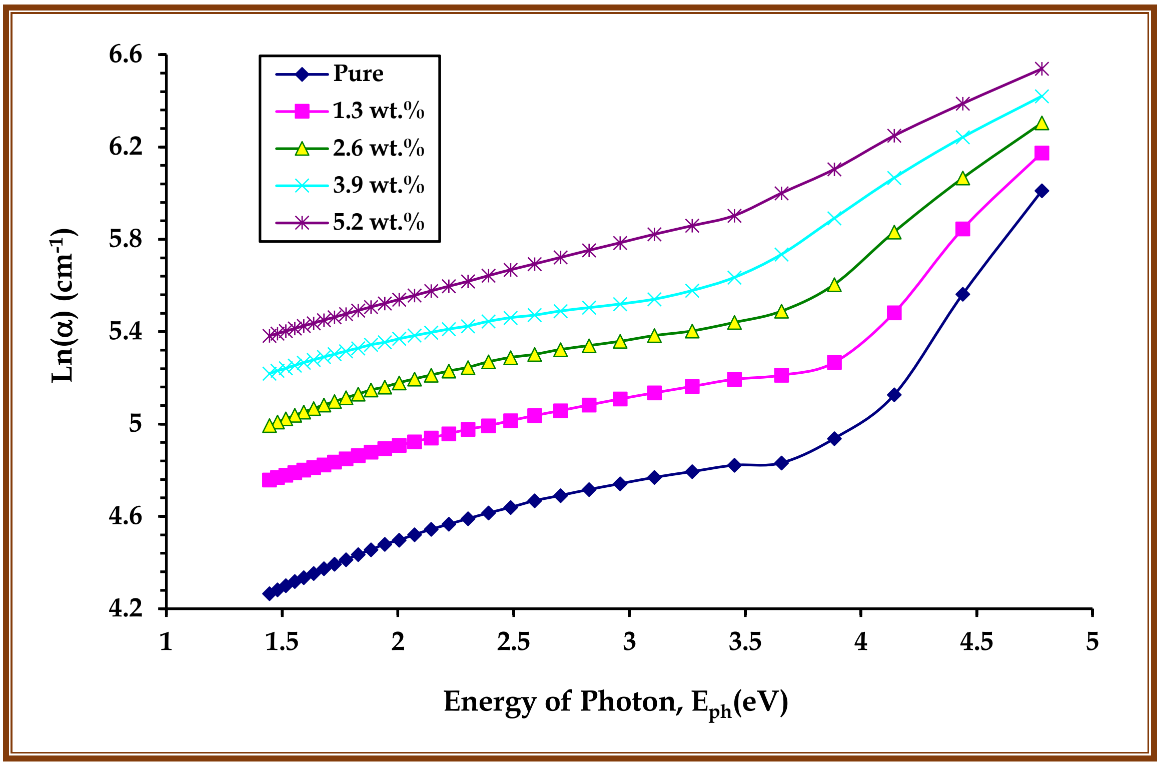

Figure 4.23: Plot of Ln(α) for (PC-PS/SiC-MnO_2) nanocomposites with photon energy at standard room temperature

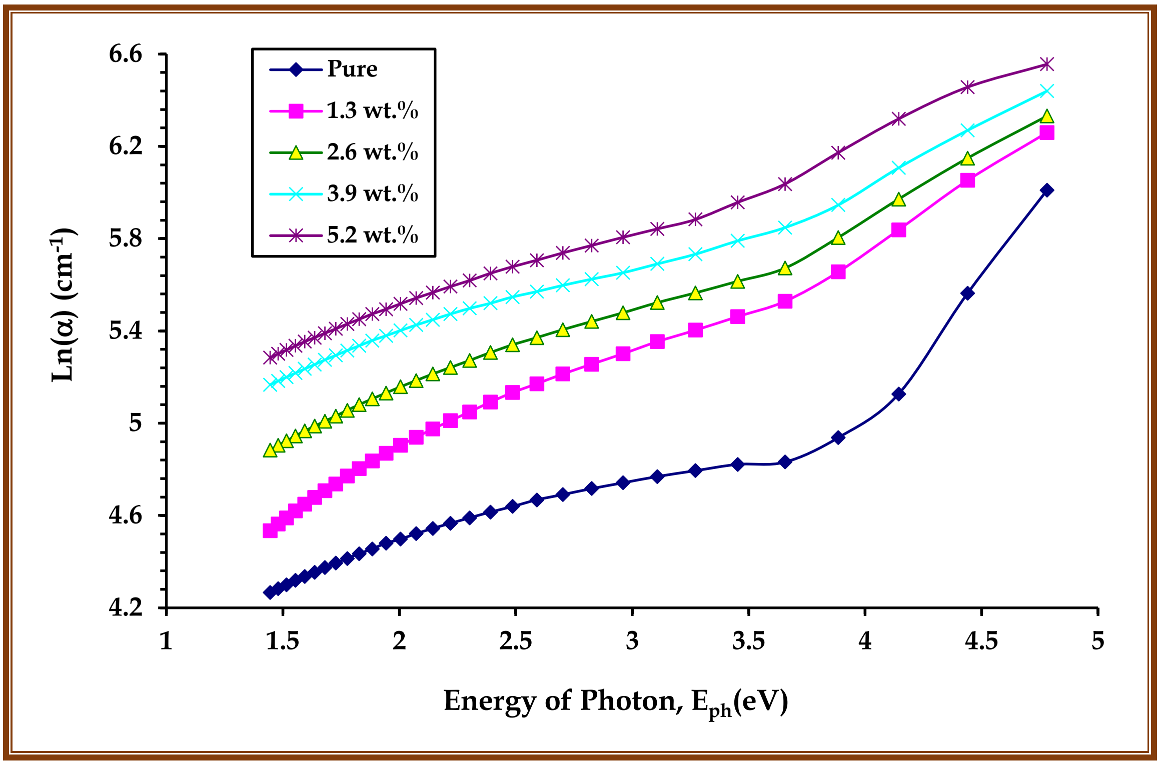

Figure 4.24: Plot of Ln(α) for (PC-PS/SiC-Co_2O_3) nanocomposites with photon energy at standard room temperature

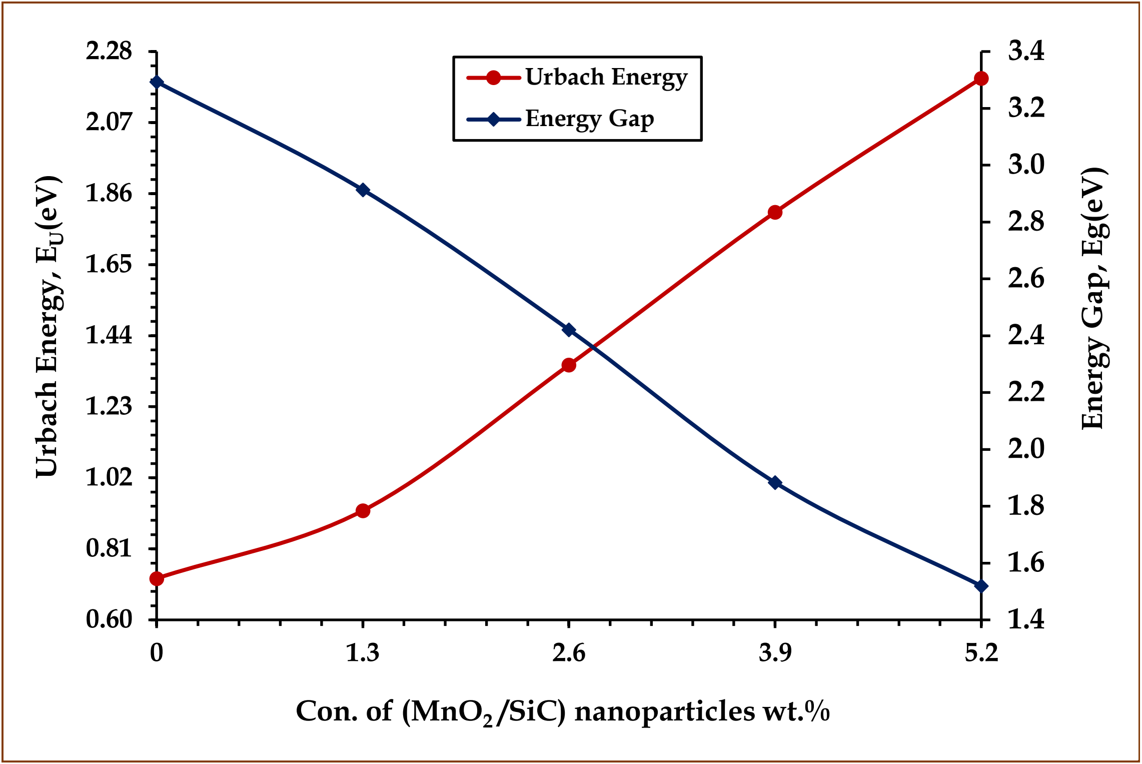

Figure 4.25: Comparison between the Urbach energy values and the energy gap values of (PC-PS/SiC-MnO₂) nanocomposites for all contents

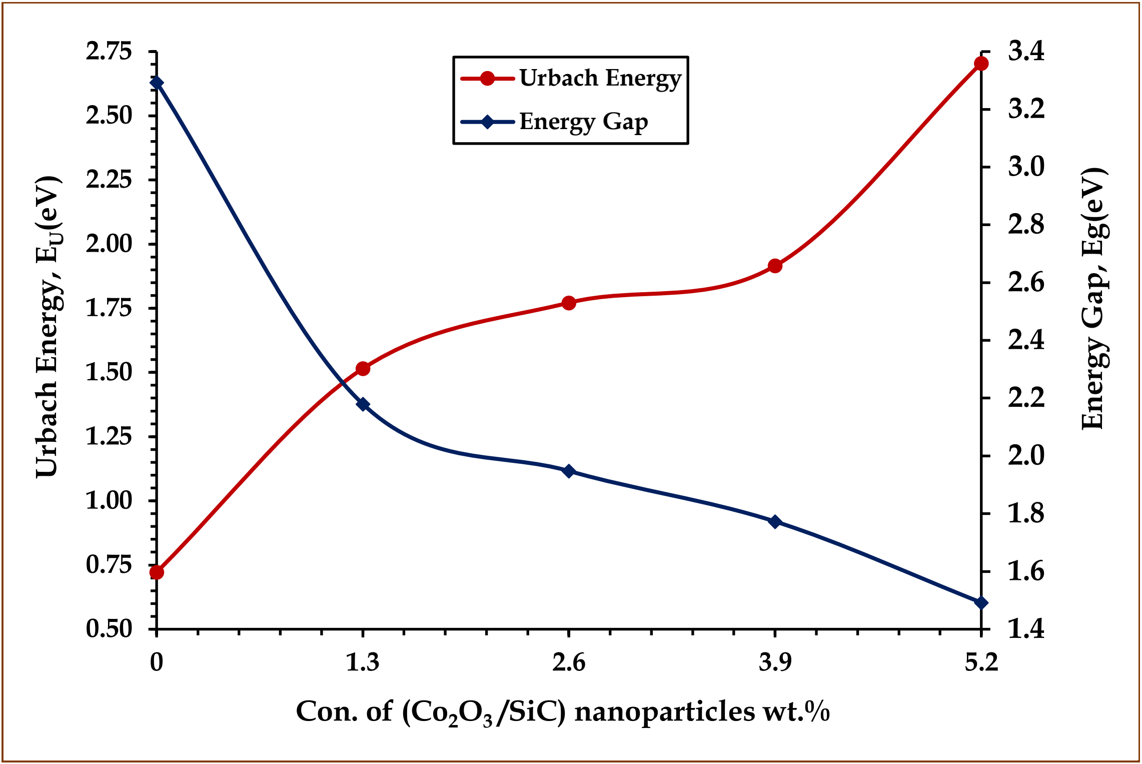

Figure 4.26: Comparison between the Urbach energy values and the energy gap values of (PC-PS/SiC-Co_2O_3) nanocomposites for all contents

Table 4.7: The band gap and Urbach energy of (PC/PS) blend and (PC-PS/SiC-MnO_2) nanocomposites at $\lambda = 560$ nm

Samples	Contents of SiC/MnO_2 nanoparticles	Indirect optical band gaps, E_g (eV)		Urbach energy, E_U (eV)
		Allowed	Forbidden	
(PC/PS) blend	Pure	3.2933	2.6410	0.7225
(PC-PS/SiC-MnO_2) nanocomposite	1.3 wt.%	2.9133	2.0695	0.9228
	2.6 wt.%	2.4210	1.3299	1.3533
	3.9 wt.%	1.8832	0.6045	1.8049
	5.2 wt.%	1.5195	0.1327	2.2013

Table 4.8: The band gap and Urbach energy of (PC/PS) blend and (PC-PS/SiC-Co_2O_3) nanocomposites at $\lambda = 560$ nm

Samples	Contents of SiC/Co_2O_3 nanoparticles	Indirect optical band gaps, E_g (eV)		Urbach energy, E_U (eV)
		Allowed	Forbidden	
(PC/PS) blend	Pure	3.2933	2.6410	0.7225
(PC-PS/SiC-Co_2O_3) nanocomposite	1.3 wt.%	2.1797	0.9677	1.5150
	2.6 wt.%	1.9478	0.6195	1.7716
	3.9 wt.%	1.7730	0.4387	1.9154

	5.2 wt.%	1.4924	0.1655	2.7045

4.3.4 Refractive index and extinction coefficient of (PC-PS/SiC-MnO_2) and (PC-PS/SiC-Co_2O_3) nanocomposites

The refractive index is measured using the equation (2.20). The refractive index of (PC-PS/SiC-MnO_2) and (PC-PS/SiC-Co_2O_3) nanocomposites as a function of wavelength are shown in Figure 4.27, and Figure 4.28 display that the refractive index of all prepared nanocomposites increases with the increase in the wavelength of the incident light. Furthermore, the refractive index of nanocomposites increases with the increase of the contents for (SiC/MnO_2, and SiC/Co_2O_3) nanoparticles. This behavior attributed to the high absorbance of all samples for nanocomposites, which causes the decrease of the reflection and transmission [186]. NCs reduced their refractive index by 18.73% and 18.75%, respectively, making them advantageous for usage in optical applications [187].

Figure 4.29, and Figure 4.30 display the variance of the extinction coefficient for (PC-PS/SiC-MnO_2) and (PC-PS/SiC-Co_2O_3) nanocomposites as a function of wavelength (λ) respectively. The Figures show that increase of the extinction coefficient of (PC-PS/SiC-MnO_2) and (PC-PS/SiC-Co_2O_3) NCs with the increasing in the wavelength of the incident light in the UV region, this is due to the high absorption of all prepared NCs at these regions. In addition, the extinction coefficient of NCs increases at the visible and near infrared regions, which may be attributed to that the absorption coefficient of NCs thus, the extinction coefficient depends on the wavelength according to equation (2.18) [185], the extinction coefficient of (PC/PS) polymeric blend increases with increasing the content of the (SiC/MnO_2, and SiC/Co_2O_3) NPs, this is related to the increased absorption coefficient of NCs [188]. The ratio of increase in extinction coefficient of (PC-PS/SiC-MnO_2) and (PC-PS/SiC-Co_2O_3) NCs was 64.32% and 64.15% respectively. The values of the refractive index and extinction coefficient of prepared NCs at wavelength (λ) shown in Table 4.9, and Table 4.10.

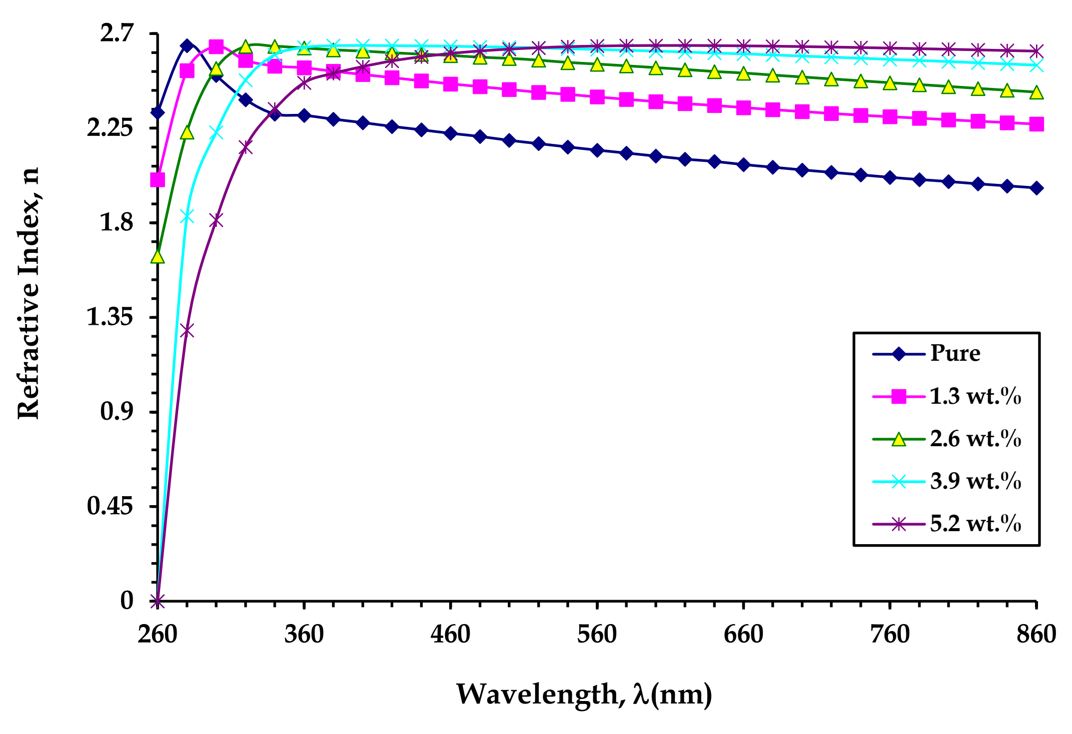

Figure 4.27: Variation of refractive index for (PC-PS/SiC-MnO_2) nanocomposites with wavelength at standard room temperature

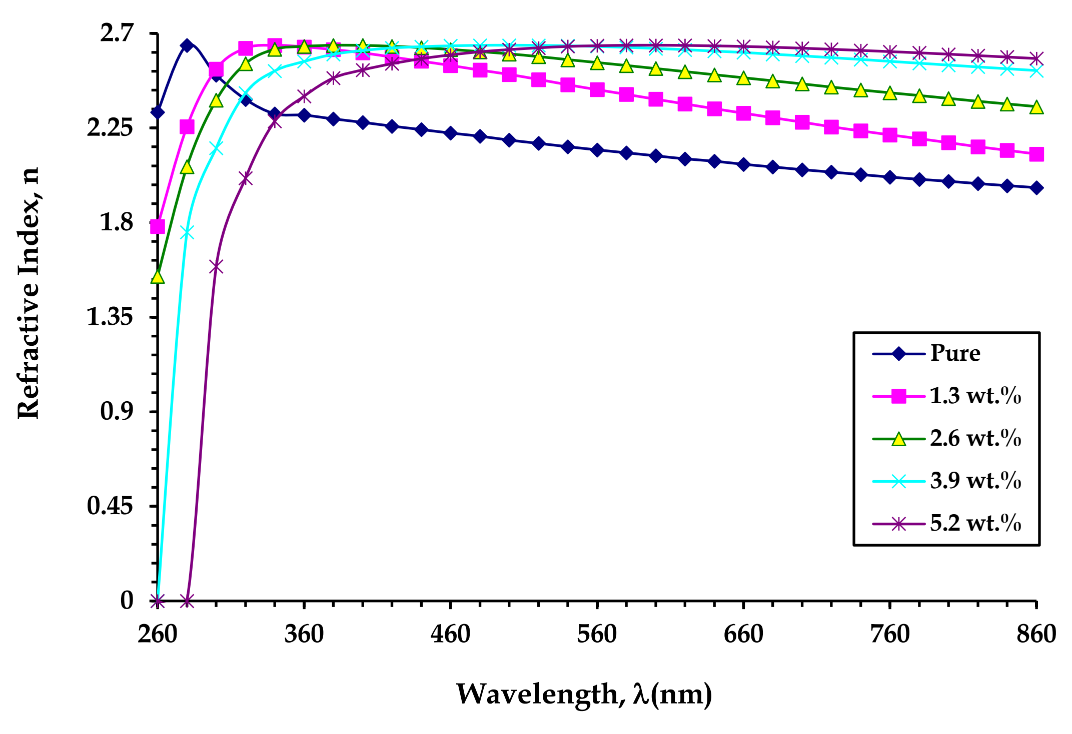

Figure 4.28: Variation of refractive index for (PC-PS/SiC-Co_2O_3) nanocomposites with wavelength at standard room temperature

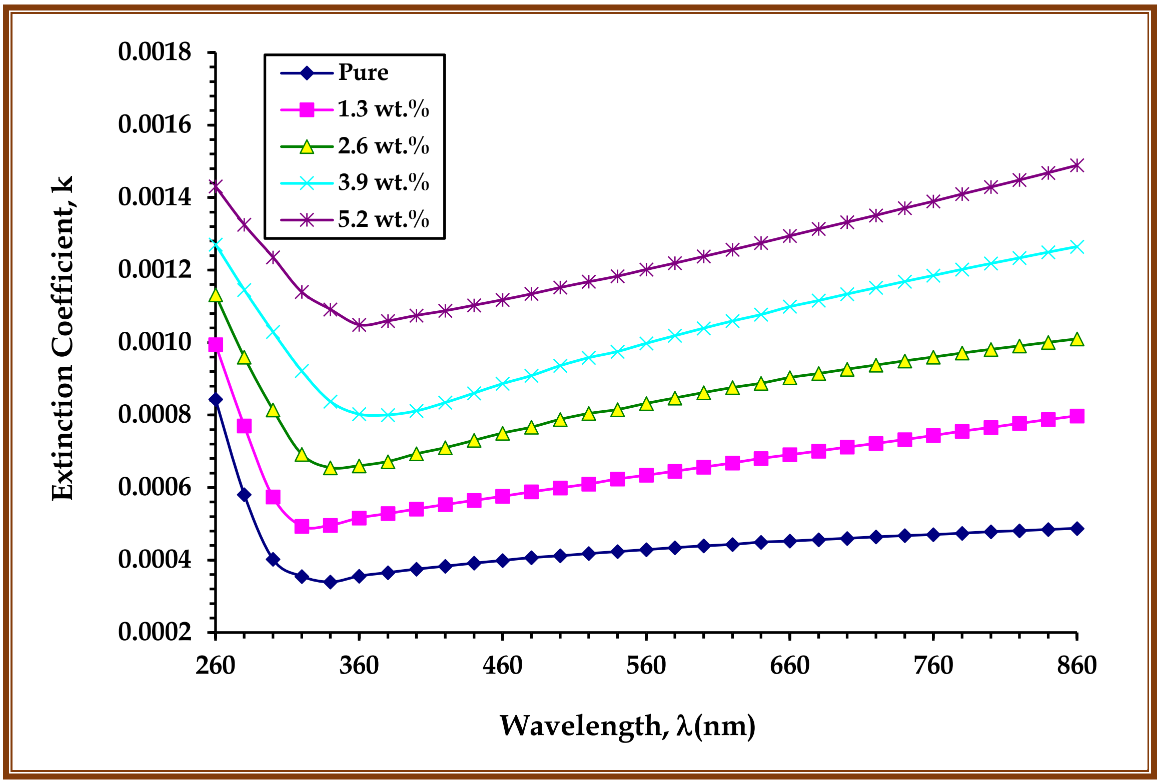

Figure 4.29: Variation of extinction coefficient for (PC-PS/SiC-MnO_2) nanocomposites with wavelength at standard room temperature

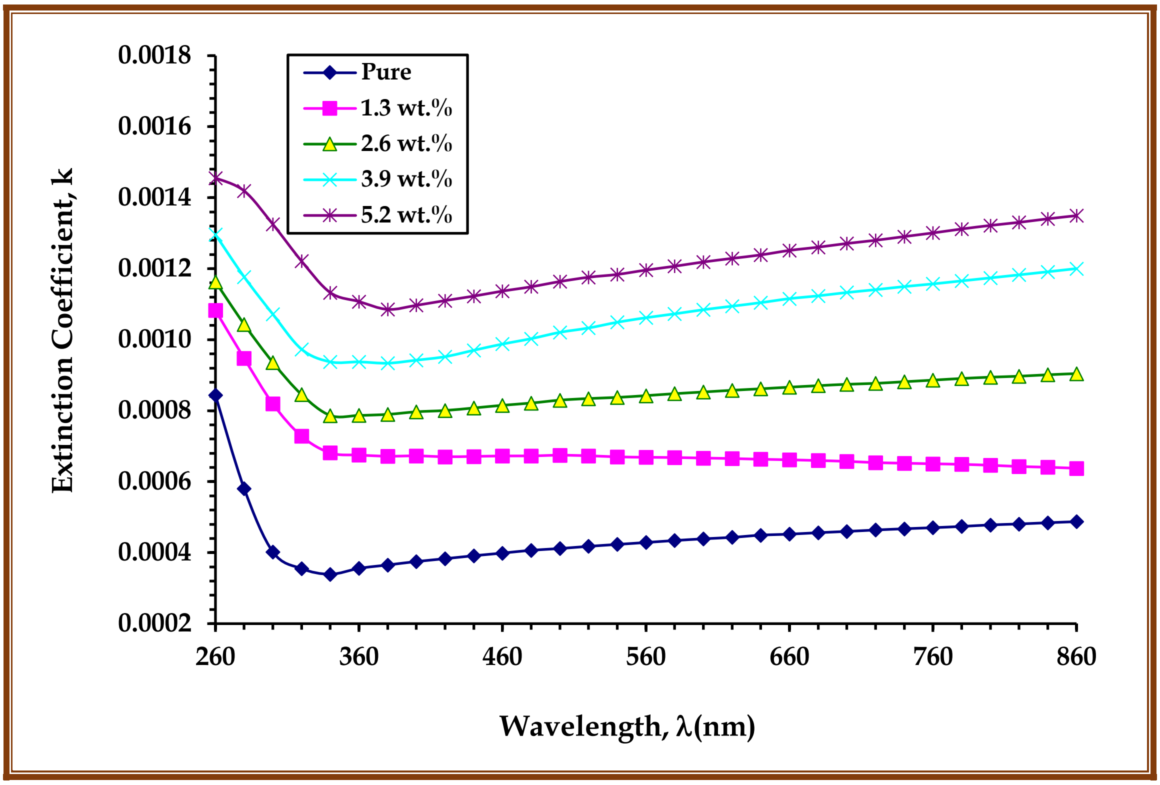

Figure 4.30:Variation of extinction coefficient for (PC-PS/SiC-Co_2O_3) nanocomposites with wavelength at standard room temperature

Table 4.9: The refractive index and extinction coefficient of (PC/PS) polymeric blend and (PC-PS/SiC-MnO_2) nanocomposites at λ = 560 nm

Samples	Contents of SiC/MnO_2 nanoparticles	Refractive index (unit less)	Extinction coefficient (unit less)
(PC/PS) blend	**Pure**	2.1459	4.29×10^{-4}
(PC-PS/SiC-MnO_2) nanocomposite	**1.3 wt.%**	2.3988	6.34×10^{-4}
	2.6 wt.%	2.5552	8.32×10^{-4}
	3.9 wt.%	2.6249	9.98×10^{-4}
	5.2 wt.%	2.6408	12.02×10^{-4}

Table 4.10: The refractive index and extinction coefficient of (PC/PS) polymeric blend and (PC-PS/SiC-Co_2O_3) nanocomposites at λ = 560 nm

Samples	Contents of SiC/Co_2O_3 nanoparticles	Refractive index (unit less)	Extinction coefficient (unit less)
(PC/PS) blend	**Pure**	2.1459	4.29×10^{-4}
(PC-PS/SiC-Co_2O_3) nanocomposite	**1.3 wt.%**	2.4322	6.69×10^{-4}
	2.6 wt.%	2.5611	8.42×10^{-4}
	3.9 wt.%	2.6378	10.62×10^{-4}
	5.2 wt.%	2.6413	11.96×10^{-4}

4.3.5 The real and imaginary parts of dielectric constant for (PC-PS/SiC-MnO_2) and (PC-PS/SiC-Co_2O_3) nanocomposites

The real and imaginary parts of dielectric constant are measured by using equations (2.24) and (2.25), respectively. Figure 4.31, and Figure 4.32 display the variation of the real part of dielectric constant (ε_r) with the wavelength for (PC-PS/SiC-MnO_2) and (PC-PS/SiC-Co_2O_3) nanocomposites respectively. The Impact of (SiC/MnO_2, and SiC/Co_2O_3) nanoparticles on the imaginary part of dielectric constant (ε_i) is shown in Figure 4.33, and Figure 4.34 for (PC/PS) polymeric blend, respectively. The behavior of the real part of the dielectric constant is similar to that of the refractive index (n) because the value of the extinction coefficient (k^2) is very small compared with refractive index (n^2), while the imaginary part of the dielectric constant is essentially proportional with extinction coefficient (k) values [189]. As shown in the Figures, the real part of the dielectric constant of (PC/PS) polymeric blend is increased with increasing the contents of (SiC/MnO_2, and SiC/Co_2O_3) nanoparticles, this attributed to decrease the scattering of the incident photon. The ratio of increased in real part of dielectric constant of nanocomposites was 33.96% and 33.99% respectively. While, the imaginary part of the dielectric constant of nanocomposites is increased with the increasing of (SiC/MnO_2, and SiC/Co_2O_3) nanoparticles contents, this is due to increase the absorption coefficient of nanocomposites. The imaginary part of the dielectric constant of nanocomposites increased about 71.01% and 70.88% respectively, when the content of (SiC/MnO_2, and SiC/Co_2O_3) nanoparticles reached to 5.2 wt.% at $\lambda = 560\ nm$. The values of optical constants of prepared nanocomposites at wavelength (λ) shown in Table 4.11, and Table 4.12.

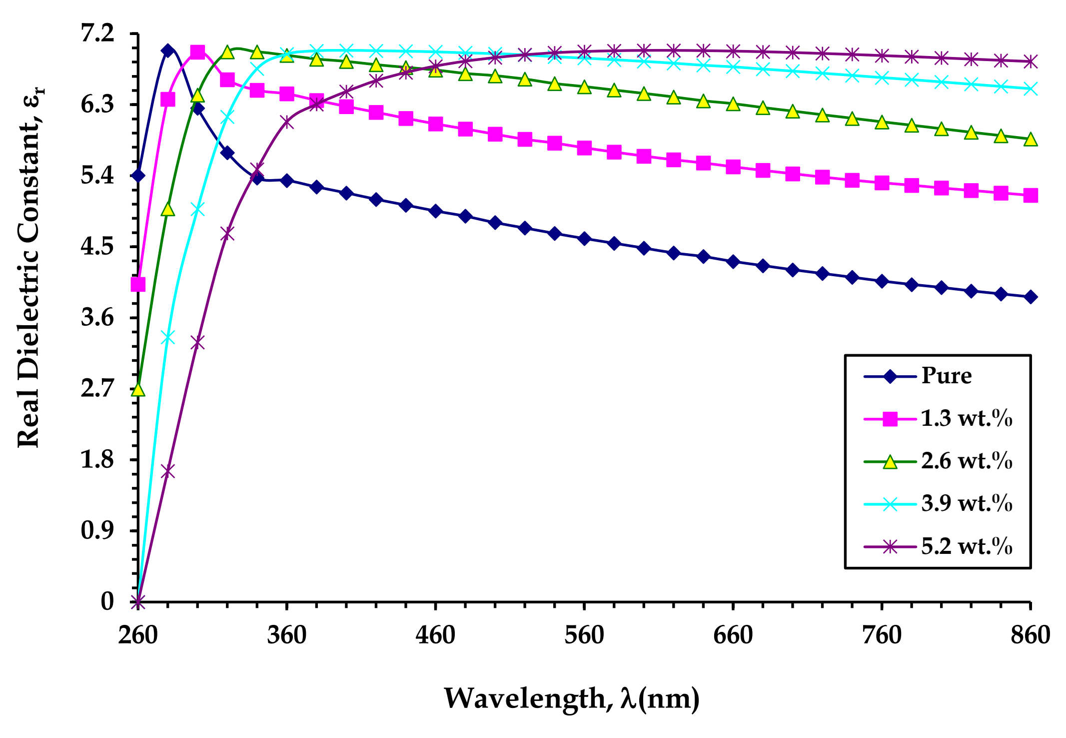

Figure 4.31: Variation of real part of dielectric constant for (PC-PS/SiC-MnO_2) nanocomposites with wavelength at standard room temperature

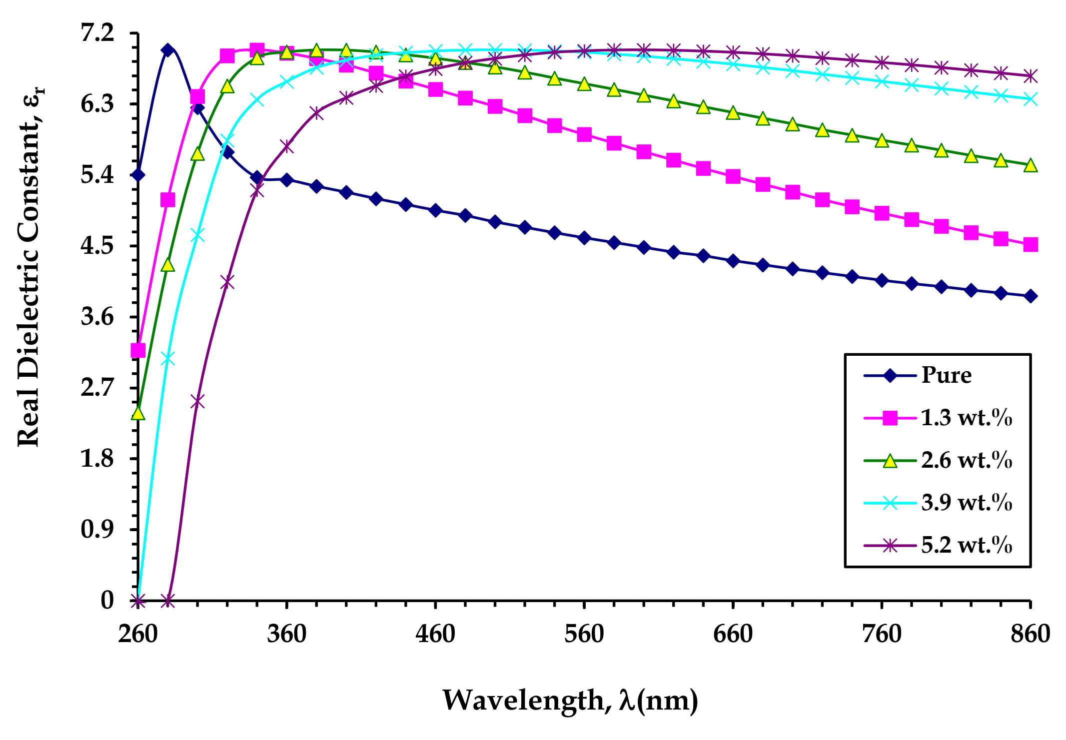

Figure 4.32: Variation of real part of dielectric constant for (PC-PS/SiC-Co_2O_3) nanocomposites with wavelength at standard room temperature

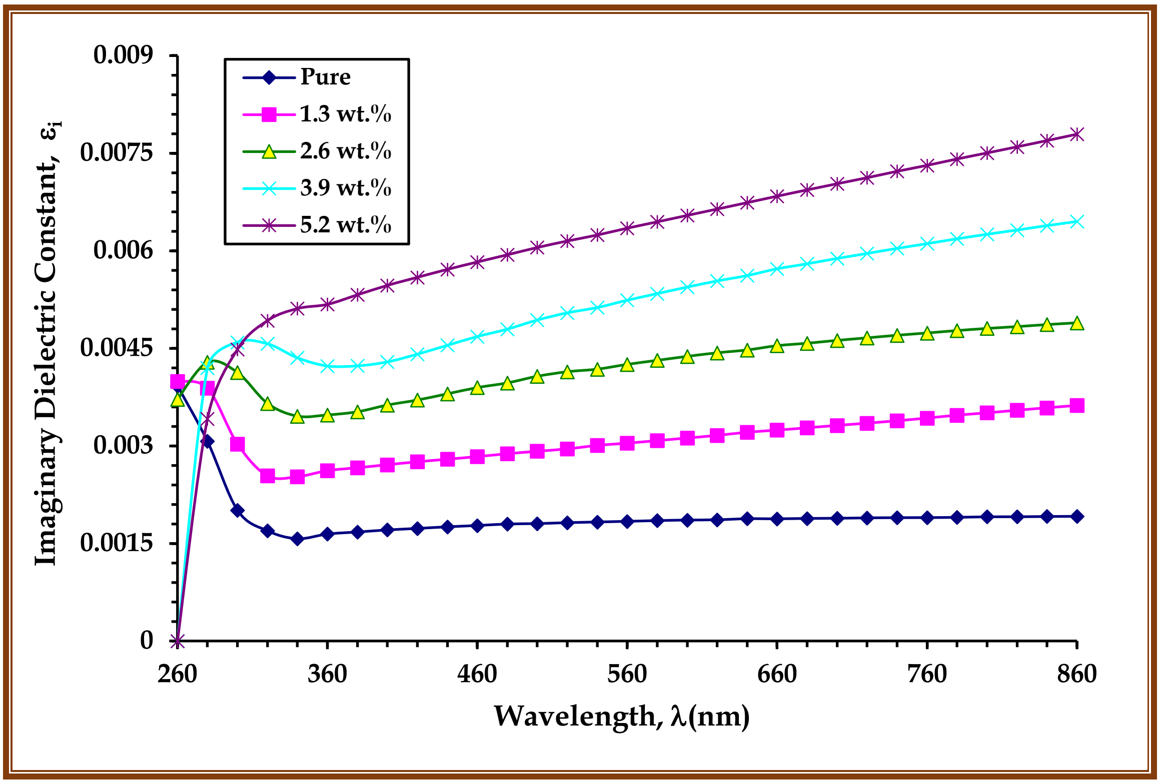

Figure 4.33: Variation of imaginary part for dielectric constant of (PC-PS/SiC-MnO_2) nanocomposites with wavelength at standard room temperature

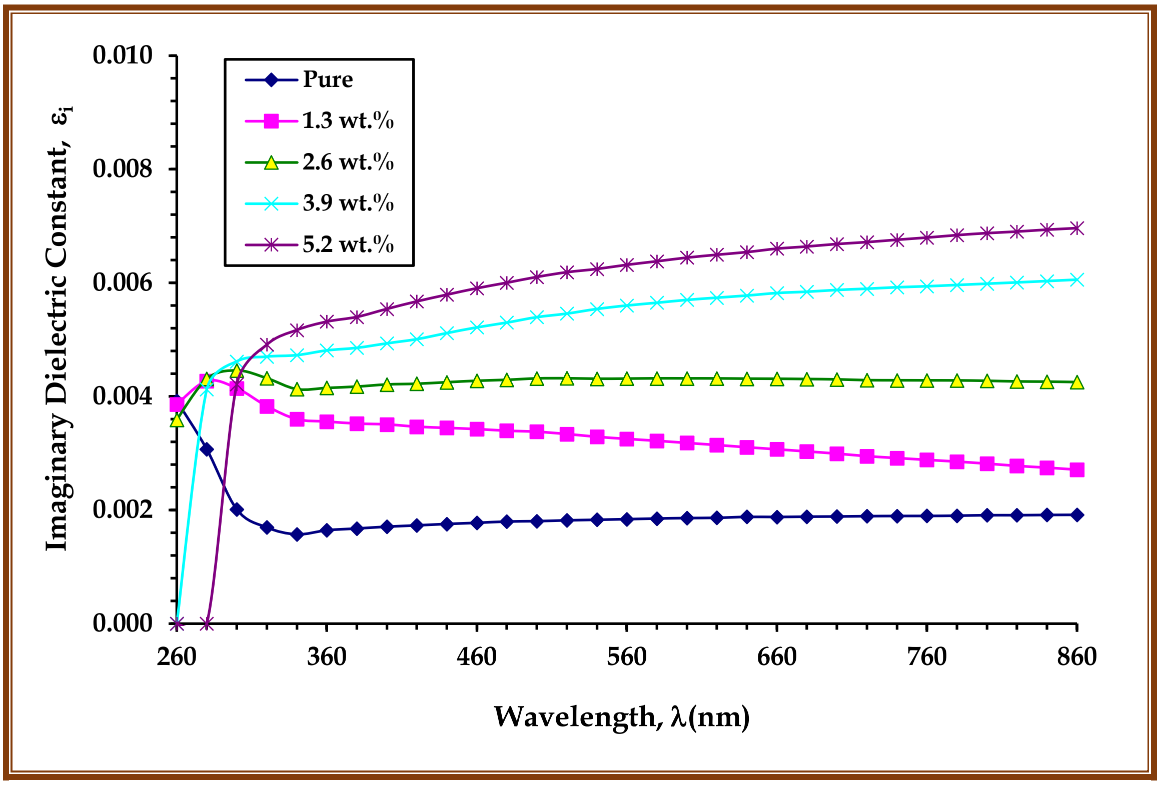

Figure 4.34: Variation of imaginary part for dielectric constant of (PC-PS/SiC-Co_2O_3) nanocomposites with wavelength at standard room temperature

Table 4.11: The real and imaginary part dielectric constant of (PC/PS) polymeric blend and (PC-PS/SiC-MnO_2) Nanocomposites at λ = 560 nm

Samples	Contents of MnO_2 nanoparticles	Real dielectric constant (unit less)	Imaginary dielectric constant (unit less)
(PC/PS) blend	Pure	4.60	18.39×10^{-4}
(PC-PS/SiC-MnO_2) nanocomposite	1.3 wt.%	5.75	30.42×10^{-4}
	2.6 wt.%	6.53	42.53×10^{-4}
	3.9 wt.%	6.89	52.39×10^{-4}
	5.2 wt.%	6.97	63.46×10^{-4}

Table 4.12: The real and imaginary part dielectric constant of (PC/PS) polymeric blend and (PC-PS/SiC-Co_2O_3) Nanocomposites at λ = 560 nm

Samples	Contents of Co_2O_3 nanoparticles	Real dielectric constant (unit less)	Imaginary dielectric constant (unit less)
(PC/PS) blend	Pure	4.61	18.39×10^{-4}
(PC-PS/SiC-Co_2O_3) nanocomposite	1.3 wt.%	5.92	32.53×10^{-4}
	2.6 wt.%	6.56	43.15×10^{-4}
	3.9 wt.%	6.96	56.02×10^{-4}
	5.2 wt.%	6.98	63.19×10^{-4}

4.3.6 The optical conductivity of (PC-PS/SiC-MnO_2) and (PC-PS/SiC-Co_2O_3) nanocomposites

The optical response of a material is mainly studied in terms of optical conductivity which can be calculated by using the equation (2.27). Figure 4.35, and Figure 4.36 display the variation of optical conductivity with the wavelength for (PC-PS/SiC-MnO_2) and (PC-PS/SiC-Co_2O_3) nanocomposites, respectively. The Figures show that the optical conductivity of all prepared nanocomposites is increased with increasing the contents of (SiC/MnO_2, and SiC/Co_2O_3) nanoparticles, this behavior attributed to the formation of localized levels in the energy gap; the increase of the contents for (SiC/MnO_2, and SiC/Co_2O_3) nanoparticles causes increase in the density of localized levels in the energy gap, thus, increase of the absorption coefficient consequently increasing the optical conductivity of nanocomposite [189]. The optical conductivity of nanocomposites increased about 71.01% and 70.88% respectively, when the content of (SiC/MnO_2, and SiC/Co_2O_3) nanoparticles reached to 5.2 wt.% at $\lambda = 560\,nm$. The optical conductivity of nanocomposites decreases as the wavelength of the incident photon increases; this is due to the optical conductivity strongly depends on the wavelength of the incident photon on the nanocomposites.

The optical conductivity of all prepared nanocomposites has high values in the UV-region; the increase of optical conductivity at low wavelength of photon is attributed to the high absorption of all prepared nanocomposite in that region, hence, increase of the charge transfer excitations. The spectrum of optical conductivity indicated that the samples are transmittance in the visible and near infrared regions [190]. The values of optical conductivity for the prepared nanocomposites at $\lambda = 560\,nm$ are shown in Table 4.13, and Table 4.14.

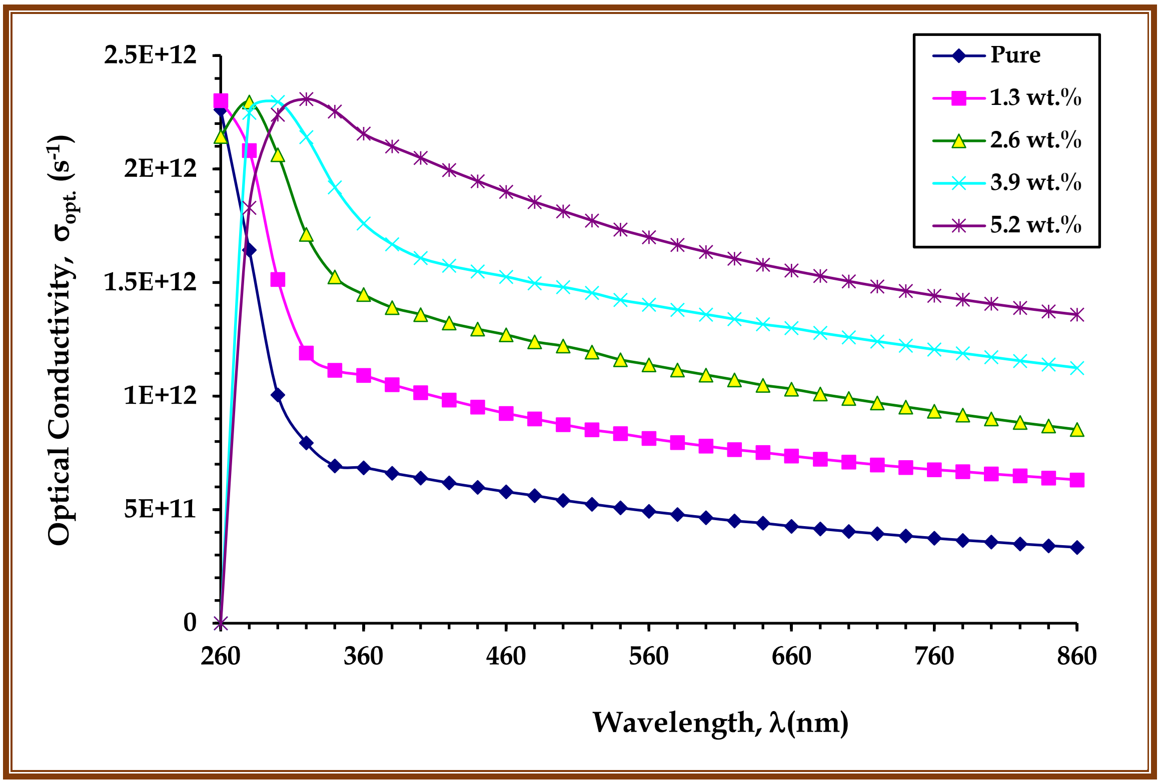

Figure 4.35: Variation of optical conductivity for (PC-PS/SiC-MnO_2) nanocomposites with wavelength at standard room temperature

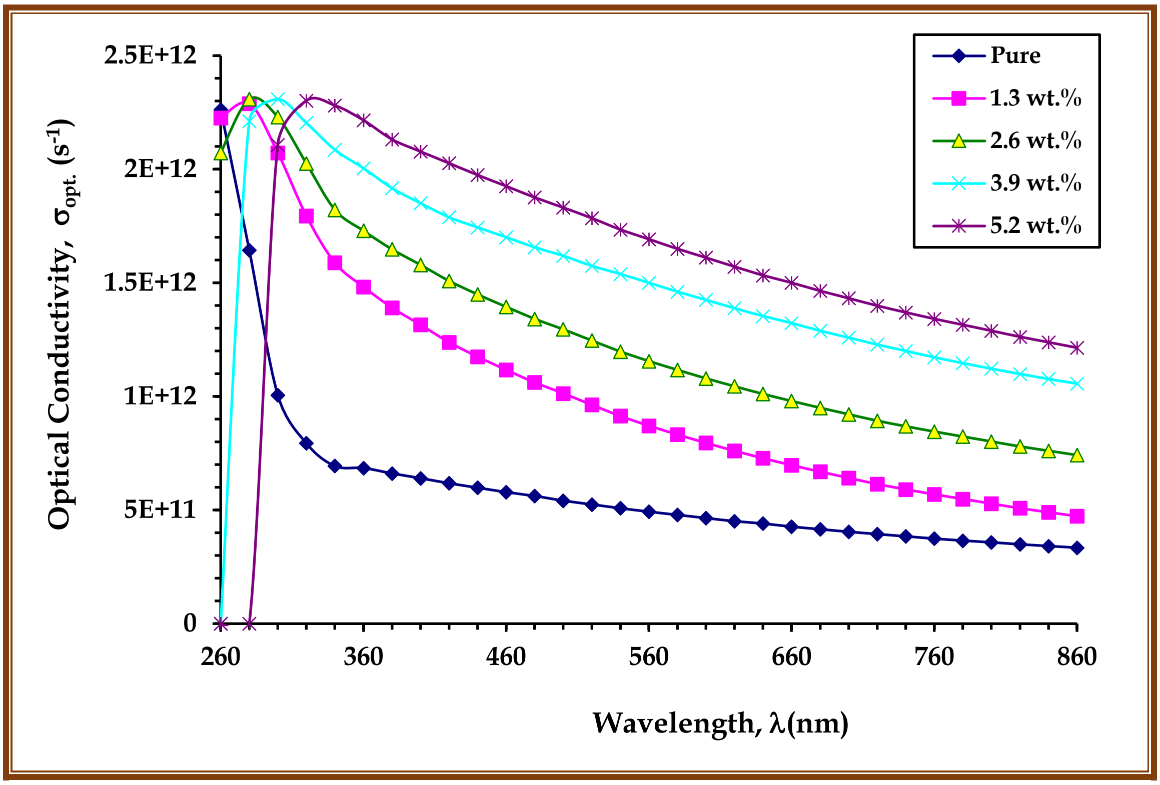

Figure 4.36: Variation of optical conductivity for (PC-PS/SiC-Co_2O_3) nanocomposites with wavelength at standard room temperature

Table 4.13: The optical conductivity values of (PC/PS) blend and (PC-PS/SiC-MnO_2) nanocomposites at λ = 560 nm.

Samples	Contents of SiC/MnO_2 nanoparticles	Optical conductivity (s^{-1})
(PC/PS) blend	Pure	0.49×10^{12}
(PC-PS/SiC-MnO_2) nanocomposite	1.3 wt.%	0.81×10^{12}
	2.6 wt.%	1.14×10^{12}
	3.9 wt.%	1.41×10^{12}
	5.2 wt.%	1.69×10^{12}

Table 4.14: The optical conductivity values of (PC/PS) blend and (PC-PS/SiC-Co_2O_3) nanocomposites at λ = 560 nm.

Simple	Contents of SiC/Co_2O_3 nanoparticles	Optical conductivity (s^{-1})
(PC/PS) blend	Pure	0.49×10^{12}
(PC-PS/SiC-Co_2O_3) nanocomposite	1.3 wt.%	0.87×10^{12}
	2.6 wt.%	1.16×10^{12}
	3.9 wt.%	1.50×10^{12}

	5.2 wt.%	1.91×10^{12}

4.4 The D.C Electrical Characteristics of Nanocomposites

The D.C electrical conductivity of (PC-PS/SiC-MnO_2) and (PC-PS/SiC-Co_2O_3) nanocomposites can be calculated by using equation (2.29), and the thermal activation energy is calculated by using equation (2.30).

4.4.1 The variation of D.C electrical conductivity for (PC-PS/SiC-MnO_2), and (PC-PS/SiC-Co_2O_3) nanocomposites with temperature

The impact of temperature on D.C electrical conductivity of (PC-PS/SiC-MnO_2), and (PC-PS/SiC-Co_2O_3) nanocomposites are shown in Figure 4.37, and Figure 4.38, respectively. The figures show that the D.C electrical conductivity of all samples of nanocomposites increases with the increasing of temperature. The behavior of electrical conductivity of nanocomposites with temperature attributed to the increase of the mobility and number of charge carriers inside of (PC-PS/SiC-MnO_2), and (PC-PS/SiC-Co_2O_3) nanocomposites [191], where (PC/PS) chains and SiC/MnO_2, and SiC/Co_2O_3 NPs could act as traps for the moving charge carriers by hopping process, the increase of temperature causes to moving the polymers chains and releasing the trapped charges [192]. So, the increase of current of (PC-PS/SiC-MnO_2), and (PC-PS/SiC-Co_2O_3) NCs with the increasing of temperature is attributed to two parameters: mobility and number of charge carriers, the increase is exponentially [193]. As temperature rises the electrical conductivity increases, due to the large number of ions is gained large kinetic energy because of charge carriers possess thermally activated hopping carriers between trapped sites, which is depending on temperature [194]. From the figures, the D.C electrical conductivity of (PC-PS/SiC-MnO_2), and (PC-PS/SiC-Co_2O_3) NCs have similarity behavior with temperature. Whereas, the percentage increase in electrical conductivity at a temperature of 50 for the two nanocomposites was about 82.29%, and 90.27%. The values of D.C electrical conductivity for the prepared nanocomposites at $T = 50\ °C$ are shown in Table 4.15 and Table 4.16.

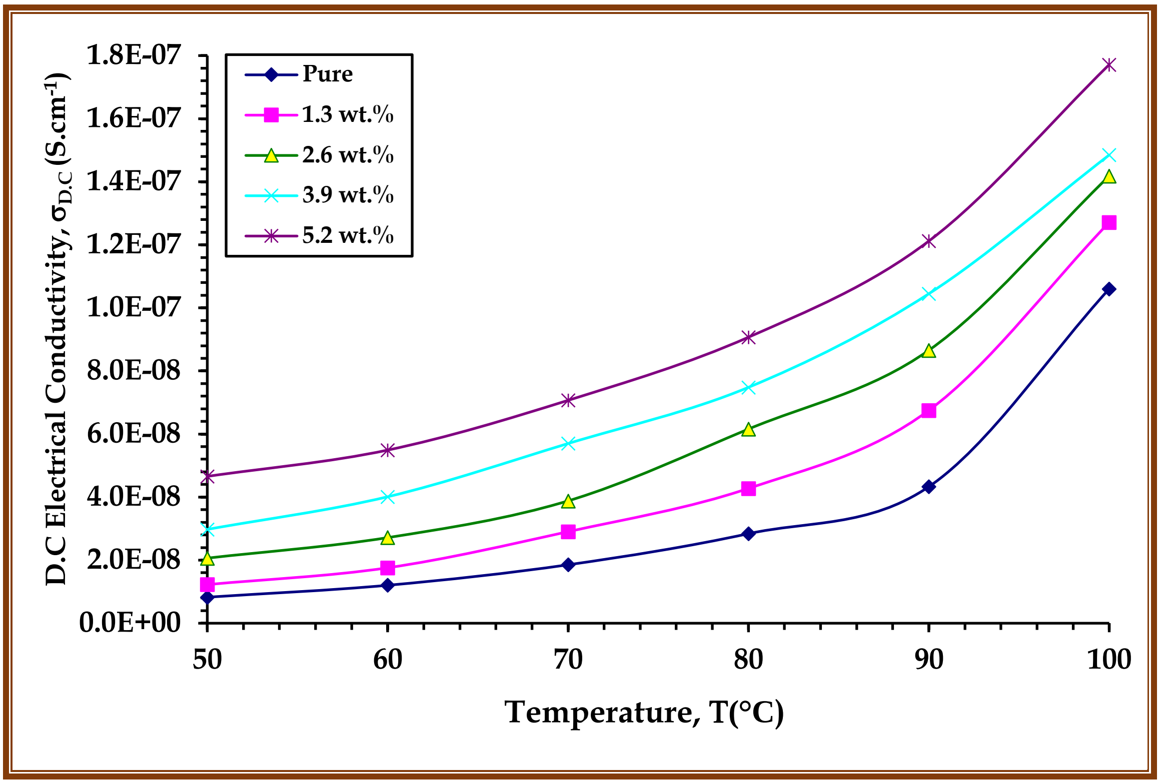

Figure 4.37: Variation of D.C electrical conductivity for (PC-PS/SiC-MnO_2) nanocomposites with temperature

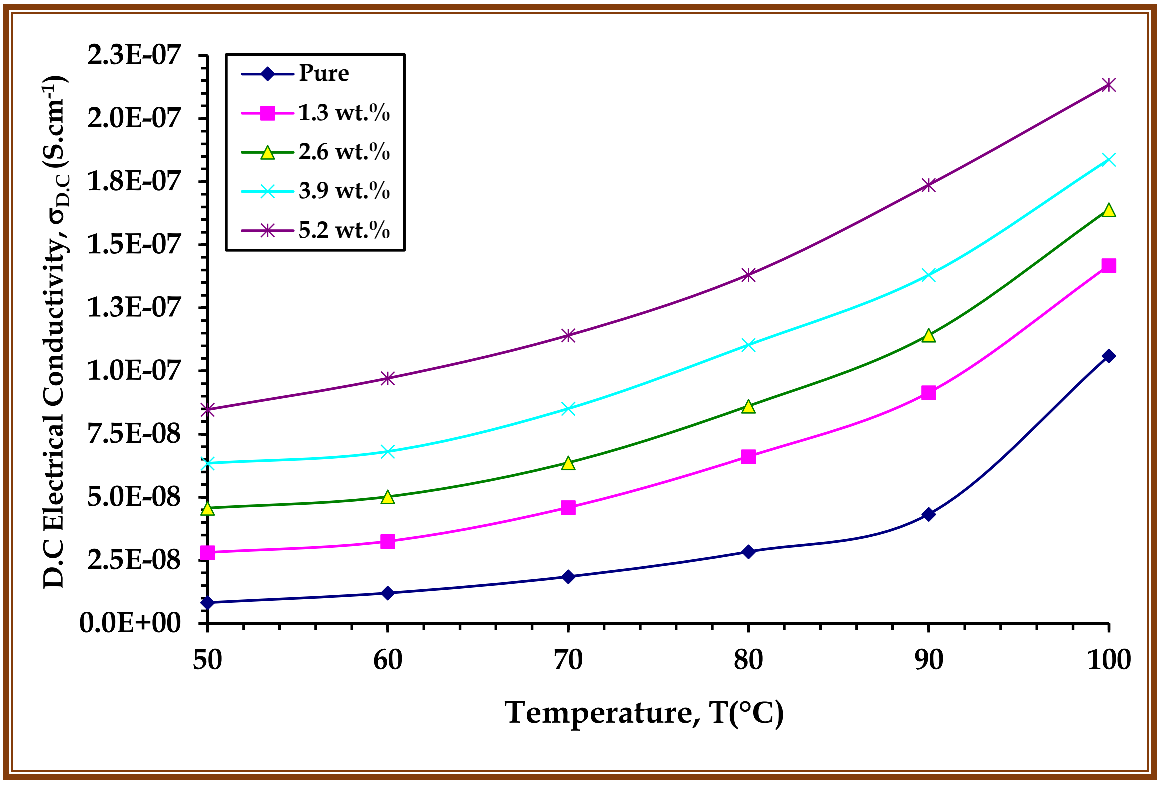

Figure 4.38: Variation of D.C electrical conductivity for (PC-PS/SiC-Co_2O_3) nanocomposites with temperature

4.4.2 Impact of SiC/MnO_2 and SiC/Co_2O_3 nanoparticles contents on D.C electrical conductivity of (PC-PS/SiC-MnO_2), and (PC-PS/SiC-Co_2O_3) nanocomposites

Figure 4.39, and Figure 4.40; displays the variation of D.C electrical conductivity of (PC-PS/SiC-MnO_2) and (PC-PS/SiC-Co_2O_3) nanocomposites with contents of nanoparticles respectively. The Figures display that the D.C electrical conductivity of (PC/PS) blend, (PC-PS/SiC-MnO_2) and (PC-PS/SiC-Co_2O_3) nanocomposites increases with the increase in the content of SiC/MnO_2 nanoparticles, and SiC/Co_2O_3 nanoparticles, as illustrate in Table 4.15, and Table 4.16; respectively.

The increase of conductivity with the increasing of SiC/MnO_2 nanoparticles, and SiC/Co_2O_3 nanoparticles, contents attributed to the increase of the number of charge carriers inside nanocomposites [191]. In addition; when the content of (PC-PS/SiC-MnO_2) and (PC-PS/SiC-Co_2O_3) nanocomposites reach to (5.2 wt.%), the SiC/MnO_2 nanoparticles, and SiC/Co_2O_3 nanoparticles form a network of paths inside the nanocomposite as displayed in Figure 4.3, and Figure 4.3 4.4; this behavior attributed to the higher probability of nanoparticles physical contact in the (PC/PS) polymeric blend. These contacts can be formed a network of paths which allowed to the free moving of charge carriers and leads to increase the conductivity [193]. Besides that; the addition of nanoparticles leads to the hosting of new energy levels within the band gap of (PC/PS) polymeric blend which leads to a reduction of the energy gap and increase in the conductivity [195].

At low contents of SiC/MnO_2 nanoparticles and SiC/Co_2O_3 nanoparticles are located in clusters, the clusters form a network at content (5.2 wt.%) of (PC-PS/SiC-MnO_2), and (PC-PS/SiC-Co_2O_3) nanocomposites have the highest electrical conductivity due to the high electrical conductivity of MnO_2 nanoparticles and Co_2O_3 nanoparticles and low density of SiC nanoparticles. This is consistent with the results of researchers [196].

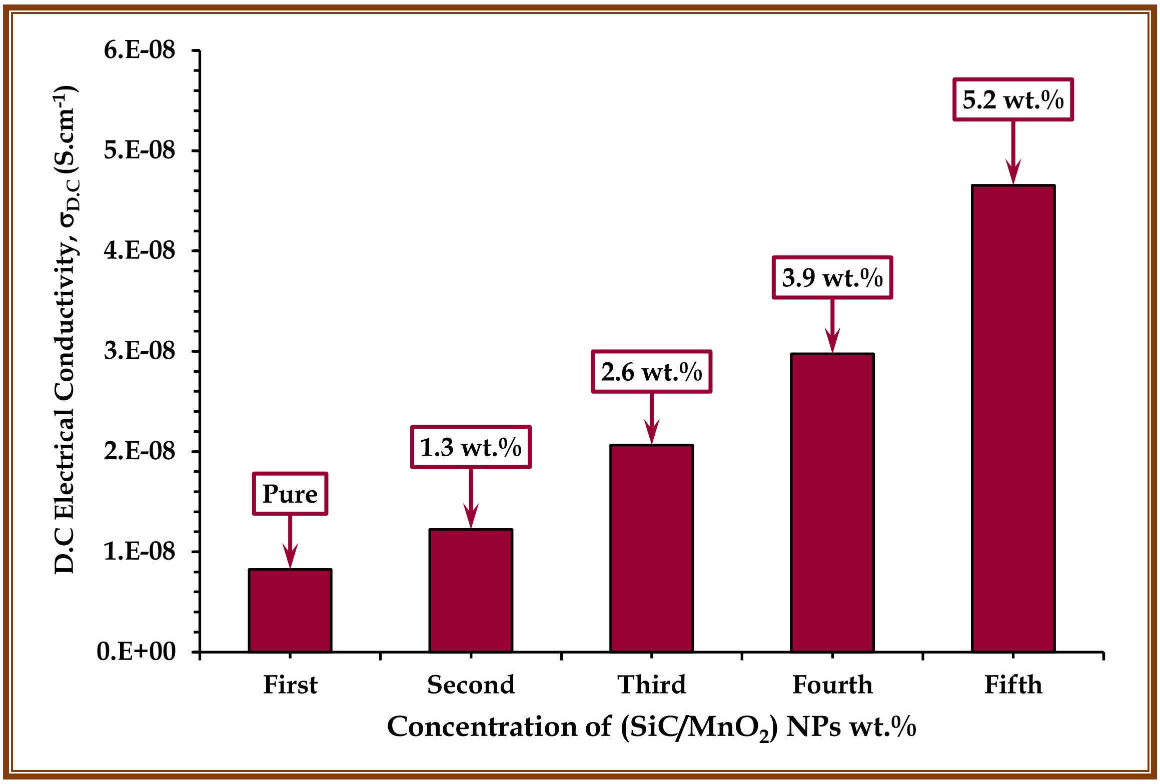

Figure 4.39: Impact of SiC/MnO$_2$ nanoparticles contents for (PC-PS/SiC-MnO$_2$) nanocomposites on D.C electrical conductivity at 50 °C

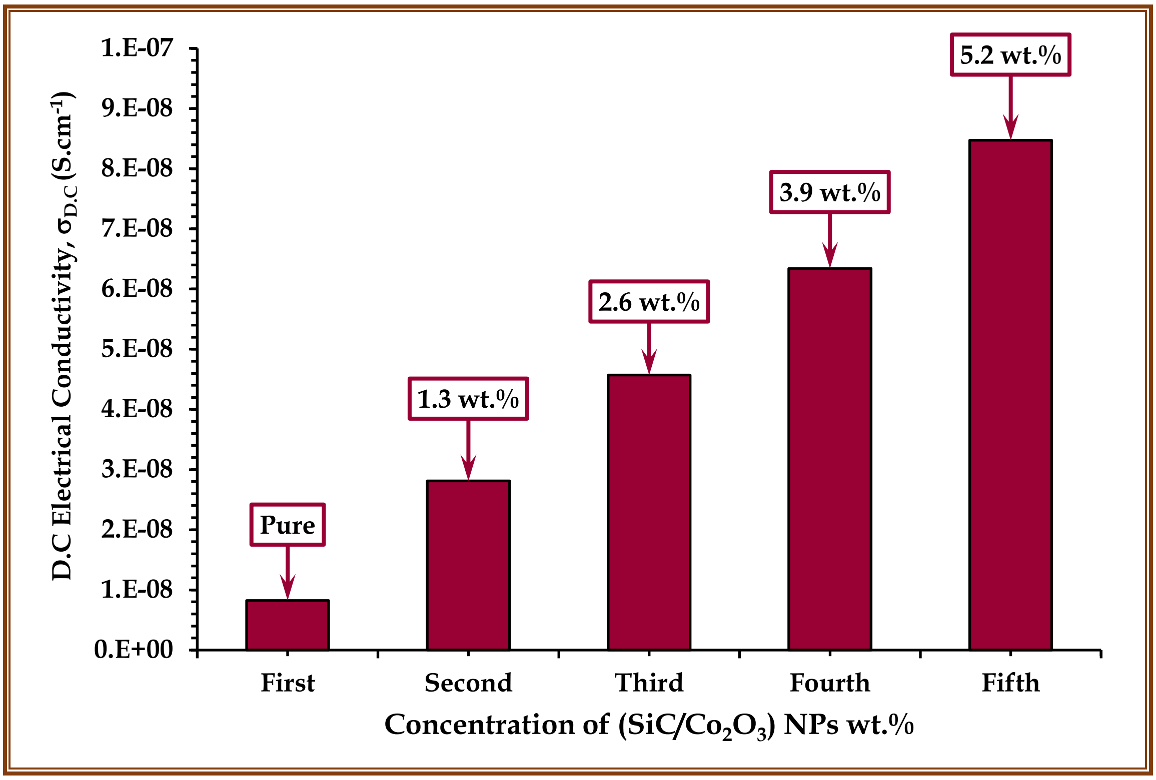

Figure 4.40: Impact of SiC/Co$_2$O$_3$ NPs contents for (PC-PS/SiC-Co$_2$O$_3$) nanocomposites on D.C electrical conductivity at 50 °C

4.4.3 The thermal activation energy of the (PC-PS/SiC-MnO_2), and the (PC-PS/SiC-Co_2O_3) Nanocomposites

Figure 4.41, and Figure 4.42 depict the plot of ($ln\sigma_{D.C}$) with ($1000/T$) of (PC-PS/SiC-MnO_2) and (PC-PS/SiC-Co_2O_3) nanocomposites, respectively to calculate the thermal activation energy of nanocomposites by using equation (2.30). The experimental results show that the thermal activation energy values of nanocomposites are ranging from (0.5026 eV) to (0.2747 eV) of (PC-PS/SiC-MnO_2) nanocomposites, and (0.5026 eV) to (0.1938 eV) of (PC-PS/SiC-Co_2O_3) nanocomposites. The high value of activation energy for pure polymers (PC/PS) blend attributed to existence of free ions in the polymers. The decrease of activation energy with the increasing of the nanoparticles contents related to increasing in localization of charge carriers causing higher electrical conductivity which is attributed to effect of space charge contribution may play an important role in the charges transport, and also to the mobility of charge carriers by the hopping process [197].

The variation of thermal activation energies of (PC-PS/SiC-MnO_2) and (PC-PS/SiC-Co_2O_3) nanocomposites with nanoparticles contents are shown in Figure 4.43 and Figure 4.44 respectively. The thermal activation energies decreases with the increasing of the nanoparticles contents for nanocomposites, this behavior attributed to creation local energy levels in the energy gap which act as traps for charge carriers [198]. At high contents of SiC, MnO_2, and Co_2O_3 nanoparticles, the thermal activation energies have lower values which attributed to formation a continuous network of nanoparticles in the nanocomposite [199], and as illustrate in Table 4.15, and Table 4.16, respectively.

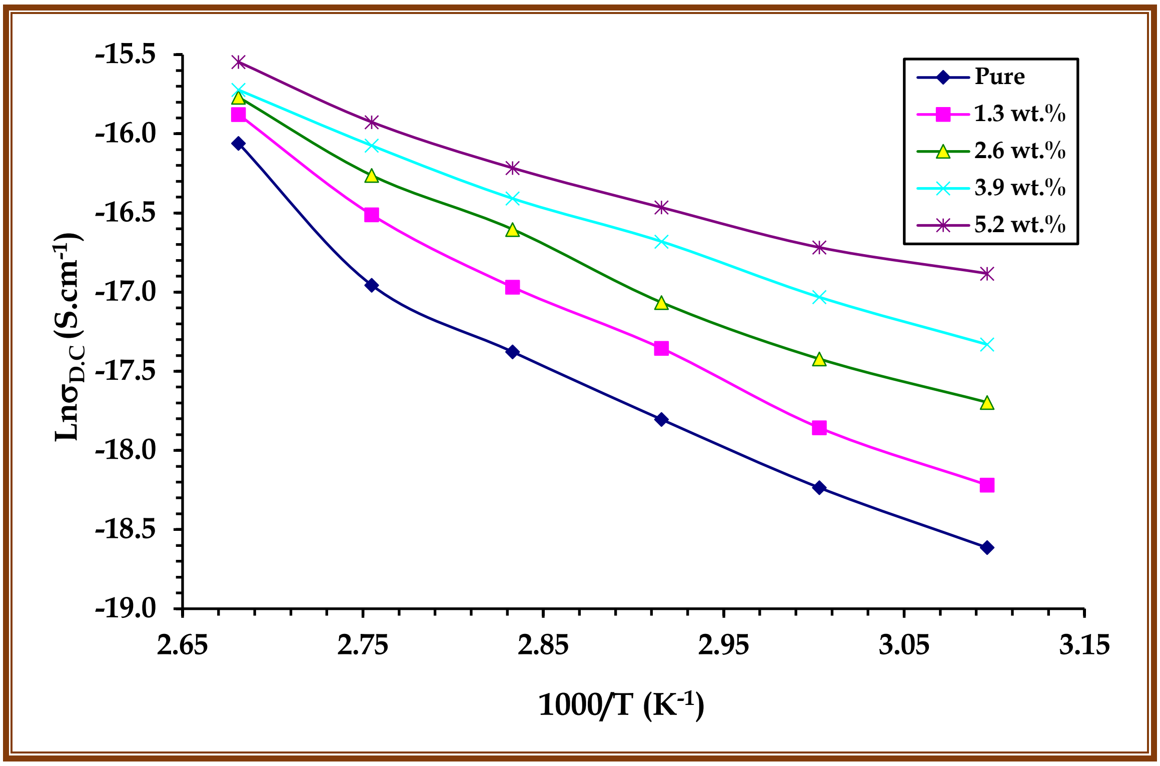

Figure 4.41: Plot of $ln(\sigma_{D.C})$ and inverted absolute temperature for (PC-PS/SiC-MnO_2) nanocomposites

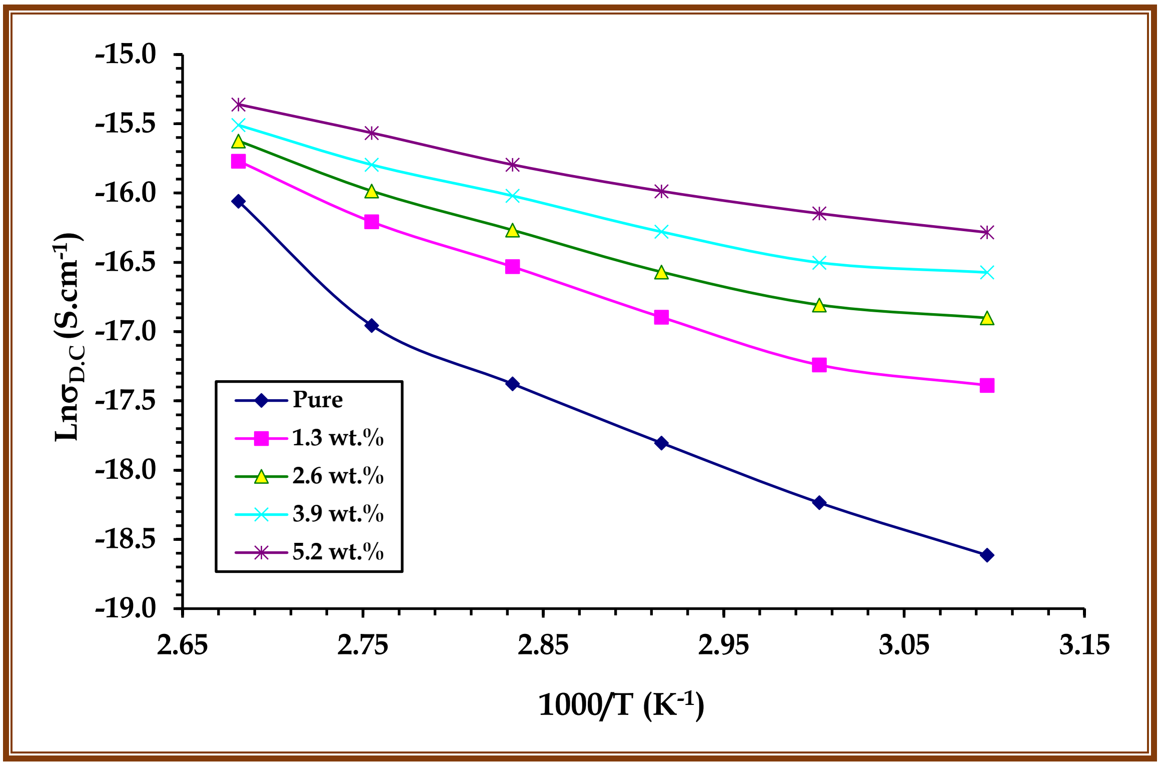

Figure 4.42: Plot of $ln(\sigma_{D.C})$ and inverted absolute temperature for (PC-PS/SiC-Co_2O_3) nanocomposites

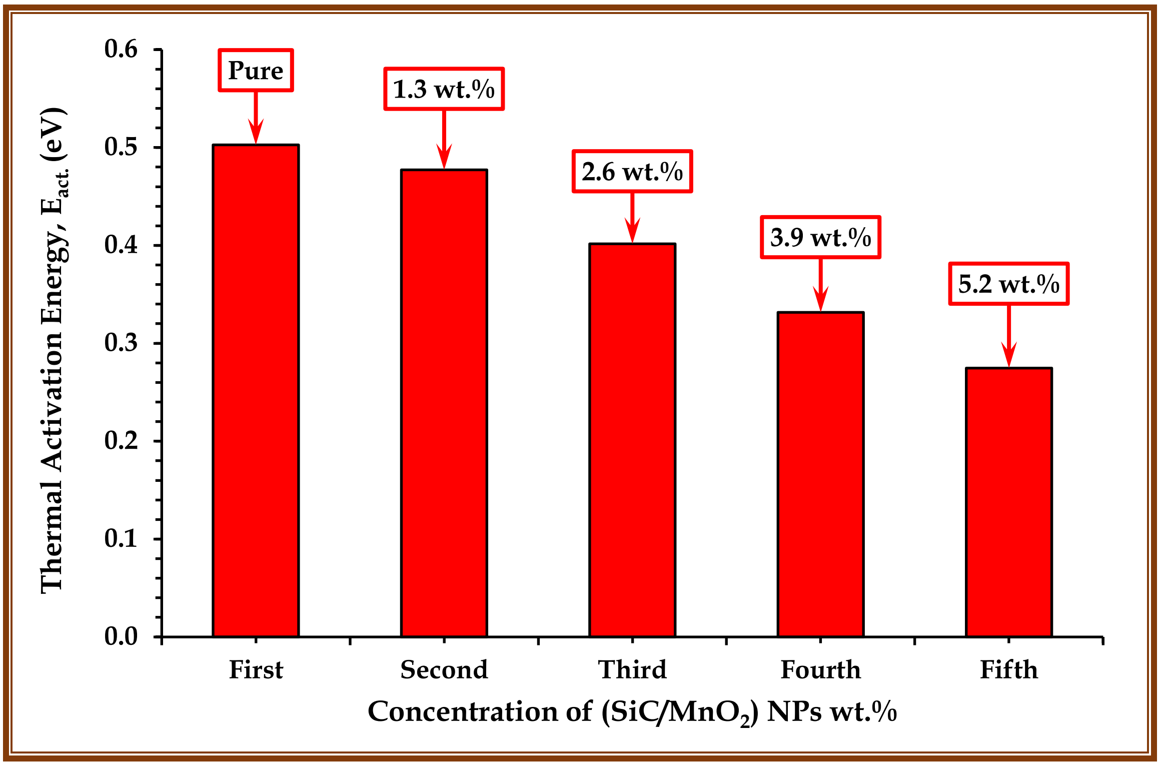

Figure 4.43 :Variation of thermal activation energy for (PC-PS/SiC-MnO_2) nanocomposites with contents of SiC/MnO_2 nanoparticles

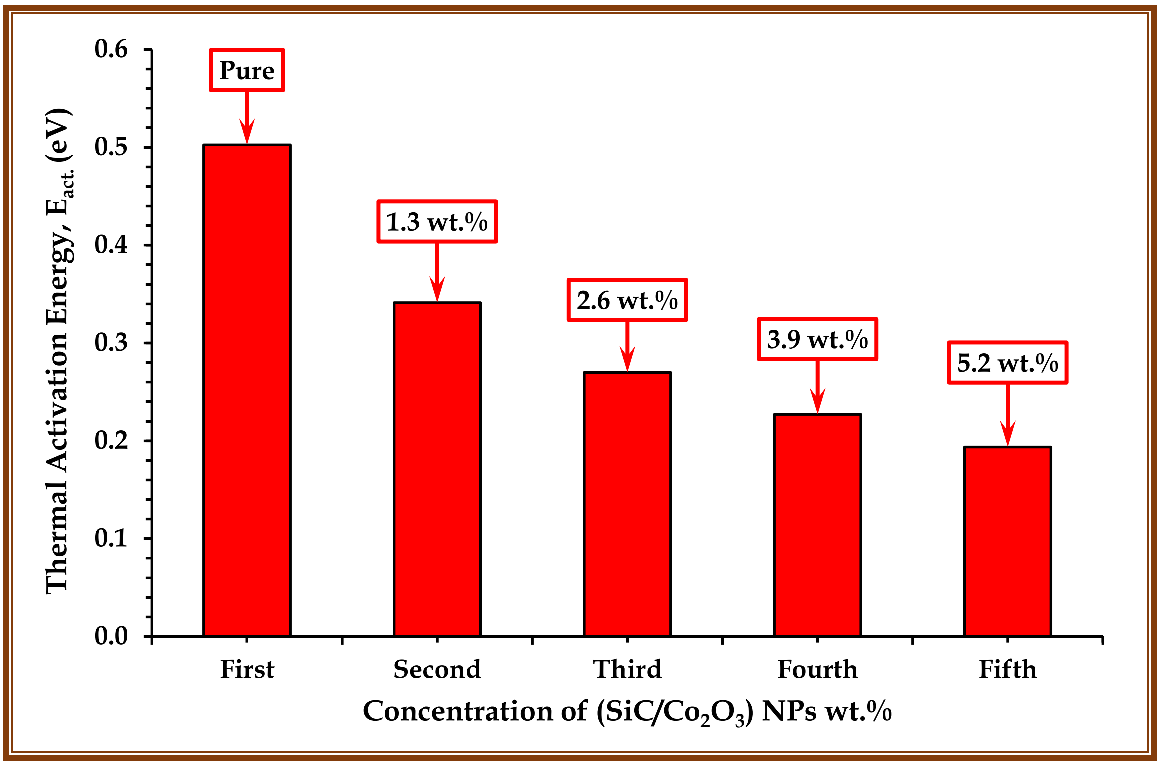

Figure 4.44: Variation of thermal activation energy for (PC-PS/SiC-Co_2O_3) nanocomposites with contents of SiC/Co_2O_3 nanoparticles

Table 4.15: Values of D.C electrical conductivity at 50 °C and thermal activation energy of (PC/PS) blend and (PC-PS/SiC-MnO2) nanocomposites

Samples	Contents of SiC/MnO_2 nanoparticles	D.C electrical conductivity ($S.cm^{-1}$)	Thermal Activation Energy (eV)
(PC/PS) blend	**Pure**	08.25×10^{-9}	0.5026
(PC-PS/SiC-MnO_2) nanocomposite	**1.3 wt.%**	12.24×10^{-9}	0.4770
	2.6 wt.%	20.64×10^{-9}	0.4016
	3.9 wt.%	29.75×10^{-9}	0.3316
	5.2 wt.%	46.56×10^{-9}	0.2747

Table 4.16: Values of D.C electrical conductivity at 50 °C and thermal activation energy of (PC/PS) blend and (PC-PS/SiC-Co_2O_3) nanocomposites

Samples	Contents of SiC/Co_2O_3 nanoparticles	D.C electrical conductivity ($S.cm^{-1}$)	Thermal Activation Energy (eV)
(PC/PS) blend	**Pure**	08.25×10^{-9}	0.5026
(PC-PS/SiC-Co_2O_3) nanocomposite	**1.3 wt.%**	28.09×10^{-9}	0.3413
	2.6 wt.%	45.69×10^{-9}	0.2700
	3.9 wt.%	63.44×10^{-9}	0.2271
	5.2 wt.%	84.71×10^{-9}	0.1938

4.5 The A.C Electrical Characteristics of Nanocomposites

The A.C electrical Characteristics of (PC-PS/SiC-MnO_2) and (PC-PS/SiC-Co_2O_3) nanocomposites are involved dielectric constant, dielectric loss and A.C electrical conductivity were studied in frequency range $(100 - 5 \times 10^6)\ Hz$ at standard room temperature.

4.5.1 The electrical dielectric constant of the (PC-PS/SiC-MnO_2) and the (PC-PS/SiC-Co_2O_3) nanocomposites

The dielectric constant (ε') of (PC-PS/SiC-MnO_2) and (PC-PS/SiC-Co_2O_3) nanocomposites were calculated from equation (2.37). The behavior of dielectric constant of (PC-PS/SiC-MnO_2) and (PC-PS/SiC-Co_2O_3) nanocomposites with frequency is shown in Figure 4.45, and Figure 4.46. It is observed that dielectric constant reduces with the rise in frequency for all samples which due to its ability of dipoles in nanocomposites specimens to turn themselves in the direction of the applied electric field and the reduce of space charges or interfacial polarization to overall polarization [200]. The variation of dielectric constant of (PC-PS/SiC-MnO_2) and (PC-PS/SiC-Co_2O_3) nanocomposites with the content of nanoparticles at $f = 100\ Hz$ is shown in Figure 4.47, and Figure 4.48 demonstration that the dielectric constant of (PC-PS/SiC-MnO_2) and (PC-PS/SiC-Co_2O_3) nanocomposites increases with the increasing of the contents for (SiC/MnO_2, and SiC/Co_2O_3) nanoparticles, as they are shown in Table 4.17 and Table 4.18 respectively. It is observed that rises with increasing of content nanoparticles for all samples of nanocomposites. This actions might be described by interfacial polarization inside the nanocomposites in the applied field alternating electric field and a rise in the charge carriers [201]. The increase of the dielectric constant reach to 19.93%, and 32.66%. which means that prepared nanocomposites have low loss, meaning low energy loss which make it suitable for nanoelectronics devices and pressure sensors applications.

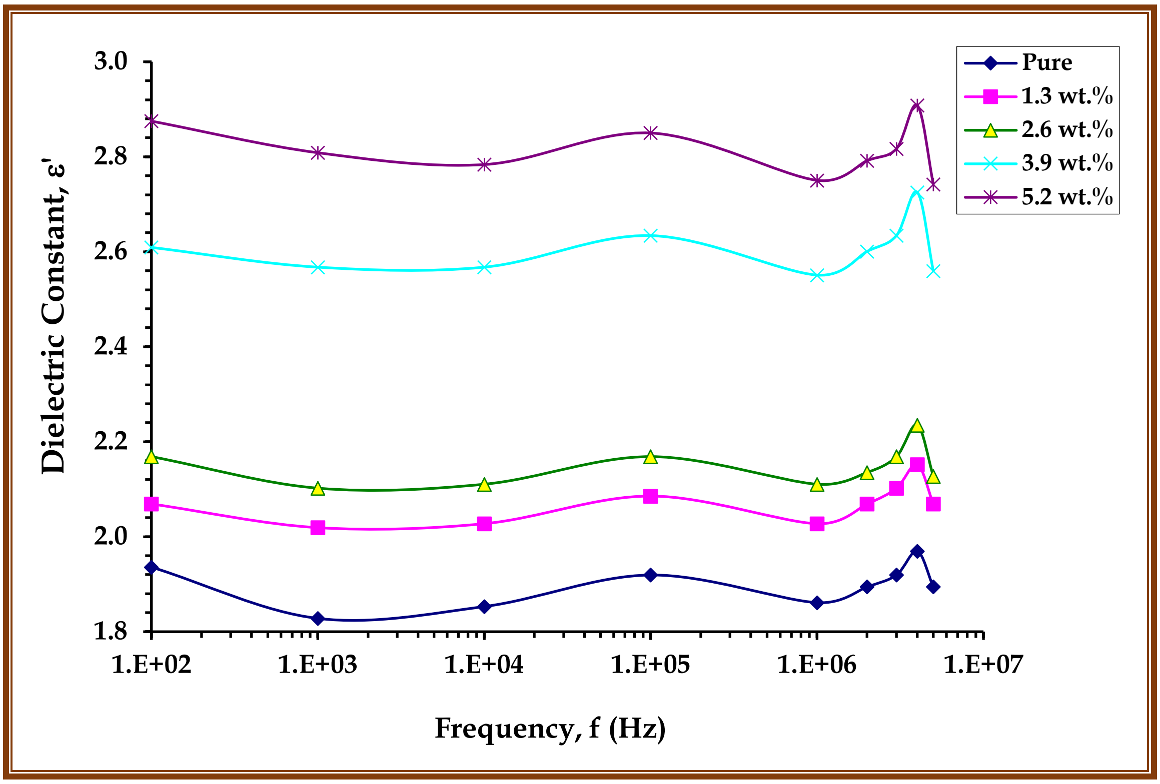

Figure 4.45: Variation of dielectric constant for (PC-PS/SiC-MnO_2) nanocomposites with frequency at standard room temperature

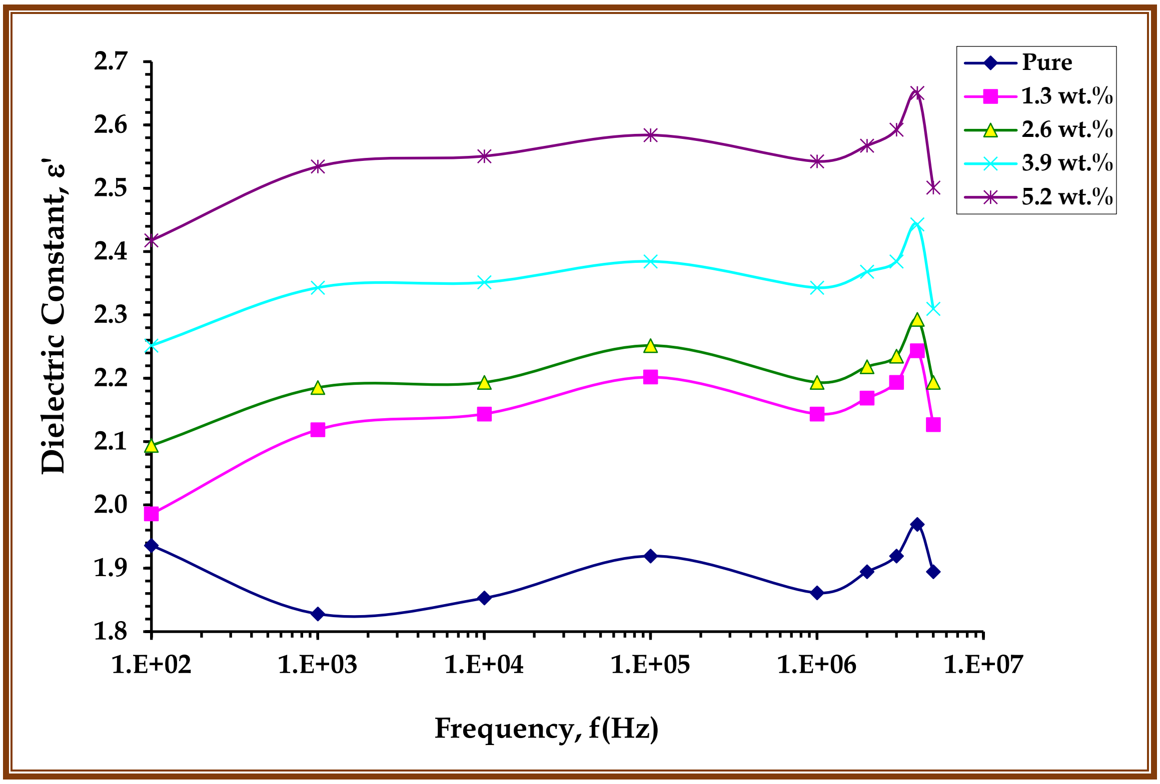

Figure 4.46: Variation of dielectric constant for (PC-PS/SiC-Co_2O_3) nanocomposites with frequency at standard room temperature

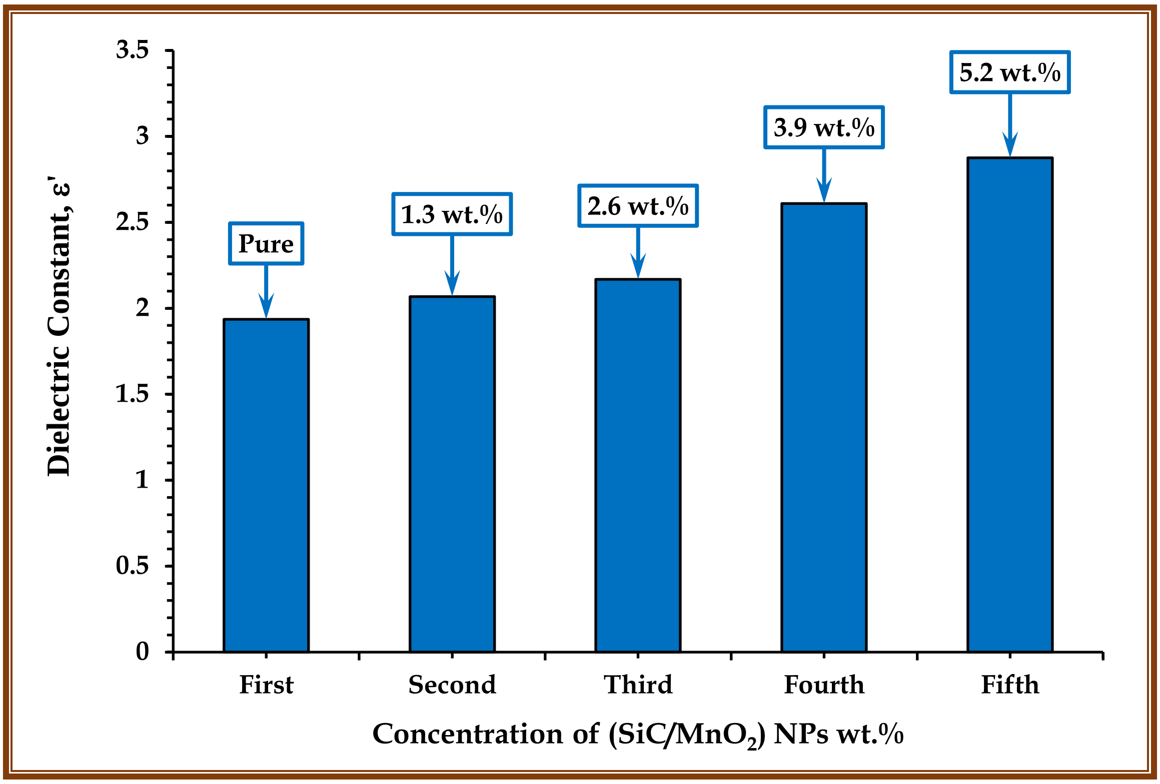

Figure 4.47: Impact of SiC/MnO_2 nanoparticles contents on dielectric constant for (PC-PS/SiC-MnO_2) nanocomposites at 100 Hz

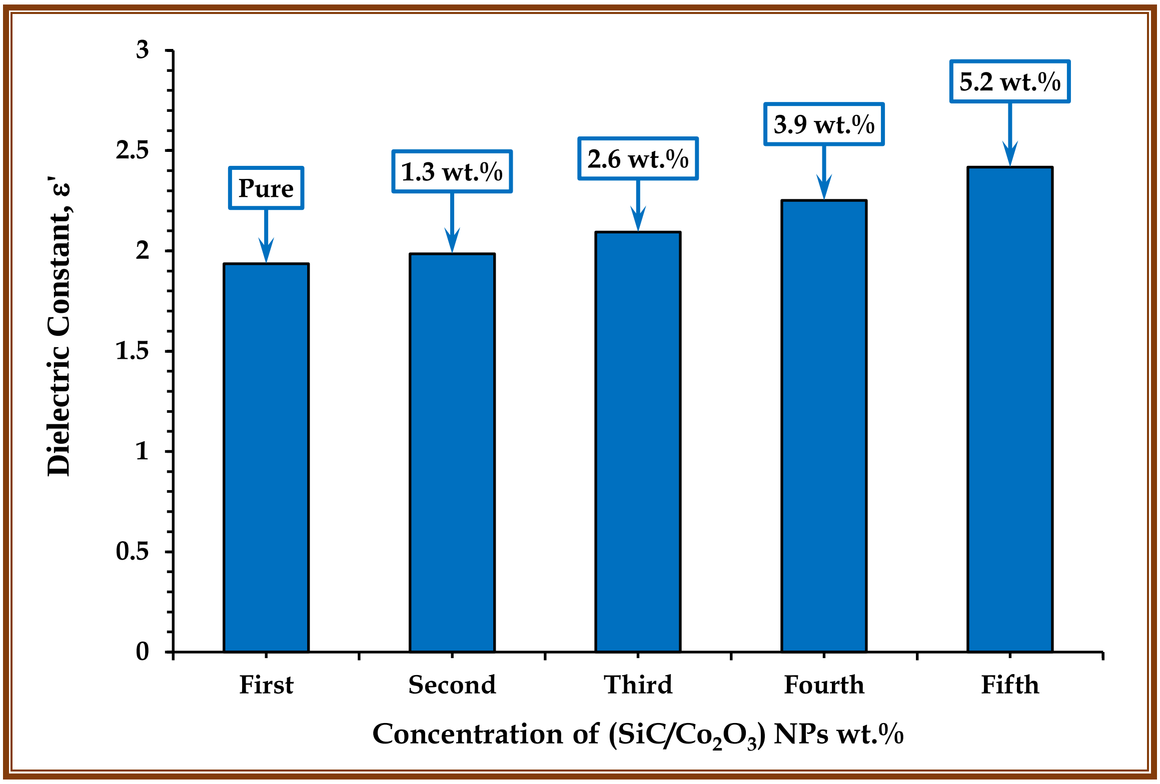

Figure 4.48: Impact of SiC/Co_2O_3 nanoparticles contents on dielectric constant for (PC-PS/SiC-Co_2O_3) nanocomposites at 100 Hz

Table 4.17: Values of dielectric constant for (PC-PS/SiC-MnO_2) nanocomposites at 100 Hz

Samples	Contents of SiC/MnO_2 nanoparticles	Electrical dielectric constant (unit less)
(PC/PS) blend	**Pure**	1.9360
(PC-PS/SiC-MnO_2) nanocomposite	**1.3 wt.%**	2.0690
	2.6 wt.%	2.1687
	3.9 wt.%	2.6091
	5.2 wt.%	2.8749

Table 4.18: Values of dielectric constant for (PC-PS/SiC-Co_2O_3) nanocomposites at 100 Hz.

Samples	Contents of SiC/Co_2O_3 nanoparticles	Electrical dielectric constant (unit less)
(PC/PS) blend	**Pure**	1.9360
(PC-PS/SiC-Co_2O_3) nanocomposite	**1.3 wt.%**	1.9859
	2.6 wt.%	2.0939
	3.9 wt.%	2.2518

	5.2 wt.%	2.4179

4.5.2 The electrical dielectric loss of the (PC-PS/SiC-MnO_2) and the (PC-PS/SiC-Co_2O_3) Nanocomposites

The dielectric loss (ε'') was calculated from equation (2.38). Figure 4.49 and Figure 4.50 demonstration the behavior of dielectric loss for (PC-PS/SiC-MnO_2) and (PC-PS/SiC-Co_2O_3) nanocomposites with frequency. It is observed that the dielectric loss of (PC-PS/SiC-MnO_2) and (PC-PS/SiC-Co_2O_3) nanocomposites reduces with the rise in frequency, which due to reduce of polarization of space charge influence. At low frequency, the dielectric loss has high values, then reduce with the rise in frequency, which attributed to the dipoles of electric has enough time to align with the electric field before change its direction [202]. From Figure 4.49 and Figure 4.50 the dielectric loss increases at ($f = 4MHz$). This is the highest absorption of applied field. This absorption happens due to Maxwell-Wagner phenomenon which is caused by A.C current due to the difference of dielectric constant and conductivity of the phases in the composite. This is electric current has the same phase as that of the applied field [203]. Figure 4.51, and Figure 4.52 display the impact of (SiC/MnO_2, and SiC/Co_2O_3) content on dielectric loss of (PC/PS) polymeric blend, respectively at $f = 100\ Hz$. The rise in a content of nanoparticles lead to increase in the dielectric loss values which attributed to the rise of the number of charge carriers [204]. At low content of nanoparticles, it create as a clusters but at high content reached to 2.6 wt.% it form a network inside the nanocomposites. As shown in the Figures, the value of dielectric loss of nanocomposites increases with the increase the contents of (SiC/MnO_2, and SiC/Co_2O_3) NPs as illustrated in Table 4.19 and Table 4.20. The increase in a value of dielectric loss reached to 33.28%, and 46.84%. The increases of dielectric loss value of (PC/PS) polymeric blend with increasing the contents of (SiC/MnO_2, and SiC/Co_2O_3) NPs attributed to the increases of the number of charge carriers for nanocomposites. These results agree with [205].

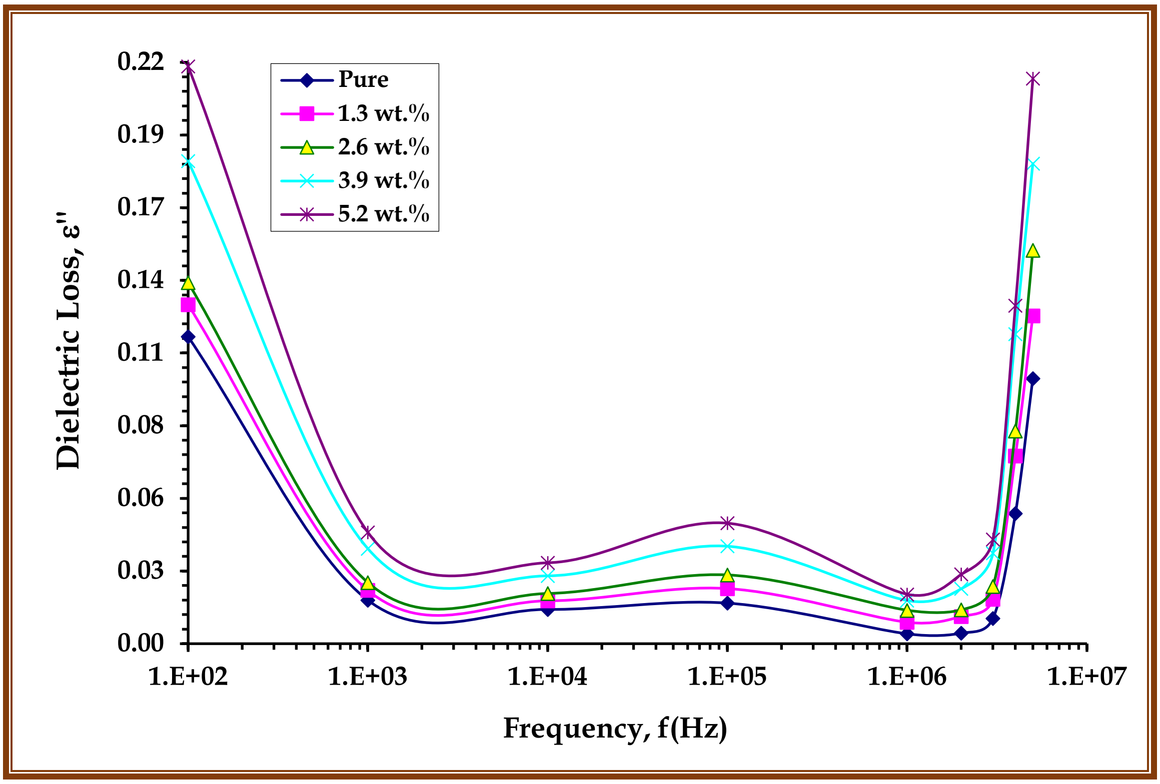

Figure 4.49: Variation of dielectric loss for (PC-PS/SiC-MnO_2) nanocomposites with frequency at standard room temperature

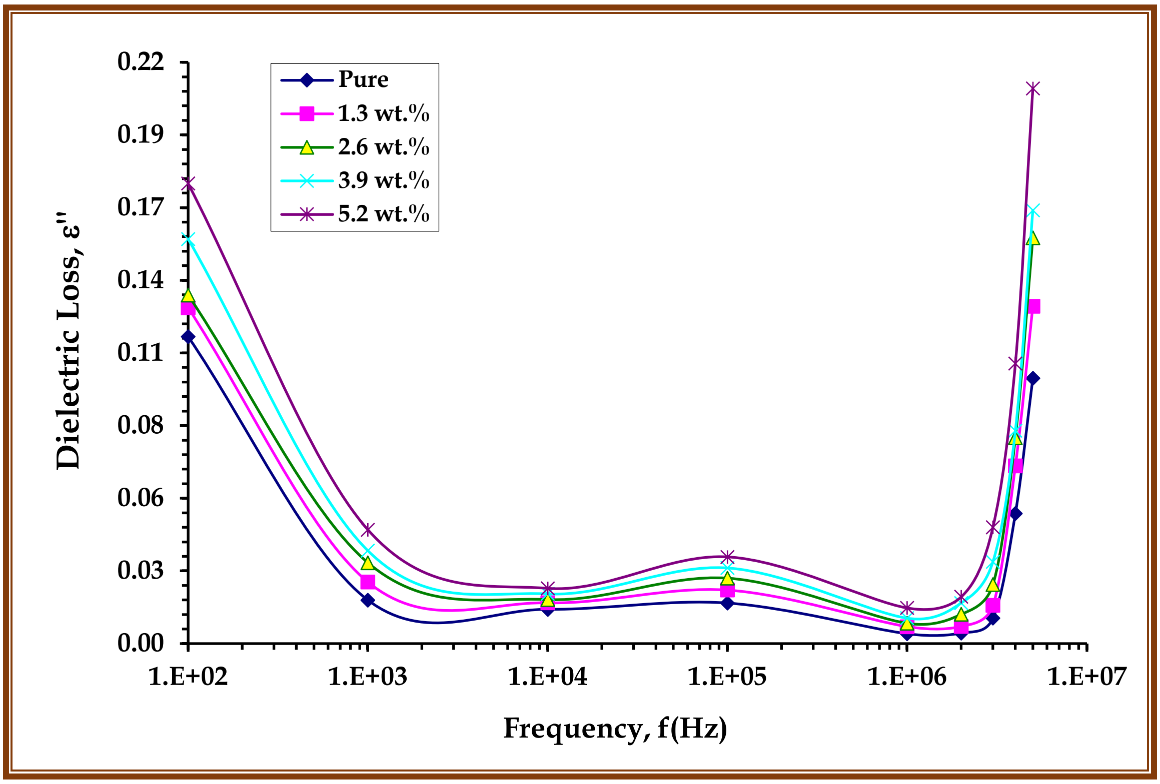

Figure 4.50: Variation of dielectric loss for (PC-PS/SiC-Co_2O_3) nanocomposites with frequency at standard room temperature

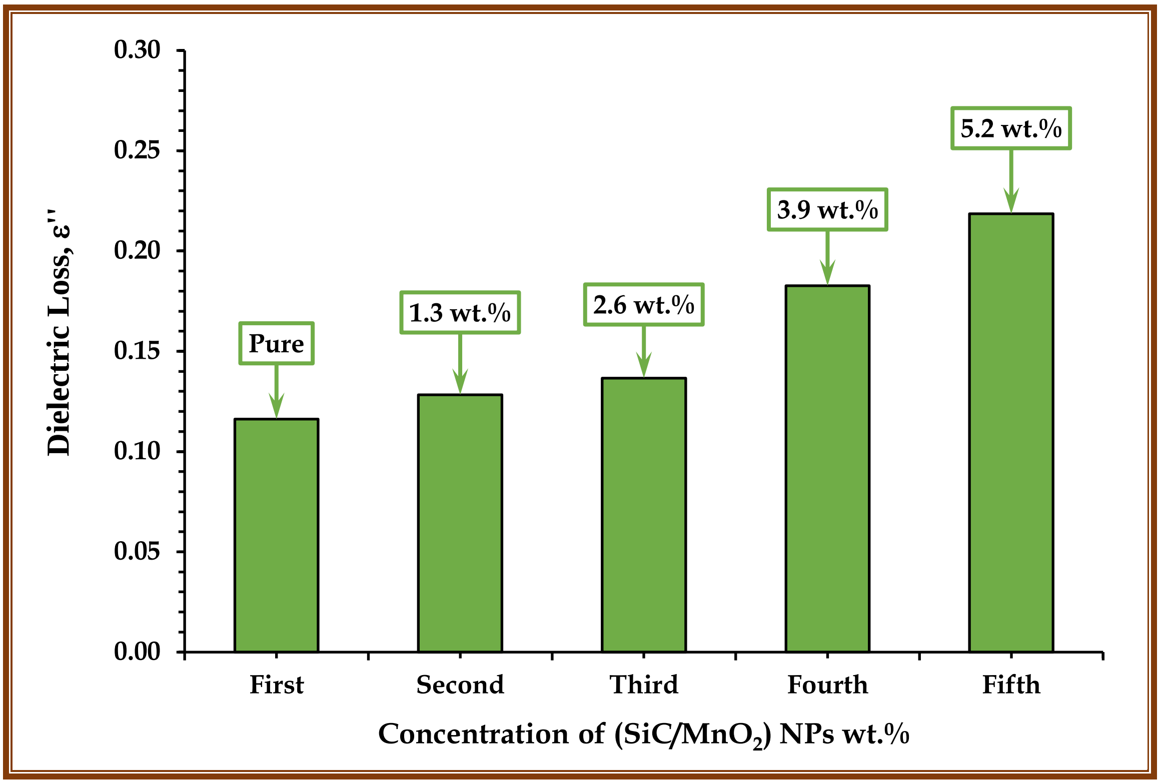

Figure 4.51: Impact of SiC/MnO_2 nanoparticles contents on dielectric loss of the (PC-PS/SiC-MnO_2) nanocomposites at 100 Hz

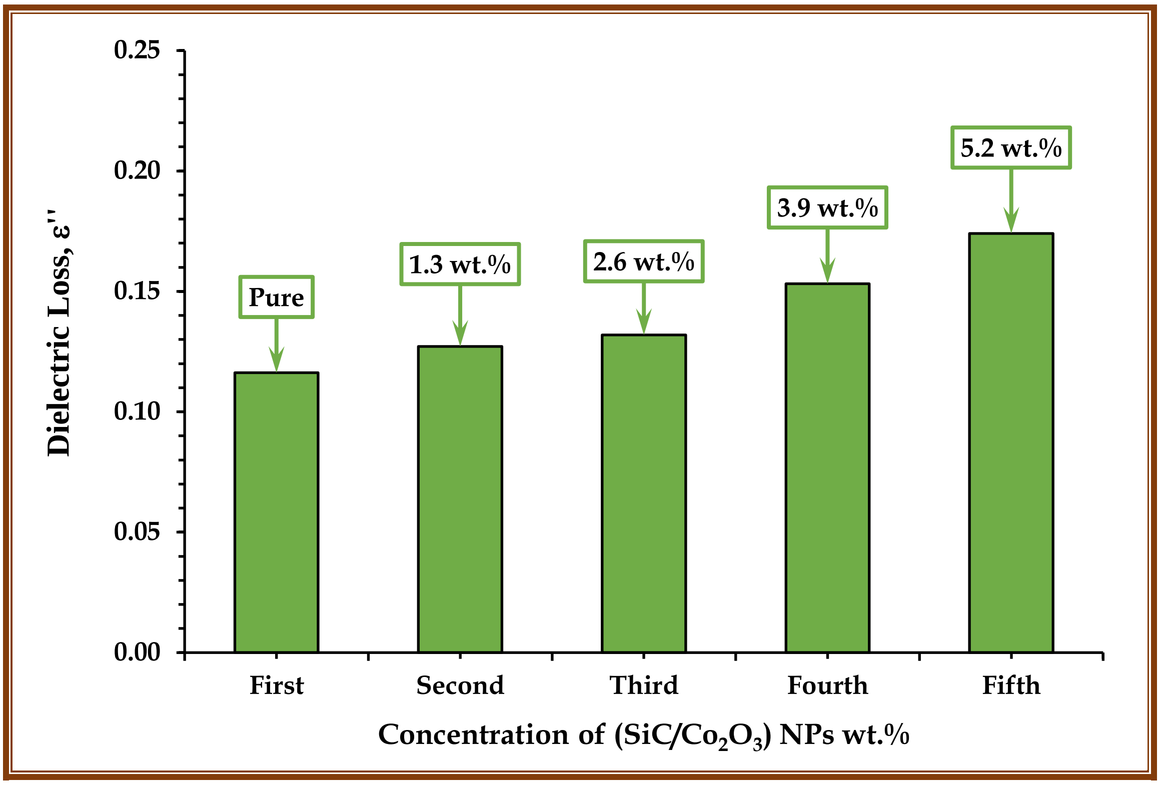

Figure 4.52: Impact of SiC/Co_2O_3 nanoparticles contents on dielectric loss of the (PC-PS/SiC-Co_2O_3) nanocomposites at 100 Hz

Table 4.19: Values of dielectric loss of (PC-PS/SiC-MnO_2) nanocomposites at 100 Hz

Samples	Contents of SiC/MnO_2 nanoparticles	Electrical dielectric loss (unit less)
(PC/PS) blend	**Pure**	0.1162
(PC-PS/SiC-MnO_2) nanocomposite	**1.3 wt.%**	0.1283
	2.6 wt.%	0.1366
	3.9 wt.%	0.1826
	5.2 wt.%	0.2185

Table 4.20: Values of dielectric loss of (PC-PS/SiC-Co_2O_3) nanocomposites at 100 Hz

Samples	Contents of SiC/Co_2O_3 nanoparticles	Electrical dielectric loss (unit less)
(PC/PS) blend	**Pure**	0.1162
(PC-PS/SiC-Co_2O_3) nanocomposite	**1.3 wt.%**	0.1271
	2.6 wt.%	0.1319
	3.9 wt.%	0.1531
	5.2 wt.%	0.1741

4.5.3 The A.C electrical conductivity of the (PC-PS/SiC-MnO_2) and the (PC-PS/SiC-Co_2O_3) Nanocomposites

The A.C electrical conductivity of nanocomposites is measured by using equation (2.39). The nanoparticles create a path network inside the nanocomposite at high contents of nanoparticles 5.2 wt.% for (PC/PS) polymeric blend. The variation of A.C electrical conductivity of (PC-PS/SiC-MnO_2) and (PC-PS/SiC-Co_2O_3) nanocomposites with frequency are shown in Figure 4.53, and Figure 4.54 at standard room temperature respectively. As shown in the Figures, for all prepared nanocomposites the A.C electrical conductivity increases with increasing the frequency of the electric field, this behavior due to the space charge polarization that occurs at low frequencies, and also to the mobility of charge carriers by the hopping process. The mobility of charge carriers was increased in the high-frequency region; thus the electrical conductivity increases with increasing the frequency for (PC-PS/SiC-MnO_2) and (PC-PS/SiC-Co_2O_3) nanocomposites [206]. This is consistent with the results of the researchers [207].

Figure 4.55, and Figure 4.56 demonstration the Impact of (SiC/MnO_2, and SiC/Co_2O_3) nanoparticles contents on A.C electrical conductivity for (PC/PS) polymeric blend at $f = 100\ Hz$ respectively. From the Figures, by increasing (SiC/MnO_2, and SiC/Co_2O_3) nanoparticles contents, the electrical conductivity of nanocomposites increases as they are illustrated in Table 4.21, and Table 4.22. The increase of the electrical conductivity with increasing the content of (SiC/MnO_2, and SiC/Co_2O_3) nanoparticles attributed to the increase in the number of charge carriers because of the composition of the dopants nanoparticles that decreases the resistance of nanocomposites gradually and increases the A.C electrical conductivity. This is consistent with the results of researchers [208].

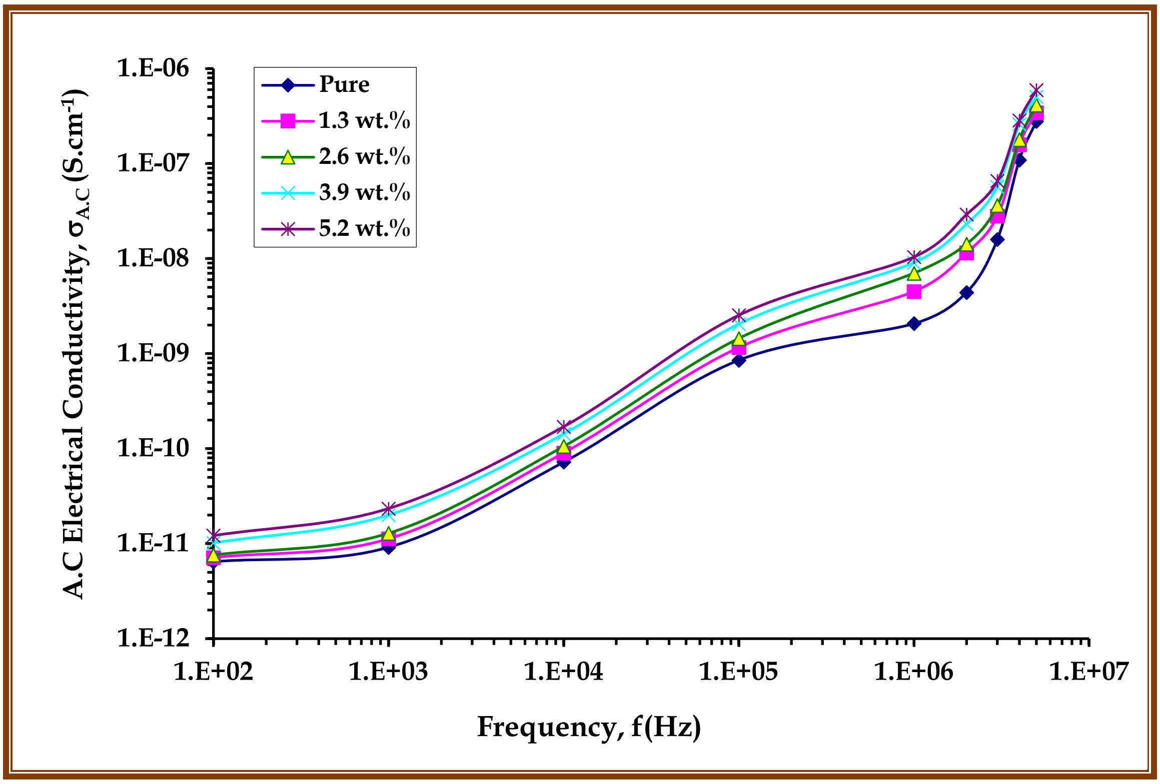

Figure 4.53: Variation of A.C electrical conductivity for (PC-PS/SiC-MnO$_2$) nanocomposites with frequency at standard room temperature

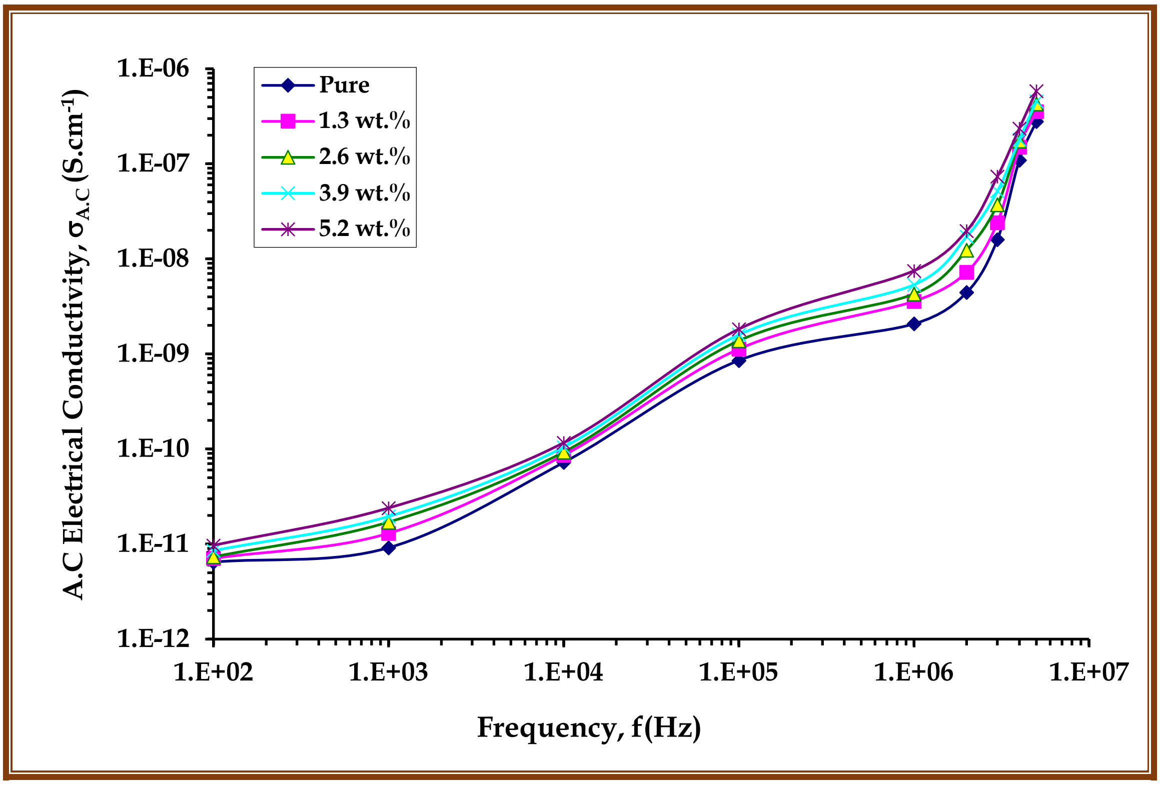

Figure 4.54: Variation of A.C electrical conductivity for (PC-PS/SiC-Co$_2$O$_3$) nanocomposites with frequency at standard room temperature

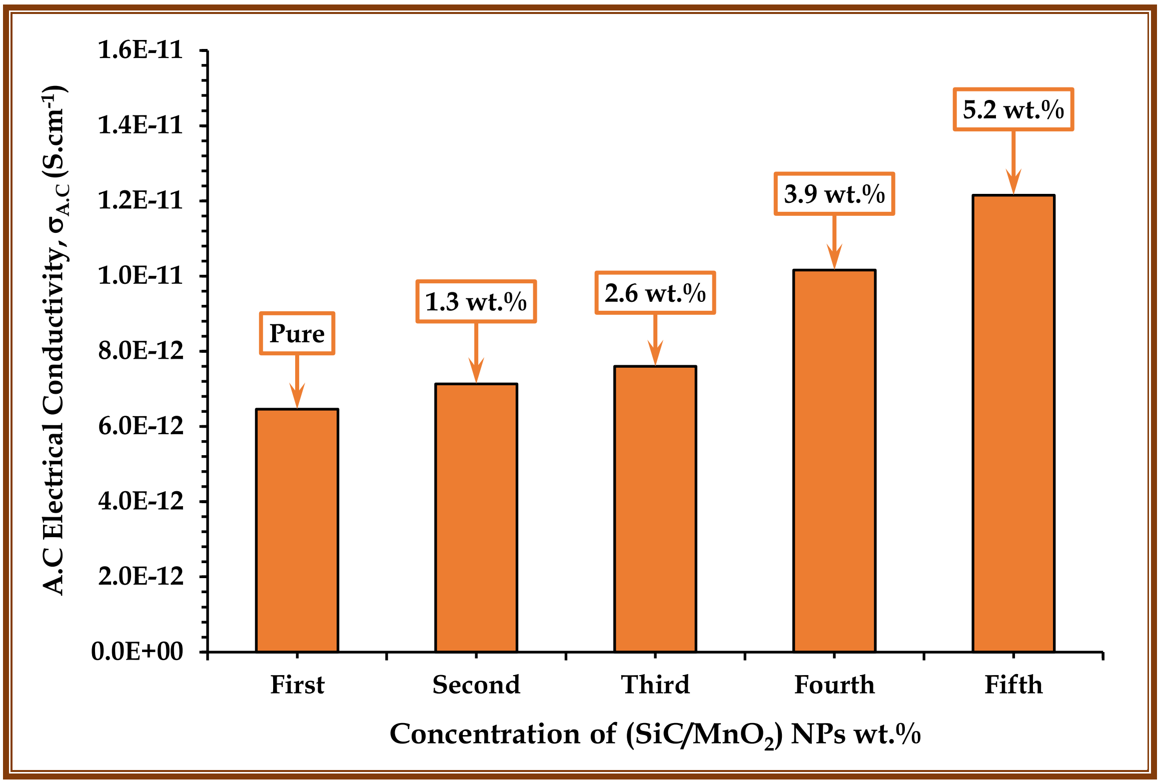

Figure 4.55: Impact of SiC/MnO$_2$ nanoparticles contents on A.C electrical conductivity for (PC-PS/SiC-MnO$_2$) nanocomposites at 100Hz

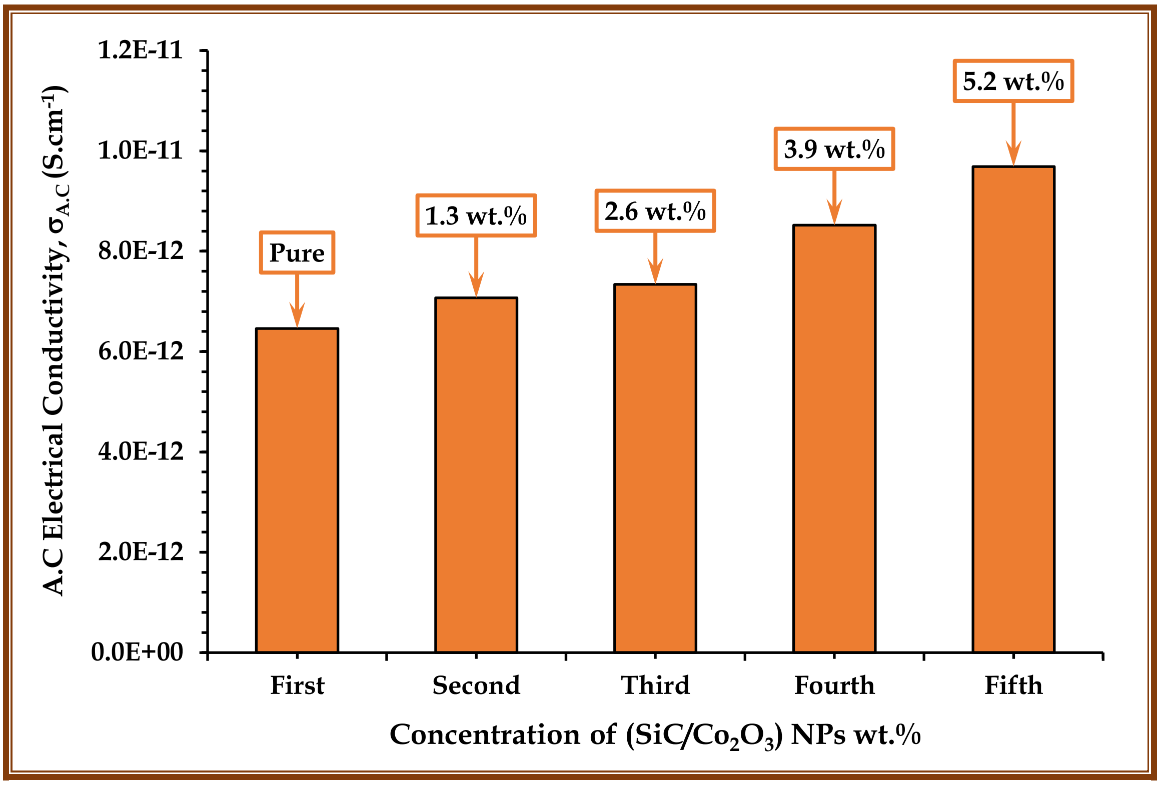

Figure 4.56: Impact of SiC/Co$_2$O$_3$ nanoparticles contents on A.C electrical conductivity for (PC-PS/SiC-Co$_2$O$_3$) nanocomposites at 100 Hz

Table 4.21: Values of A.C electrical conductivity of (PC-PS/SiC-MnO_2) nanocomposites at 100 Hz

Samples	Contents of SiC/MnO_2 nanoparticles	A.C Electrical conductivity ($S.cm^{-1}$)
(PC/PS) blend	Pure	6.46×10^{-12}
(PC-PS/SiC-MnO_2) nanocomposite	1.3 wt.%	7.14×10^{-12}
	2.6 wt.%	7.60×10^{-12}
	3.9 wt.%	10.16×10^{-12}
	5.2 wt.%	12.15×10^{-12}

Table 4.22: Values of A.C electrical conductivity of (PC-PS/SiC-Co_2O_3) nanocomposites at 100 Hz

Samples	Contents of SiC/Co_2O_3 nanoparticles	A.C Electrical conductivity ($S.cm^{-1}$)
(PC/PS) blend	Pure	6.46×10^{-12}
(PC-PS/SiC-Co_2O_3) nanocomposite	1.3 wt.%	7.07×10^{-12}
	2.6 wt.%	7.34×10^{-12}
	3.9 wt.%	8.52×10^{-12}
	5.2 wt.%	9.68×10^{-12}

4.6 Applications of (PC-PS/SiC-MnO_2) and (PC-PS/SiC-Co_2O_3) Bionanocomposites

4.6.1 The application of (PC-PS/SiC-MnO_2), and (PC-PS/SiC-Co_2O_3) bionanocomposites for antibacterial activity

The antibacterial Characteristics of the (PC-PS/SiC-MnO_2), and (PC-PS/SiC-Co_2O_3) nanocomposites were tested against Gram-positive (Staphylococcus aureus) and Gram-negative (Salmonella enterica), and the obtained data are presented in Figure 4.57 and Figure 4.58. As shown in the Figures, the inhibition zone increases with increasing the contents of SiC, MnO_2, and Co_2O_3 nanoparticles.

The results exhibited very high toxicity against Gram-negative bacteria, lower toxicity against Gram-positive bacteria. The presence of SiC, MnO_2, and Co_2O_3 nanoparticles from the (PC-PS/SiC-MnO_2) and (PC-PS/SiC-Co_2O_3) nanocomposites explains the antimicrobial properties found in the prepared nanocomposites. In addition to this, the antimicrobial properties that have been exhibited in our results are similar with [209] who reported that small size nanoparticles may pass through cell membranes generating cell malfunction [210].

The positive charge on the nanoparticles is crucial for its antimicrobial activity through the electrostatic attraction between the negative charge on the cell membrane of microorganism and positively charged nanoparticles [211].

When the attraction is established, the nanoparticles will penetrate the cell membrane and bound with the electron donor functional groups such as phosphates, thiols, and indoles which contain sulfur and phosphorous compounds. All of these compounds are a presence in DNA or ribosomes. Thus the DNA function will be disrupted and the DNA cannot replicate. As a result, the microbial cell will not grow and eventually die [212].

A typical characteristic of any metal nanoparticle is begin able of reducing or removing microorganisms through two essential mechanisms: (**I**) the free metal ion toxicity that arises from dissolving metals from the surface of nanoparticles [213], and (**II**) releasing reactive oxygen species (ROS) and Barium ions [214].

The nanocomposites are carrying the positive charges and the microbes are having the negative charges, which create the electromagnetic attraction between the nanoparticles of nanocomposites and the microbes, will the microbes get oxidized and die instantly [215]. The main mechanism that caused the antibacterial activity of nanocomposites by the nanoparticles, (ROS) includes radicals like super oxide radicals (O^{-2}), hydroxyl radicals (OH) and hydrogen peroxide (H_2O_2); and singlet oxygen $({}_1O^2)$ could be the reason damaging the proteins and DNA of bacteria [216]. The (PC-PS/SiC-$\mathrm{MnO_2}$), and (PC-PS/SiC-$\mathrm{Co_2O_3}$) bionanocomposites have been shown to have the strongest antibacterial activity against Staphylococcus aureus, and Salmonella enterica, which is attributed to the high antibacterial activity of (SiC/$\mathrm{Co_2O_3}$) nanoparticles [217]. Table 4.23, and Table 4.24 display the inhibition zone diameter of (PC-PS/SiC-$\mathrm{MnO_2}$), and (PC-PS/SiC-$\mathrm{Co_2O_3}$) bionanocomposites, Where the inhibition percentages of bacteria were calculated compared to uninhibited samples using equation (2.41) for all samples of the bionanocomposites, and the inhibition percentages were obtained at content (5.2 wt.%) about (26.11% and 55.67%) of Gram-positive (Staphylococcus aureus) and about (48.85% and 59.71%) of Gram-negative (Salmonella enterica), respectively. And as shown in each of Figure 4.63 and Figure 4.64 of Gram-positive (Staphylococcus aureus), and Figure 4.65 and Figure 4.66 of Gram-negative (Salmonella enterica) for all concentrations.

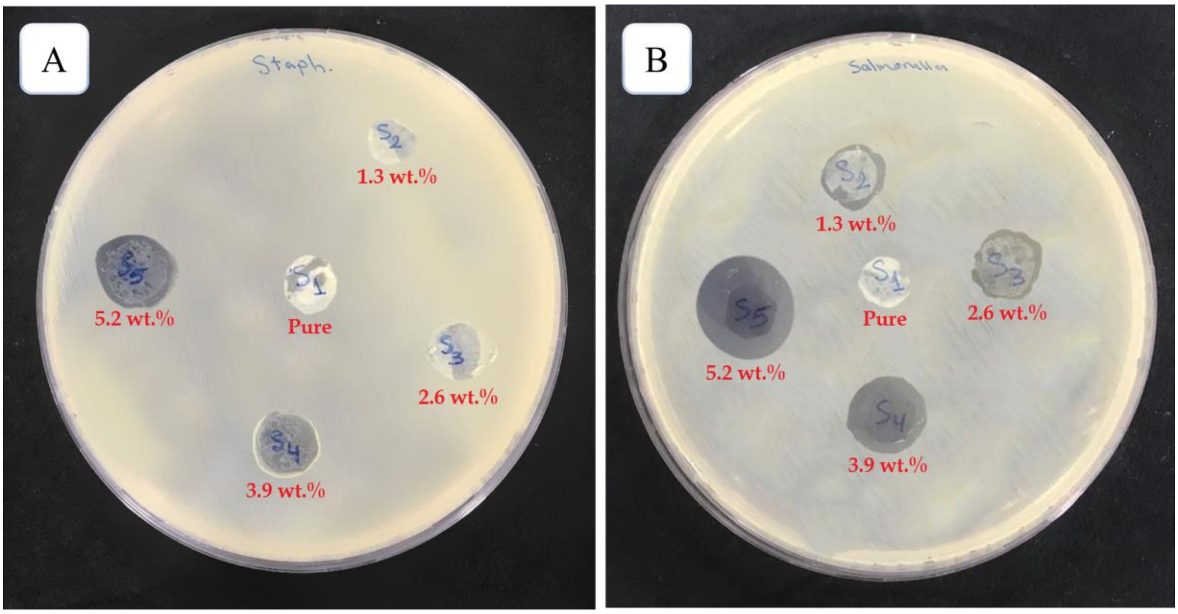

Figure 4.57: Antibacterial activity of (PC-PS/SiC-MnO$_2$) nanocomposite: (A) Images for inhibition zone of Gram-positive bacteria and (B) Images for inhibition zone of Gram-negative bacteria against Staphylococcus aureus and Salmonella enterica.

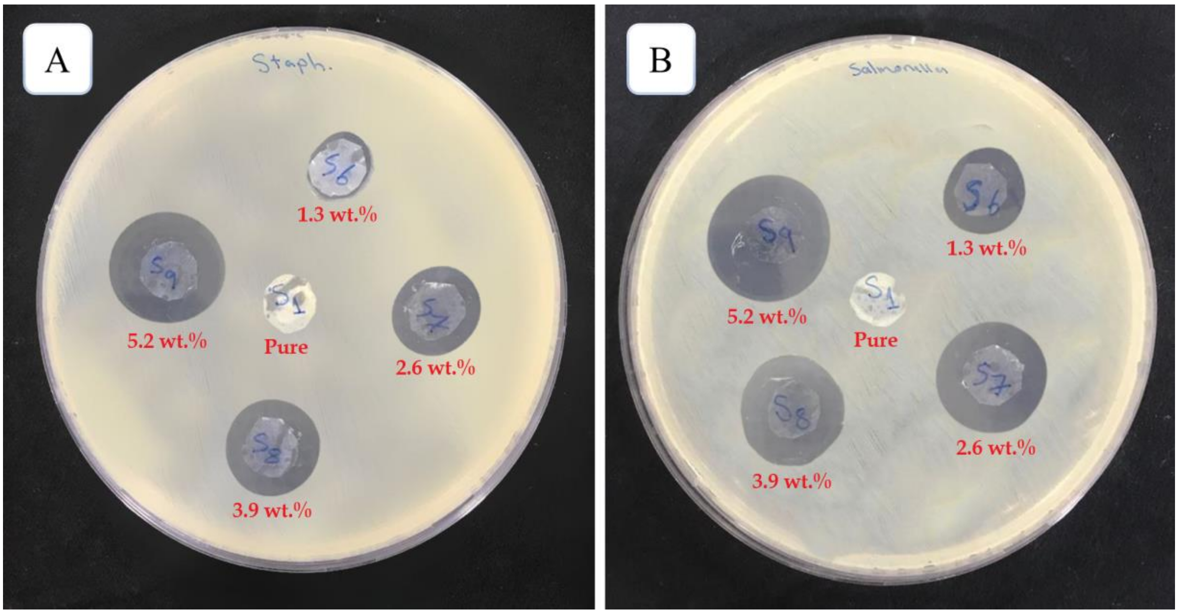

Figure 4.58: Antibacterial activity of (PC-PS/SiC-Co$_2$O$_3$) nanocomposites: (A) Images for inhibition zone of Gram-positive bacteria and (B) Images for inhibition zone of Gram-negative bacteria against Staphylococcus aureus and Salmonella enterica.

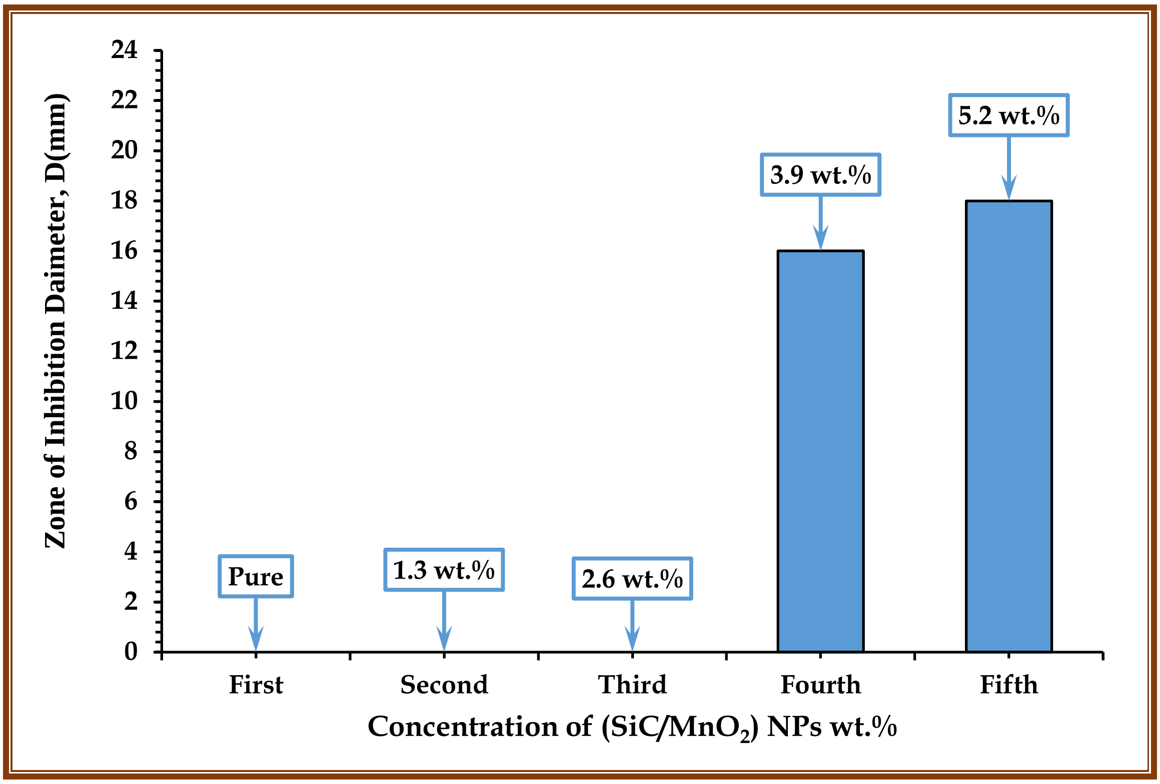

Figure 4.59: Diagram for antibacterial activity of (PC-PS/SiC-MnO$_2$) nanocomposite for inhibition zone of Gram-positive bacteria against Staphylococcus aureus

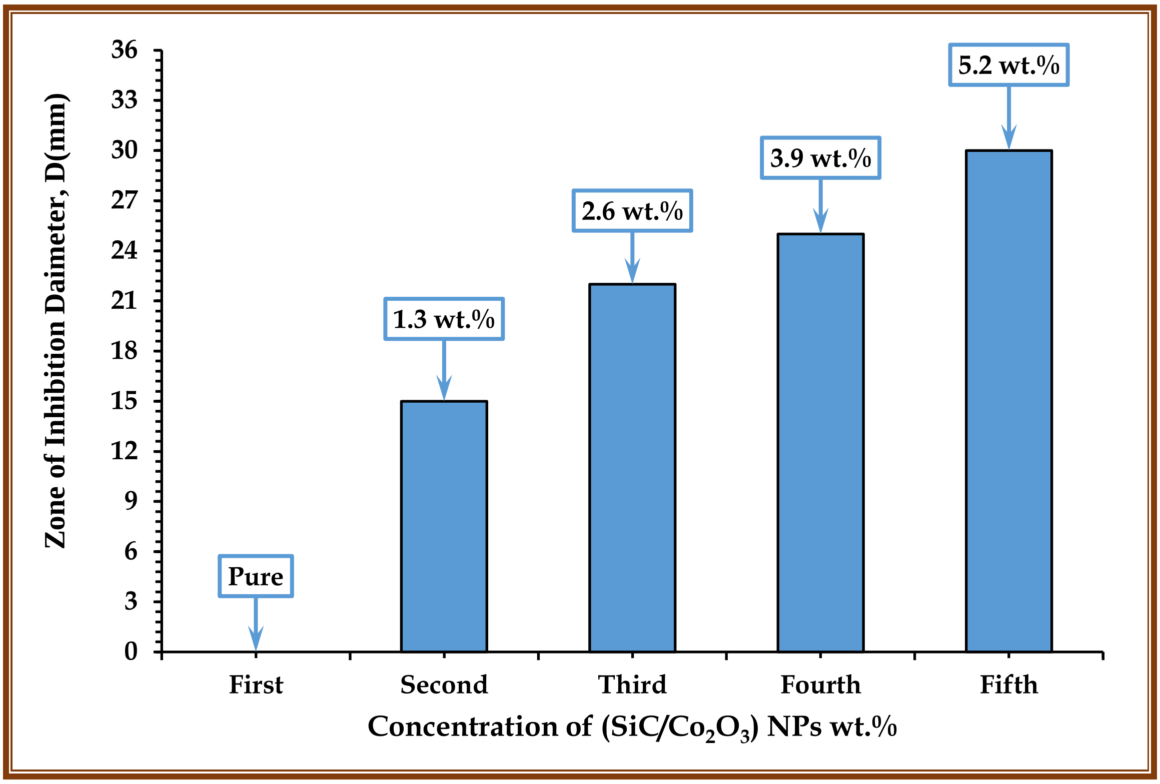

Figure 4.60: Diagram for antibacterial activity of (PC-PS/SiC-Co$_2$O$_3$) nanocomposite for inhibition zone of Gram-positive bacteria against Staphylococcus aureus

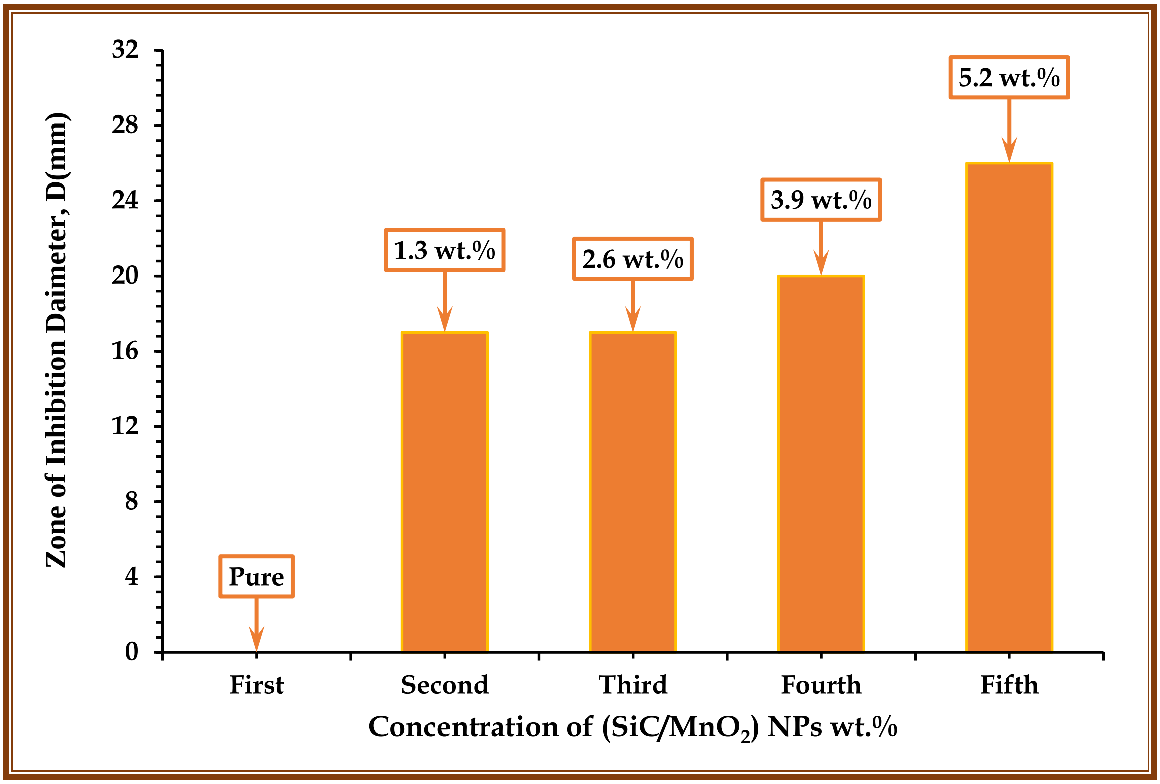

Figure 4.61: Diagram for antibacterial activity of (PC-PS/SiC-MnO$_2$) nanocomposites for inhibition zone of Gram-negative bacteria against Salmonella enterica

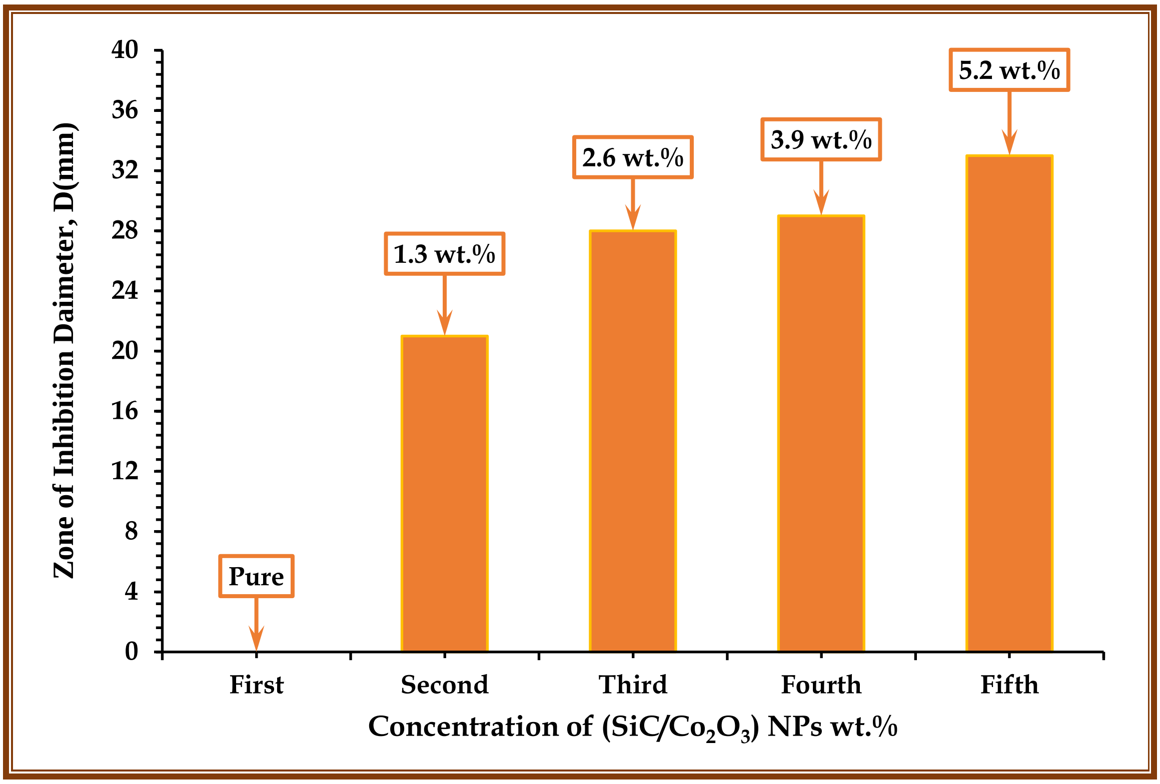

Figure 4.62: Diagram for antibacterial activity of (PC-PS/SiC-Co$_2$O$_3$) for inhibition zone of Gram-negative bacteria against Salmonella enterica

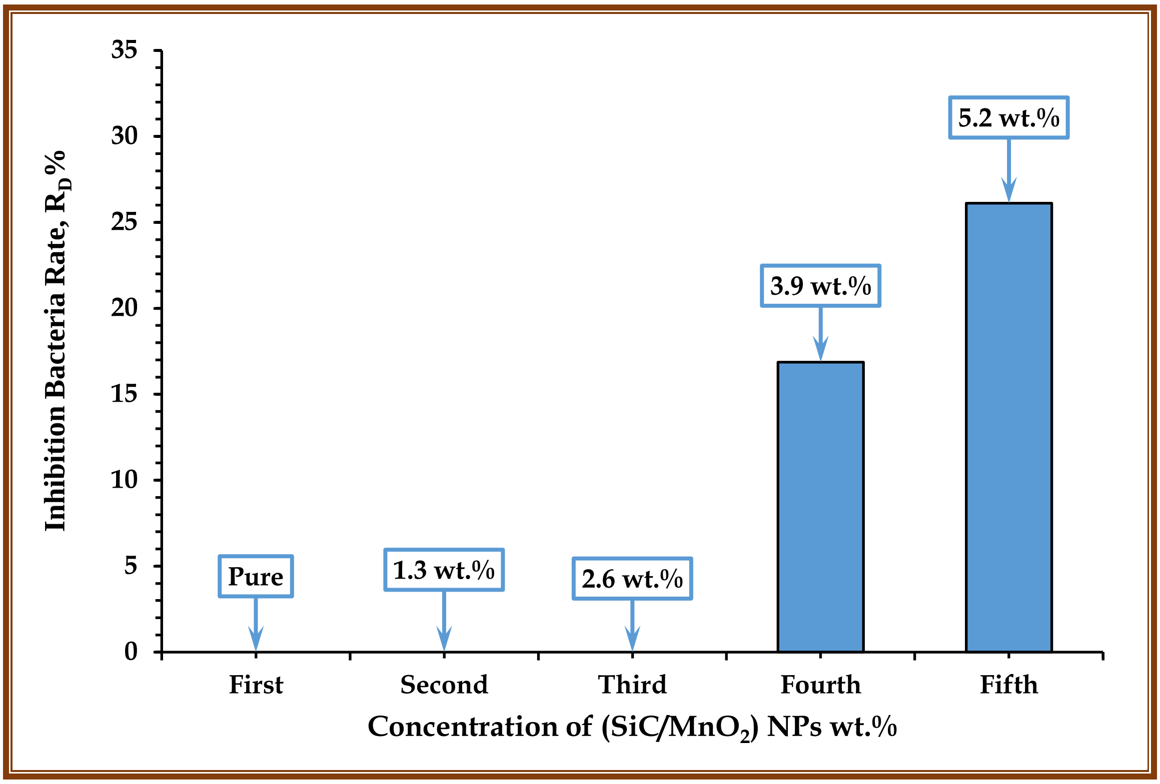

Figure 4.63: Impact of SiC/MnO_2 nanoparticles on inhibition zone rate of Gram-positive bacteria against Staphylococcus aureus

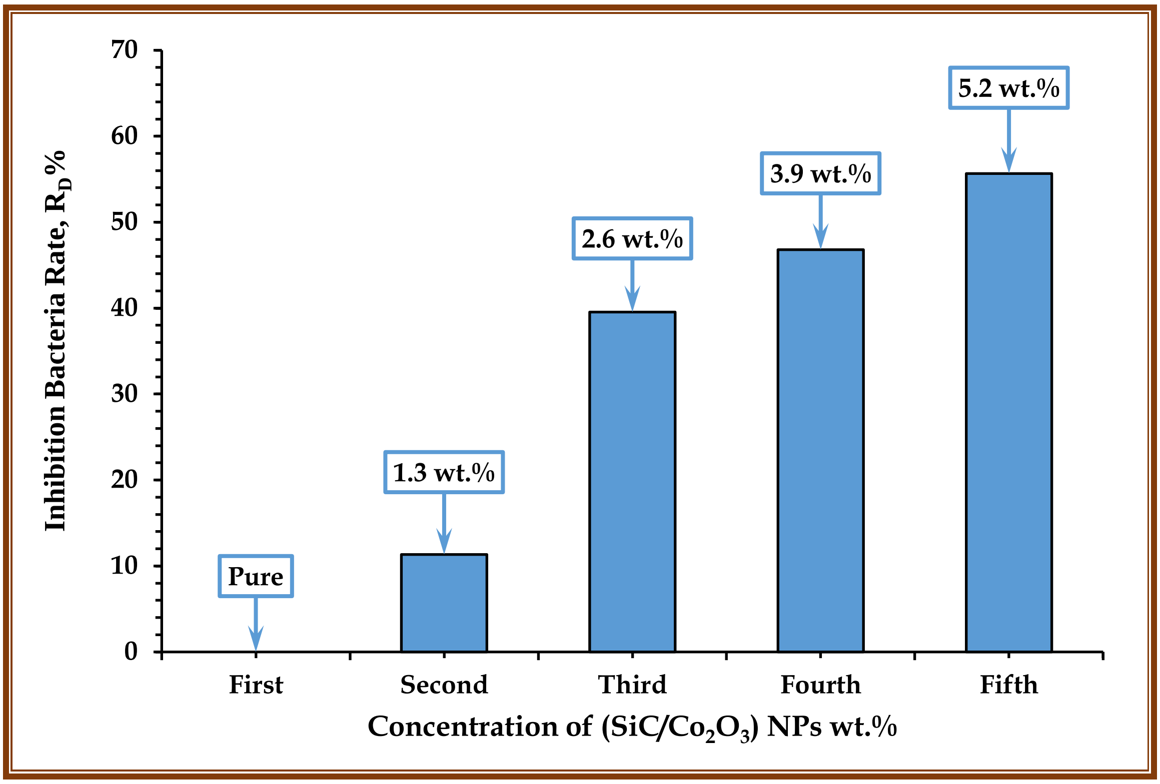

Figure 4.64: Impact of SiC/Co_2O_3 on inhibition zone rate of Gram-positive bacteria against Staphylococcus aureus

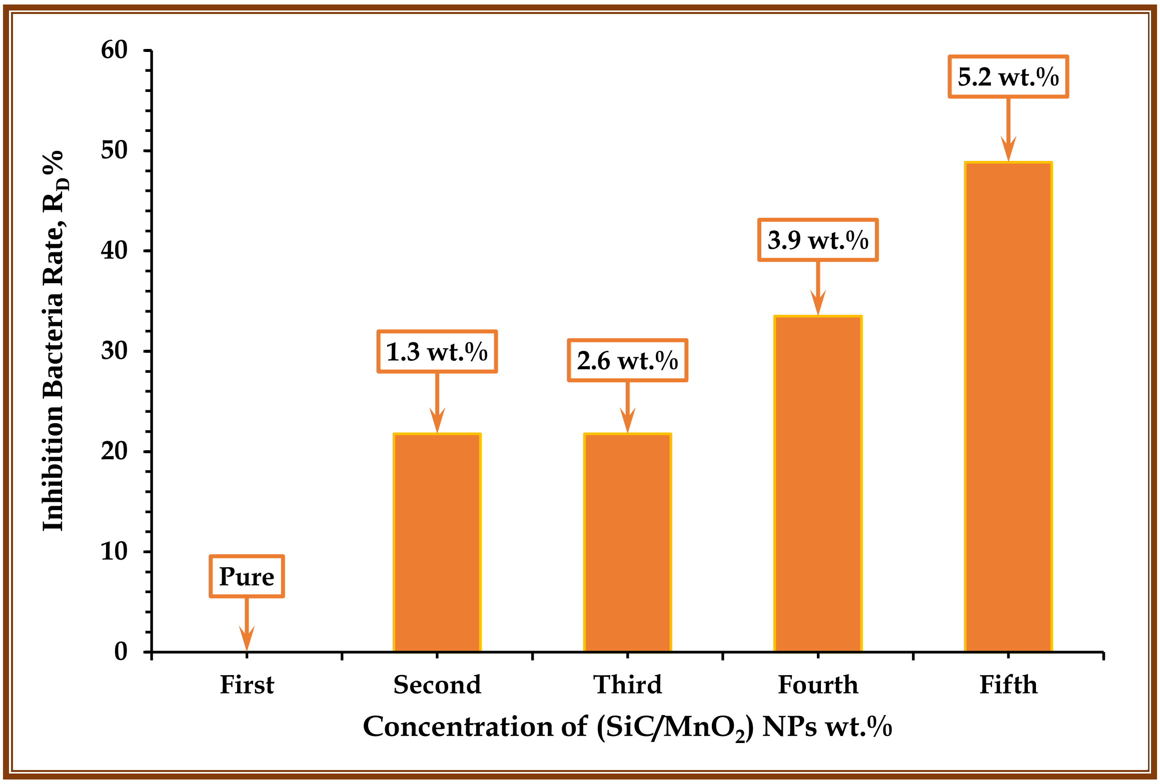

Figure 4.65: Impact of SiC/MnO_2 nanoparticles on inhibition zone rate of Gram-negative bacteria against Salmonella enterica

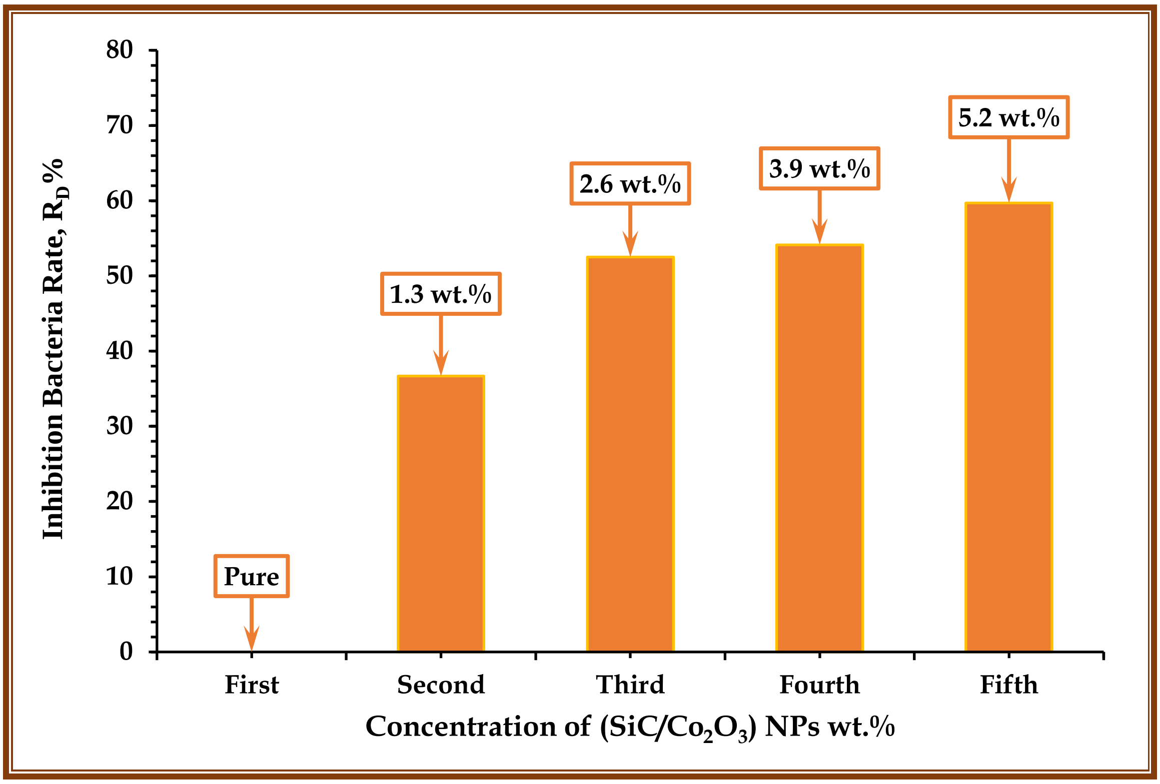

Figure 4.66: Impact of SiC/Co_2O_3 on inhibition zone rate of Gram-negative bacteria against Salmonella enterica

Table 4.23: The values inhibitions zone diameter of (PC/PS) blend and (PS-PC/SiC-MnO_2) nanocomposites

Samples	**Contents of SiC/MnO_2 nanoparticles**	**Gram-Positive (Staphylococcus aureus)**		**Gram-Negative (Salmonella enterica)**	
		D(mm)	**R_D%**	**D(mm)**	**R_D%**
(PC/PS) blend	**Pure**	0	0	0	0
(PC-PS/SiC-MnO_2) nanocomposite	**1.3 wt.%**	0	0	17	21.76
	2.6 wt.%	0	0	17	21.76
	3.9 wt.%	16	16.88	20	33.50
	5.2 wt.%	18	26.11	26	48.85

Table 4.24: The values inhibitions zone diameter of (PC/PS) blend and (PC-PS/SiC-Co_2O_3) nanocomposites

Samples	**Contents of SiC/Co_2O_3 nanoparticles**	**Gram-Positive (Staphylococcus aureus)**		**Gram-Negative (Salmonella enterica)**	
		D(mm)	**R_D%**	**D(mm)**	**R_D%**
(PC/PS) blend	**Pure**	0	0	0	0
(PC-PS/SiC-Co_2O_3) nanocomposite	**1.3 wt.%**	15	11.33	21	36.67
	2.6 wt.%	22	39.55	28	52.50
	3.9 wt.%	25	46.80	29	54.14

	5.2 wt.%	30	55.67	33	59.70

4.6.2 Application of (PC-PS/SiC-MnO_2), and (PC-PS/SiC-Co_2O_3) bionanocomposites for photodegradation activity

Photocatalytic activity of the prepared samples for (PC/PS) polymeric blend, (PC-PS/SiC-MnO_2) and (PC-PS/SiC-Co_2O_3) nanocomposites was studied by measuring the photodegradation percentage of methylene orange (MO) dye as a pollutant model according to the procedure described in the section (2.6.2). The absorbance of MO dye is taken as a measure for its degradation. display the behavior of MO dye photodegradation for (PC/PS) polymeric blend, (PC-PS/SiC-MnO_2) and (PC-PS/SiC-Co_2O_3) nanocomposites at wavelength ranging from $200\,nm$ to $600\,nm$, respectively. The Figures showed that the degradation of MO dye increases with increasing the percentages of nanoparticles.

Time-dependent absorbance spectrum behavior of MO dye solution for (PC/PS) polymeric blend, (PC-PS/SiC-MnO_2) and (PC-PS/SiC-Co_2O_3) nanocomposites at $\lambda_{max} = 460\,nm$ are shown from Figure 4.67 to Figure 4.86 respectively. The Figures display that the absorbance of MO dye decreases with increasing the time of the irradiation. From the obtained results, we note that the photodegradation of methyl orange molecules reduced the absorbance at $\lambda_{max} = 460\,nm$ by 2.65% during 30 min. and by 5.44% during 90 min. The results display that the (PC/PS) polymeric blend reduces the absorbance of the dye to 8.08% within 30 min and 16.14% within 90 min, the (PC-PS/SiC-MnO_2) with 1.3 wt.% content of SiC/MnO_2 nanoparticles reduces the absorbance of the dye to 7.97% within 30 min and to 17.82% within 90 min, the (PC-PS/SiC-MnO_2) nanocomposites reduces the absorbance of the dye to 10.32% within 30 min and to 28.36% within 90 min for 2.6 wt.% content of SiC/MnO_2 nanoparticles, the reduce in the absorbance of the MO dye about 11.61% within 30 min and 33.51% within 90 min with content of 5.2 wt.% of MnO_2 nanoparticle for (PC-PS/SiC-Co_2O_3) nanocomposites, and the (PC-PS/SiC-MnO_2) nanocomposites reduces the absorbance of the dye to 13.98% within 30 min and 54.05% within 90 min for 5.2 wt.% content of SiC/MnO_2 nanoparticles.

In comparison, the (PC-PS/SiC-Co_2O_3) nanocomposites has a higher photocatalytic activity with 1.3 wt.% content of SiC/Co_2O_3 nanoparticles reduces the absorbance of the dye to 7.41% within 30 min and 19.97% within 90 min, the (PC-PS/SiC-Co_2O_3) nanocomposites with content of 2.6 wt.% of SiC/Co_2O_3 nanoparticles decreases the absorbance of the dye to 13.23% within 30 min and 32.53% within 90 min, the reduce in the absorbance of the MO dye about 19.70% within 30 min and 45.35% within 90 min with content of 3.9 wt.% of MnO_2 nanoparticle for (PC-PS/SiC-Co_2O_3) nanocomposites, and the reduce in the absorbance of the MO dye about 27.94% within 30 min and 73.26% within 90 min with content of 5.2 wt.% of MnO_2 nanoparticle for (PC-PS/SiC-Co_2O_3) nanocomposites. The difference in photocatalytic activities of nanocomposites is related to their band gap.

The MO dye degradation percentage ($D_{MO}\%$) of nanocomposites can be calculated by equation (2.51). The influence of UV irradiation time on degradation percentage of MO dye for (PC/PS) polymeric blend, (PC-PS/SiC-MnO_2) and (PC-PS/SiC-Co_2O_3) nanocomposites at $\lambda_{max} = 460\ nm$ are shown from Figure 4.89 to Figure 4.96, respectively. From the Figures, it's clear that the photodegradation percentage increases with increasing the time of the irradiation as shown in Table 4.25, and Table 4.26. The behavior photodegradation percentage with the time of the irradiation is due to an increase in the electron–hole pairs and a decrease in the recombination of these pairs, which leads to an increase in the decomposition percentages and thus an increase in the photocatalytic activity [218]. The sample of (PC-PS/SiC-Co_2O_3) nanocomposites with 5.2 wt.% content of SiC/Co_2O_3 nanoparticles are considered as the optimized sample, show more absorbance decay than that of the other samples. This result indicates that the presence of the photocatalyst increased the efficiency of hydrogen peroxide decomposition, and consequently the MO dye degradation.

To describe the kinetic mechanism of the photodegradation of methyl orange molecules induced by UV-Irradiation in the absence and presence of catalysts, for each of (PC/PS) polymeric blend, (PC-PS/SiC-MnO_2) and (PC-PS/SiC-Co_2O_3) nanocomposites. The reaction rate is proportional to initial absorbance when the reaction is first-order kinetics [152, 219]. Figure 4.97, and Figure 4.98 shows the linear relationship between ln (A_t/A_0) and UV-Irradiation time. The results indicate that the photodegradation of methyl orange dye follows first-order kinetics. The rate constant (κ_d) values, which calculated by using equation (2.52) increase into 0.0088 min $^{-1}$ for the (5.2 wt.%) content of (PC-PS/SiC-MnO_2) nanocomposites and into 0.0145 min $^{-1}$ for the (5.2 wt.%) content of (PC-PS/SiC-Co_2O_3) nanocomposites.

The half-life time $(\tau_{1/2})$ was obtained for first-order kinetics using equation (2.53). It is inferred that the rate constant decreases with different dosages. The half-life time $(\tau_{1/2})$ values decrease about 78.19% for the (5.2 wt.%) content of (PC-PS/SiC-MnO_2) NCs and from 86.77% min for the (5.2 wt.%) content of (PC-PS/SiC-Co_2O_3) NCs. The higher rate constant and lower half-life time for all dosages confirm that the prepared contents blend and NCs are effective catalysts. The calculated rate regular, half-life time and linear regression coefficient (coefficient of determination) (R^2) (COD) are given in Table 4.27, and Table 4.28. The (R^2) for the fitted lines was calculated to be between 0.9739 (dye), 0.9758 (blend) and 0.9899 (1.3 t.%) 0.9984 (2.6 t.%) 0.9791 (3.9 wt.%) 0.9758 (5.2 wt.%) of (PC-PS/SiC-MnO_2) NCs and 0.9851 (1.3 t.%) 0.9973 (2.6 t.%) 0.9985 (3.9 wt.%) 0.9830 (5.2 wt.%) of (PC-PS/SiC-Co_2O_3) NCs, respectively indicating that the photocatalytic degradation of methyl orange can be described by a first-order kinetic model. This will enable the separation of electron–hole pairs created by UV-irradiation. Thus, the recombination of electron–hole pairs in (SiC/MnO_2, and SiC/Co_2O_3) NPs were prevented, and photocatalytic activity is increased [220].

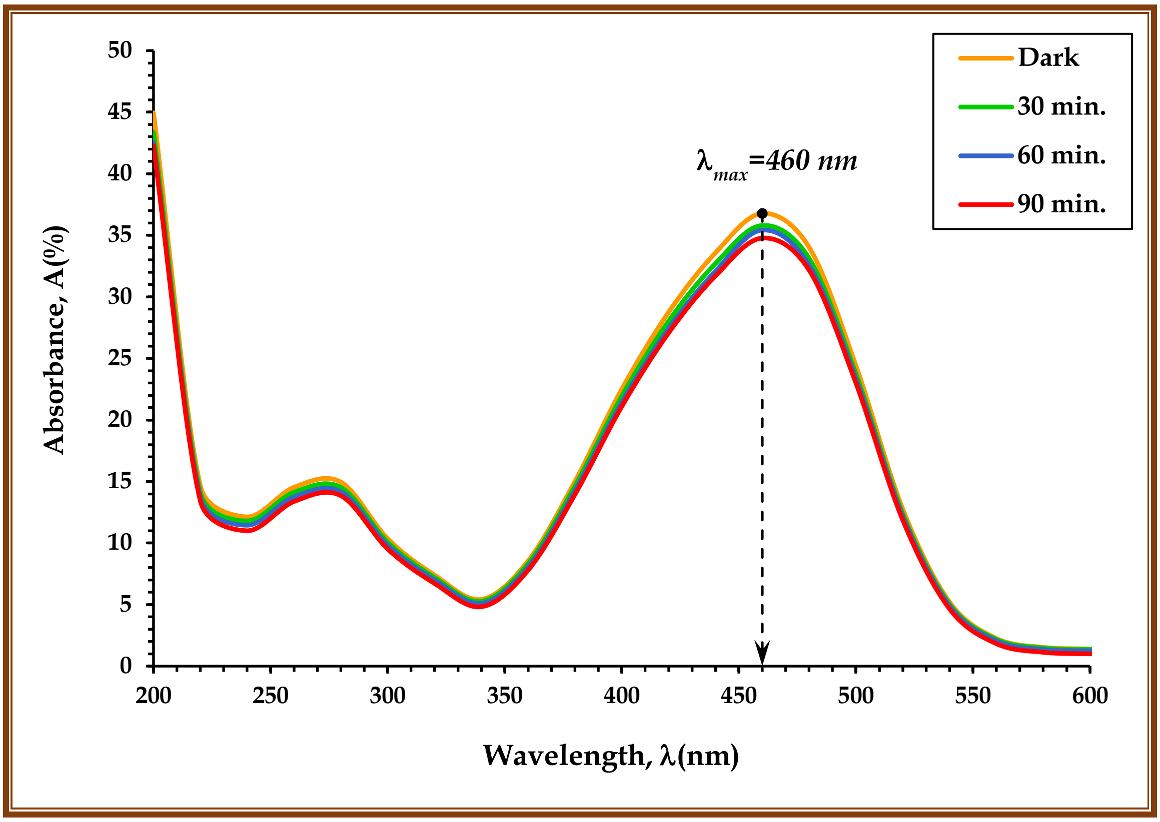

Figure 4.67: Time-dependent absorbance spectrum behavior of MO dye solution illuminated by UV-radiation for MO dye molecules with wavelength

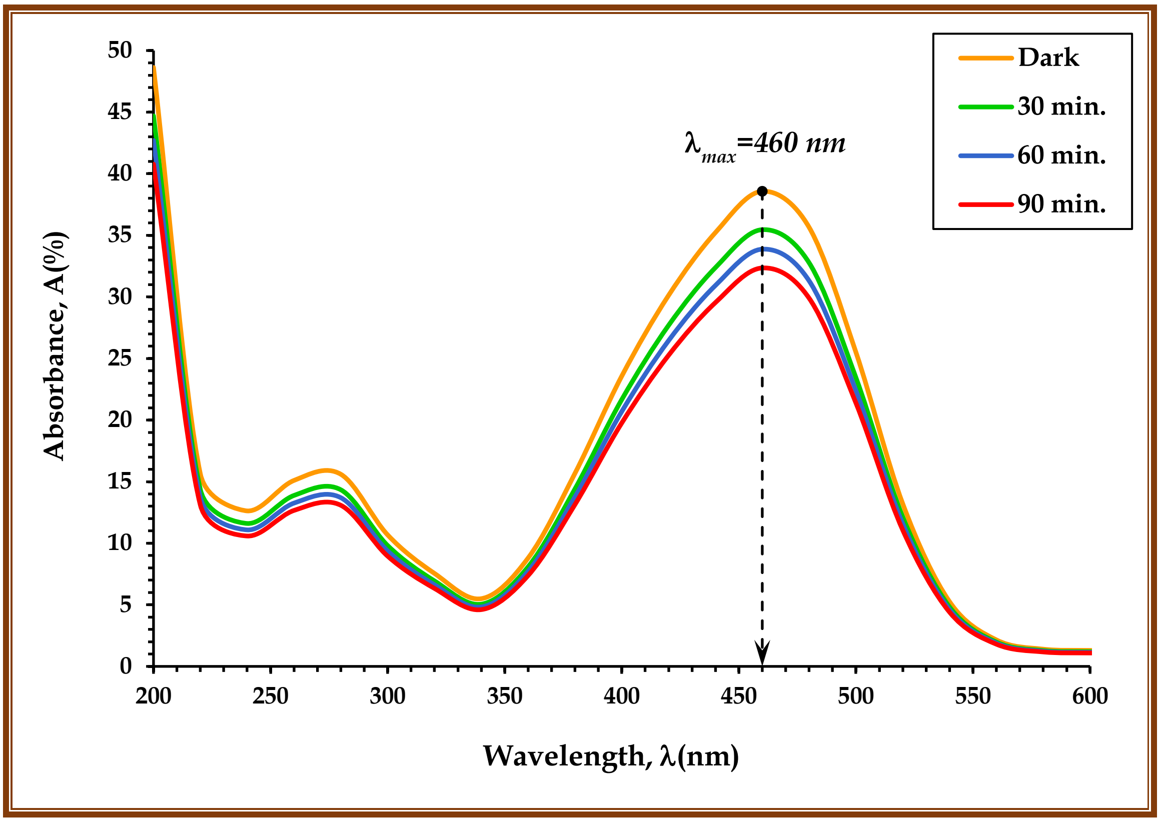

Figure 4.68: Time-dependent absorbance spectrum behavior of MO dye solution illuminated by UV-radiation for Pure (PC/PS) blend with wavelength

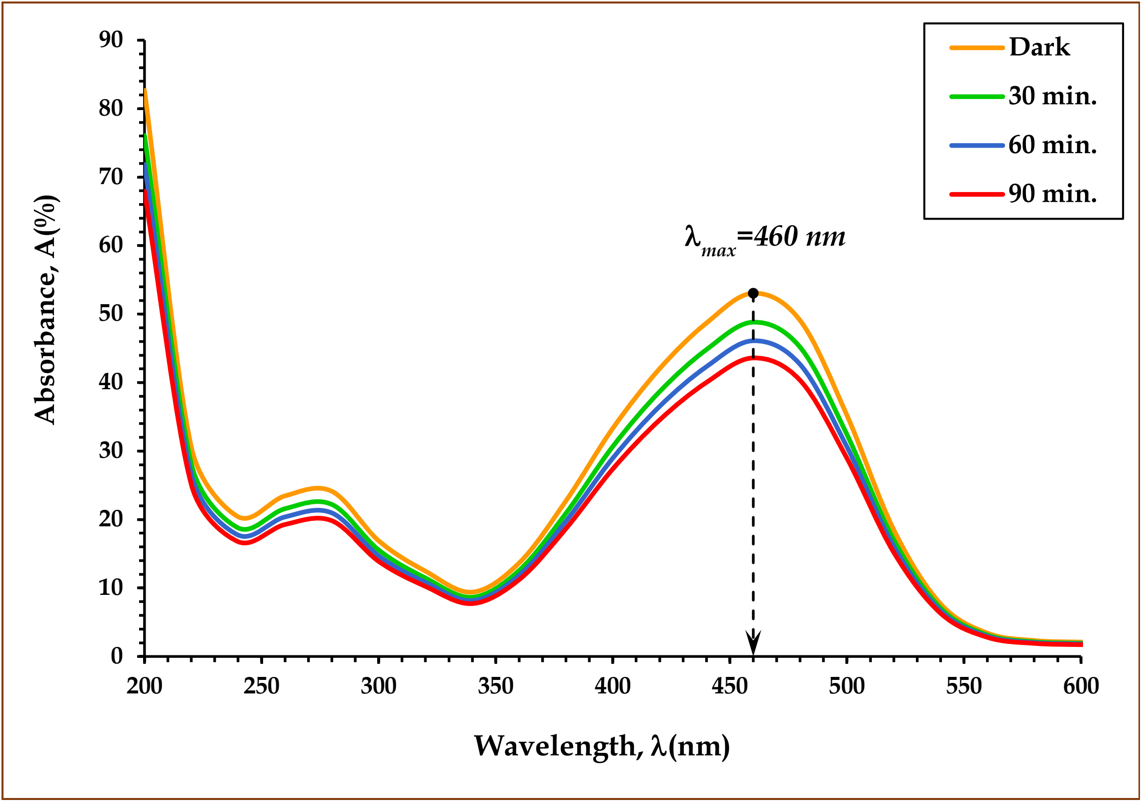

Figure 4.69: Time-dependent absorbance spectrum behavior of MO dye solution illuminated by UV-radiation for 1.3 wt.% content of SiC/MnO_2 NPs with wavelength

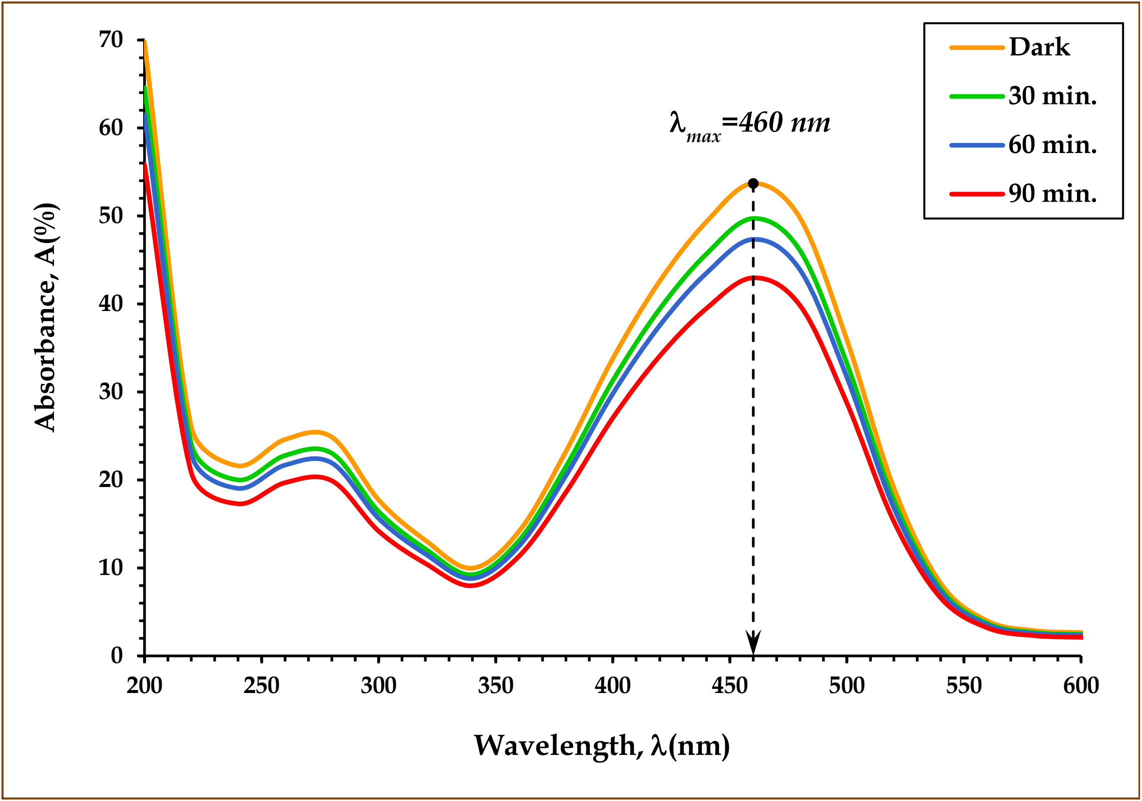

Figure 4.70: Time-dependent absorbance spectrum behavior of MO dye solution illuminated by UV-radiation for 1.3 wt.% content of SiC/Co_2O_3 NPs with wavelength

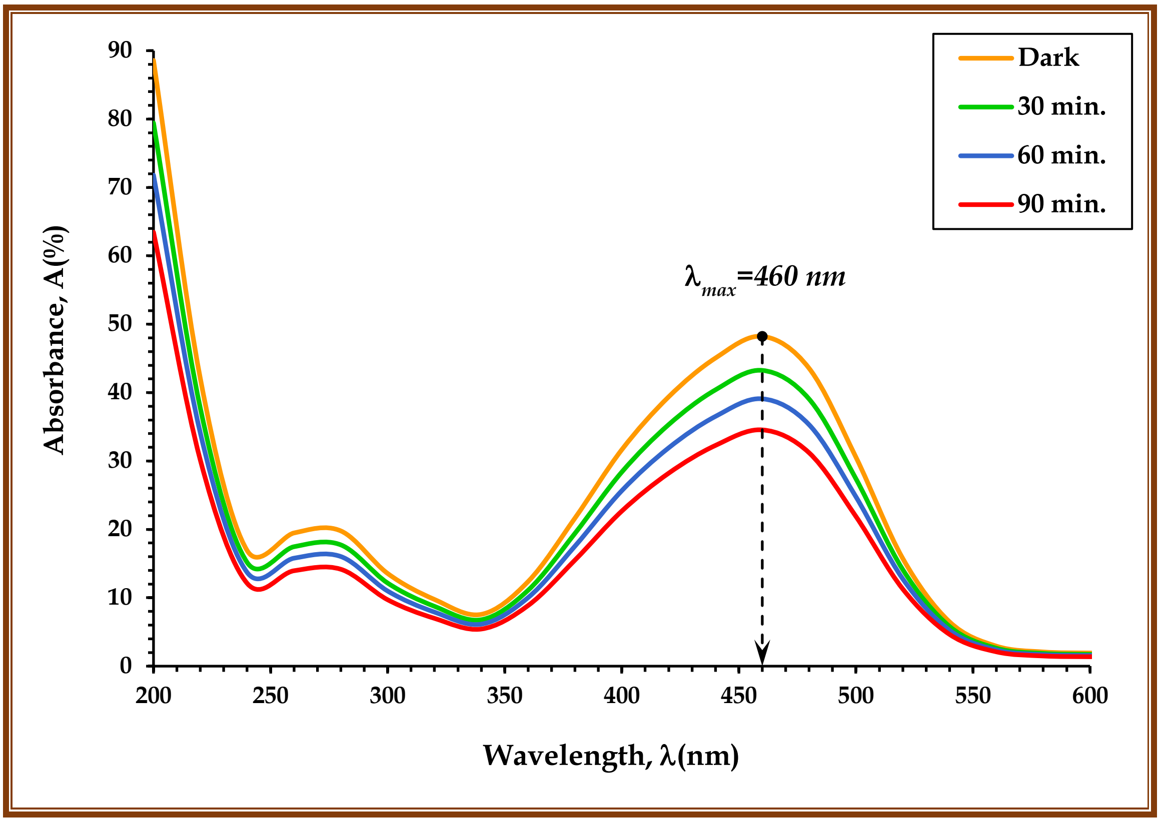

Figure 4.71: Time-dependent absorbance spectrum behavior of MO dye solution illuminated by UV-radiation for 2.6 wt.% content of SiC/MnO₂ NPs with wavelength

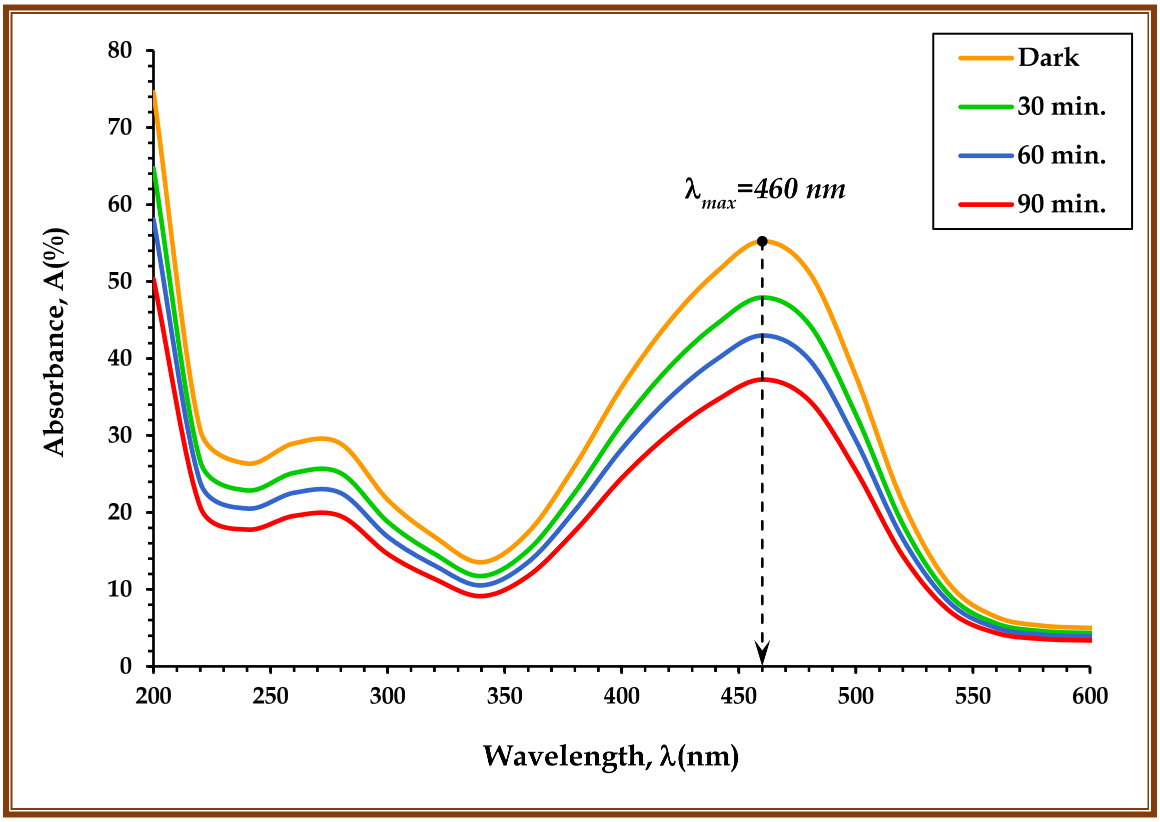

Figure 4.72: Time-dependent absorbance spectrum behavior of MO dye solution illuminated by UV-radiation for 2.6 wt.% content of SiC/Co₂O₃ NPs with wavelength

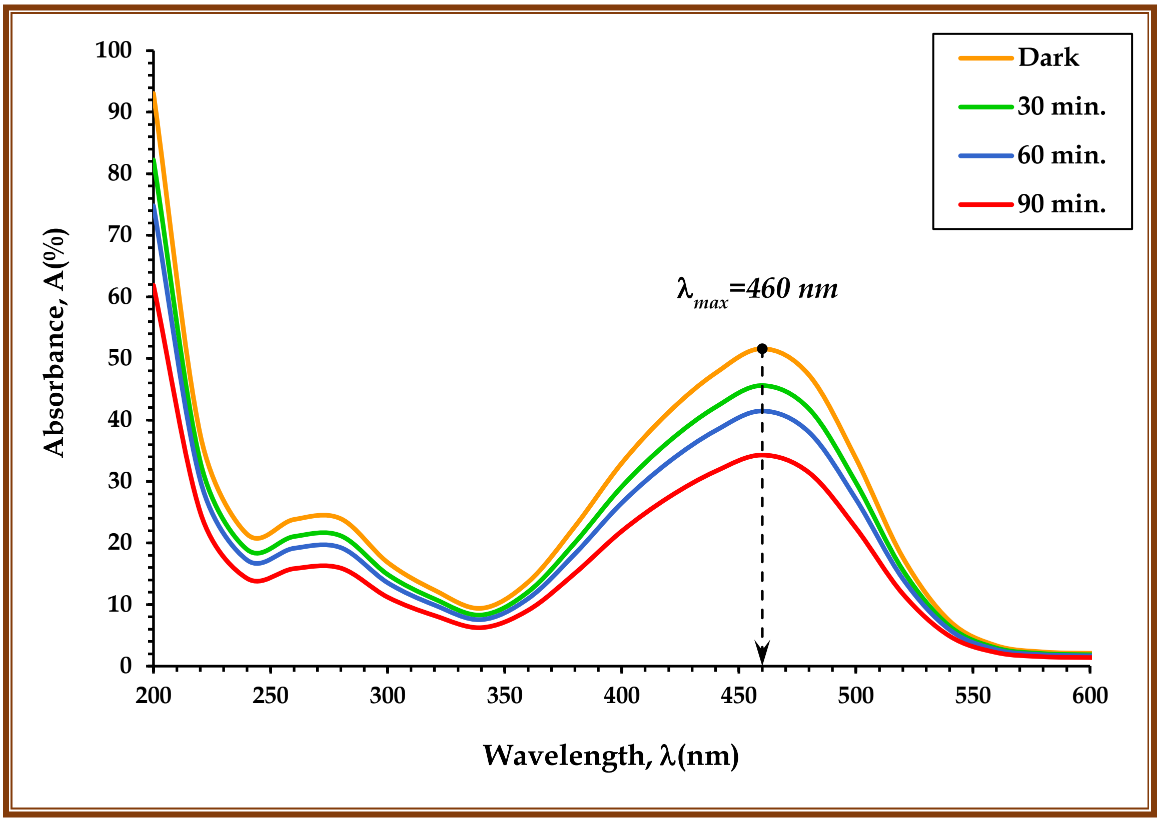

Figure 4.73: Time-dependent absorbance spectrum behavior of MO dye solution illuminated by UV-radiation for 3.9 wt.% content of SiC/MnO_2 NPs with wavelength

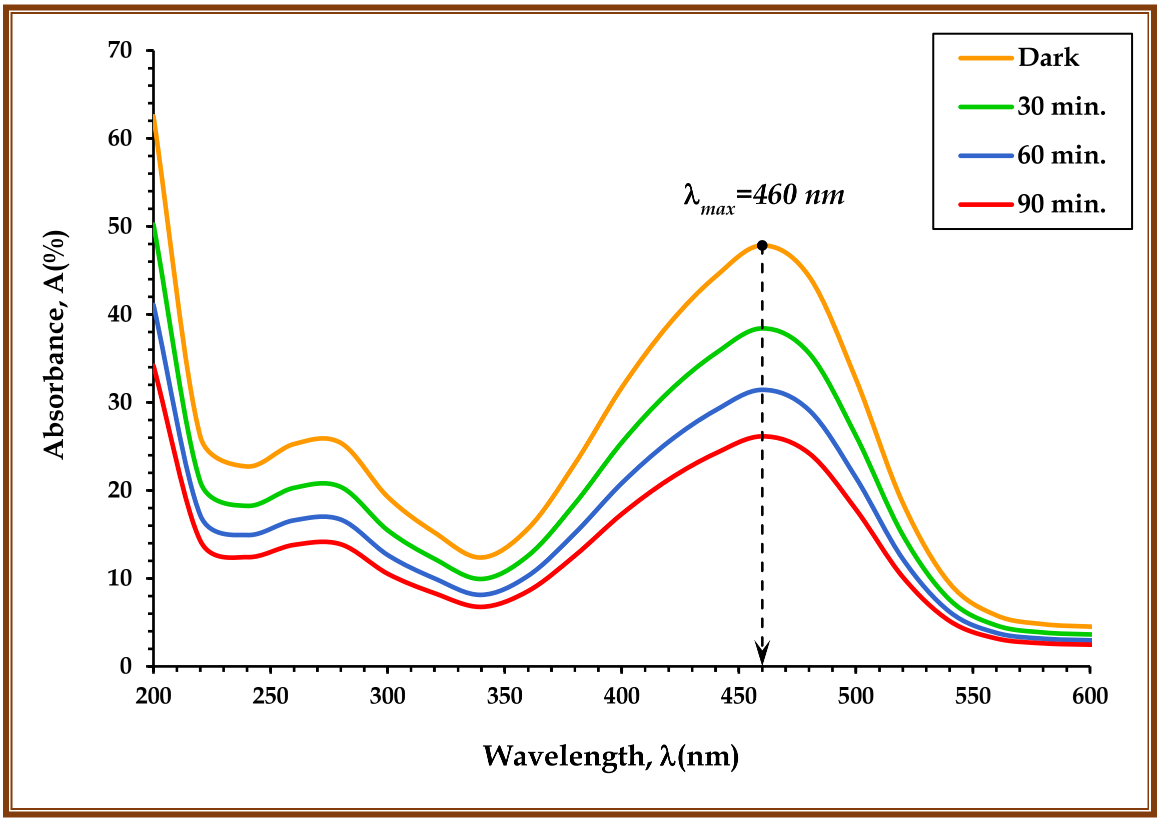

Figure 4.74: Time-dependent absorbance spectrum behavior of MO dye solution illuminated by UV-radiation for 3.9 wt.% content of SiC/Co_2O_3 NPs with wavelength

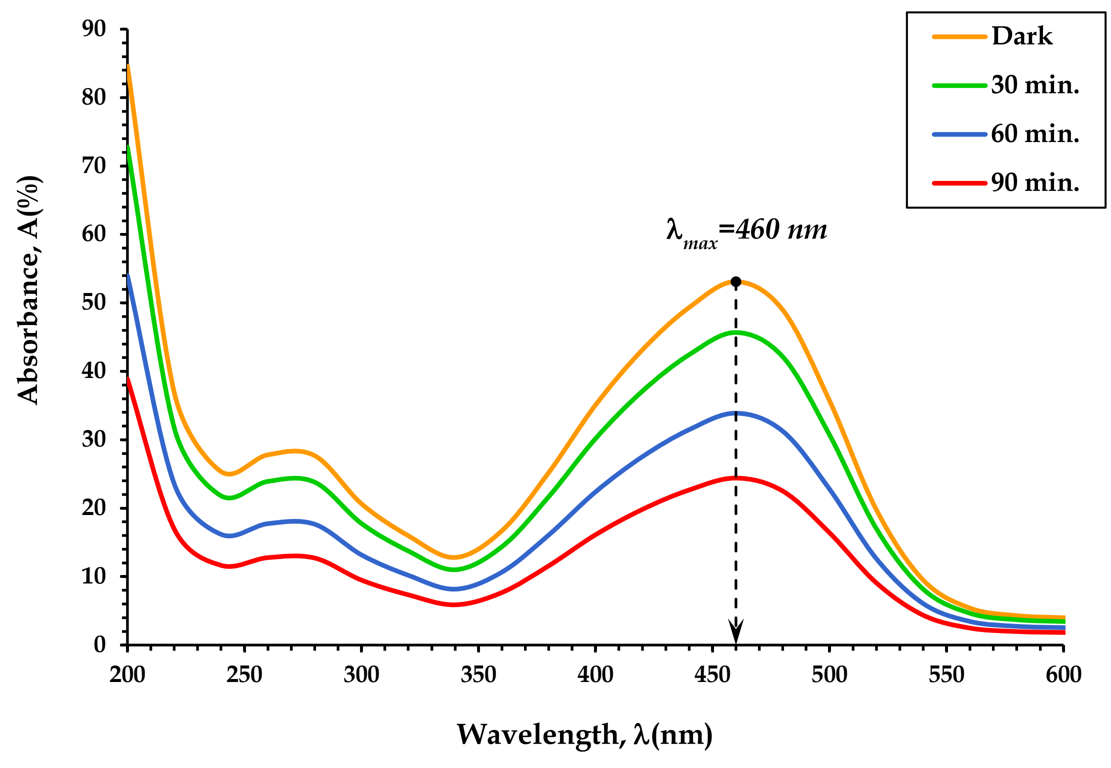

Figure 4.75: Time-dependent absorbance spectrum behavior of MO dye solution illuminated by UV-radiation for 5.2 wt.% content of SiC/MnO_2 NPs with wavelength

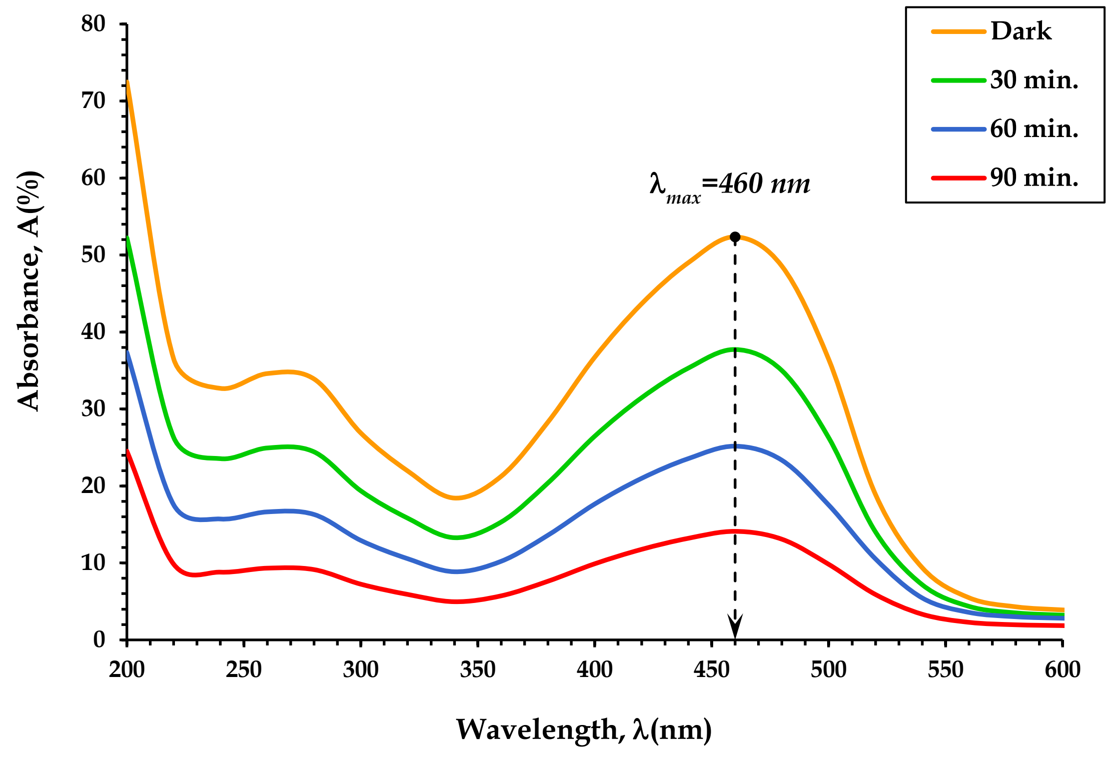

Figure 4.76: Time-dependent absorbance spectrum behavior of MO dye solution illuminated by UV-radiation for 5.2 wt.% content of SiC/Co_2O_3 NPs with wavelength

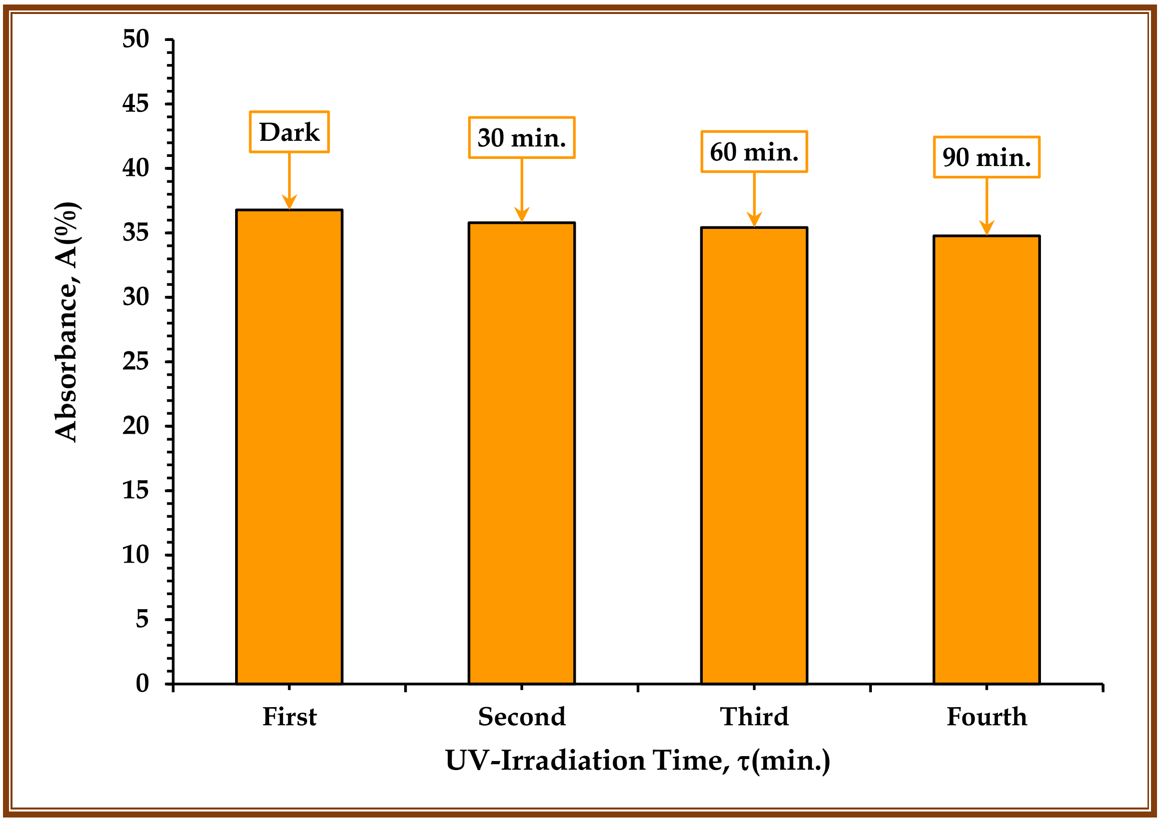

Figure 4.77: Photodegradation performance for MO dye with UV-irradiation time at λ_{max}=460 nm

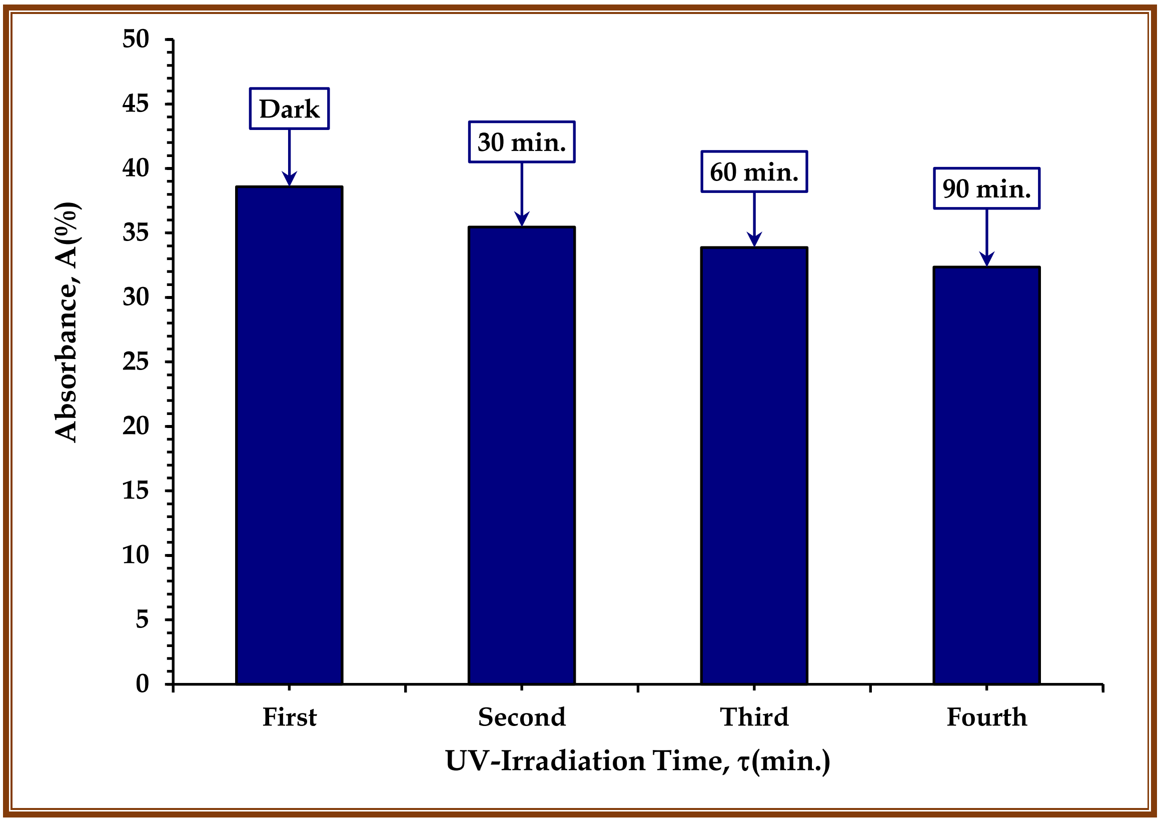

Figure 4.78: Photodegradation performance for (PC/PS) polymeric blend with UV-irradiation time at λ_{max}=460 nm

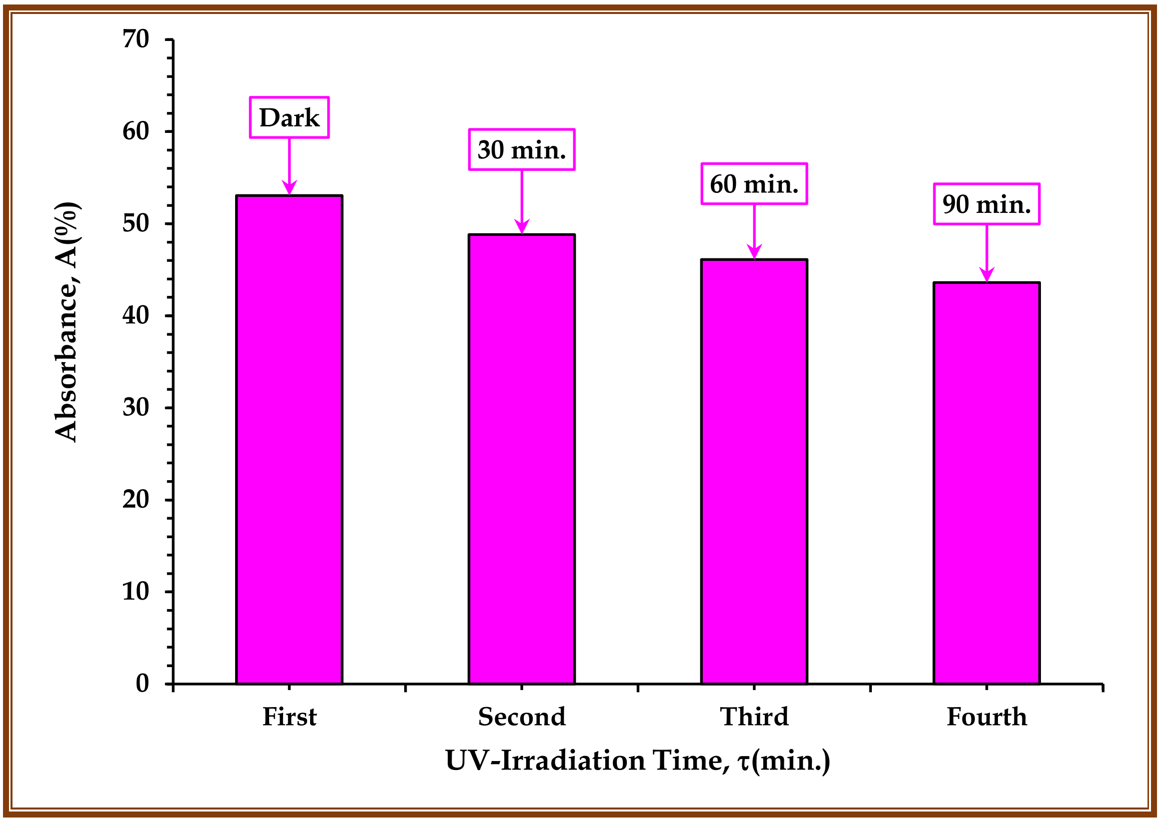

Figure 4.79: Photodegradation performance for (PC-PS/SiC-MnO_2) NCs against MO dye with UV-irradiation time of 1.3 wt.% content of SiC/MnO_2 NPs at λ_{max}=460 nm

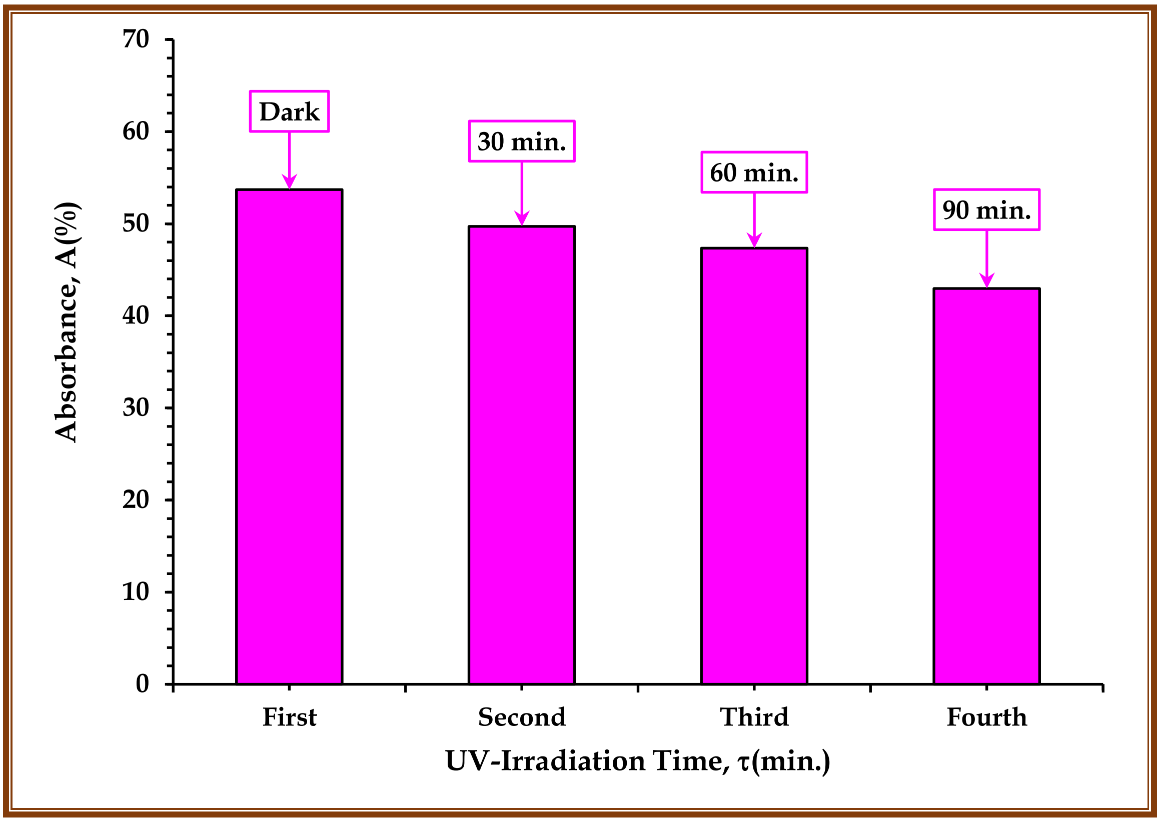

Figure 4.80: Photodegradation performance for (PC-PS/SiC-Co_2O_3) NCs against MO dye with UV-irradiation time for 1.3 wt.% content of SiC/Co_2O_3 NPs at λ_{max}=460 nm

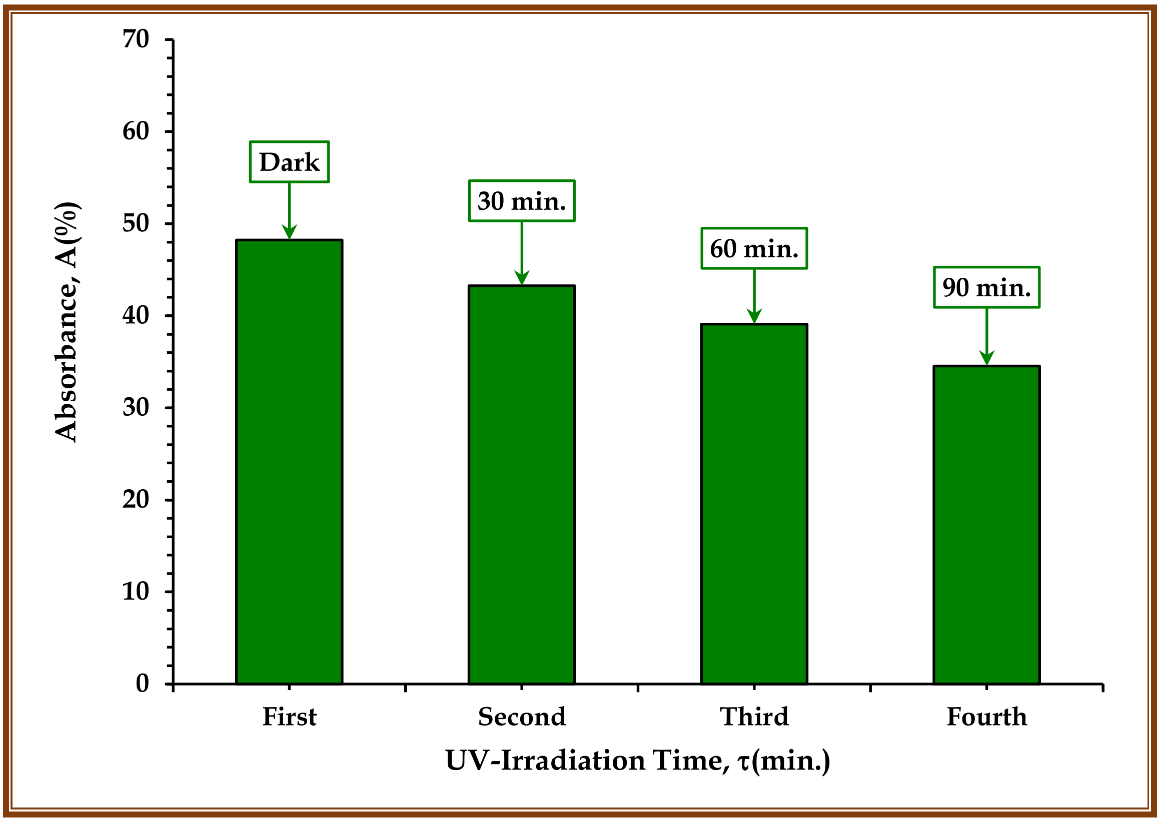

Figure 4.81: Photodegradation performance for (PC-PS/SiC-MnO_2) NCs against MO dye with UV-irradiation time for 2.6 wt.% content of SiC/MnO_2 NPs at λ_{max}=460 nm

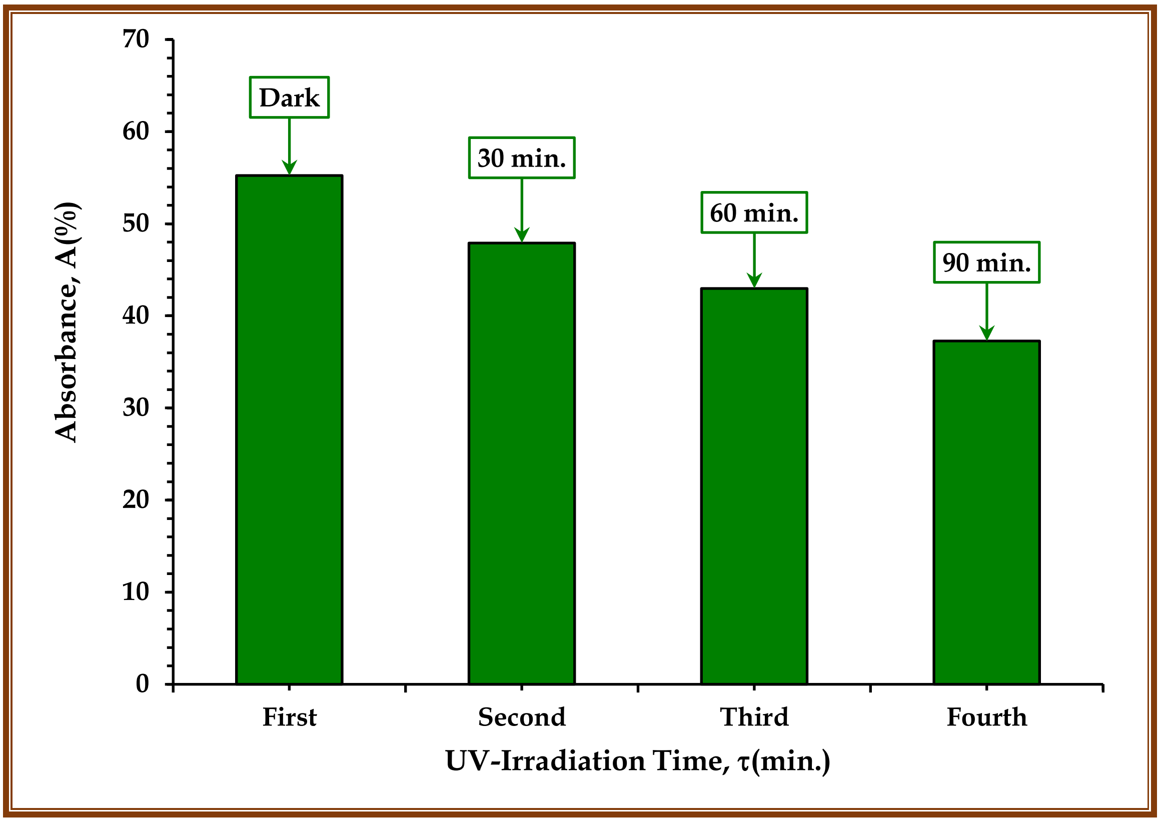

Figure 4.82: Photodegradation performance for (PC-PS/SiC-Co_2O_3) NCs against MO dye with UV-irradiation time for 2.6 wt.% content of SiC/Co_2O_3 NPs at λ_{max}=460 nm

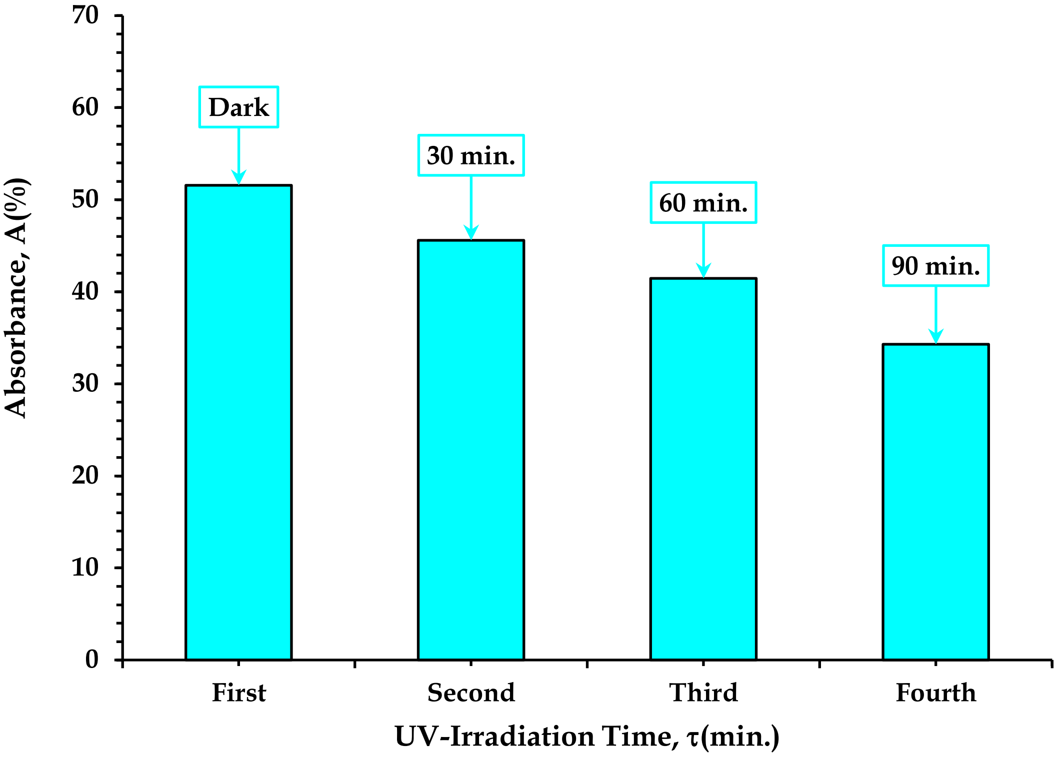

Figure 4.83: Photodegradation performance for (PC-PS/SiC-MnO_2) NCs against MO dye with UV-irradiation time for 3.9 wt.% content of SiC/MnO_2 NPs at λ_{max}=460 nm

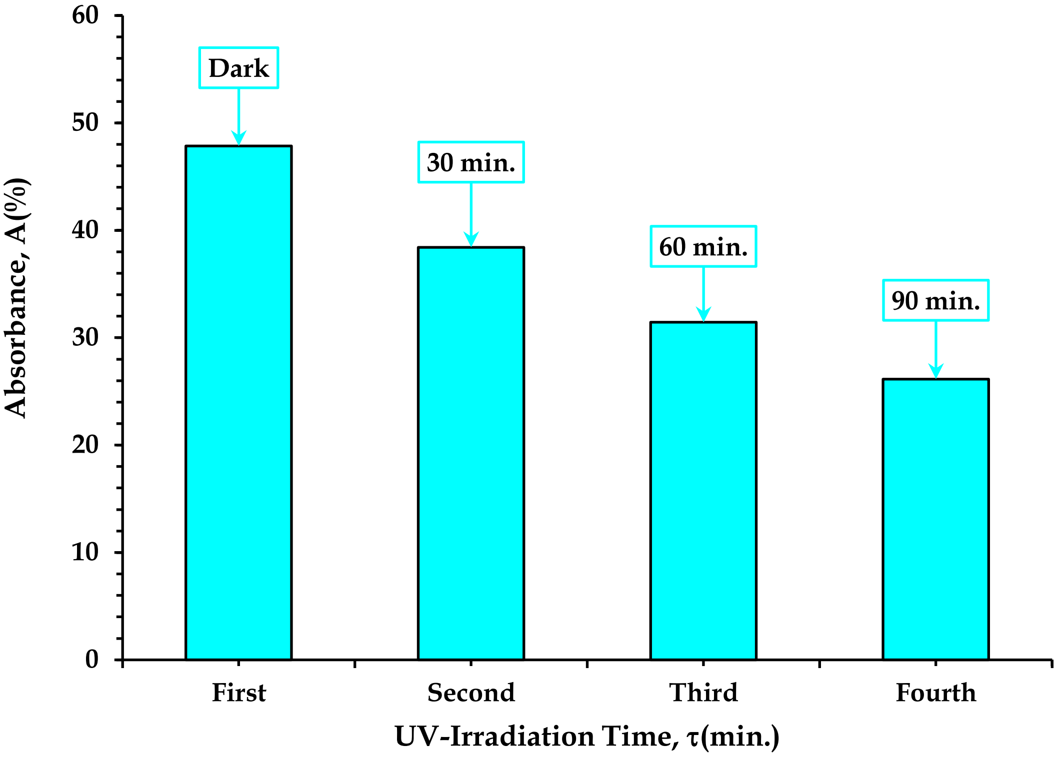

Figure 4.84: Photodegradation performance for (PC-PS/SiC-Co_2O_3) NCs against MO dye with UV-irradiation time for 3.9 wt.% content of SiC/Co_2O_3 NPs at λ_{max}=460 nm

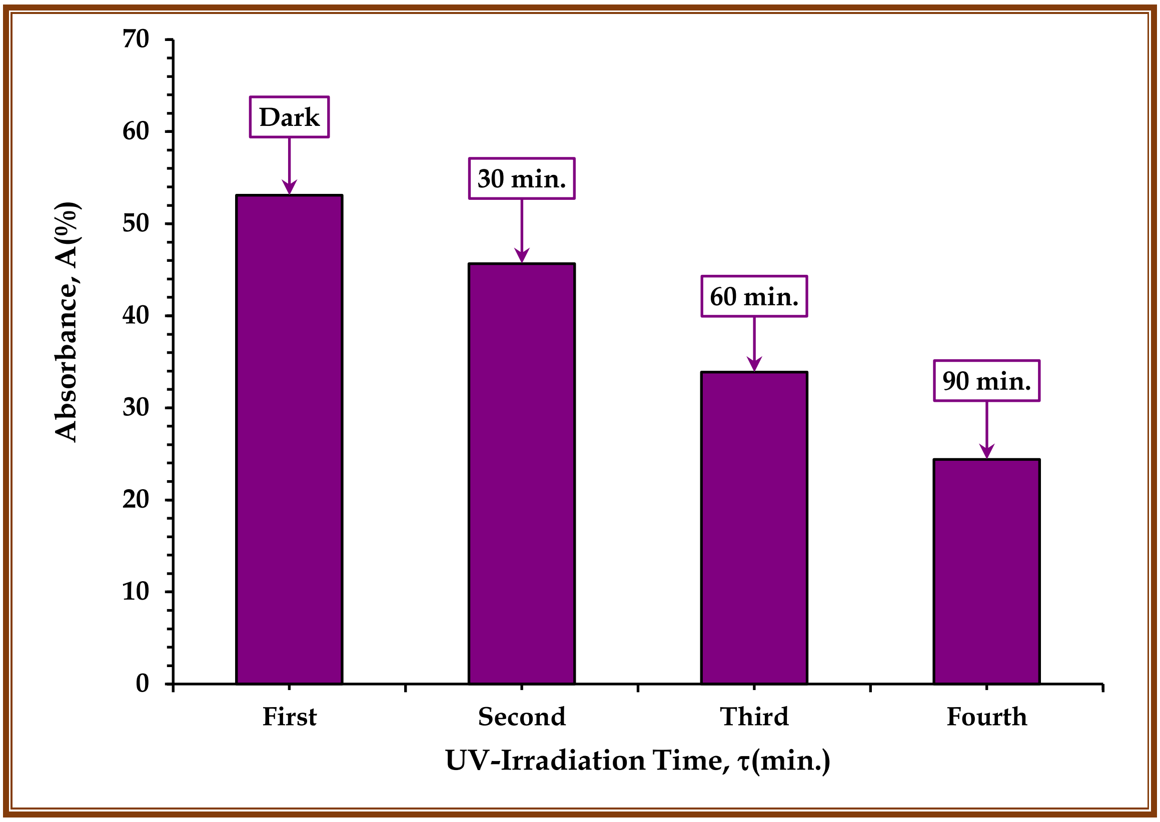

Figure 4.85: Photodegradation performance for (PC-PS/SiC-MnO_2) NCs against MO dye with UV-irradiation time for 5.2 wt.% content of SiC/MnO_2 NPs at λ_{max}=460 nm

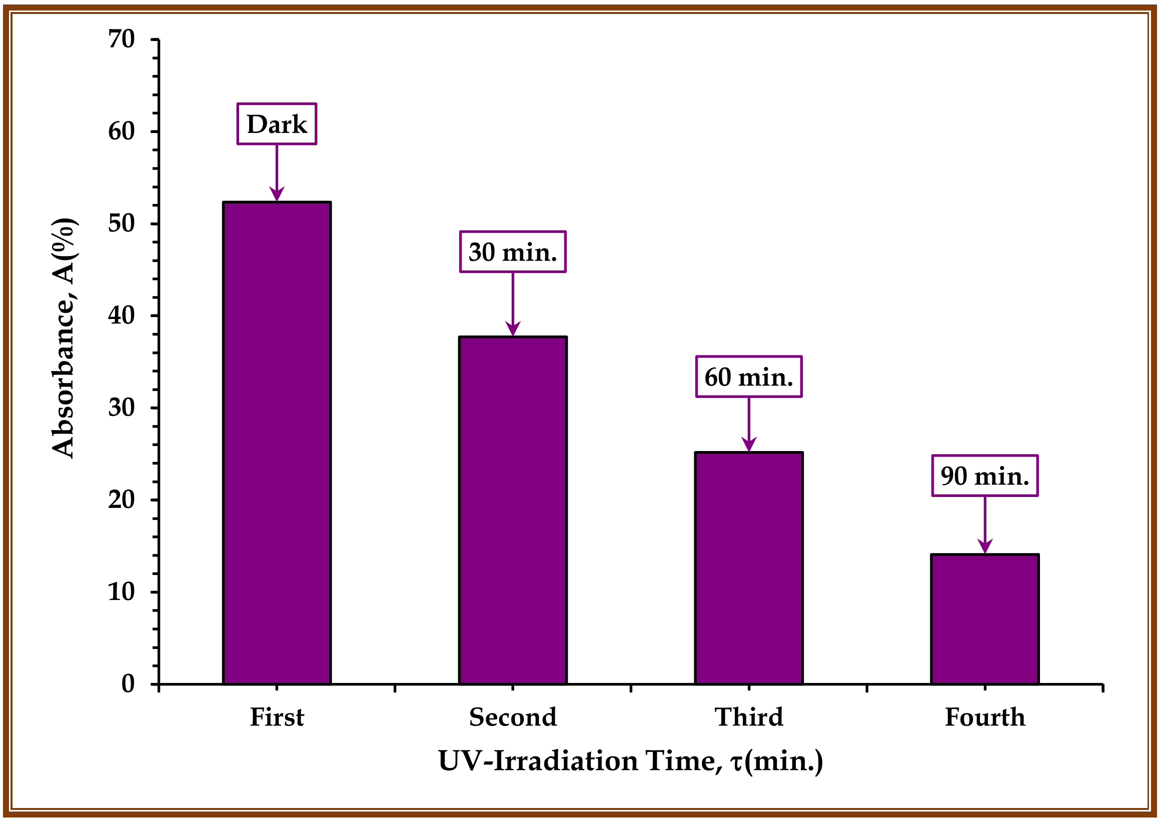

Figure 4.86: Photodegradation performance for (PC-PS/SiC-Co_2O_3) NCs against MO dye with UV-irradiation time of 5.2 wt.% content of SiC/Co_2O_3 NPs at λ_{max}=460 nm

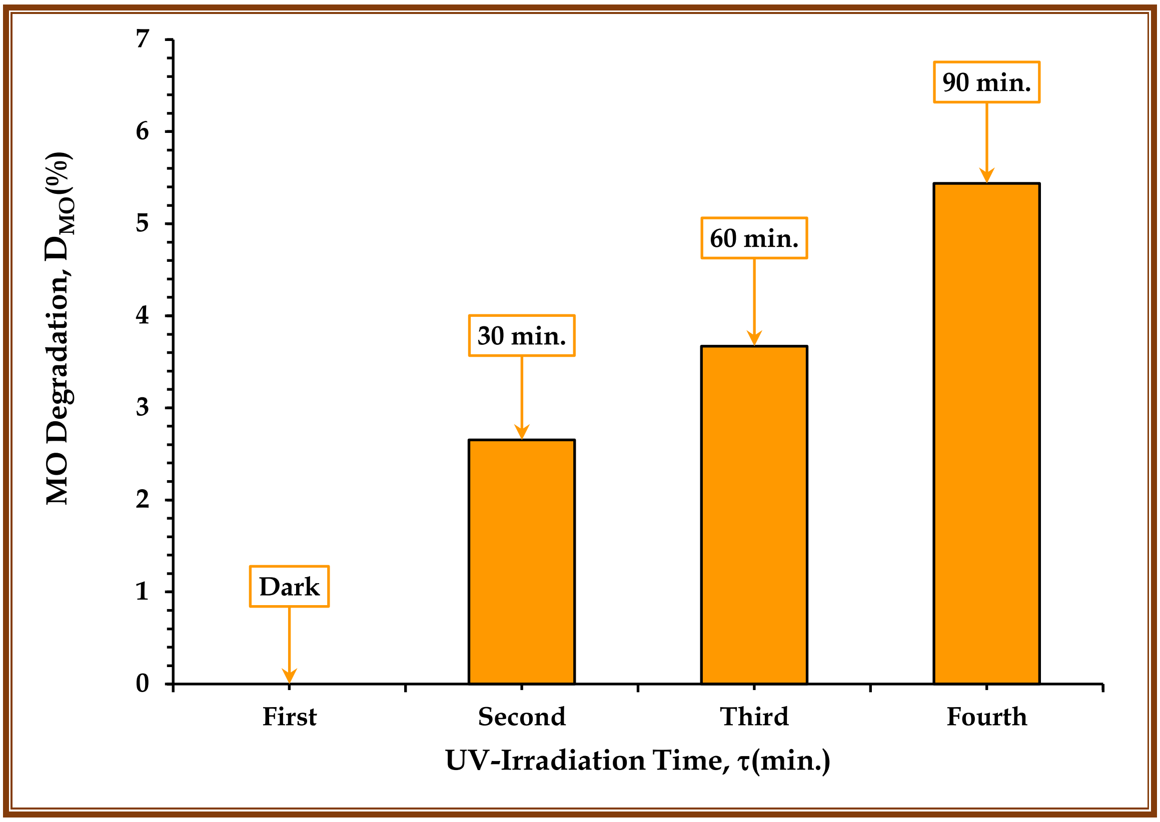

Figure 4.87: Impact of UV-Irradiation time on MO dye degradation percentage for MO dye solution at λ_{max}=460 nm

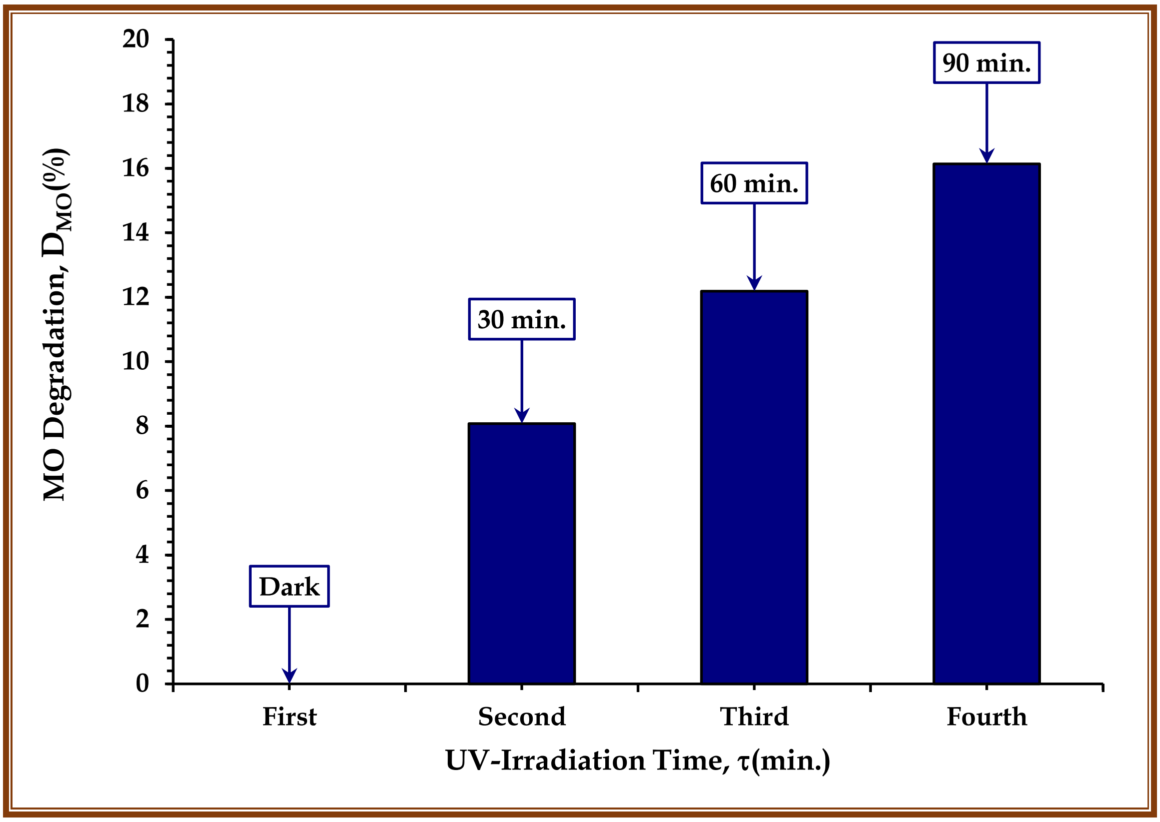

Figure 4.88: Impact of UV-Irradiation time on MO dye degradation percentage for (PC/PS) polymeric blend at λ_{max}=460 nm.

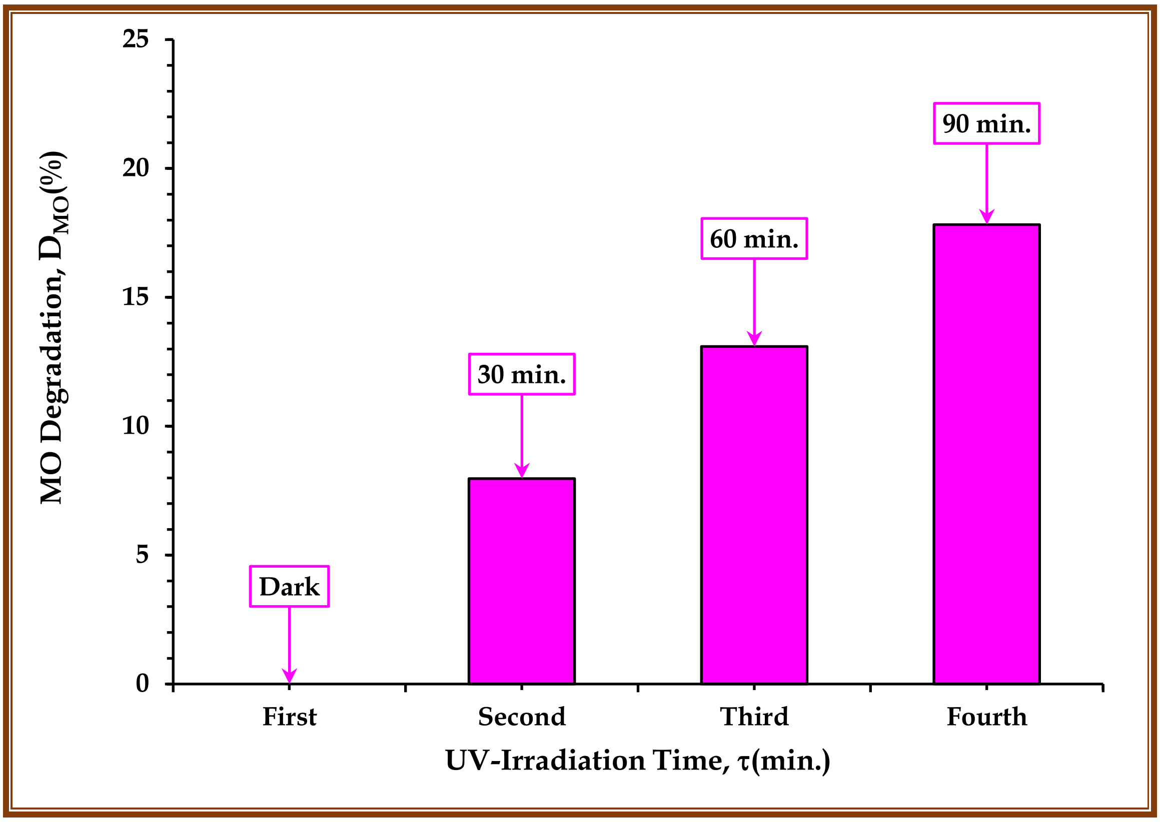

Figure 4.89: Impact of UV-irradiation time on MO dye degradation percentage for (PC-PS/SiC-MnO_2) NCs for 1.3 wt.% content of SiC/MnO_2 NPs at λ_{max}=460 nm

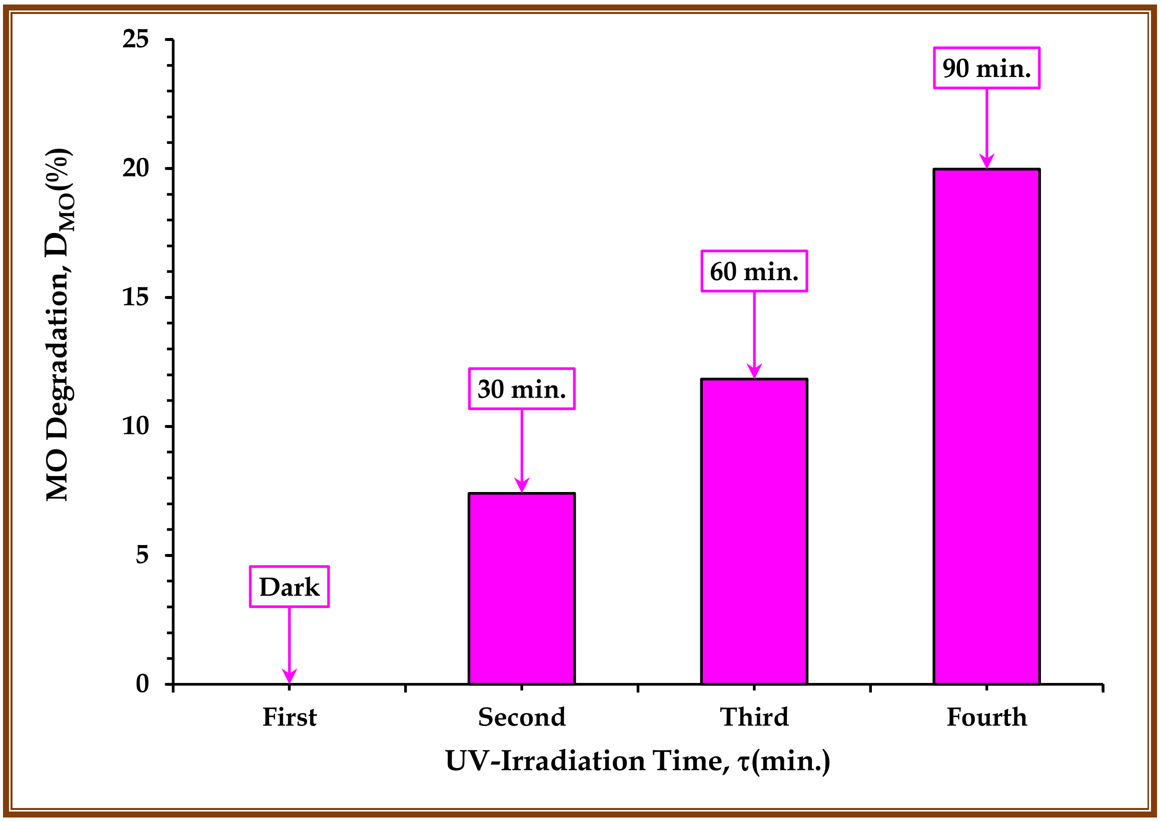

Figure 4.90: Impact of UV-irradiation time on MO dye degradation percentage for (PC-PS/SiC-Co_2O_3) NCs for 1.3 wt.% content of SiC/Co_2O_3 NPs at λmax=460 nm

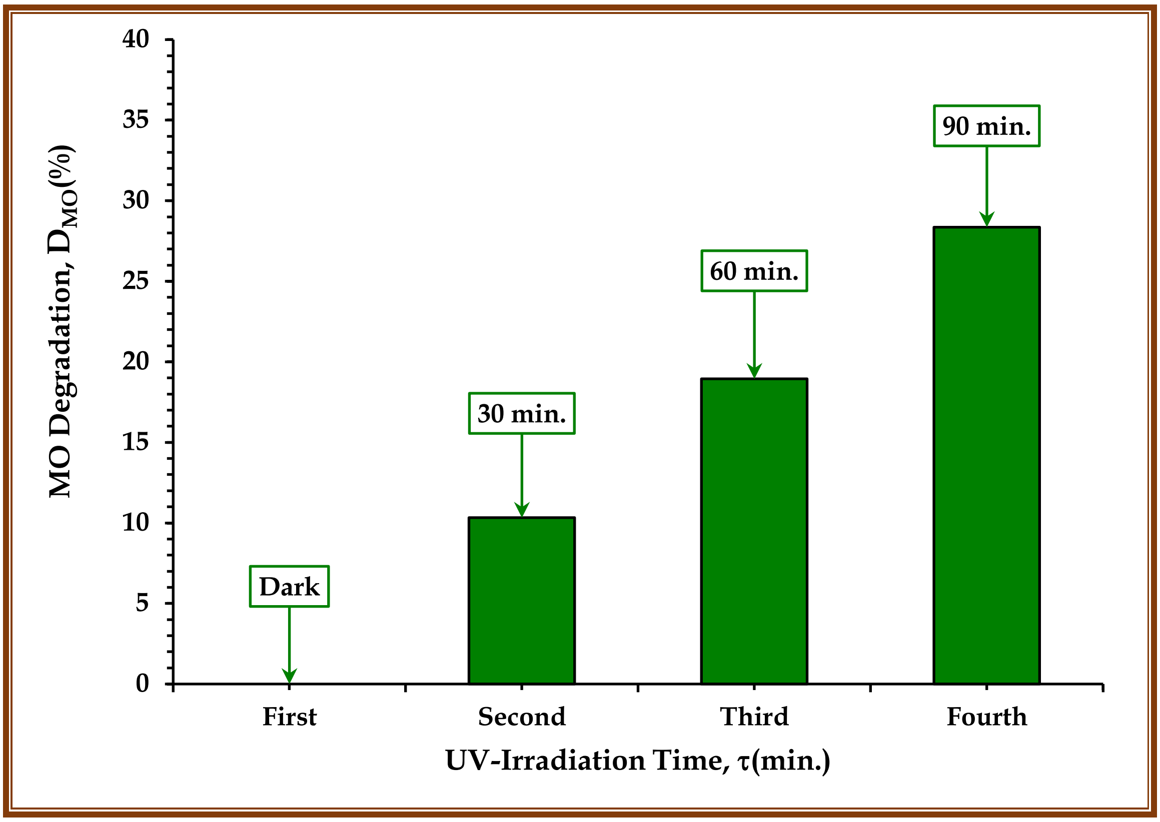

Figure 4.91: Impact of UV-irradiation time on MO dye degradation percentage for (PC-PS/SiC-MnO_2) NCs for 2.6 wt.% content of SiC/MnO_2 NPs at λ_{max}=460 nm

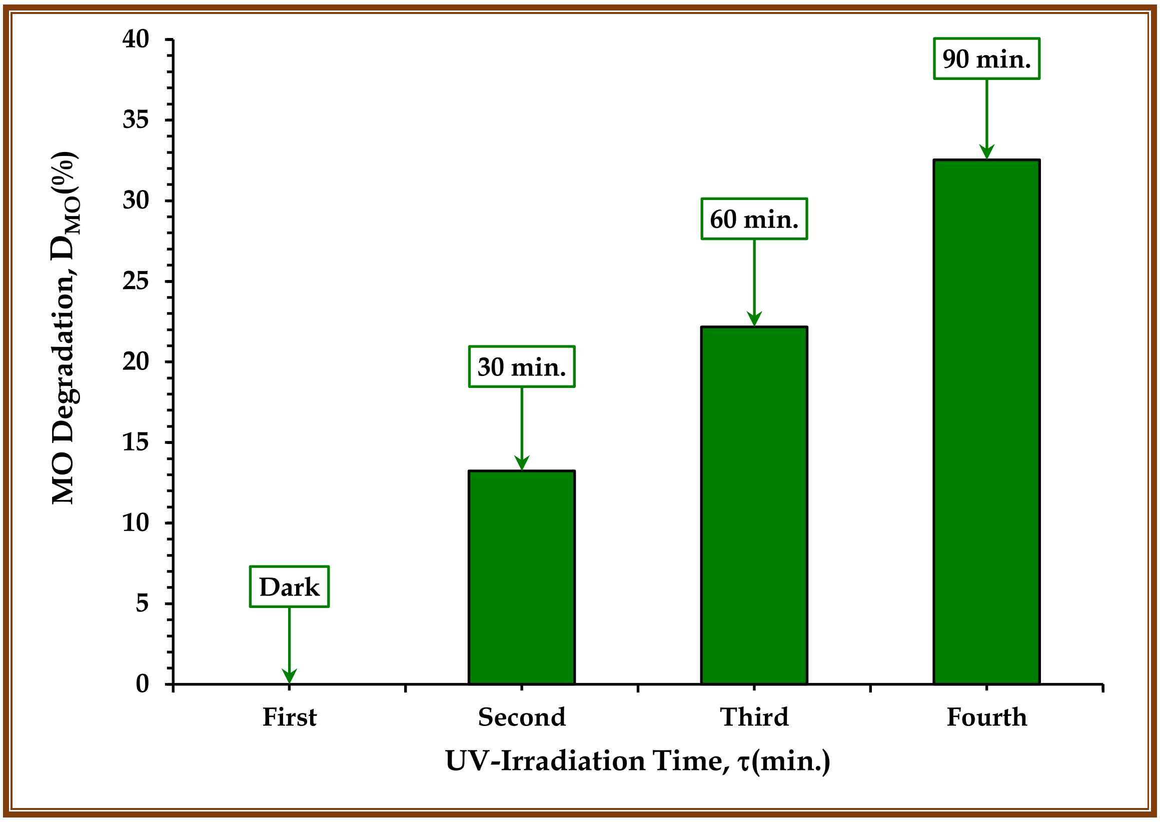

Figure 4.92: Impact of UV-irradiation time on MO dye degradation percentage for (PC-PS/SiC-Co_2O_3) NCs for 2.6 wt.% content of SiC/Co_2O_3 NPs at λ_{max}=460 nm

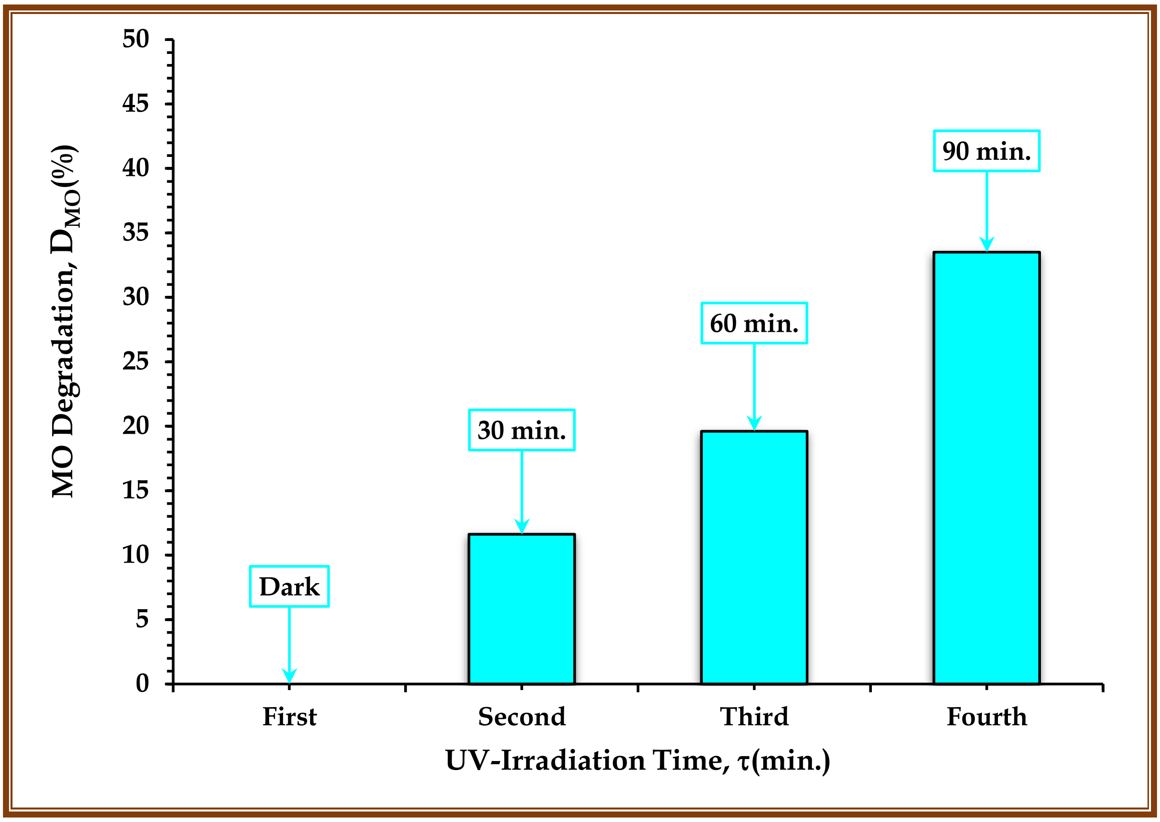

Figure 4.93: Impact of UV-irradiation time on MO dye degradation percentage for (PC-PS/SiC-MnO_2) NCs for 3.9 wt.% content of SiC/MnO_2 NPs at λ_{max}=460 nm

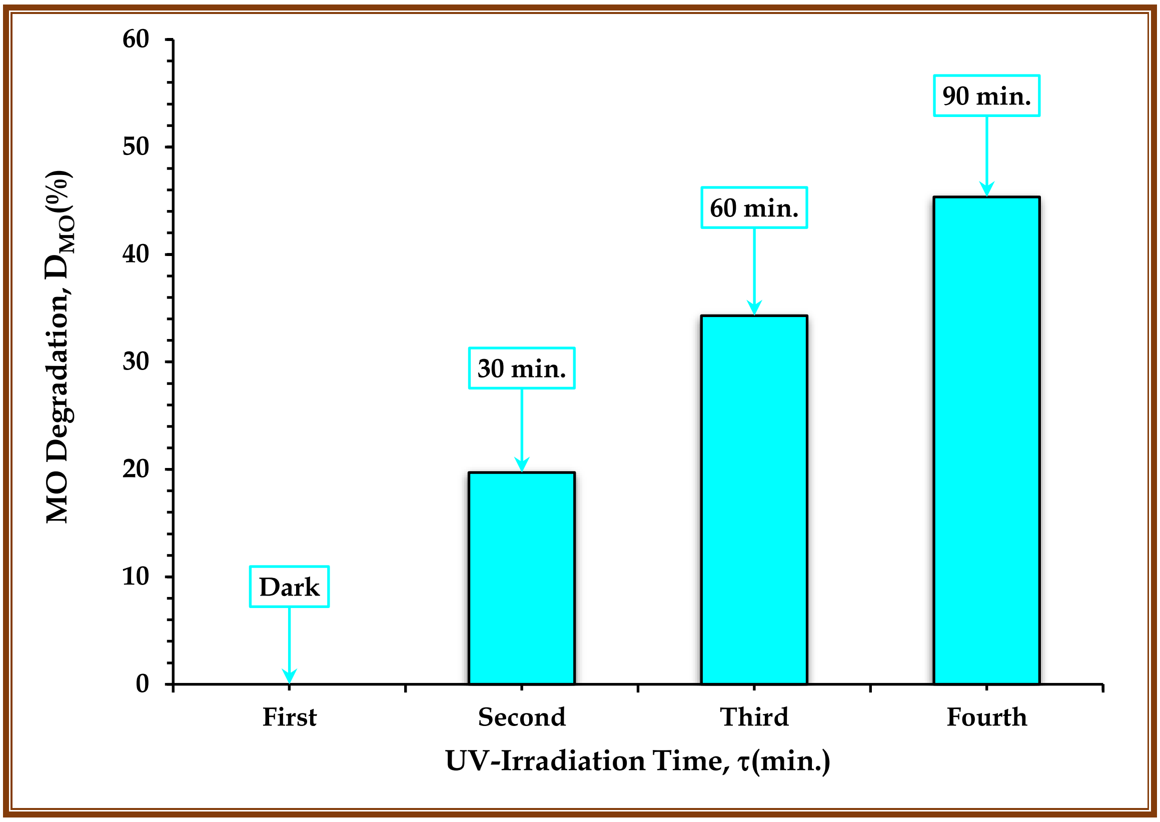

Figure 4.94: Impact of UV-irradiation time on MO dye degradation percentage for (PC-PS/SiC-Co_2O_3) NCs for 3.9 wt.% content of SiC/Co_2O_3 NPs at λ_{max}=460 nm

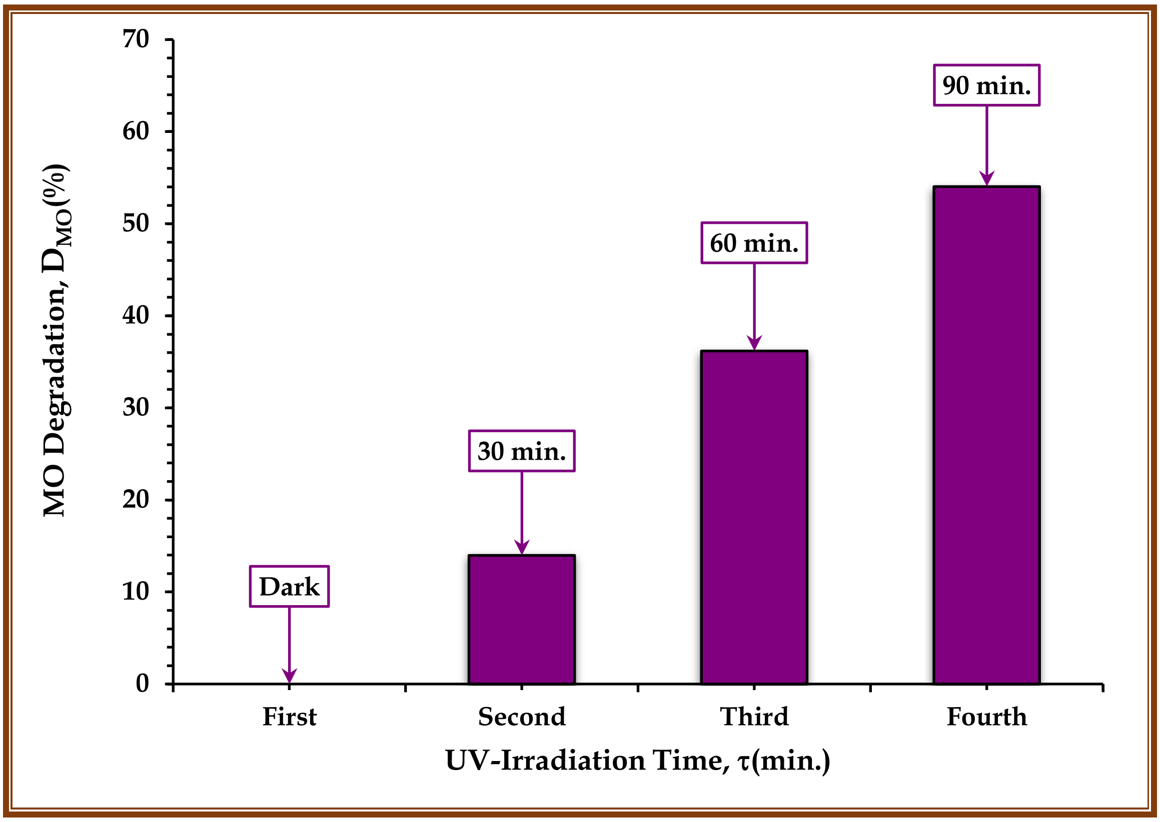

Figure 4.95: Impact of UV-irradiation time on MO dye degradation percentage for (PC-PS/SiC-MnO_2) NCs for 5.2 wt.% content of SiC/MnO_2 NPs at λ_{max}=460 nm

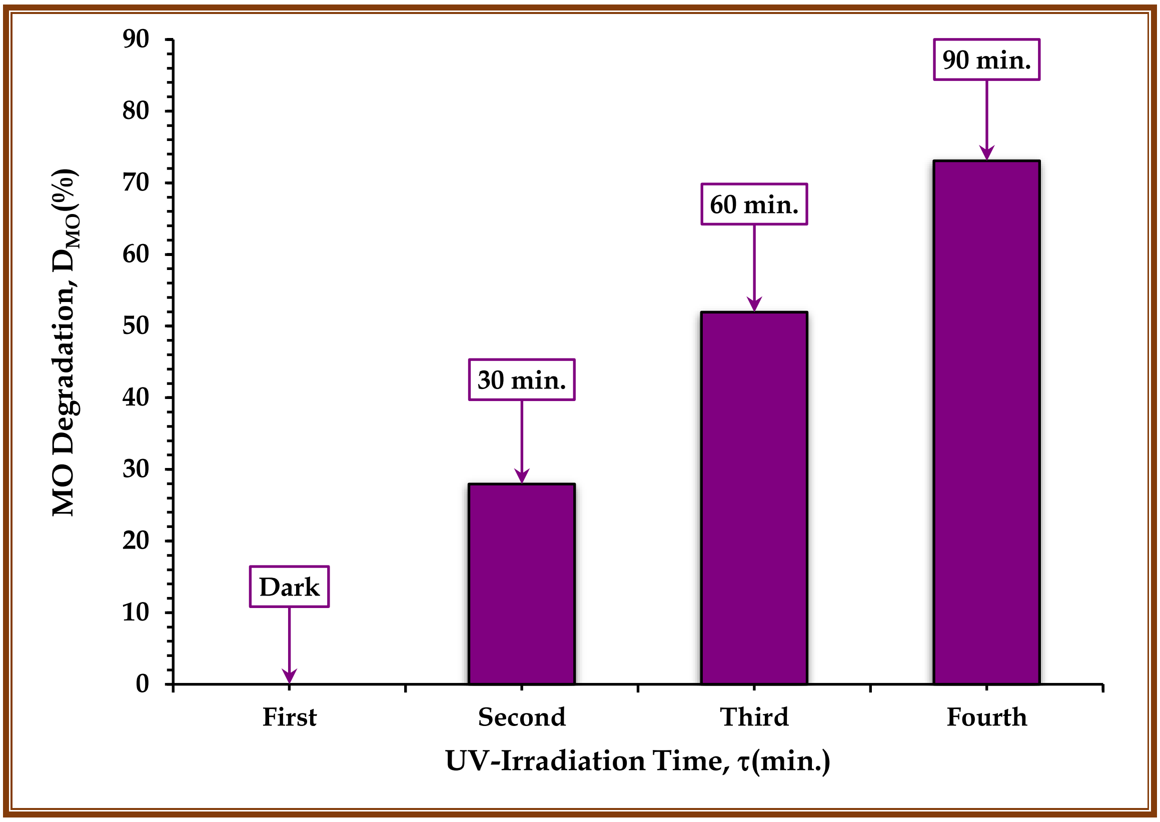

Figure 4.96: Impact of UV-irradiation time on MO dye degradation percentage for (PC-PS/SiC-Co_2O_3) NCs for 5.2 wt.% content of SiC/Co_2O_3 NPs at λ_{max}=460 nm

Table 4.25: MO degradation percentage of (PC/PS) blend, and (PC-PS/SiC-MnO_2) nanocomposites at λ_{max}=460 nm

Time (min)	MO degradation %					
	Dye	Pure	1.3 wt.%	2.6 wt.%	3.9 wt.%	5.2 wt.%
Dark	0	0	0	0	0	0
30	2.65	8.08	7.97	10.32	11.61	13.98
60	3.67	12.19	13.09	18.94	19.62	36.19
90	5.44	16.14	17.82	28.36	33.51	54.05

Table 4.26: MO degradation percentage of (PC/PS) blend, and (PC-PS/SiC-Co_2O_3) nanocomposites at λ_{max}=460 nm

Time (min)	MO degradation %					
	Dye	Pure	1.3 wt.%	2.6 wt.%	3.9 wt.%	5.2 wt.%
Dark	0	0	0	0	0	0
30	2.65	8.08	7.41	13.23	19.70	27.94
60	3.67	12.19	11.83	22.17	34.30	51.93
90	5.44	16.14	19.97	32.53	45.35	73.26

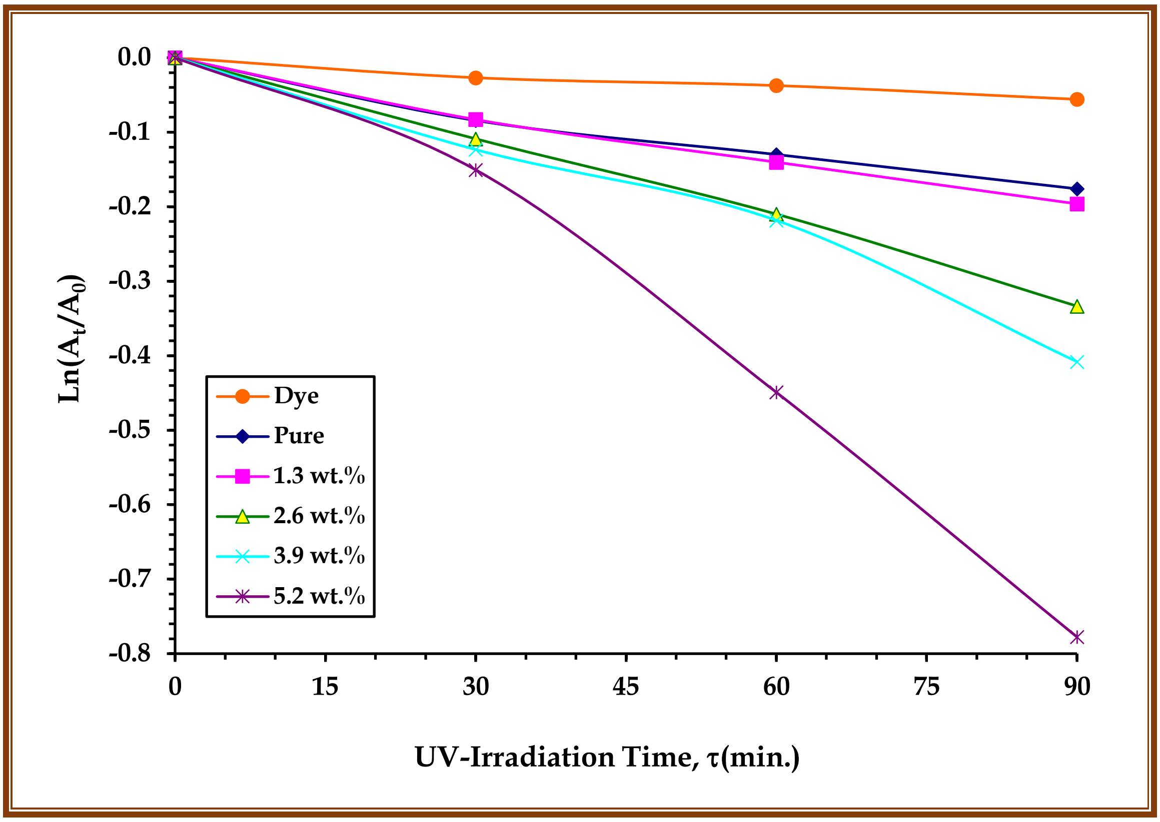

Figure 4.97: Plot of Ln (A_t/A_0) of MO dye solution in contact with (PC-PS/SiC-MnO_2) nanocomposite films as a function of UV-Irradiation time at λ_{max} = 460 nm

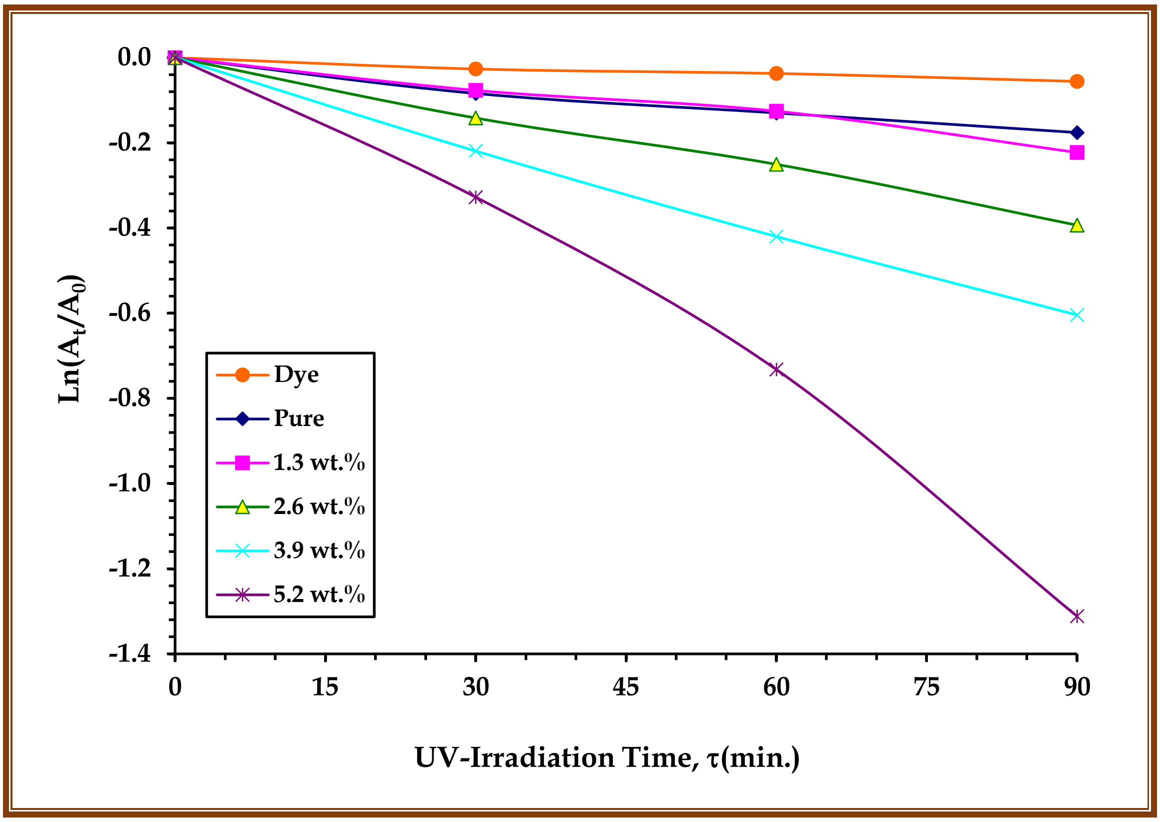

Figure 4.98: Plot of Ln (A_t/A_0) of MO dye solution in contact with (PC-PS/SiC-Co_2O_3) nanocomposite films as a function of UV-Irradiation time at λ_{max} = 460 nm

Table 4.27: Comparison values of MO dye degradation constant, half-life, and linear regression coefficient values for (PC-PS/$SiC-MnO_2$) nanocomposites

Samples		κ_d (min^{-1})	$\tau_{1/2}$ (min)	R^2 (COD)
MO dye		0.0006	1166.33	0.9713
(PC/PS) blend		0.0019	362.39	0.9739
(PC-PS/$SiC-MnO_2$) nanocomposites	**1.3 wt.%**	0.0022	321.89	0.9899
	2.6 wt.%	0.0037	188.76	0.9984
	3.9 wt.%	0.0045	157.61	0.9791
	5.2 wt.%	0.0088	79.02	0.9758

Table 4.28: Comparison values of MO dye degradation constant, half-life, and linear regression coefficient values for (PC-PS/$SiC-Co_2O_3$) nanocomposites

Samples		κ_d (min^{-1})	$\tau_{1/2}$ (min)	R^2 (COD)
MO dye		0.0006	1166.33	0.9713
(PC/PS) blend		0.0019	362.39	0.9739
(PC-PS/$SiC-Co_2O_3$) nanocomposites	**1.3 wt.%**	0.0024	289.93	0.9851
	2.6 wt.%	0.0043	161.30	0.9973
	3.9 wt.%	0.0067	103.28	0.9985
	5.2 wt.%	0.0145	47.92	0.9830

4.6.3 Application of (PC-PS/SiC-MnO_2), and (PC-PS/SiC-Co_2O_3) bionanocomposites for pressure sensors

The variation of electrical capacitance for (PC-PS/SiC-MnO_2), and (PC-PS/SiC-Co_2O_3) nanocomposites with pressure at $(f = 10^5\ Hz)$ are shown in Figure 4.99 and Figure 4.100, respectively. From the Figures, the electrical capacitance of nanocomposites increases with increasing the pressure. The explanation of the electrical capacitance behavior for nanocomposites with the pressure attributed to the nanocomposite samples has a crystalline region that has an internal dipole moment. These dipole moments are randomly oriented without any mechanical or electrical mechanism and the net dipole moment in this state is zero. When the pressure is applied, it will change the local dipole distributions and induced an electric field. The induced electric field collects the charges at the top and bottom of the samples [221].

This is due to the geometry of the atomic structure of SiC/MnO_2 nanoparticles, and SiC/Co_2O_3 nanoparticles changes and the ions in the structure separated to form dipole moment then the electrical dipoles appear. In addition to oxygen vacancies for (PC/PS) polymeric blend form localized levels below the conduction band. This means the mobility of charge carriers and the hopping of ions from the cluster. Then the current increase due to the internal stress increasing, indicate that the capacitance will be increase [222].

The impact of SiC/MnO_2 nanostructures, and SiC/Co_2O_3 nanostructures contents on the electrical capacitance of (PC-PS/SiC-MnO_2), and (PC-PS/SiC-Co_2O_3) nanocomposites is shown in Figure 4.101 and Figure 4.102, respectively. As shown in Figures, the electrical capacitance of nanocomposites increases with increase in the content of SiC/MnO_2 nanoparticles, and SiC/Co_2O_3 nanoparticles as displayed in Table 4.29, and Table 4.30. The increase of electrical capacitance with increase in SiC/MnO_2 nanoparticles, and SiC/Co_2O_3 nanoparticles contents attributed to the increase of the charge carriers number [86, 223].

While, the impact of applied pressure on the parallel capacitance, (C_P) of (PC-PS/SiC-MnO_2), and (PC-PS/SiC-Co_2O_3) nanocomposites is shown in Figure 4.103 and Figure 4.104, respectively. The percentage increase in electrical capacitance became about 36.08% and 28.69% when the applied pressure changed from 80 bar to 160 bar at a content of 5.2 wt.%.

Figure 4.105, and Figure 4.106 display the impact of MnO_2 nanoparticles, and Co_2O_3 nanoparticles contents on the sensitivity of (PC-PS/SiC-MnO_2), and (PC-PS/SiC-Co_2O_3) nanocomposites. The sensitivity of nanocomposites can be calculated by using the equation (2.55). From the Figures, the sensitivity of prepared nanocomposites increases with the increase in MnO_2 nanoparticles, and Co_2O_3 nanoparticles contents as shown in Table 4.29, and Table 4.30. Finally, the increase percentage in the sensitivity of (PC-PS/SiC-MnO_2), and (PC-PS/SiC-Co_2O_3) nanocomposites are 69.85% and 83.46% at $P = 80\ bar$, respectively at 5.2 wt.% content of SiC/MnO_2 nanoparticles, and SiC/Co_2O_3 nanoparticles, this behavior makes the nanocomposites suitable to be used in different electronic, optical, and electric fields [224].

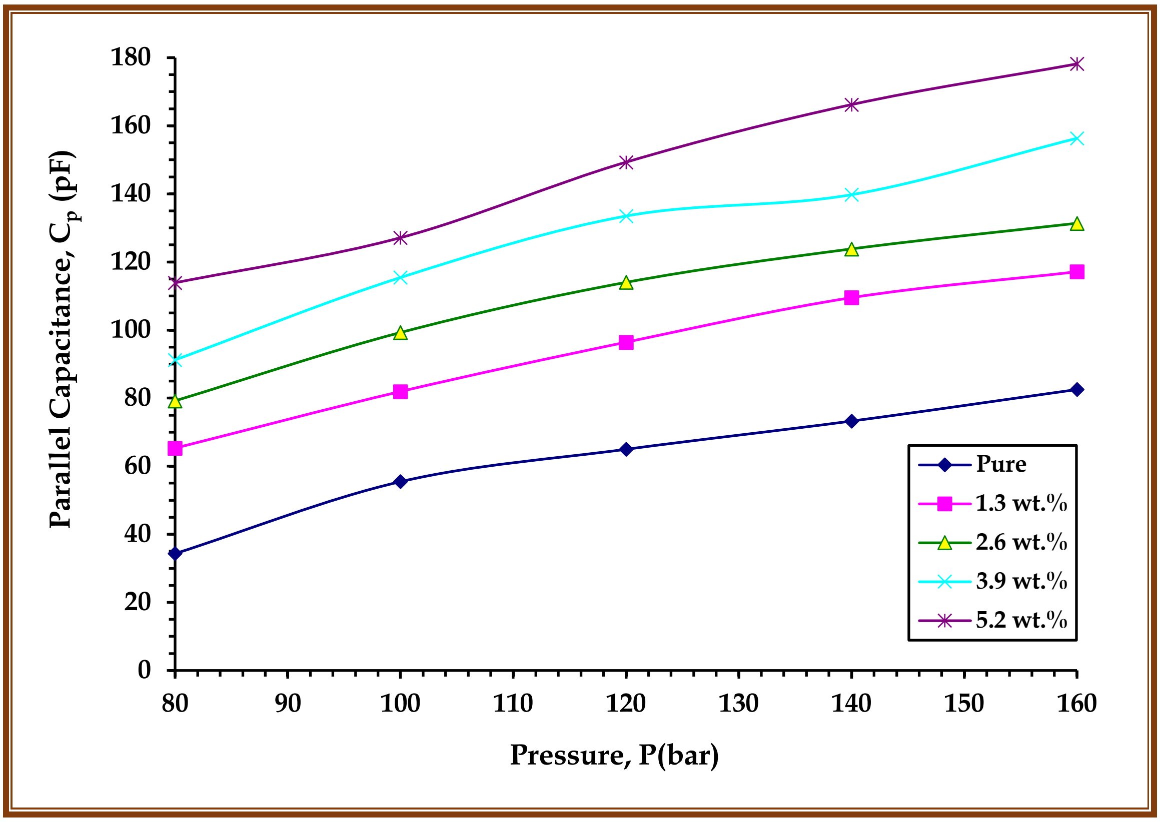

Figure 4.99: Variation of parallel capacitance for (PC-PS/SiC-MnO_2) nanocomposites with applied pressure at $f=10^5$ Hz

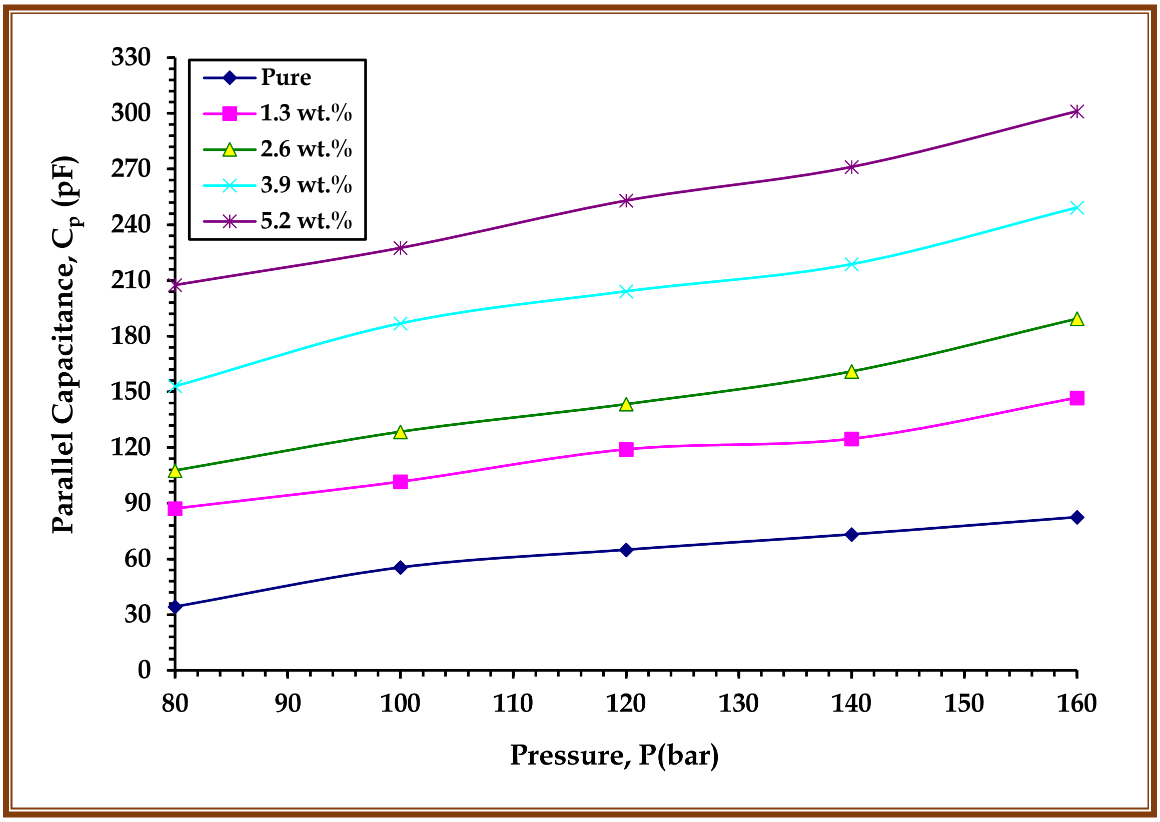

Figure 4.100: Variation of parallel capacitance for (PC-PS/SiC-Co_2O_3) nanocomposites with applied pressure at $f=10^5$ Hz

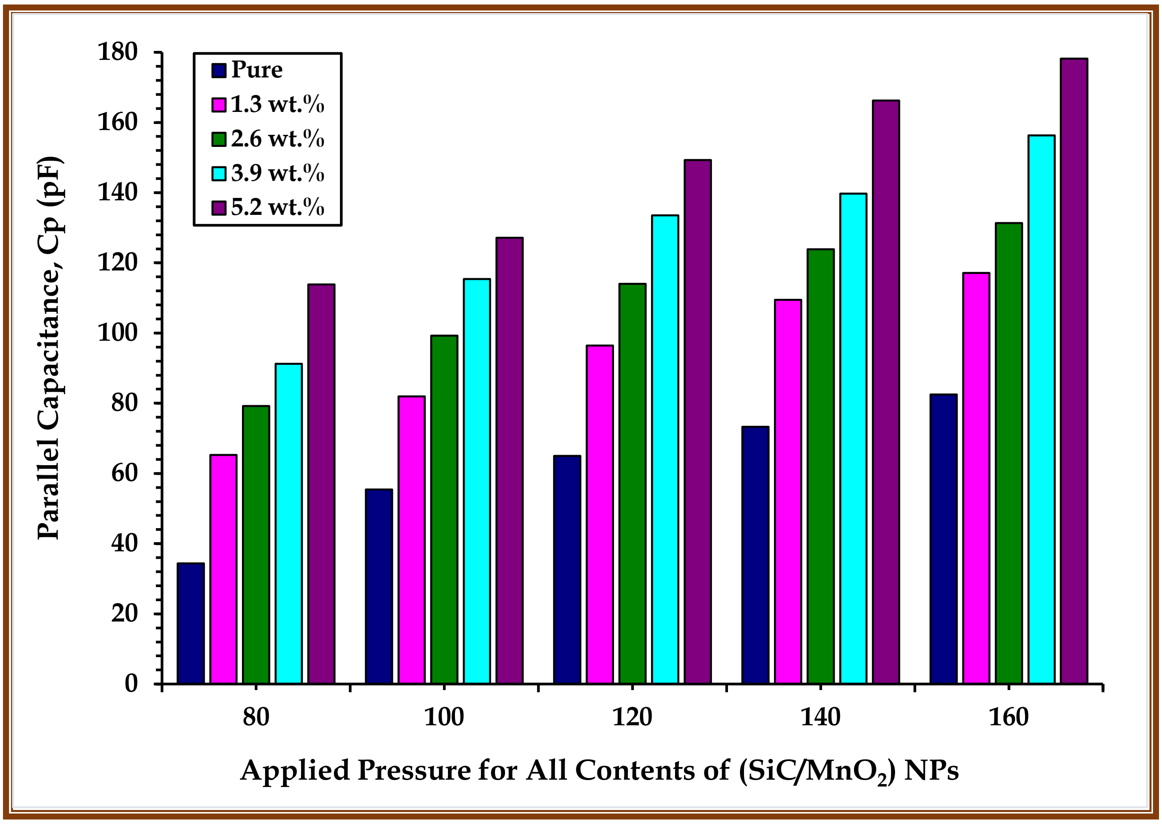

Figure 4.101: Impact of applied pressure on parallel capacitance for contents of (SiC/MnO_2) nanoparticles at f=10^5 Hz

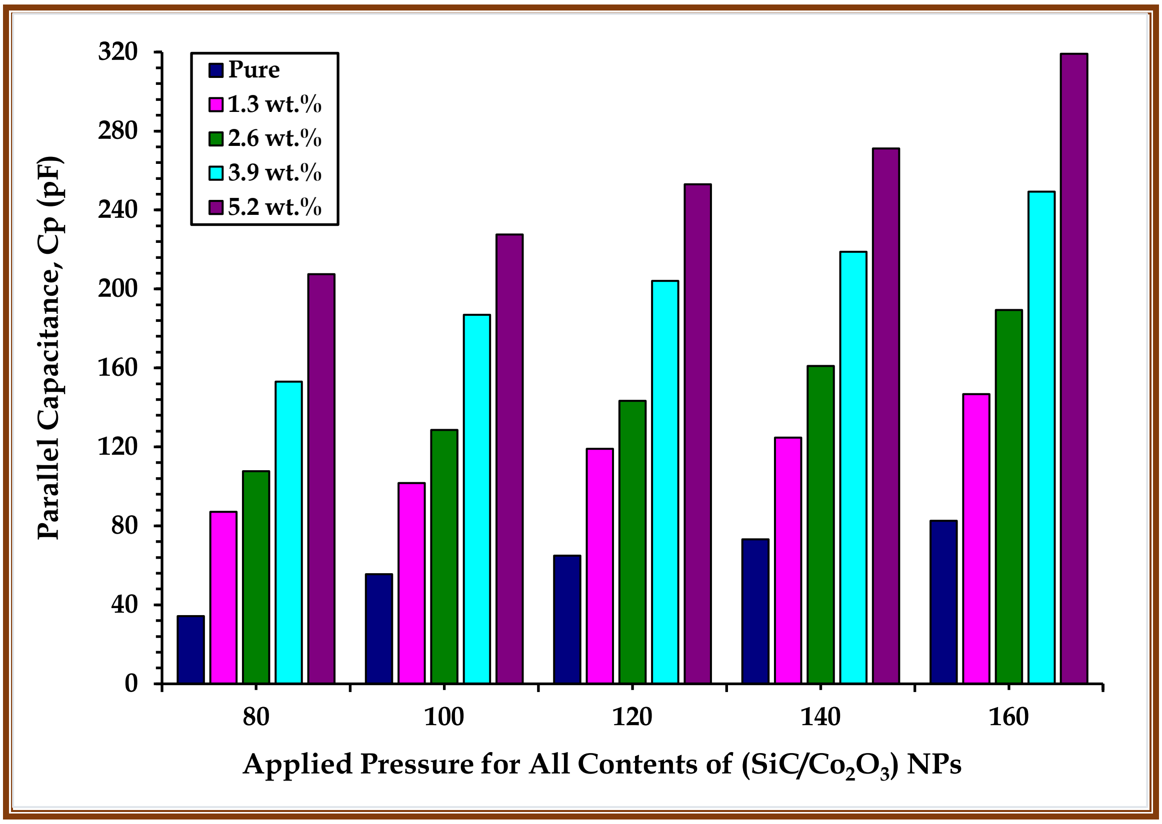

Figure 4.102: Impact of applied pressure on parallel capacitance for contents of (SiC/Co_2O_3) nanoparticles at f=10^5 Hz

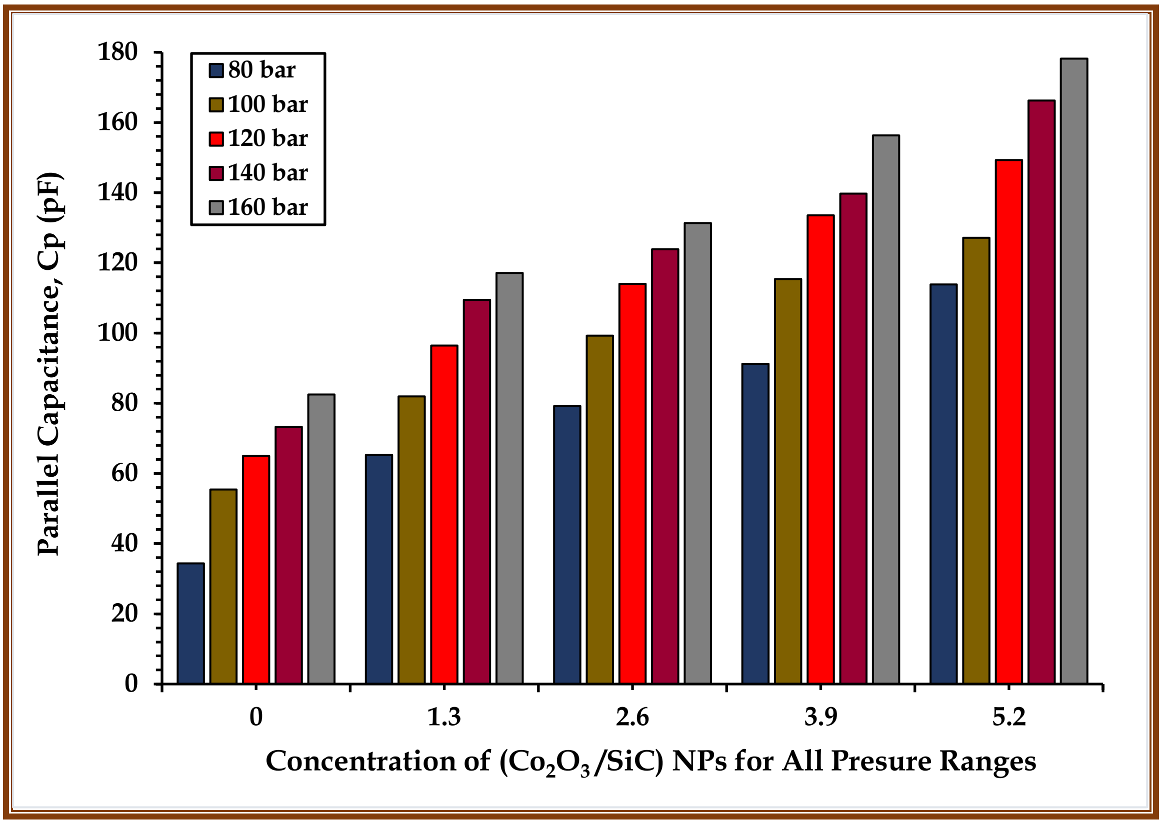

Figure 4.103: Impact of (SiC/MnO_2) nanoparticles contents on parallel capacitance for (PC/PS) polymeric blend at f=10^5 Hz

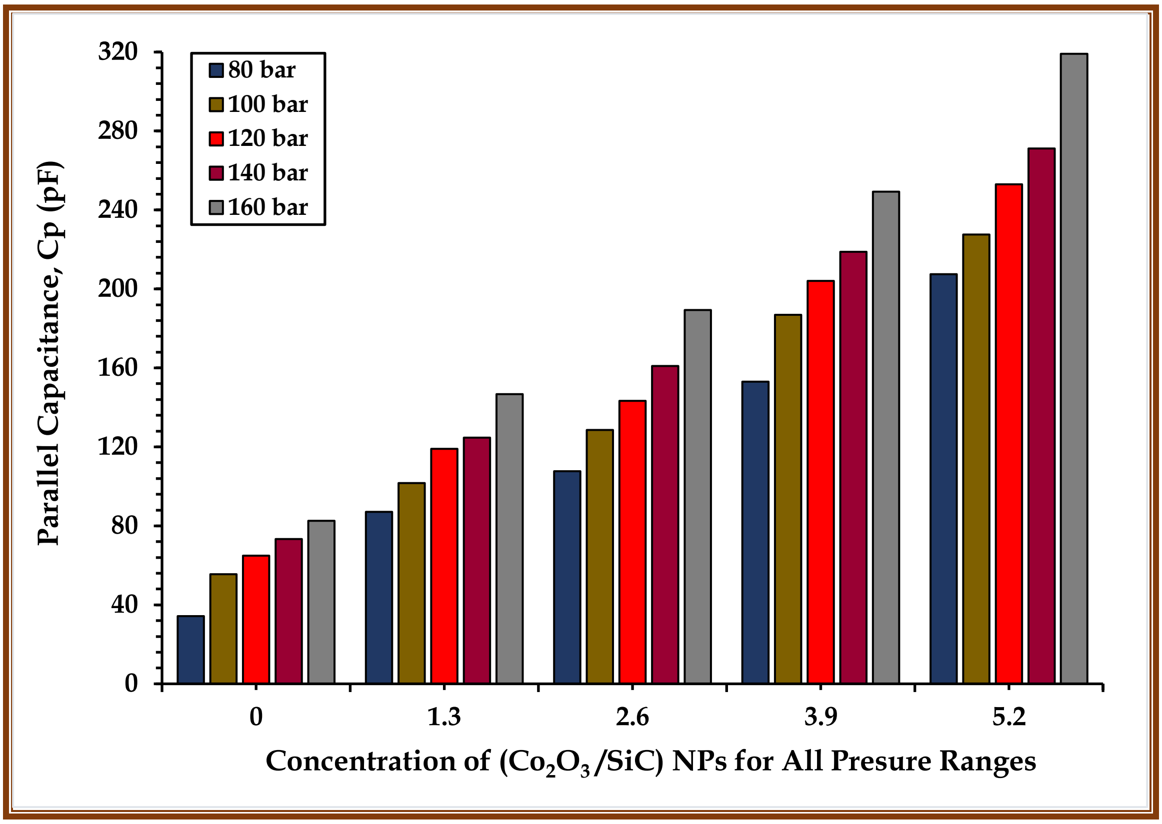

Figure 4.104: Impact of (SiC/Co_2O_3) nanoparticles contents on parallel capacitance for (PC/PS) polymeric blend at f=10^5 Hz

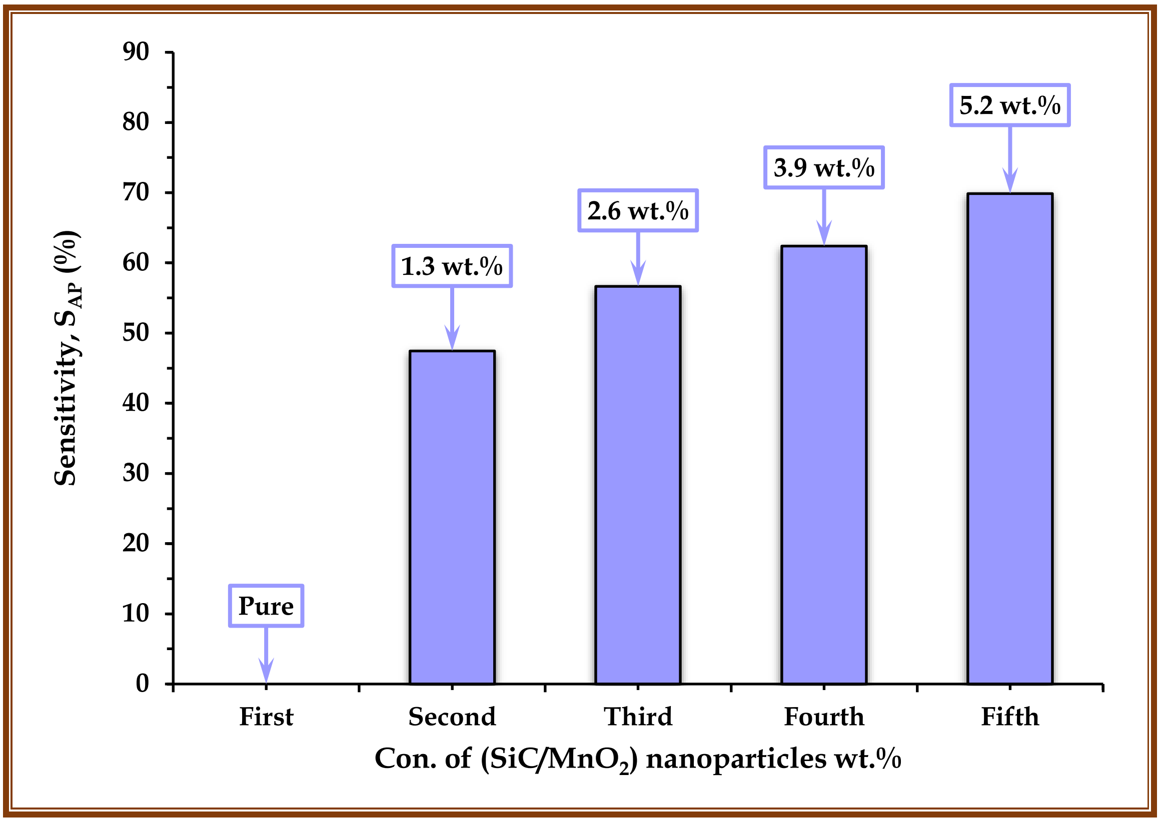

Figure 4.105: Impact of (SiC/MnO_2) nanoparticles contents on applied pressure sensitivity for (PC-PS/SiC-MnO_2) nanocomposites at P=80 bar

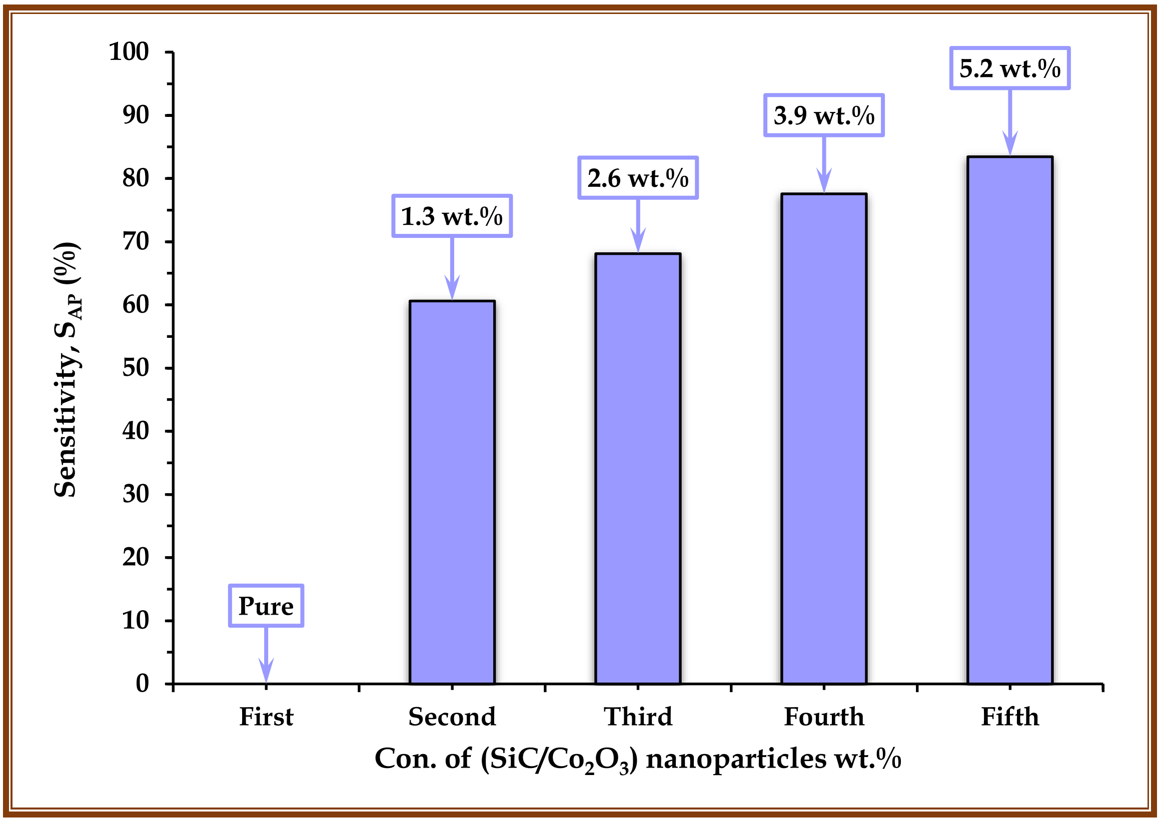

Figure 4.106: Impact of (SiC/Co_2O_3) nanoparticles contents on applied pressure sensitivity for (PC-PS/SiC-Co_2O_3) nanocomposites at P=80 bar

Table 4.29: Parallel capacitance (pF), and applied pressure sensitivity of (PC-PS/SiC-MnO_2) nanocomposites at P=80 bar

Samples	Contents of SiC/MnO_2 nanoparticles	Parallel Capacitance (pF)	Applied pressure sensitivity (%)
(PC/PS) blend	**Pure**	34.33	0.00
(PC-PS/SiC-MnO_2) nanocomposite	**1.3 wt.%**	65.31	47.44
	2.6 wt.%	79.21	56.66
	3.9 wt.%	91.23	62.37
	5.2 wt.%	113.88	69.85

Table 4.30: Parallel capacitance (pF) and applied pressure sensitivity of (PC-PS/SiC-Co_2O_3) nanocomposites at P=80 bar

Samples	Contents of SiC/Co_2O_3 nanoparticles	Parallel Capacitance (pF)	Applied pressure sensitivity (%)
(PC/PS) blend	**Pure**	34.33	0.00
(PC-PS/SiC-Co_2O_3) nanocomposite	**1.3 wt.%**	87.18	60.62
	2.6 wt.%	107.69	68.12
	3.9 wt.%	153.02	77.57

	5.2 wt.%	207.53	83.46

Conclusions and Future Works

Chapter Five

5.1 Introduction

This chapter includes a review of the conclusions obtained from this present work, as well as possible suggestions for future work for each of (PC/PS) polymeric blend, (PC-PS/SiC-MnO_2), and (PC-PS/SiC-Co_2O_3) nanocomposites.

5.2 Conclusions

In our present work, the following results were obtained:

1. The absorbance, absorption coefficient, Urbach energy, refractive index, extinction coefficient, (real and imaginary) dielectric constants and optical conductivity of (PC/PS) polymeric blend increase with increasing the weight percentages of SiC/MnO_2 nanoparticles, and SiC/Co_2O_3 nanoparticles. The results showed that the (PC-PS/SiC-MnO_2), and (PC-PS/SiC-Co_2O_3) nanocomposites have higher absorbance in the UV region. The transmittance, energy gap, and skin depth of (PC/PS) polymeric blend decrease with increasing in the concentrations of the SiC/MnO_2 nanoparticles, and SiC/Co_2O_3 nanoparticles. The absorbance of (PC/PS) polymeric blend increases about 41.04% and 42.06% with adding of 5.2 wt.% SiC/MnO_2 nanoparticles, and SiC/Co_2O_3 nanoparticles, while the optical conductivity increased with percentage 34% and 35%, respectively. The energy gaps decreased for the allowed transition about 60.39% and 61.09%, respectively and the indirect forbidden energy gaps decreased with percentage 96.16% and 95.22% respectively an refractive index increased with percentage 23.56% and 32.94%, respectively, by adding of 5.2 wt.% SiC/MnO_2 nanoparticles, and SiC/Co_2O_3 nanoparticles.
2. D.C electrical conductivity of (PC-PS/SiC-MnO_2), and (PC-PS/SiC-Co_2O_3) nanocomposites increases with increasing in the contents of SiC/MnO_2 nanoparticles, and SiC/Co_2O_3 nanoparticles.

3. The dielectric constant, dielectric loss and A.C electrical conductivity of (PC/PS) polymeric blend increase with increasing the percentages of SiC/MnO_2 nanoparticles, and SiC/Co_2O_3 nanoparticles. The dielectric constant and dielectric loss of nanocomposites are decreased with increase the frequency. The A.C electrical conductivity of nanocomposites is increased with increase in the frequency.
4. The inhibition zone of ($PC-PS/SiC-MnO_2$), and ($PC-PS/SiC-Co_2O_3$) nanocomposites against Gram-positive (Staphylococcus aureus) and Gram-negative (Salmonella enterica) is increased with the increasing the concentrations of SiC/MnO_2 nanoparticles, and SiC/Co_2O_3 nanoparticles. The results showed that the ($PC-PS/SiC-MnO_2$), and ($PC-PS/SiC-Co_2O_3$) nanocomposites may be used as coating materials for high antibacterial activity applications.
5. The absorbance of methylene orange dye solution of ($PC-PS/SiC-MnO_2$), and ($PC-PS/SiC-Co_2O_3$) nanocomposites decreases with increasing the concentrations of SiC/MnO_2 nanostructures, and SiC/Co_2O_3 nanostructures. The absorbance of methylene orange dye solution for ($PC-PS/SiC-MnO_2$), and ($PC-PS/SiC-Co_2O_3$) nanocomposites decreases with increasing the time of the irradiation. The photodegradation percentage of MO dye increases with increasing the time of the irradiation which leads to increase in the photodegradation reaction and reduced electron/hole recombination. The best photodegradation activity for ($PC-PS/SiC-Co_2O_3$) nanocomposites was 27.94% within 30 min and 73.26% within 90 min at contents 5.2 wt.% of SiC/Co_2O_3 nanoparticles.
6. The electrical capacitance of ($PC-PS/SiC-MnO_2$), and ($PC-PS/SiC-Co_2O_3$) nanocomposites increases with increase of the pressure; the nanocomposites have a higher sensitivity to pressure with low weight, flexibility, low cost. The electrical capacitance of (PC/PS) polymeric blend increases with increase in the concentration of SiC/MnO_2 nanostructures, and SiC/Co_2O_3 nanostructures. The sensitivity of nanocomposites increases with the increase in the contents of SiC/MnO_2 nanoparticles, and SiC/Co_2O_3 nanoparticles. From the sensing properties measurements of nanocomposites of 160 bar, it is shown that the nanocomposites are good sensors to this pressure. It is found the best sensitivity of ($PC-PS/SiC-Co_2O_3$) nanocomposites is 83.46% at concentration 5.2 wt.%.

5.3 Suggestions for Future Works

1. Study of mechanical and thermal characteristics of (PC/PS) polymeric blend, (PC-PS/SiC-MnO_2) and (PC-PS/SiC-Co_2O_3) nanocomposites.

2. Impact of natural and synthetic dyes on optical and electrical characteristics of (PC/PS) polymeric blend, (PC-PS/SiC-MnO_2), and (PC-PS/SiC-Co_2O_3) nanocomposites and used as smart windows applications

3. Studying the photodetectors application of (PC-PS/SiC-MnO_2) and (PC-PS/SiC-Co_2O_3) nanocomposites.

4. Studying the Gamma-ray shielding application of (PC-PS/SiC-MnO_2) and (PC-PS/SiC-Co_2O_3) nanocomposites.

5. Studying the humidity sensors application of (PC-PS/SiC-MnO_2) and (PC-PS/SiC-Co_2O_3) nanocomposites.

Appendix A

Flow Charts for Studied Characteristics

A.1 Linear Optical Characteristics Flow Chart

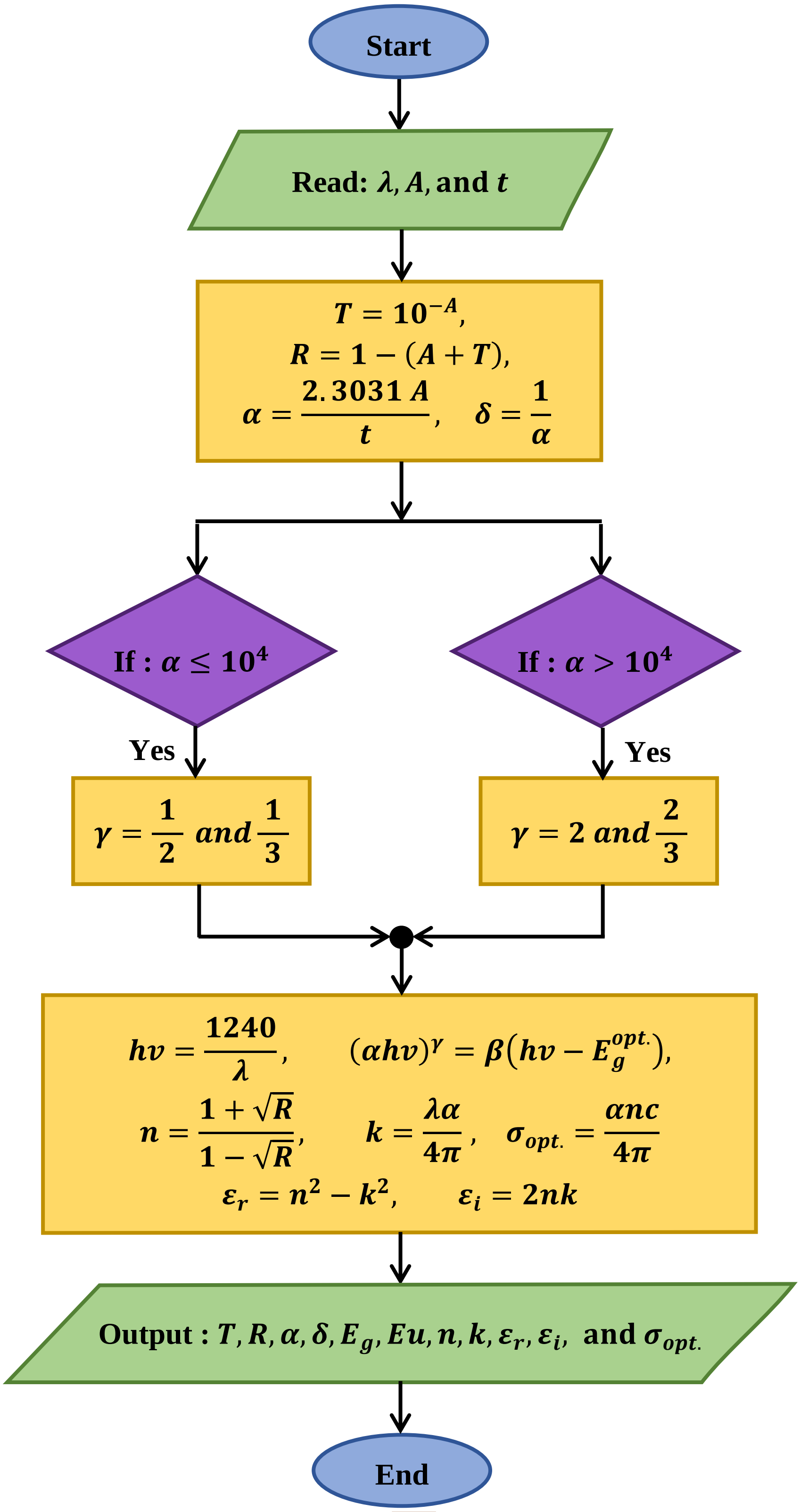

A.2 D.C Electrical Characteristics Flow Chart

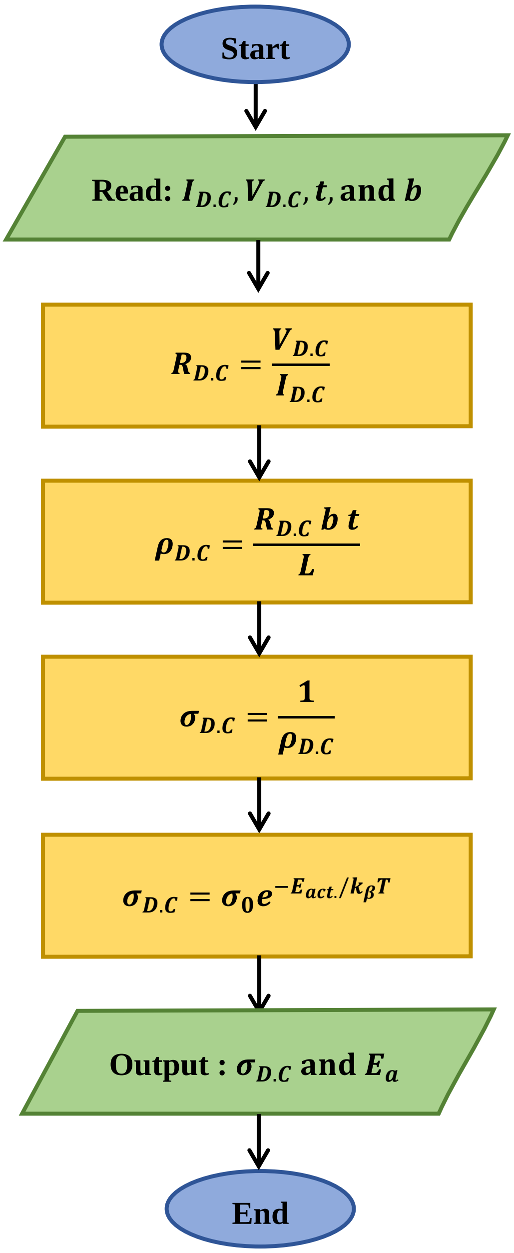

A.3 A.C Electrical Characteristics Flow Chart

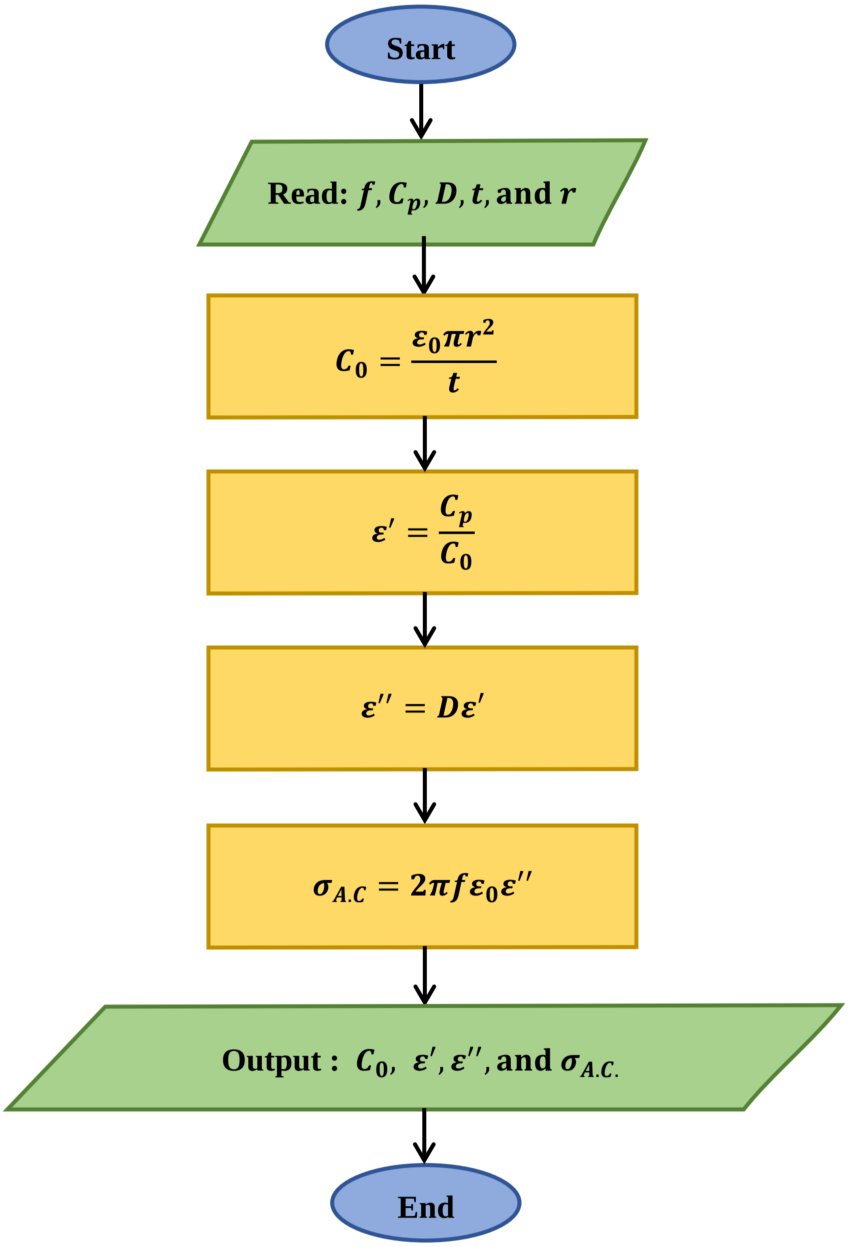

Appendix B

Flow Charts for Nanocomposites Applications

B.1 Antibacterial Activity Applications

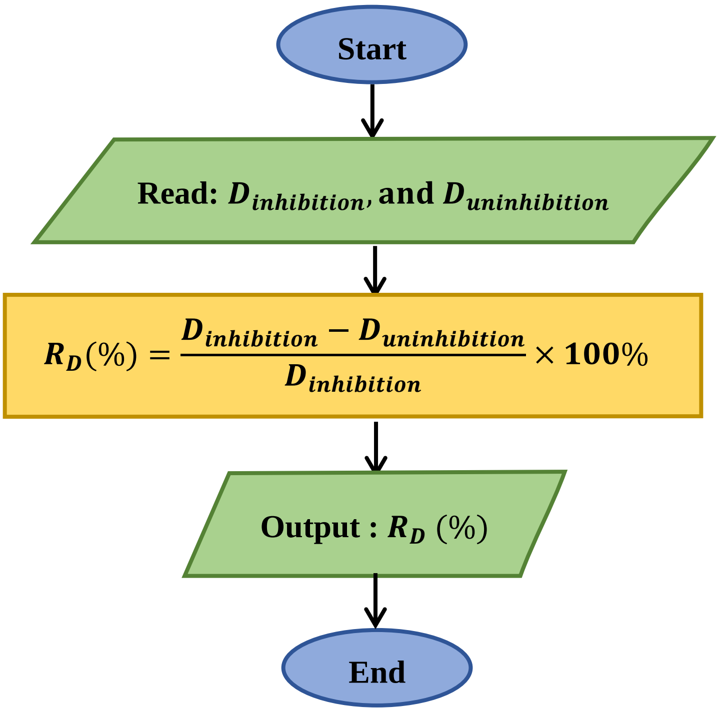

B.2 Photodegradation Applications

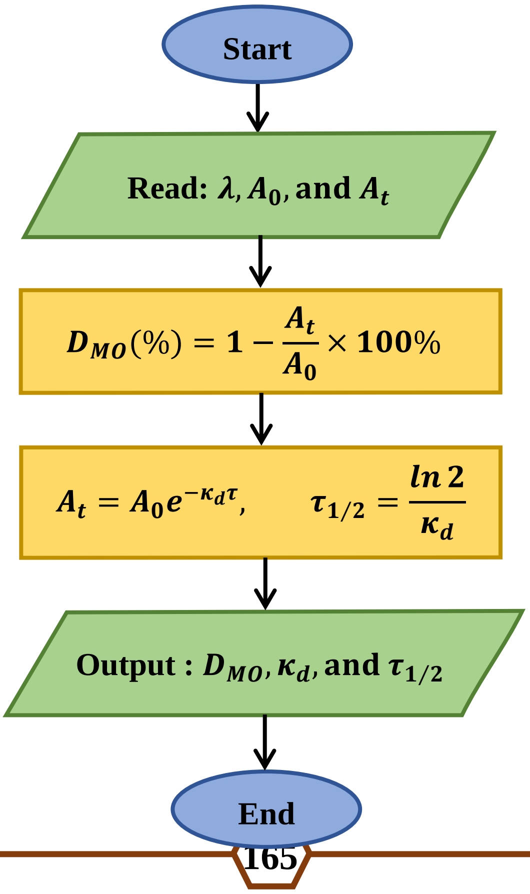

B.3 Pressure Sensors Applications

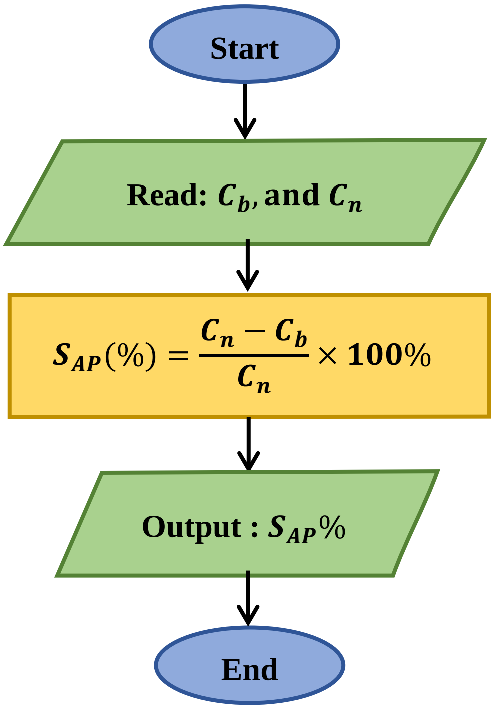

References

[1] G. Sahu, M. Das, M. Yadav, B. P. Sahoo, J. Tripathy, "Dielectric relaxation behavior of silver nanoparticles and graphene oxide embedded poly (vinyl alcohol) nanocomposite film: An effect of ionic liquid and temperature." Poly. **12**(2), 374 (2020).

[2] R. K. Venkateswara, "CuO nanoparticles Synthesis and Characterization for Humidity Sensor Application." J. Nanotech. Mater. Sci. **3**(1), 1-5 (2016).

[3] A. Ruhal, J. S. Rana, P. Ruhal, A. Kumar, M. Ruhil, C. Ram, "Antimicrobial nanocomposite of silver and gelatin nanofibers for medical applications." Int. J. Technol. Res. Eng. **1**(4), 177–182 (2013).

[4] J. Premkumar, K. SonicaSree, T. Sudhakar, "Chapter 1-Polymers in Biomedical Use." In: Handbook of Polymer and Ceramic Nanotechnology. Springer, 1329–1355. (2021).

[5] R. Malik, S. Lata, U. Soni, P. Rani, R. S. Malik, "Carbon quantum dots intercalated in polypyrrole (PPy) thin electrodes for accelerated energy storage." Electrochim. Acta. **364**, 137281 (2020).

[6] C. Pramanik, D. Nepal, M. Nathanson, J. R. Gissinger, A. Garley, R. J. Berry, S. Kumar, H. Heinz, "Molecular engineering of interphases in polymer/carbon nanotube composites to reach the limits of mechanical performance." Compos. Sci. Technol. **166**, 86–94 (2018).

[7] K. Namsheer, C. S. Rout, "Conducting polymers: A comprehensive review on recent advances in synthesis, properties and applications." RSC Adv. **11**(10), 5659–5697 (2021).

[8] R. K. Nayak, K. K. Mahato, B. C. Ray, "Chapter 4-Processing of Polymer-Based Nanocomposites." Reinf. Polym. Compos. Process. Charact. Post Life Cycle Assess. 55–75 (2019).

[9] D. M. Diamond, A. M. Campbell, C. R. Park, J. Halonen, P. R. Zoladz, "The temporal dynamics model of emotional memory processing: a synthesis on the neurobiological basis of stress-induced amnesia, flashbulb and traumatic memories, and the Yerkes-Dodson law." Neural Plast. **2007**, 1-33 (2007).

[10] C. I. Idumah, C. M. Obele, E. O. Emmanuel, A. Hassan, "Recently emerging nanotechnological advancements in polymer nanocomposite coatings for anti-corrosion, anti-fouling and self-healing." Surfaces and Interfaces. **21**, 100734 (2020).

[11] M. Bustamante-Torres, D. Romero-Fierro, B. Arcentales-Vera, S. Pardo, E. Bucio, "Interaction between filler and polymeric matrix in nanocomposites: Magnetic approach and applications." Polym. **13**(17), 2998 (2021).

[12] N. Karak, "Chapter 1-Fundamentals of nanomaterials and polymer nanocomposites. In: Nanomaterials and polymer nanocomposites." Elsevier, 1–45 (2019).

[13] Y. Naciri, A. Hsini, A. Ahdour, B. Akhsassi, Z. Ajmal, R. Djellabi, A. Bouziani, A. Taoufyq, B. Bakiz, A. Benlhachemi, "Recent advances of bismuth titanate based photocatalysts engineering for enhanced organic contaminates oxidation in water: A review." Chemosphere. **300**, 134622 (2022).

[14] Z. Ajmal, Y. Naciri, M. Ahmad, A. Hsini, A. Bouziani, M. Laabd, W. Raza, A. Murtaza, A. Kumar, S. Ullah, "Use of Conductive Polymer-Supported Oxide-based Photocatalysts for Efficient VOCs & SVOCs Removal in Gas/Liquid Phase." J. Environ. Chem. Eng. **11**(1), 108935 (2023).

[15] M. El Hajam, N. I. Kandri, G. I. Plavan, A. H. Harrath, L. Mansour, F.

Boufahja, A. Zerouale, "Pb^{2+} ions adsorption onto raw and chemically activated Dibetou sawdust: Application of experimental designs." J. King Saud Univ. **32**(3), 2176–2189 (2020).

[16] Y. Naciri, A. Hsini, A. Bouziani, K. Tanji, B. El Ibrahimi, M. N. Ghazzal, B. Bakiz, A. Albourine, A. Benlhachemi, J. A. Navío, "Z-scheme WO3/PANI heterojunctions with enhanced photocatalytic activity under visible light: A depth experimental and DFT studies." Chemosphere. **292**, 133468 (2022).

[17] H. Boulika, M. El Hajam, M. H. Nabih, I. R. Karim, N. I. Kandri, A. Zerouale, "Definitive screening design applied to cationic & anionic adsorption dyes on Almond shells activated carbon: Isotherm, kinetic and thermodynamic studies." Mater. Today Proc. **72**(7), 3336–3346 (2023).

[18] O. Moradi, H. Alizadeh, S. Sedaghat, "Removal of pharmaceuticals (diclofenac and amoxicillin) by maltodextrin/reduced graphene and maltodextrin/reduced graphene/copper oxide nanocomposites." Chemosphere. **299**, 134435 (2022).

[19] D. R. Paul, L. M. Robeson, "Polymer nanotechnology: nanocomposites." Polymer. **49**(15), 3187–3204 (2008).

[20] D. Lukkassen, A. Meidell, "Advanced materials and structures and their fabrication processes." Narrik University College Hin. 23-25 (2007).

[21] K. M. Ziadan, H. F. Hussein, K. I. Ajeel, "Study of the electrical characteristics of poly (o-toluidine) and application in solar cell." Energy Procedia. **18**, 157–164 (2012).

[22] B. Abd-Alkareem, "Effect of Nano-Copper Oxide on the Electrical and Optical Properties of (PMMA) Polymer." PhD diss., College of Education for pure sciences, University of Babylon, (2016).

[23] R. Singh, M. S. Smitha, S. P. Singh, "The role of nanotechnology in combating multi-drug resistant bacteria." J. Nanosci. Nanotechnol. **14**(7), 4745–4756 (2014).

[24] K. Strzelec, N. Sienkiewicz, T. Szmechtyk, "Chapter-Classification of shape-memory polymers, polymer blends, and composites." Shape Mem. Polym. Blends Compos. Adv. Apps. **115**, 21–52 (2020).

[25] M. M. Prabhakar, A. K. Saravanan, A. H. Lenin, K. Mayandi, P. S. Ramalingam, "A short review on 3D printing methods, process parameters and materials." Mater. Today Proc. **45**, 6108–6114 (2021).

[26] H. G. El Gohary, I. A. Alhagri, T. F. Qahtan, A. N. Al-Hakimi, A. Saeed, F. Abolaban, E. M. Alshammari, G.M. Asnag, "Reinforcement of structural, thermal and electrical properties and antibacterial activity of PVA/SA blend filled with hybrid nanoparticles (Ag and TiO2 NPs): Nanodielectric for energy storage and food packaging industries." Ceram. Inter. **49**(12), 20174-20184 (2023).

[27] G. A. Kontos, A. L. Soulintzis, P. K. Karahaliou, G. C. Psarras, S. N. Georga, C. A. Krontiras, M. N. Pisanias, "Electrical relaxation dynamics in TiO_2-polymer matrix composites." Express Polym Lett. **1**(12), 781–789 (2007).

[28] E. Sharifzadeh, I. Ghasemi, M. Karrabi, H. Azizi, "A new approach in modeling of mechanical properties of binary phase polymeric blends." Iran. Polym. J. **23**(5), 525–530 (2014).

[29] E. Jawad, S. H. Khudhair, H. N. Ali, "A thermodynamic study of adsorption of some days on Iraqi Bentoniet modified clay." Eur. J. Sci. Res. **60**(1), 63–70 (2011).

[30] V. C. Tung, M. J. Allen, Y. Yang, R. B. Kaner, "High-throughput solution processing of large-scale graphene." Nat. Nanotechnol. **4**(1), 25–29 (2009).

[31] N. Mahmood, C. Zhang, H. Yin, Y. Hou, "Graphene-based nanocomposites for energy storage and conversion in lithium batteries,

supercapacitors and fuel cells." J. Mater. Chem. A. **2**(1), 15–32 (2014).

[32] S. S. Al-abbas, R. A. Ghazi, A. K. Al-shammari, N. R. Aldulaimi, A. R. Abdulridha, S. H. Al-nesrawy, E. Al-bermany, "Materials Today: Proceedings Influence of the polymer molecular weights on the electrical properties of Poly (vinyl alcohol) – Poly (ethylene glycols)/ Graphene oxide nanocomposites." Mater. Today Proc. **42**, 2469–2474 (2021).

[33] R. Muthuraj, M. Misra, A. K. Mohanty, "Biodegradable compatibilized polymer blends for packaging applications: A literature review." J. Appl. Polym. Sci. **135**(24), 45726 (2018).

[34] A. Adeniyi, O. Agboola, E. R. Sadiku, M. O. Durowoju, P. A. Olubambi, A. B. Reddy, I. D. Ibrahim, W. K. Kupolati, "Chapter 2-Thermoplastic-thermoset nanostructured polymer blends. In: Design and Applications of Nanostructured Polymer Blends and Nanocomposite Systems." pp. 15–38. Elsevier (2016).

[35] A. Ganguly, P. Channe, R. Jha, S. Mitra, S. Saha, "Review on transesterification in polycarbonate–poly (butylene terephthalate) blend." Polym. Eng. Sci. **61**(3), 650–661 (2021).

[36] V. Duin, C. Pagnoulle, R. Jerome," Strategies for Compatibilization of Polymer Blends, Prg." Polym. Sci. **23**(4), 707-757 (1998).

[37] V. B. Sadhu," Creation of crosslinkable interphases in polymer blends by means of novel coupling agents." PhD diss., der Fakultät Mathematik und Naturwissenschaften der Technische Universität Dresden (2004).

[38] M. Si, T. Araki, H. Ade, A. L. D. Kilcoyne, R. Fisher, J. C. Sokolov, M. H. Rafailovich, "Compatibilizing bulk polymer blends by using organoclays. Macromolecules." **39**(14), 4793–4801 (2006).

[39] S. Thomas, Y. Grohens, P. Jyotishkumar,"Chapter 7-Characterization of polymer blends: miscibility, morphology and interfaces." university of Copenhagen, John Wiley & Sons (2014).

[40] H. Hu, L. Onyebueke, A. Abatan, "Characterizing and modeling mechanical properties of nanocomposites-review and evaluation." J.

Miner. Mater. Charact. Eng. **9**, 275 (2010).

[41] A. N. Alias, Z. M. Zabidi, A. M. M. Ali, M. K. Harun, M. Z. A. Yahya, "Optical characterization and properties of polymeric materials for optoelectronic and photonic applications." Int. J. Appl. Sci. Technol. **3**(5), 11-38 (2013).

[42] J. P. Jose, K. Joseph, " Chapter 1-Advances in polymer composites: macro-and microcomposites–state of the art, new challenges, and opportunities." Polym. Compos., John Wiley & Sons, 1–16 (2012).

[43] M. L. Etheridge, S. A. Campbell, A. G. Erdman, C. L. Haynes, S. M. Wolf, J. McCullough, "The big picture on nanomedicine: the state of investigational and approved nanomedicine products." Nanomedicine nanotechnology, Biol. Med. **9**, 1–14 (2013).

[44] M. B. Ahmad, K. Shameli, W. Yunus, N. A. Ibrahim, M. Darroudi, "Synthesis and characterization of silver/clay/starch bionanocomposites by green method." Aust J Basic Appl Sci. **4**, 2158–2165 (2010).

[45] R. A. Hule, D. J. Pochan, "Polymer nanocomposites for biomedical applications." MRS Bull. **32**, 354–358 (2007).

[46] R. Roy, R. A. Roy, D. M. Roy, "Alternative perspectives on “quasi-crystallinity”: non-uniformity and nanocomposites." Mater. Lett. **4**, 323–328 (1986).

[47] J. Cuppoletti, "Chapter 10-Nanocomposites and polymers with analytical methods." BoD–Books on Demand, (2011).

[48] C. Sun, "Controlling the rheology of polymer/silica nanocomposites.", PhD diss., Eindhoven University of Technology (2010).

[49] K. A. Shenoy, "Effects of multi-wall carbon nanotubes on the mechanical properties of polymeric nanocomposites." PhD diss., Wichita State University, (2008).

[50] O. Kanoun, A. Bouhamed, R. Ramalingame, J. R. Bautista-Quijano, D. Rajendran, A. Al-Hamry, "Review on conductive polymer/CNTs nanocomposites based flexible and stretchable strain and pressure

sensors." Sensors. **21**, 341 (2021).

[51] R. Pathak, V. D. Punetha, S. Bhatt, M. Punetha, "Multifunctional role of carbon dot-based polymer nanocomposites in biomedical applications: a review." J. Mater. Sci. **58**(15), 6419-6443 (2023).

[52] M. S. Aziz, H. M. El-Mallah, "A.C. Conductivity and Dielectric Properties of Polycarbonate Sheet." Int. J. Polym. Mater. Polym. Biomater. **54**, 1157–1168 (2005).

[53] S. Perez, R. P. Scaringe, "Crystalline features of 4,4'-isopropylidenediphenylbis(phenyl carbonate) and conformational analysis of the polycarbonate of 2,2-bis(4-hydroxyphenyl)propane." Macromolecules. **20**, 68–77 (1987).

[54] W. Zhang, Y. Xu, "Mechanical properties of polycarbonate: experiment and modeling for aeronautical and aerospace applications." Elsevier (2019).

[55] A. E. Giannakas, C. E. Salmas, A. Karydis-Messinis, D. Moschovas, E. Kollia, V. Tsigkou, C. Proestos, A. Avgeropoulos, N. E. Zafeiropoulos, "Nanoclay and polystyrene type efficiency on the development of polystyrene/montmorillonite/oregano oil antioxidant active packaging nanocomposite films." Appl. Sci. **11**(20), 9364 (2021).

[56] L. A. Fakhri, B. Ghanbarzadeh, J. Dehghannya, F. Abbasi, H. Ranjbar, "Optimization of mechanical and color properties of polystyrene/nanoclay/nano ZnO based nanocomposite packaging sheet using response surface methodology." Food packaging and shelf life, **17**, 11-24 (2018).

[57] J. Scheirs, D. B. Priddy, "Chapter 3-Modern Styrenic Polymers: Polystyrenes and Styrenic Copolymers." (2003).

[58] C. Lynwood, "Chapter 1 and 5-Polystyrene: synthesis, characteristics, and applications." Nova publishers (2014).

[59] G. Meenakshi, A. Sivasamy, S. J. GA, S. Kavithaa, "Preparation, characterization and enhanced photocatalytic activities of zinc oxide

nano rods/silicon carbide composite under UV and visible light irradiations." J. Mol. Catal. A Chem. **411**, 167–178 (2016).

[60] D. A. M. Dutra, G. K. R. Pereira, K. Z. Kantorski, L. F. Valandro, F. B. Zanatta, "Does finishing and polishing of restorative materials affect bacterial adhesion and biofilm formation? A systematic review." Oper. Dent. **43**, E37–E52 (2018).

[61] I. P. Okokpujie, L. K. Tartibu, "Aluminum Alloy Reinforced with Agro-Waste, and Eggshell as Viable Material for Wind Turbine Blade to Annex Potential Wind Energy: A Review." J. Compos. Sci. **7**, 161 (2023).

[62] T. Kimoto, J. A. Cooper, "Fundamentals of silicon carbide technology: growth, characterization, devices and applications." John Wiley & Sons (2014).

[63] M. Souri, V. Hoseinpour, A. Shakeri, N. Ghaemi, "Optimisation of green synthesis of MnO nanoparticles via utilising response surface methodology." IET nanobiotechnology. **12**, 822–827 (2018).

[64] K. S. Prasad, A. Patra, "Green synthesis of MnO_2 nanorods using Phyllanthus amarus plant extract and their fluorescence studies." Green Process. Synth. **6**, 549–554 (2017).

[65] V. Hoseinpour, N. Ghaemi, "Green synthesis of manganese nanoparticles: Applications and future perspective–A review." J. Photochem. Photobiol. B Biol. **189**, 234–243 (2018).

[66] S. W. Donne, "Chapter-Manganese oxides for energy storage and conversion." Pan Stanford Publishing (2016).

[67] S. Mittler, "Nutritional Availability of Cobaltic Oxide, Co_2O_3." Nature. **174**, 88–89 (1954).

[68] S. S. Kanakkillam, B. Krishnan, D. A. Avellaneda, S. Shaji, "A simple synthesis of ZnO: Co_2O_3 nanocomposites by pulsed laser irradiation in liquid." Mater. Today Proc. **33**, 1444–1452 (2020).

[69] J. Mei, T. Liao, G. A. Ayoko, J. Bell, Z. Sun, "Cobalt oxide-based

nanoarchitectures for electrochemical energy applications." Prog. Mater. Sci. **103**, 596–677 (2019).

[70] B. Raveau, M. Seikh, "Chapter-Cobalt oxides: from crystal chemistry to physics." John Wiley & Sons (2012).

[71] B. S. Rathore, M. S. Gaur, K. S. Singh, "Optical properties of swift heavy ion beam irradiated polycarbonate/polystyrene composites films." In: Macromolecular Symposia. **315**(1), 169–176 (2012).

[72] B. Tripathi, "Testing of Multiwall Carbon Nanotube/Polycarbonate Nanocomposites for Chemical Capacitive Energy Storage." Adv. Electrochem. **1**(1), 27–30 (2013).

[73] R. Augustine, H. N. Malik, D. K. Singhal, A. Mukherjee, D. Malakar, N. Kalarikkal, S. Thomas, "Electrospun polycaprolactone/ZnO nanocomposite membranes as biomaterials with antibacterial and cell adhesion properties." J. Polym. Res. **21**(2), 1–17 (2014).

[74] M. S. Gaur, B. S. Rathore, "Structural and thermal properties of swift heavy ion beam irradiated polycarbonate/zinc oxide nanocomposites." J. Therm. Anal. Calorim. **119**(2), 1105–1112 (2015).

[75] S. Agarwal, Y. K. Saraswat, V. K. Saraswat, "Study of optical constants of ZnO dispersed PC/PMMA blend nanocomposites." Open Phys. J. **3**(1), 63-72 (2016).

[76] G. Santhosh, G. P. Nayaka, J. Aranha, "Investigation on Electrical and Dielectric Behaviour of Halloysite Nanotube Incorporated Polycarbonate Nanocomposite Films." Trans. Indian Inst. Met. **70**(1), 549–555 (2017).

[77] S. Li, S. Zhao, S. Qiang, G. Chen, Y. Chen, Y. Chen, "A novel zein/poly (propylene carbonate)/nano-TiO_2 composite films with enhanced photocatalytic and antibacterial activity." Process Biochem. **70**, 198–205 (2018).

[78] I. Fajriati, M. Mudasir, E. T. Wahyuni, "Adsorption and photodegradation of cationic and anionic dyes by TiO_2-chitosan

nanocomposite." Indones. J. Chem. **19**(2), 441–453 (2019).

[79] A. M. Patki, A. A. Maharanwar, S. K. Harde, R. K. Goyal, "Polycarbonate–hexagonal boron nitride composites with better dielectric properties for electronic applications." SN Appl. Sci. **1**(6), 1–8 (2019).

[80] M. F. H. Al-Kadhemy, R. A. Al-Mousawi, F. J. Kadhum, "Effects of Adding Coumarin Dye on Physical Properties of Blend (PC-PS) Film." Iraqi J. of Sci. **61**(7), 1633-1644 (2020).

[81] N. A. Al-Aaraji, A. Hashim, A. Hadi, H. M. Abduljalil, "Effect of silicon carbide nanoparticles addition on structural and dielectric characteristics of PVA/CuO nanostructures for electronics devices." Silicon. **14**(8), 4699–4705 (2022).

[82] Y. K. Saraswat, S. Agarwal, V. K. Saraswat, "Tailoring the Optical Properties of Polymers Blend Nanocomposites." Non-Metallic Mater. Sci. **3**(1), 24–30 (2021).

[83] Y. Chen, T. Wang, J. Pan, M. Wang, A. Chen, Y. Chen, "Fabrication, characterization and photocatalytic degradation activity of PS/PANI/CeO_2 tri-layer nanostructured hybrids. Bull. Mater. Sci. **45**(1), 45 (2022).

[84] A. H. Mohammed, M. A. Habeeb, "Co_2O_3 Nanofiller-Based Polymer Blend Nanocomposites for Enhanced Optical Properties for Optoelectronics Devices and as a Model of Antibacterial." HIV Nurs. **22**(2), 1167–1172 (2022).

[85] H. A. J. Hussien, R. G. Kadhim, A. Hashim, "Augmented structural and optical characteristics of SnO_2/MnO_2-doped PEO/PVP blend for photodegradation against organic pollutants." Polym. Bull. **79**(7), 5219–5234 (2022).

[86] A. J. K. Algidsawi, A. Hashim, A. Hadi, M. A. Habeeb, H. H. Abed, "Influence of MnO_2 Nanoparticles Addition on Structural, Optical and Dielectric Characteristics of PVA/PVP for Pressure Sensors." Phys.

Chem. Solid State. **23**(2), 353–360 (2022).

[87] A. A. El-Gamal, "Optical and Electrical Properties of Polystyrene/Poly-methyl methacrylate Polymeric Blend Filled with Semiconductor and Insulator Nanofillers." Phys. Status Solidi RRL. **2300145**, 1-11 (2023).

[88] S. O. Adeosun, G. I. Lawal, S. A. Balogun, E. I. Akpan, "Review of green polymer nanocomposites." J. Miner. Mater. Charact. Eng. **11**(04), 385 (2012).

[89] T. Sharma, M. Garg, "Polystyrene/ZnO Nanocomposite Films with Optimized Optical Properties for UV-shielding Applications." Transactions on Electrical and Electronic Materials, **24**(3), 217-227 (2023).

[90] C.U. Devi, A.K. Sharma, V. V. R. N. Rao, "Electrical and optical properties of pure and silver nitrate-doped polyvinyl alcohol films." Mater. Lett. **56**(3), 167-174 (2002).

[91] M.F. Al-Mudhaffer, M.A. Nattiq, M.A. Jaber, "Linear optical properties and energy loss function of Novolac: epoxy blend film." Arch. Appl. Sci. Res. **4**(4), 1731–7140 (2012).

[92] J. I. Kroschwitz, "Electrical and electronic properties of polymers: A state-of-the-art compendium." Wiley-Interscience (1988).

[93] T. K. Hamad, R. M. Yusop, B. Abdullah, E. Yousif, "Laser induced modification of the optical properties of nano-ZnO doped PVC films." Int. J. Polym. Sci. **2014**, (2014).

[94] O. Stenzel, "The physics of thin film optical spectra." Berlin/Heidelberg, Germany: Springer, 978-3 (2015).

[95] J. I. Pankove, "Optical processes on semiconductors Dover publication." Inc. New york. (1971).

[96] A. Begum, A. Hussain, A. Rahman, "Optical and electrical properties of doped and undoped Bi_2S_3–PVA films prepared by chemical drop method." Mater. Sci. Appl. **2**, 163–168 (2011).

[97] K. C. Lalithambika, K. Shanthakumari, S. Sriram, "Optical properties of

CdO thin films deposited by chemical bath method." Int. J. ChemTech Res. **6**(5), 3071–3077 (2014).

[98] A. M. Andriesh, M. S. Iovu, S. D. Shutov, "Chalcogenide non-crystalline semiconductors in optoelectronics." J. Optoelectron. Adv. Mater. **4**(3), 631–647 (2002).

[99] J. Tauc, A. Menth, D. L. Wood, "Optical and magnetic investigations of the localized states in semiconducting glasses." Phys. Rev. Lett. **25**(11), 749 (1970).

[100] M. H. Lakhdar, B. Ouni, M. Amlouk, "Thickness effect on the structural and optical constants of stibnite thin films prepared by sulfidation annealing of antimony films." Optik. **125**(10), 2295-2301 (2014).

[101] A. S. Hassanien, A. A. Akl, "Effect of Se addition on optical and electrical properties of chalcogenide CdSSe thin films." Superlattices Microstruct. **89**(1), 153–169 (2016).

[102] O. V. Rambadey, A. Kumar, A. Sati, P. R. Sagdeo, "Exploring the Interrelation between Urbach Energy and Dielectric Constant in Hf-Substituted $BaTiO_3$." ACS Omega. **6**(47), 32231-32238 (2021).

[103] J. H. Nahida, R. F. Marwa, "Study of the optical constants of the PMMA/PC blends." AIP Conference Proceedings, Amer. Inst. Phys. **1400**(1), 585-595 (2011).

[104] T. S. Soliman, S. A. Vshivkov, "Effect of Fe nanoparticles on the structure and optical properties of polyvinyl alcohol nanocomposite films." J. Non. Cryst. Solids. **519**, 119452 (2019).

[105] A. S. Hassanien, I. M. El Radaf, "Optical characterizations of quaternary Cu_2MnSnS_4 thin films: novel synthesis process of film samples by spray pyrolysis technique." Phys. B Condens. Matter. **585**, 412110 (2020).

[106] M. M. Nofal, S. B. Aziz, J. M. Hadi, W. O. Karim, E. M. A. Dannoun, A. M. Hussein, S.A. Hussen, "Polymer composites with 0.98 transparencies and small optical energy band gap using a promising green methodology: Structural and optical properties." Polymers (Basel).

13(10), 1648 (2021).

[107] S. A. Salman, M. H. Abdu-allah, N. A. Bakr, "Optical characterization of red methyl doped poly (vinyl alcohol) films." Int. J. Eng. Tech. Res. **2**(4), 126-128 (2014).

[108] W. Cun, W. Xinming, Z. Jincai, M. Bixian, S. Guoying, P. Ping'an, F. Jiamo, "Synthesis, characterization and photocatalytic property of nano-sized Zn_2SnO_4." J. Mater. Sci. **37**(13), 2989–2996 (2002).

[109] A. A. Nathan, A. Onoja, A. Amah, "Influence of PVA, PVP on crystal and optical properties of europium doped strontium aluminate nanoparticles." Amer. J. Eng. Res. **4**(4), 85-91 (2015).

[110] O. G. Abdullah, D. A. Tahir, S. S. Ahmad, H. T. Ahmad, "Optical properties of PVA:$CdCl_2.H_2O$ polymer electrolytes." IOSR J. Appl. Phys. **4**(3), 52–57 (2013).

[111] S. H. Brewer, S. Franzen, "Optical properties of indium tin oxide and fluorine-doped tin oxide surfaces: correlation of reflectivity, skin depth, and plasmon frequency with conductivity." J. Alloys Compd. **338**(1-2), 73–79 (2002).

[112] J. H. Nahida, "Spectrophotometric analysis for the UV-irradiated (PMMA)." Int. J. Basic Appl. Sci. **12**(2), 58–67 (2012).

[113] K. H. H. Al-Attiyah, A. Hashim, S. F. Obaid, "Fabrication of novel (carboxy methyl cellulose–polyvinylpyrrolidone–polyvinyl alcohol)/lead oxide nanoparticles: structural and optical properties for gamma rays shielding applications." Int. J. Plast. Technol. **23**(1), 39–45 (2019).

[114] M. Banerjee, A. Jain, G. S. Mukherjee, "Spectroscopic evaluation of optical parameters of a transition metal salt filled polymer material." Def. Sci. J. **68**(2), 225 (2018).

[115] M. H. Hassouni, K. A. Mishjil, S. S. Chiad, N. F. Habubi, "Effect of gamma irradiation on the optical properties of Mg doped CdO Thin films deposited by Spray Pyrolysis." Int. Lett. Chem. Phys. Astron. **11**, 26–37

(2013).

[116] T. G. Abdel-Malik, R. M. Abdel-Latif, A. Sawaby, S. M. Ahmed, "Electrical properties of pure and doped polyvinyl alcohol (PVA) films using gold and aluminum electrodes." J. Appl. Sci. Res. **4**(3), 331–336 (2008).

[117] R. V. Waghmare, N. G. Belsare, F. C. Raghuwanshi, S. N. Shilaskar, "Study of dc electrical conductivity of paranitroaniline doped (1:1) polyvinylchloride and poly (methyl methacrylate) polyblends." Bull. Mater. Sci. **30**(2), 167–172 (2007).

[118] M. S. Ahmad, A. M. Zihilif, E. Martuscelli, G. Ragosta, E. Scafora, "The electrical conductivity of polypropylene and nickel-coated carbon fiber composite." Polym. Compos. **13**(1), 53–57 (1992).

[119] P. Heitjans, E. Tobschall, M. Wilkening, "Ion transport and diffusion in nanocrystalline and glassy ceramics: Impedance and NMR spectroscopy measurements on Li ion conductors." Eur. Phys. J. Spec. Top. **161**(1), 97–108 (2008).

[120] F. Jensen, "Activation energies and the Arrhenius equation." Qual. Reliab. Eng. Int. **1**(1), 13–17 (1985).

[121] S .I. Martínez-Monteagudo, V. M. Balasubramaniam, "Chapter-Fundamentals and Applications of High-Pressure Processing Technology." In. High Pressure Processing of Food. Food Engineering Series. Springer, New York, NY. (2016).

[122] Ali, R., Ali, M.: Effect of cobalt chloride ($CoCl_2$) on the electrical and optical Properties of (PVA-PVP-$CoCl_2$) films. Adva. Phys. Theor. Appli. **18**, 47–53 (2013).

[123] J. Cao, D. D. L. Chung, "Electric polarization and depolarization in cement-based materials, studied by apparent electrical resistance measurement." Cem. Concr. Res. **34**(3), 481–485 (2004).

[124] A. Hashim, "Experimental Study of Electrical Properties of (PVA-$CoNO_3$, $AgCO_3$) Composites." Am. Jou. Sci. Res. 68, 56–61 (2012).

[125] H. N. Najeeb, "Dielectrical and electrical properties of PVA-NaI composites." Iraqi J. Phys. **11**(22), 56–63 (2013).

[126] B. M. Tareev, "Physics of dielectric materials." Mir Publshers (1975).

[127] J. Guo, T. Bamber, M. Chamberlain, L. Justham, M. Jackson, "Optimization and experimental verification of coplanar interdigital electroadhesives." J. Phys. D. Appl. Phys. **49**(41), 415304 (2016).

[128] P. Barber, S. Balasubramanian, Y. Anguchamy, S. Gong, A. Wibowo, H. Gao, H. J. Ploehn, H. C. Zur Loye, "Polymer composite and nanocomposite dielectric materials for pulse power energy storage." Materials (Basel). **2**(4), 1697-1733 (2009).

[129] T. Putjuso, P. Sangarun, "Influence of annealing on the giant dielectric properties of cuo ceramics prepared by a simple pva sol-gel." Asia-Pacific J. Sci. Technol. **17**(2), 203–210 (2012).

[130] M. Akram, A. Javed, T. Z. Rizvi, "Dielectric properties of industrial polymer composite materials." Turkish J. Phys. **29**(6), 355–362 (2005).

[131] S. Kitouni, "Dielectric properties of triaxial porcelain prepared using raw native materials without any additions." Balk. J. Electr. Comput. Eng. **2**(3), 93-165 (2014).

[132] S. Prasher, M. Kumer, S. Singh, "Analysis of electrical properties of Li^{3+} ion beam irradiated lexan polycarbonate." Asian J. Chem. **21**(10), 43-46 (2009).

[133] A. Hashim, "Enhanced structural, optical, and electronic properties of In_2O_3 and Cr_2O_3 nanoparticles doped polymer blend for flexible electronics and potential applications." J. Inorg. Organomet. Polym. Mater. **30**(4), 3894–3906 (2020).

[134] U. K. Mishra, J. Singh, "Chapter-Semiconductor device physics and design." Springer (2008).

[135] M. Bin Ahmad, J. J. Lim, K. Shameli, N. A. Ibrahim, M. Y. Tay, B. W. Chieng, "Antibacterial activity of silver bionanocomposites synthesized by chemical reduction route." Chemistry Central Journal, **6**, 1-9 (2012).

[136] D. Sistemática, S. S. Gabriela, F. R. Daniela, B. T. Helia, "Copper nanoparticles as potential antimicrobial agent in disinfecting root canals. A systematic review." Int. J. Odontostomat. **10**(3), 547-554 (2016).

[137] G. Tong, M. Yulong, G. Peng, X. Zirong, "Antibacterial effects of the Cu (II)-exchanged montmorillonite on Escherichia coli K88 and Salmonella choleraesuis." Vet. Microbiol. **105**(2), 113-122 (2005).

[138] D. Adamovic, B. Ristic, F. Zivic, "Chapter-Review of existing biomaterials-method of material selection for specific applications in orthopedics." Biomater. Clin. Pract. Adv. Clin. Res. Med. devices. 47–99 (2018).

[139] L. Wang, C. Hu, L. Shao, "The antimicrobial activity of nanoparticles: present situation and prospects for the future." Int. J. Nanomedicine. **12**, 1227 (2017).

[140] Y. Zheng, P. Zhiming, W. Xinchen, "Advances in photocatalysis in China." Chinese J. Catal. **34**(3), 524-535 (2013).

[141] M. A. Lazar, S. Varghese, S. S. Nair, "Photocatalytic water treatment by titanium dioxide: recent updates." Catalysts. **2**(4), 572-601 (2012).

[142] A. Gnanaprakasam, V. M. Sivakumar, M. Thirumarimurugan, "Influencing parameters in the photocatalytic degradation of organic effluent via nanometal oxide catalyst: a review." Indian J. Mater. Sci. **2015**, 1–16 (2015).

[143] T. B. Mekonnen, A. T. Mengesha, H. H. Dube, "Photocatalytic Degradation of Organic Pollutants: The Case of Conductive Polymer Supported Titanium Dioxide (TiO_2) Nanoparticles: A Review." Nanosci. Nanometrology. **7**(1), 1-13 (2021).

[144] A. Hernández-Ramírez, I. Medina-Ramírez, "Chapter-Semiconducting materials. Photocatalytic Semicond. Synth. Charact. Environ. Appl. 1–40 (2015).

[145] G. Jian, Y. Jiao, Q. Meng, Z. Wei, J. Zhang, C. Yan, K. S. Moon, C. P. Wong, "Enhanced dielectric constant and energy density in a

$BaTiO_3$/polymer-matrix composite sponge." Commun. Mater. **1**(1), 91 (2020).

[146] K. J. Shieh, M. Li, Y. H. Lee, S. D. Sheu, Y. T. Liu, Y. C. Wang, "Antibacterial performance of photocatalyst thin film fabricated by defection effect in visible light." Nanomedicine Nanotechnology, Biol. Med. **2**(2), 121-126 (2006).

[147] A. Mills, S. Le Hunte, "An overview of semiconductor photocatalysis. J. Photochem. Photobiol. A Chem. **108**(1), 1-35 (1997).

[148] H. Selçuk, V. Naddeo, L. Rizzo, V. Belgiorno, "Advanced treatment by ozonation and sonolysis for domestic wastewater reuse." In: Proceeding of the 10th International Conference on Environmental Science and Technology, Kos Island, Greece. 5–7 (2007).

[149] F. Fazlali, A. reza Mahjoub, R. Abazari,"A new route for synthesis of spherical NiO nanoparticles via emulsion nano-reactors with enhanced photocatalytic activity." Solid State Sci. **48**, 263–269 (2015).

[150] Z. Mengyue, C. Shifu, T. Yaowu, "Photocatalytic degradation of organophosphorus pesticides using thin films of TiO_2." J. Chem. Technol. Biotechnol. **64**(4), 339-344 (1995).

[151] M. M. Baig, E. Pervaiz, M. J. Afzal, "Catalytic activity and kinetic studies of Core@Shell nanostructure $NiFe_2O_4$@TiO_2 for photocatalytic degradation of methyl orange dye." J. Chem. Soc. Pak. **42**(04), 531 (2020).

[152] N. Xu, Z. Shi, Y. Fan, J. Dong, J. Shi, M. Z. C. Hu, "Effects of particle size of TiO_2 on photocatalytic degradation of methylene blue in aqueous suspensions." Ind. Eng. Chem. Res. **38**(2), 373-379 (1999).

[153] Y. Shu, H. Tian, Y. Yang, C. Li, Y. Cui, W. Mi, Y. Li, Z. Wang, N. Deng, B. Peng, "Surface-modified piezoresistive nanocomposite flexible pressure sensors with high sensitivity and wide linearity." Nanoscale. **7**(18), 8636-8644 (2015).

[154] Q. T. Lai, Q. J. Sun, Z. Tang, X. G. Tang, X. H. Zhao, "Conjugated

Polymer-Based Nanocomposites for Pressure Sensors. Molecules." **28**(4), 1627 (2023).

[155] H. Mei, C. Zhang, R. Wang, J. Feng, T. Zhang, "Impedance characteristics of surface pressure-sensitive carbon black/silicone rubber composites." Sensors Actuators A Phys. **233**, 118–124 (2015).

[156] A. Hadi, A. Hashim, Y. Al-Khafaji, "Structural, optical and electrical properties of PVA/PEO/SnO_2 new nanocomposites for flexible devices." Trans. Electr. Electron. Mater. **21**(1), 283–292 (2020).

[157] A. A. Al-Muntaser, R. A. Pashameah, K. Sharma, E. Alzahrani, A. E. Tarabiah, "Reinforcement of structural, optical, electrical, and dielectric characteristics of CMC/PVA based on GNP/ZnO hybrid nanofiller: nanocomposites materials for energy-storage applications." Int. J. Energy Res. **46**(15), 23984-23995 (2022).

[158] A. Yusuf, A. R. Z. Almotairy, H. Henidi, O. Y. Alshehri, M. S. Aldughaim, "Nanoparticles as Drug Delivery Systems: A Review of the implication of nanoparticles' physicochemical properties on responses in biological systems." Polymers (Basel). **15**(7), 1596 (2023).

[159] J. Li, S. Wang, H. Liu, S. Wang, L. You, "Preparation and characterization of polystyrene/polycarbonate composite hollow microspheres by microencapsulation method." J. Mater. Sci. **46**(1), 3604–3610 (2011).

[160] A. B. D. Nandiyanto, R. Oktiani, R. Ragadhita, "How to read and interpret FTIR spectroscope of organic material." Indones. J. Sci. Technol. **4**(1), 97–118 (2019).

[161] H. Wu, Z. Su, A. Takahara, Molecular composition distribution of polycarbonate/polystyrene blends in cylindrical nanopores. Polym. J. **43**(7), 600-605 (2011).

[162] G. Mitchell, F. France, A. Nordon, P. L. Tang, L. T. Gibson, "Assessment of historical polymers using attenuated total reflectance-Fourier transform infra-red spectroscopy with principal component

analysis." Herit. Sci. **1**(1), 1-10 (2013).

[163] M. Haghighi-Yazdi, P. Lee-Sullivan, "FTIR analysis of a polycarbonate blend after hygrothermal aging." J. Appl. Polym. Sci. **132**(3), 41316 (2015).

[164] A. M. El Sayed, W. M. Morsi, "α-Fe_2O_3/(PVA-PEG) nanocomposite films; synthesis, optical, and dielectric characterizations." J. Mater. Sci. **49**(8), 5378-5387 (2014).

[165] Y. Li, J. Pionteck, P. Pötschke, B. Voit, "Organic vapor sensing behavior of polycarbonate/polystyrene/multi-walled carbon nanotube blend composites with different microstructures." Mater. Des. **179**, 107897 (2019).

[166] X. Zhi, J. Liu, H. B. Zhang, S. Hong, Z. Z. Yu "Simultaneous enhancements in electrical conductivity and toughness of selectively foamed polycarbonate/polystyrene/carbon nanotube microcellular foams. Compos." Part B Eng. **143**, 161–167 (2018).

[167] C. Z. Chuai, K. Almdal, I. Johannsen, J. Lyngaae-Jørgensen, "Morphology evolution of polycarbonate–polystyrene blends during compounding." Polymer (Guildf). **42**(19), 8217–8223 (2001).

[168] M. Afeworki, R. A. McKay, J. Schaefer, "Selective observation of the interface of heterogeneous polycarbonate/polystyrene blends by dynamic nuclear polarization carbon-13 NMR spectroscopy." Macromolecules. **25**(16), 4084-4091 (1992).

[169] O. G. Abdullah, D. R. Saber, L.O. Hamasalih, "Complexion formation in PVA/PEO/$CuCl_2$ solid polymer electrolyte." Univers. J. Mater. Sci. **3**(1), 1-5 (2015).

[170] H. Abduljalil, A. Hashim, A. Jewad, "The effect of addition titanium dioxide on electrical properties of poly-methyl methacrylate." Eur. J. Sci. Res. **63**(2), 231-235 (2011).

[171] A. Mahapatra, "Fabrication and characterization of novel iron oxide/alumina nanomaterials for environmental applications." PhD diss.,

Abhipsa Mahapatra to the National Institute of Technology, Rourkela, India, (2013).

[172] A. Salama, "Cellulose/silk fibroin assisted calcium phosphate growth: Novel biocomposite for dye adsorption." Int. J. Biol. Macromol. **165**(B), 1970–1977 (2020).

[173] A. Hashim, "Fabrication and characteristics of flexible, lightweight, and low-cost pressure sensors based on PVA/SiO_2/SiC nanostructures." J. Mater. Sci. Mater. Electron. **32**(3), 2796-2804 (2021).

[174] V. Wallqvist, P. M. Claesson, A. Swerin, J. Schoelkopf, P. A. C. Gane, "Interaction forces between talc and hydrophobic particles probed by AFM. Colloids Surfaces A Physicochem. Eng. Asp. **277**(1-3), 183-190 (2006).

[175] G. A. M. Amin, M. H. Abd-El Salam, "Optical, dielectric and electrical properties of PVA doped with Sn nanoparticles." Mater. Res. Express. **1**(2), 025024 (2014).

[176] A. P. Indolia, M. S. Gaur, "Optical properties of solution grown PVDF-ZnO nanocomposite thin films." J. Polym. Res. **20**(12), 1–8 (2013).

[177] H. M. Shanshool, M. Yahaya, W. M. M. Yunus, I. Y. Abdullah, "Measurements of nonlinear optical properties of PVDF/ZnO using Z-scan technique." Brazilian J. Phys. **45**(3), 538–544 (2015).

[178] P. Phukan, D. Saikia, "Optical and structural investigation of CdSe quantum dots dispersed in PVA matrix and photovoltaic applications." Int. J. Photoenergy. **2013**, 1-6 (2013).

[179] Y. Feng, N. Dong, G. Wang, Y. Li, S. Zhang, K. Wang, L. Zhang, W. J. Blau, J. Wang, "Saturable absorption behavior of free-standing graphene polymer composite films over broad wavelength and time ranges." Opt. Express. **23**(1), 559-569 (2015).

[180] E. Fortunati, F. Luzi, D. Puglia, R. Petrucci, J. M. Kenny, L. Torre, "Processing of PLA nanocomposites with cellulose nanocrystals extracted from Posidonia oceanica waste: Innovative reuse of coastal

plant." Ind. Crops Prod. **67**, 439–447 (2015).

[181] N. B. Kumar, V. Crasta, B. M. Praveen, "Advancement in microstructural, optical, and mechanical properties of PVA (Mowiol 10-98) doped by ZnO nanoparticles." Phys. Res. Int. **2014**, 1-9 (2014).

[182] Y. M. Jawad, M. F. H. Al-Kadhemy, J. A. S. Salman, "Synthesis structural and optical properties of CMC/MgO nanocomposites." In: Materials Science Forum. **1039**, 104-114 (2021).

[183] M. A. Morsi, A. M. Abdelghany, "UV-irradiation assisted control of the structural, optical and thermal properties of PEO/PVP blended gold nanoparticles." Mater. Chem. Phys. **201**, 100–112 (2017).

[184] F. Gharbi, K. Benthami, T. H. Alsheddi, M. M. E. Barakat, N. Alnaim, A. Alshoaibi, S. A. Nouh, "Structural, Thermal, and Optical Studies of Gamma Irradiated Polyvinyl Alcohol-, Lignosulfonate-, and Palladium Nanocomposite Film." Polymers (Basel). **14**(13), 2613 (2022).

[185] A. J. Kadham, D. Hassan, N. Mohammad, A. H. Ah-yasari, "Fabrication of (polymer blend-magnesium oxide) nanoparticle and studying their optical properties for optoelectronic applications." Bull. Electr. Eng. Informatics. **7**(1), 28-34 (2018).

[186] E. F. dos Reis, F. S. Campos, A. P. Lage, R. C. Leite, L. G. Heneine, W. L. Vasconcelos, Z. I. P. Lobato, H. S. Mansur, "Synthesis and characterization of poly (vinyl alcohol) hydrogels and hybrids for rMPB70 protein adsorption." Mater. Res. **9**(2), 185–191 (2006).

[187] F. A. Mustafa, "Optical properties of NaI doped polyvinyl alcohol films. Phys. Sci. Res. Int. **1**(1), 1–9 (2013).

[188] Z. Hossein Esfahani, M. Ghanipour, D. Dorranian, "Effect of dye concentration on the optical properties of red-BS dye-doped PVA film." J. Theor. Appl. Phys. **8**(2), 117–121 (2014).

[189] V. Sangawar, M. Golchha, "Evolution of the optical properties of polystyrene thin films filled with zinc oxide nanoparticles." Int. J. Sci. Eng. Res. **4**(6), 2700–2705 (2013).

[190] E. T. Abd-Al Hussein, A. M. Hameed, "Studying some optical properties of polyethylene glycol doped with Al-nanoparticles." Mater. Sci. Foru. **1002**, 104–113 (2020).

[191] M. Pandey, G. M. Joshi, K. Deshmukh, J. Ahmad, "Impedance spectroscopy and conductivity studies of $CdCl_2$ doped polymer electrolyte." Adv. Mater. Lett. **6**(2), 165-171 (2015).

[192] J. R. Babu, K. V. Kumar, "Studies on structural and electrical properties of $NaHCO_3$ doped PVA films for electrochemical cell applications." Int. J. Chem-Tech Res. **7**(1), 2014-2015 (2015).

[193] S.P. Ansari, F. Mohammad, "Electrical studies on the composite of polyaniline with Zinc oxide nanoparticles." IUP J. Chem. **3**(4), 7–18 (2010).

[194] M. P. Aji, S. Bijaksana, M. Abdullah, "Electrical and magnetic properties of polymer electrolyte (PVA: LiOH) containing in situ dispersed Fe_3O_4 nanoparticles." Int. Sch. Res. Not. **2012**, 1-7(2012).

[195] S. D. Meshram, R. V. Rupnarayan, S. V. Jagtap, V. G. Mete, V. S. Sangawar, "Synthesis and characterization of lead oxide nanoparticles." Int. J. Chem. Phys. Sci. **4**(Special Issue), 83–88 (2015).

[196] S. S. Shinde, J. A. Kher, M. V. Kulkarni, "Synthesis, characterization and electrical property of silver doped polypyrrole nanocomposites." Synthesis (Stuttg). **3**(6), 14021- 14026 (2014).

[197] P.A. Fartode, S. S. Yawale, S. P. Yawale, "Study of transport and electrical properties of PEO:PVP:$NaClO_2$ based polymer electrolyte." Int. J. Chem. Phys. Sci. **4**(Special Issue), 60–64 (2015).

[198] R. Divya, M. Meena, C. K. Mahadevan, C. M. Padma, "Formation and properties of ZnO nanoparticle dispersed PVA films." Inter. J. Eng. Res. Technol. **3**(7), 722 (2014).

[199] M. F. Ahmer, S. Hameed, "Studies on the electrical conductivity measurement of organic/organic composite polyvinyl alcohol/polyaniline (PVA/PANI)." Studies. **3**(10), 12731- 12736 (2014).

[200] P.L. Reddy, K. Deshmukh, K. Chidambaram, M. M. N. Ali, K. K. Sadasivuni, Y. R. Kumar, R. Lakshmipathy, S.K.K. Pasha, "Dielectric properties of polyvinyl alcohol (PVA) nanocomposites filled with green synthesized zinc sulphide (ZnS) nanoparticles." J. Mater. Sci. Mater. Electron. **30**(4), 4676–4687 (2019).

[201] L. H. Gaabour, "Effect of addition of TiO_2 nanoparticles on structural and dielectric properties of polystyrene/polyvinyl chloride polymer blend." AIP Adv. **11**(10), 105120 (2021).

[202] S. C. Mishra, "Dielectric behavior of bio-waste reinforced polymer composites." **1**(9), 32-44 (2014).

[203] A. Hashim, A. Hadi, "synthesis and characterization of novel piezoelectric and energy storage nanocomposites: biodegradable materials–magnesium oxide nanoparticles." Ukr. J. Phys. **62**(12), 1050 (2017).

[204] S. Ju, M. Chen, H. Zhang, Z. Zhang, "Dielectric properties of nanosilica/low-density polyethylene composites: The surface chemistry of nanoparticles and deep traps induced by nanoparticles." Express Polym. Lett. **8**(9), 682–691 (2014).

[205] X. Huang, S. Wang, M. Zhu, K. Yang, P. Jiang, Y. Bando, D. Golberg, C. Zhi, "Thermally conductive, electrically insulating and melt-processable polystyrene/boron nitride nanocomposites prepared by in situ reversible addition fragmentation chain transfer polymerization. Nanotechnology." **26**(1), 015705 (2014).

[206] H. Shivashankar, K. A. Mathias, P. R. Sondar, M. H. Shrishail, S.M. Kulkarni, "Study on low-frequency dielectric behavior of the carbon black/polymer nanocomposite." J. Mater. Sci. Mater. Electron. **32**(20), 28674–28686 (2021).

[207] T. E. Somesh, L. R. Shivakumar, M. A. Sangamesh, D. T. Siddaramaiah, "Polymer nanocomposites comprising PVA matrix and $AgGaO_2$ nanofillers: probing the effect of intercalation on optical and dielectric

response for optoelectronic applications." Ind. J. Sci. Technol. **31**(1), 2579–2589 (2021).

[208] M. Barala, M. Mehkoom, D. Mohan, S. Sanghi, S. M. Afzal, "Nonlinear optical characterization and optical limiting of silver nanoparticles embedded polystyrene foils." J. Mater. Sci.: Mater. Elec. **33**(32), 24631-24645 (2022).

[209] J. R. Morones, J. L. Elechiguerra, A. Camacho, K. Holt, J. B. Kouri, J. T. Ramírez, M. J. Yacaman, "The bactericidal effect of silver nanoparticles. Nanotechnology. **16**(10), 2346 (2005).

[210] O. Choi, K. K. Deng, N. J. Kim, L. Ross Jr, R.Y. Surampalli, Z. Hu, "The inhibitory effects of silver nanoparticles, silver ions, and silver chloride colloids on microbial growth." Water Res. **42**(12), 3066–3074 (2008).

[211] I. Sondi, B. Salopek-Sondi, S. D. Škapin, S. Šegota, I. Jurina, B. Vukelić, "Colloid-chemical processes in the growth and design of the bio-inorganic aragonite structure in the scleractinian coral Cladocora caespitosa." J. Colloid Interface Sci. **354**(1), 181–189 (2011).

[212] G. Franci, A. Falanga, S. Galdiero, L. Palomba, M. Rai, G. Morelli, M. Galdiero, "Silver nanoparticles as potential antibacterial agents." Molecules **20**(5), 8856–8874 (2015).

[213] M. Alizadeh-Sani, H. Hamishehkar, A. Khezerlou, M. Maleki, M. Azizi-Lalabadi, V. Bagheri, P. Safaei, T. Azimi, M. Hashemi, A. Ehsani, "Kinetics analysis and susceptibility coefficient of the pathogenic bacteria by titanium dioxide and zinc oxide nanoparticles." Adv. Pharm. Bull. 10(1), 56 (2020).

[214] P. P. Mahamuni, P. M. Patil, M. J. Dhanavade, M. V. Badiger, P. G. Shadija, A. C. Lokhande, R. A. Bohara, "Synthesis and characterization of zinc oxide nanoparticles by using polyol chemistry for their antimicrobial and antibiofilm activity." Biochem. Biophys. reports. **17**, 71–80 (2019).

[215] S. Ravikumar, R. Gokulakrishnan, "The inhibitory effect of metal oxide

nanoparticles against poultry pathogens." Int. J. Pharm. Sci. Drug Res. **4**(2), 157–159 (2012).

[216] S. S. Behera, J. K. Patra, K. Pramanik, N. Panda, H. Thatoi, "Characterization and evaluation of antibacterial activities of chemically synthesized iron oxide nanoparticles." J. Nano Sci. Eng. **2**, 196-200 (2012)

[217] Y. T. Prabhu, K. V. Rao, B. S. Kumari, V. S. S. Kumar, T. Pavani, "Synthesis of Fe_3O_4 nanoparticles and its antibacterial application." Int. Nano Lett. **5**, 85–92 (2015).

[218] M. Jarvin, D. R. Rosaline, T. Gopalakrishnan, M. B. R. Kamalam, E. L. Foletto, G. L. Dotto, S. S. R. Inbanathan, "Remarkable photocatalytic performances towards pollutant degradation under sunlight and enhanced electrochemical properties of TiO_2/polymer nanohybrids." Environ. Sci. Pollut. Res. **30**(22), 62832-62846 (2023).

[219] A. Bhosale, J. Kadam, T. Gade, K. Sonawane, K. Garadkar, "Efficient photodegradation of methyl orange and bactericidal activity of Ag doped ZnO nanoparticles." J. Indian Chem. Soc. **100**(2), 100920 (2023).

[220] F. K. Algethami, K. Trabelsi, A. Hajjaji, M. B. Rabha, L. Khezami, M. R. Elamin, B. Bessais, M. A. El Khakani, "Photocatalytic activity of silicon nanowires decorated with PbS nanoparticles deposited by pulsed laser deposition for efficient wastewater treatment." Materials (Basel). **15**(4), 4970 (2022).

[221] T. Hoon Kim, A. C. Arias, "Characterization and applications of piezoelectric polymers." Electr. Eng. Comput. Sci. Univ. Calif. Berkeley, CA, USA. (2015).

[222] N. Sanguanwong, "Effects of titanium dioxide on properties of polyvinyl alcohol with and without surfactant." PhD diss., Silpakorn University (2012).

[223] R. Ramalingame, A. Lakshmanan, F. Müller, U. Thomas, O. Kanoun, "Highly sensitive capacitive pressure sensors for robotic applications

based on carbon nanotubes and PDMS polymer nanocomposite." J. Sensors Sens. Syst. **8**(1), 87–94 (2019).

[224] H. A. J. Hussien, R.G. Kadhim, A. Hashim, "Investigation of Structural and Dielectric Properties of (Polymer Blend/Oxides Nanoparticles) for Pressure Sensors." J. Phys. Conf. Ser. **1818**(1), 012187 (2021).

الخلاصة

في هذه الدراسة ، تم تصنيع نوعين جديدين من المتراكبات النانوية الحيوية ($PC-PS/SiC-MnO_2$) و ($PC-PS/SiC-Co_2O_3$) بتوظيف تقنية صب المحلول . صنع المتراكب الأساس المتمثل بالخليط البوليمري (PC/PS) بتركيز (50 wt.%) من البولي كربونيت مع (50 wt.%) من البولي ستايرين وكذلك تم إضافة جسيمات كاربيد السيليكون النانوية (SiC) للخليط البوليمري (PC/PS) بعد ذلك تم إضافة جسيمات ثنائي أوكسيد المنغنيز النانوية (MnO_2) وجسيمات ثلاثي أوكسيد الكوبلت النانوية (Co_2O_3) الى الخليط البوليمري بنسب وزنية مختلفة وهي (1.3 ، 2.6 ، 3.9 ، 5.2) %.

تمت دراسة تأثير تراكيز جسيمات كاربيد السيليكون النانوية وثنائي أوكسيد المنغنيز وثلاثي أوكسيد الكوبلت النانوية المضافة على الخصائص التركيبية والمورفولوجية والبصرية والكهربائية (التيار المستمر والتيار المتناوب) للخليط البوليمري والمتراكبات النانوية ($PC-PS/SiC-MnO_2$) و($PC-PS/SiC-Co_2O_3$) وتطبيقاتها في الأنشطة المضادة للبكتيريا والتحلل الضوئي ومستشعرات الضغط .

أظهرت نتائج التحليل الطيفي لتحويل فوريير (FT-IR) بأنهُ لا توجد تفاعلات كيميائية بين الأساس البوليمري والجسيمات النانوية (SiC/MnO_2) و (SiC/Co_2O_3). وكما تم تحليل المورفولوجية السطحية بوساطة المجهر البصري (OM) والمجال المنبعث للمجهر الإلكتروني الماسح (FE-SEM) والتي أظهرت تجانساً جيداً وقد تم توزيعها بشكل موحد في جميع أنحاء الخليط البوليمري (PC/PS) .

تمت دراسة الخصائص البصرية للخليط البوليمري والمتراكبات النانوية في مدى الطول الموجي (260-860) نانومتر . أظهرت النتائج التجريبية زيادة الامتصاصية ومعامل الامتصاص وطاقة أورباخ ومعامل الانكسار ومعامل الخمود وثابت العزل (الحقيقي والخيالي) والتوصيلية البصرية للمتراكبات النانوية بزيادة التراكيز النانوية المضافة (SiC/MnO_2) و (SiC/Co_2O_3) ، بينما تناقصت النفاذية وعمق الاختراق وفجوة الطاقة مع زيادة التراكيز للجسيمات النانوية المضافة (SiC/MnO_2) و (SiC/Co_2O_3) .

أظهرت النتائج إن الموصلية الكهربائية (التيار المستمر) للمتراكبات النانوية تزداد مع زيادة تراكيز الجسيمات النانوية والمضافة (SiC/MnO_2) و (SiC/Co_2O_3) ودرجة الحرارة . كما تم دراسة الخصائص الكهربائية (التيار المتناوب) عند درجة حرارة الغرفة القياسية في مدى تردد ($100-5\times10^6$) هيرتز . أظهرت النتائج التجريبية إن ثابت العزل الكهربائي والفقدان العزلي والتوصيلية الكهربائية قد ازدادت مع زيادة التراكيز النانوية (SiC/MnO_2) و (SiC/Co_2O_3) . كما إنخفض ثابت العزل

الكهربائي والفقدان العزلي الكهربائي للمتراكبات النانوية مع زيادة تردد المجال الكهربائي المطبق بينما زادت التوصيلية الكهربائية (التيار المتناوب) مع زيادة التردد والتراكيز النانوية المضافة (SiC/MnO_2) و (SiC/Co_2O_3) .

تم اختبار الأنشطة المضادة للبكتيريا للخليط البوليمري والمتراكبات النانوية الحيوية ضد مسببات الأمراض (Staphylococcus aureus) كبكتيريا إيجابية الكرام ، و (Salmonella enterica) كبكتيريا سالبة الكرام .أظهرت النتائج أن قطر منطقة التثبيط يزداد مع زيادة نسبة وزن إضافات الجسيمات النانوية (SiC/MnO_2) و (SiC/Co_2O_3) ، كما أن البكتيريا موجبة الكرام لديها مقاومة أكبر لهذه الجسيمات النانوية مقارنة بالبكتيريا سالبة الكرام. أظهرت النتائج أن الفعالية القوية التي تكون منطقة التثبيط تزداد بزيادة تراكيز الجسيمات النانوية (SiC/MnO_2) و (SiC/Co_2O_3) .

انخفضت امتصاصية صبغة برتقال الميثيلين مع إضافة تراكيز الجسيمات النانوية (SiC/MnO_2) و (SiC/Co_2O_3) . كما أن امتصاصية صبغة برتقال الميثيلين للخليط البوليمري والمتراكبات النانوية الحيوية تتناقص مع زيادة وقت التشعيع. تزداد نسب التحلل الضوئي للمركبات النانوية مع زيادة وقت التشعيع مما يؤدي إلى زيادة التفاعل التحفيزي الضوئي وتقليل إعادة التركيب إلكترون/فجوة. أظهرت النتائج أن النشاط التحفيزي الضوئي للمتراكبات النانوية قد زاد مع زيادة تراكيز الجسيمات النانوية . وجد أن أفضل نشاط تحفيزي ضوئي للمركبات النانوية ($PC-PS/SiC-Co_2O_3$) كان 27.94% خلال 30 دقيقة و 73.26% خلال 90 دقيقة عند التركيز (5.2 wt.%) من الجزيئات النانوية (SiC/Co_2O_3) . نتيجة لذلك ، فإن المتراكبات النانوية لها تحلل ضوئي جيد للملوثات العضوية.

تمت دراسة قياسات مستشعرات الضغط للمتراكبات الحيوية في نطاق الضغط المطبق (80-160) بار باستخدام نظام محلي الصنع عالي الحساسية. أظهرت النتائج أن السعة الكهربائية للمتراكبات النانوية تزداد مع زيادة تراكيز المواد المضافة والضغط المطبق. من خلال قياسات خصائص الاستشعار للمتراكبات النانوية لـ 160 بار ، يتضح أن المتراكبات النانوية هي مستشعر جيد لهذا الضغط. وجد أن أفضل حساسية للمتراكبات النانوية ($PC-PS/SiC-MnO_2$) هي 69.85% عند التركيز (5.2 wt.%) ونتيجة لذلك فإن المتراكبات النانوية ($PC-PS/SiC-Co_2O_3$) لديها حساسية أعلى للضغط .

جمهورية العراق
وزارة التعليم العالي والبحث العلمي
جامعة بابل
كلية التربية للعلوم الصرفة
قسم الفيزياء

تصنيع متراكبات نانوية حيوية جديدة وتطبيقاتها الحديثة في المجالات البيئية

إطروحة مقدمة
إلى مجلس كلية التربية للعلوم الصرفة في جامعة بابل
وهي جزء من متطلبات نيل درجة الدكتوراه فلسفة في التربية / الفيزياء

من قبل الطالب

مهند حسن متعب فليفل

بكالوريوس تربية / علوم (الفيزياء)
جامعة بابل ٢٠١٠ م

ماجستير علوم في الفيزياء
جامعة بابل ٢٠١٨ م

بأشراف

أ.د. بهاء حسين صالح ربيع

أ.د. أحمد هاشم محيسن حمد

١٤٤٥ هـ ٢٠٢٣ م